CONSTRAINTS ON THE GENESIS OF LODE-STYLE TIN MINERALIZATION: EVIDENCE FROM THE SAN RAFAEL TIN-COPPER DEPOSIT, PERU

Michal S.J. Mlynarczyk

Department of Earth & Planetary Sciences
McGill University, Montreal

March 2005

A thesis submitted to McGill University in partial fulfillment of the requirements of the degree of Doctor of Philosophy

The late Boleslaw Mlynarczyk (third from the right) in the company of his students, after a lecture at the Institut Agronomique et Vétérinaire Hassan II, in Rabat, Morocco, in the early 1980s.

I dedicate this work to my late, beloved father, **Boleslaw Mlynarczyk** (1935-2000) who supported me so much at its beginnings, but sadly did not have the chance to witness its completion.

Once upon a time, in a far away land

We walked together hand in hand

You taught me everything you knew

And, thus, I owe to you who I now am.

Today, with a regret, when you're so early gone

I have to continue walking on my own

Reach the limits of knowledge and move every stone

Both for you and for me raise a new dawn...

ABSTRACT

Fluid evolution at the Peruvian San Rafael deposit, which represents the world's largest hydrothermal tin lode was marked by two contrasting episodes. The early stage, characterized by intense sericitic and tourmaline alteration was barren and produced numerous tourmaline-quartz veins, which are sealed and reflect largely lithostatic conditions of formation. A subsequent reopening of the vein-breccia system initiated the ore stage, which was characterized by a distinctive chloritic alteration and an open fracture-filling vein style. The first part of the ore stage was dominated by tin deposition and resulted in the formation of abundant cassiterite-quartz-chlorite-bearing veins and breccias, at depth in the lode. This was followed by copper deposition (with subordinate tin), which concentrated sulfide ores in the upper part of the vein system. The waning stages of hydrothermal activity superimposed late, barren quartz veins on earlier mineralization.

The $\delta^{34}S$ values of sulfide minerals from San Rafael range between +2 and +6 ‰, suggesting a large-scale hydrothermal system, supplied by a relatively homogenous, presumably magmatic source of sulfur. Stability relationships of the ore minerals indicate that the ore fluids were reducing, which is consistent with their capacity to transport significant quantities of tin.

Microthermometric studies of fluid inclusions in cassiterite, quartz, tourmaline and fluorite showed that the fluids responsible for the early, barren stage were hot, hypersaline magmatic brines (>340-535°C, 34-62 wt.% NaCl eq.), whereas the ore stage fluids had a moderate temperature and salinity (>230-360°C, 0-21 wt.% NaCl eq.). The local association of minor hematite with cassiterite, and the ubiquitous replacement of pyrrhotite by pyrite, marcasite and hematite, indicate that the ore fluids became progressively more oxidizing. In addition, the stable isotope compositions of tourmaline, cassiterite, wolframite, quartz, chlorite, calcite, and siderite reveal that the early fluid had a magmatic signature, but its $\delta^{18}O$ value markedly decreased with time. These trends are consistent with mixing of the ore fluids with a cooler, dilute fluid, enriched in the light oxygen isotope, and cannot be explained by boiling or simple cooling. Fluid-rock

interaction was not a control on tin deposition either, as chloritic alteration of granitic rocks increases the fluid acidity, and this in turn increases tin solubility.

I infer that the creation of several large fault-jogs at depth in the lode, synchronous with hydrothermal activity at the San Rafael igneous center, focused an influx of heated meteoric waters, which mixed with tin- and iron-rich magmatic brines. The oxidation, dilution, cooling and acid neutralization of the ore fluids destabilized chloride complexes of tin and iron, and triggered the massive precipitation of cassiterite with chlorite, in localized, high-grade ore shoots, as opposed to a dissemination of tin in the chloritic alteration.

The formation of the San Rafael deposit took place in Late Oligocene, at the onset of a major metallogenic episode in the Inner Arc of the Central Andes. We propose that Tertiary tin-tungsten(-silver) mineralization in this province (and possibly some of the earlier metallogenic episodes) was produced by a recurrent compressional interaction between the Farallon/Nazca oceanic plate and the South American continent. Periodic "collisions" between the tectonic plates were focused on this segment of the Andean orogen and generated in its back arc voluminous peraluminous magmas, which evolved by fractional crystallization and exsolved the fluids responsible for the rich Sn-W(-Ag) mineralization.

RÉSUMÉ

Le gîsement péruvien San Rafael, le plus riche gîsement d'étain de type filonien au monde, s'est formé en deux étapes, caractérisées par un hydrothermalisme bien différent. Le stage précoce, dominé par des conditions lithostatiques, a intensément séricitisé et tourmalinisé les roches encaissantes et a produit de nombreux filons à quartz et tourmaline qui, toutefois, ne contiennent pas d'étain. Une fracturation tectonique du système filonien a suivi et a donné lieu au stage minéralisant, caractérisé par une très forte chloritisation de l'encaissant et des filons de type ouvert, typiques de conditions hydrostatiques. Après une période de formation de riche minéralisation d'étain qui, sous forme de filons et de brèches à cassitérite, quartz et chlorite, occupe la partie inférieure du

gîsement, un dépôt de sulfures de cuivre (avec de la cassitérite mineure) a eu lieu dans la partie supérieure du système filonien. Finalement, le stage tardif de l'hydrothermalisme fut dominé par la formation de nombreux filons de quartz, superposés aux filons des stages précédents.

Les valeurs de $\delta^{34}S$ des sulfures de San Rafael sont entre +2 et +6 ‰, ce qui suggère leur formation dans un système hydrothermal à grande échelle, et avec une source de soufre relativement homogène, probablement d'origine magmatique. Les relations de stabilité entre les sulfures indiquent que les fluides minéralisateurs avaient un caractère réducteur, ce qui explique bien leur capacité à transporter une grande quantité d'étain.

L'étude microthermométrique des inclusions fluides contenues dans la cassitérite, le quartz, la tourmaline et la fluorite indique que, pendant le stage précoce des solutions magmatiques très chaudes et très salines (>340-535°C, 34-62 wt.% NaCl eq.) circulaient dans le système. A l'opposé, les fluides minéralisateurs étaient de température et de salinité moyennes (>230-360°C, 0-21 wt.% NaCl eq.). L'association locale d'hématite avec la cassitérite, ainsi que le très commun remplacement de la pyrrhotite par la pyrite, la marcasite, et l'hématite indiquent que les fluides minéralisateurs étaient sujets à une oxidation croissante. Par ailleurs, la composition des isotopes stables de la tourmaline, de la cassitérite, de la wolframite, du quartz, de la chlorite, et des carbonates indiquent que les fluides précoces avaient une signature isotopique magmatique, mais que la valeur de $\delta^{18}O$ des fluides minéralisateurs diminuait progressivement. Ces tendances, qui ne peuvent être expliquées par l'ébullition des fluides précoces ou leur simple refroidissement, suggèrent qu'ils ont subi un mixage avec des fluides plus froids, de moindre salinité, et appauvris en ^{18}O. L'interaction des fluides minéralisants avec les roches encaissantes n'a pas non plus causé la précipitation de l'étain, car la chloritisation des roches granitiques augmente l'acidité des fluides et, par conséquent, augmente la solubilité de l'étain.

Nous estimons qu'une fracturation tectonique majeure a eu lieu durant l'activité hydrothermale reliée à l'intrusion granitique de San Rafael. Ceci a causé un afflux soudain d'eaux météoriques dans les espaces ainsi créés et leur mixage intense avec les

fluides magmatiques salins, riches en fer et en étain. L'oxidation, la dilution, le refroidissement et la neutralisation de l'acidité des fluides minéralisateurs ont déstabilisé les chlorures d'étain et de fer et causé une précipitation massive de cassitérite et de chlorite. Ceci a donné lieu à des corps de minerai localisés, à l'opposé d'une minéralisation disséminée dans la zone de chloritisation.

La formation du gisement de San Rafael a eu lieu à l'Oligocène, et a marqué le début d'un épisode métallogénique majeur dans la Cordillère Orientale des Andes Centrales. Nous estimons que la minéralisation d'âge Tertiaire en étain, tungstène et argent de cette province (et possiblement certains des épisodes métallogeniques précédents) a été le produit d'interactions compressives répétées entre la plaque de Nazca/Farallon et le continent Sud-Américain. La région des Andes Centrales a ainsi subi des "collisions" périodiques entres ces deux plaques tectoniques, ce qui a donné lieu à la génération de grands volumes de magmas péralumineux dans l'arrière-arc de l'orogène. Ces magmas ont ensuite évolué par cristallisation fractionnée et ont séparé les fluides responsables de la riche minéralisation de Sn-W-(Ag) de cette région.

ACKNOWLEDGEMENTS

I wish to express my most sincere thanks to my indefatigable supervisor, Professor Anthony E. Williams-Jones, for pointing to me, years ago, the existence of the remarkable San Rafael deposit and offering me to study its genesis as the subject of my doctoral research. I am grateful for his encouragement and enthusiasm, for patiently reviewing my work, and for his most precious advice and support, which more than once extended well beyond science.

I wish to thank the faculty, staff and students of the Earth & Planetary Sciences Department, who made this long stay overseas enjoyable for me and provided friendship and laughter, when it was most needed. In particular, I owe a lot to my closest friends Ardeshir Hezarkhani, David Dolejš, Thomas Wagner and Oliver Schatz (in the order I met them), to mention just a few... In addition, I wanted to thank Aldemar Arze-Rodriguez from Bolivia, for his steadfast moral support over a very long distance. Gracias Hermano !

Last, but not least, I would not have made it this far, had it not been for the constant, loving support of my Parents, Hanna and Boleslaw Mlynarczyk, with whom we always maintained a daily e-mail exchange, that was extremely precious during difficult times. I wish to especially thank my late Father, an academic himself, who accompanied me with his thoughts at the onset of this long endeavor, but was not granted the chance to see its fullfillment. He is most truly missed.

TABLE OF CONTENTS

CONTRIBUTIONS OF AUTHORS

The research presented in this thesis is the outcome of a collaboration between the author and his advisor, Professor Anthony E. Williams-Jones. The thesis is divided into seven chapters, one of which has been published (Chapter 2) and four of which are manuscripts intended for publication. The remaining two chapters are a general introduction and a conclusion. Each manuscript is co-authored by Prof. A.E. Williams-Jones, who provided advice on research methodology, helped evaluate and interpret the data and critically reviewed the text. Dr. R. Sherlock is the second author of Chapter 2. He provided useful information on surface geology and some structural data on the uppermost part of the San Rafael deposit. Dr. D. Dolejš is the second author of Chapter 3, for which he recalculated the microprobe analyses of silicate minerals and the normative mineralogy of alteration profiles. He also assisted with some aspects of the thermodynamic calculations (mixing properties of silicate solid solutions) and provided helpful comments on the manuscript. Dr. T. Wagner is the second author of Chapter 5. He carried out the sulfur, oxygen and carbon isotope analyses and modeled the effect of cooling and fluid mixing on the oxygen isotope composition of ore and gangue minerals.

Field work, including surface and underground mapping, structural analysis, core logging and the collection of an extensive 1,700 kg of samples were carried out by the author in the summers of 1997 and 1999. The preparation of wall-rock and mineral samples for chemical analysis, host-rock and ore petrography, fluid inclusion studies, and preparation of samples for stable isotope analysis were carried out by the author, who is also responsible for interpretation of the data, thermodynamic modeling, drafting of figures, and writing of papers.

Electron microprobe analyses were conducted by the author with the assistance of G. Poirier and, subsequently, Lang S. Major element compositions of whole rocks were analysed using X-ray fluorescence by T. Ahmedali at the Department of Earth and Planetary Sciences, McGill University. Trace and rare earth elements were analyzed by ICP-MS by Dr. E. Hoffmann at Activation Laboratories, Ancaster, Ontario. Hydrogen isotope analyses were determined by Dr. K. Kyser at Queen's University in Kingston, Ontario.

CHAPTER I

General Introduction

INTRODUCTION

Large-scale, structurally complex, cassiterite-bearing hydrothermal veins are referred to as tin lodes and are commonly characterized by very high grade (1-5 wt.% Sn) and tonnage, making them economically the most important type of primary tin deposit. Although their geology has been well described (e.g., Taylor, 1979; Hosking, 1988), much less is known about key issues related to their genesis, such as the source of the tin and associated metals, the timing of hydrothermal processes, the origin of the ore fluids, and the controls on ore deposition. As Eugster (1986) pertinently remarked (paraphrasing the saying about famous men and their women: "behind every important mineral, there once was a fluid"), the key to understanding the genesis of high-grade tin mineralization lies in investigating the physical and chemical evolution of the ore fluids, which deposited it. With this in mind, the San Rafael tin-copper deposit, located in the high Andes of the Eastern Cordillera of SE Peru and considered the largest lode-type tin deposit in the world was selected as a particularly suitable natural laboratory, where different genetic scenarios could be tested. A comprehensive investigation of the deposit's structural geology, host-rock petrology, hydrothermal alteration and mineralization was undertaken and the results available to date are presented in this thesis.

Overview of hydrothermal tin lodes

Lode-type tin deposits typically occur in orogenic belts (e.g., those of Bolivia, Cornwall, Russian Far East or Tasmania) and are associated with the roof zones and margins of shallow-level, reduced, S-type granitoid plutons (Taylor, 1979; Hosking, 1988; Lehmann, 1990). The mineralization is spatially associated with the stocks of later (more evolved) granitic phases, which are commonly represented by biotite and/or muscovite leucogranites and are geochemically specialized, i.e., enriched in tin and other incompatible elements (e.g., B, F, Cl, Li, Be, P, W, Sb, Nb, Ta and U). Thus, their average tin content is commonly between 15-30 ppm, versus 3-3.5 ppm in "ordinary" granites (Lehmann, 1982; 1990). The tin lodes consist of fracture fillings and/or replacement bodies, and typically occur as part of extensive vein-breccia systems, which

crosscut the host granitoids and the surrounding (meta-)sedimentary rocks. The lodes have strike lengths of up to several kilometers, vertical extents from several hundred to over a thousand meters, and widths from tens of centimeters to more than 15 meters. The ore typically occurs in well-defined shoots, commonly grading more than 1 % Sn and is associated with the steepest dips (Hosking, 1951; Turneaure, 1971; Taylor, 1979; Sinclair, 1995). Prolonged brittle deformation produces repetitive, selective reopening of the lodes and results in their mineralogical and textural complexity. The lodes commonly have a laminated and/or brecciated fabric, and locally are manifested by dense veining of the wall-rock. They display vertical mineralogical zoning with cassiterite (SnO_2) occurring in their deepest parts, followed upwards by arsenopyrite and wolframite, then chalcopyrite and Fe-rich sphalerite, and finally galena, sphalerite, Ag sulfides and sulfosalts at the shallowest levels. Hydrothermal alteration is restricted to the proximity of the lodes and rarely extends farther than a few meters. In general, early sericitization is followed by tourmalinization and later by chloritization and hematitization, which are broadly coeval. Extensive silicification is also very common, and can occur at any stage of this temporal sequence. The different alteration types are generally superimposed or very close to each other, with the exception of hematitization, which, if present, may extend up to 10 meters away from the lodes (Taylor, 1979; Hosking, 1988). The principal mineral of tin is cassiterite, which occurs in several varieties (wood-tin, needle tin, massive botryoidal cassiterite). Other tin minerals, such as stannite, are present in relatively small proportions. The gangue mineral is quartz, but chlorite, tourmaline, sericite and sulfides may also be present in appreciable proportions (Hosking, 1951; Hosking et al., 1987; Taylor, 1979).

The ore fluids responsible for the formation of vein/lode tin deposits are believed to transport most of the tin in its reduced form (Sn^{2+}), mostly as chloride complexes, and less commonly as hydroxy- and fluoride complexes. Experimental studies indicate that the precipitation of cassiterite is likely triggered by decreases in temperature and ligand ion activity, and increases in pH and fO_2 (Eugster and Wilson, 1985; Jackson and Helgeson, 1985; Pabalan 1986; Taylor and Wall, 1993; Müller and Seward, 2001). Cassiterite deposition is typically inferred to take place between 480 and 280°C, from

acidic aqueous fluids with a low to moderate salinity, i.e., 5-25 wt % NaCl eq. (Kelly and Turneaure, 1970; Pirajno, 1992).

Despite much being already known about this type of tin deposit, there is still a considerable debate about various aspects of their genesis. Thus, ore metals such as tin and tungsten could be partitioned directly from an evolved granitic melt into a magmatic aqueous phase or could be leached from crystallized magmatic minerals by later fluids. On the other hand, copper and sulfur could be provided by periodic incursions of mafic melts, during episodes of bimodal magmatism, and could be transported largely by the vapour phase, as proposed by Heinrich et al. (1990, 1999). A variety of fluid types have been invoked to explain the formation of these deposits, e.g., primary magmatic fluids, meteoric waters, basinal brines, metamorphic fluids, and mixtures of the former; and various timings of their circulation and interaction have been proposed (e.g., Primmer, 1985; Alderton and Harmon, 1991; Farmer and Halls, 1993; Sheppard 1994; Wilkinson et al., 1995). Finally, mechanisms proposed for ore deposition include cooling, pressure decrease, boiling, fluid-rock interaction, redox-coupled precipitation, or the mixing of fluids of contrasting chemistry (Eadington, 1985; Heinrich and Eadington, 1986; Heinrich, 1990; 1995). This thesis aims at investigating some of the above problems and is part of an ongoing program of research, which has the long-term goal of building a comprehensive, quantitative genetic model applicable to hydrothermal tin lodes in general.

The San Rafael tin deposit

Hydrothermal tin lodes typically have very high ore grades (half of the deposits grade > 1.3 % Sn, and a tenth of them > 2.3 %), and most of them contain in excess of 1,000 t Sn, with some hosting > 50,000 t Sn (Menzie et al., 1988; Singer et al., 1993). Compared to most tin lodes, the Peruvian San Rafael Sn-Cu deposit, the subject of this thesis, is a giant member of this deposit clan. Hosting a total resource of ~1,000,000 t Sn (metal) and having an average grade of 4.7 wt.% Sn (Minsur, unpub. data, December 2002), it is responsible for ~13 % of the annual global hard-rock tin production (J. Carlin, USGS, written comm. 2000) and is considered the world's richest hydrothermal tin lode.

The deposit lies in the Cordillera Carabaya, a sub-unit of the Eastern Cordillera of southeastern Peru, in what is considered to be the northern extension of the Central Andean tin belt. This is a well-known, elongated metallogenic province, confined to the Inner Arc of the Andean orogen and extending for more than 1,000 km from southeastern Peru, through Bolivia, to northern Argentina. It hosts hundreds of Sn-W-(Ag-base metal) deposits of Late Triassic-Early Jurassic or mid-Tertiary age, several of which are world-class (e.g., Llallagua, Cerro Rico de Potosi, Oruro). The deposits are associated with felsic to intermediate, plutonic and subvolcanic rocks and typically consist of systems of rather small (< 1.5 km long), high-grade hydrothermal veins, exhibiting a diversified sulfide and sulfosalt mineralogy and a distinct metal zonation (Ahlfeld and Schneider-Scherbina, 1964; Kelly and Turneaure, 1970; Turneaure, 1971; Rivas, 1979; Urquidi-Barrau, 1989). In addition, southern Bolivia hosts giant, low-grade deposits referred to as "porphyry tin" deposits (so named after their similarity to porphyry copper deposits; *cf.* Sillitoe et al., 1975; Grant et al., 1980), in which the ores occur as disseminations, stockworks and breccia fillings.

In the San Rafael deposit, the high-grade mineralization is of the cassiterite-sulfide type, and the bulk of it is hosted by a large, vertically extensive, single complex vein, referred to as the San Rafael lode. This lode is part of a vein-breccia system, which is centered on a Late Oligocene granitoid stock, shallowly emplaced in Lower Paleozoic clastic metasedimentary rocks. The tin ores form cassiterite-quartz-chlorite-bearing veins and breccias, hosted by several large fault-jogs at depth in the lode. By contrast, the copper ores, which contain disseminated acicular cassiterite, are localized in the upper part of the system. Both ore types are associated with a very distinctive strong chloritic alteration, which was preceded by intense sericitization, tourmalinization and tourmaline veining.

The San Rafael lode is not only remarkable because of its unusually rich tin resource, but also because it is very young (~25 Ma), therefore, remained undisturbed by any later processes, and exhibits rich tin-copper ores over a vertical extent of > 1,300 m, allowing a fresh, unprecedented insight into a deposit of this type. Owing to intense mining activity by MINSUR S.A. over the past four decades, this exceptional deposit is presently very well exposed. Nevertheless, prior to the research presented in this thesis,

no studies had been conducted on the deposit site since the early 1980s, because of political instability in the region (i.e., the presence of the "Shining Path" guerilla). Thus, previous research on the deposit (Arenas, 1980; Palma, 1981; Clark et al., 1983; Kontak and Clark, 1988; Kontak and Clark, 2002) was largely limited to surface geology, the granitic host rocks and the deposit's uppermost, copper-rich part.

THESIS ORGANIZATION

This thesis is divided into six chapters, five of which (Chapters 2 to 6) are manuscripts. Chapter 2 presents the structural geology of the San Rafael deposit and an overview of its alteration and paragenesis. It suggests that both tin and copper mineralization were introduced during a single, protracted hydrothermal event, albeit with copper being paragenetically later than tin, and that the rich ore-shoots at depth in the lode represent large fault-jogs, created by sinistral-normal, strike-slip movement. It also proposes a tentative genetic model, according to which these fault-jogs focused synkinematic magmatic fluids and permitted their effective mixing with meteoric waters, leading to an in-situ oxidation of the tin transported by the ore fluids and its massive precipitation as cassiterite in localized, high-grade orebodies.

Chapters 3 and 4 investigate in detail the alteration styles developed in the deposit. Chapter 3 outlines the existence of two discrete hydrothermal episodes (early sericitization + tourmalinization, versus ore-stage chloritization) and characterizes quantitatively the associated mass-transfer and alteration mineralogy. It also establishes important physico-chemical constraints on the fluid evolution and suggests that ore deposition took place from fluids, which were the product of mixing of early, hypersaline magmatic brines with meteoric waters, rather than a separate hydrothermal pulse, exsolved from a discrete injection of granitic magma. Chapter 4 examines the multiple generations of vein and alteration tourmaline, a ubiquitous mineral in the early stages of the paragenesis. It demonstrates that tourmaline composition evolved in time from magnesian to iron-rich and confirms the observation from Chapter 3, that cassiterite precipitated from strongly Fe-rich fluids.

Chapter 5 presents an extensive study of the stable isotope (S,O,H,C) composition of ore and gangue minerals from San Rafael, combined with microthermometric studies of fluid inclusions. It establishes that the hydrothermal system was very homogenous, with a clear magmatic signature and constrains the physico-chemical conditions of ore deposition. The evidence that ore fluid temperature and salinity fluctuated markedly in time, becoming cooler, very dilute, and isotopically lighter (O), strengthens the hypothesis that ore deposition took place upon mixing of tin-rich fluids of magmatic origin with heated meteoric waters.

Finally, Chapter 6 places the San Rafael deposit in the broader context of the Tertiary Central Andean metallogeny, for which a new geotectonic model is proposed. The case is made that periodic compressional interactions took place between the South American plate and the Nazca slab and sub-slab mantle during the ongoing Andean orogeny. These recurrent "collisions", were focused in the Inner Arc region and led to the generation of voluminous, peraluminous magmas, which upon fractional crystallization exsolved the fluids responsible for rich Sn-W mineralization.

REFERENCES

Ahlfeld F and Schneider-Scherbina A (1964) Los yacimientos minerales y de hidrocarburos de Bolivia. Bol Esp Dept Nac Geol (Bol) 5, 388 p

Alderton DHM and Harmon RS (1991) Fluid inclusion and stable isotope evidence for the origin of mineralizing fluids in south-west England. Mineral Mag 55: 605-611

Arenas MJ (1980) El distrito minero San Rafael, Puno: estaño en el Perú. Bol Soc Geol Peru 6: 1-12

Clark AH, Palma VV, Archibald DA, Farrar E, Arenas MJ, and Robertson RCR (1983) Occurrence and age of tin mineralization in the Cordillera Oriental, Southern Peru. Econ Geol 78: 514-520

Eadington PJ (1985) The solubility of cassiterite in hydrothermal solutions in relation to some lithological and mineral associations of tin ores. *In:* Recent Advances in the

Geology of Granite-Related Mineral Deposits, Taylor RP and Strong DF (eds), Can Inst Mining and Metall, Spec Vol 39: 25-32

Eugster HP (1986) Minerals in hot water. Am Mineral 71: 655-673

Eugster HP and Wilson GA (1985) Transport and deposition of ore-forming elements in hydrothermal systems associated with granites. *In:* High heat production (HHP) granites, hydrothermal circulation and ore genesis, Halls C (chairman), Inst Mining and Metall Conference, (London), 87-98

Farmer CB and Halls C (1993) Paragenetic evolution of cassiterite-bearing lodes at South Crofty Mine, Cornwall, United Kingdom. *In:* Proceedings of the 8th IAGOD Symposium, Ottawa 1990, Maurice Y (ed.) E. Schweizerbart'sche Verlagsbusch-handlung, (Stuttgart), 365-382

Grant JN, Halls C, Sheppard SMF, and Avila W (1980) Evolution of the porphyry tin deposits of Bolivia. Mining Geol Spec Iss 8: 151-173

Heinrich CA (1990) The chemistry of hydrothermal tin (-tungsten) ore deposition. Econ Geol 85: 457-481

Heinrich CA (1995) Geochemical evolution and hydrothermal mineral deposition in Sn (-W-base metal) and other granite-related ore systems: some conclusions from Australian examples. *In:* Magmas, fluids and ore deposits, Thompson JFH (ed), MAC Short Course 23: 203-220

Heinrich CA and Eadington PJ (1986) Thermodynamic predictions of the hydrothermal chemistry of arsenic, and their significance for the paragenetic sequence of some cassiterite-arsenopyrite-base metal sulfide deposits. Econ Geol 81: 511-529

Heinrich CA, Ryan CG, Mernagh TP and Eadington PJ (1990) Segregation of ore metals between magmatic brine and vapor: a fluid inclusion study using PIXE microanalysis. Econ Geol 87: 1566-1583

Heinrich CA, Günther D, Audétat A, Ulrich T, and Frischknecht R (1999) Metal fractionation between magmatic brine and vapor, determined by microanalysis of fluid inclusions. Geology 27: 755-758

Hosking KFG (1951) Primary ore deposition in Cornwall. Trans R Geol Soc Cornwall 18: 309-356

Hosking KFG (1988) The world's major types of tin deposit. *In:* Geology of tin deposits in Asia and the Pacific - selected papers from the International Symposium on the Geology of Tin Deposits, Nanning, China, October 1984, Hutchison CS (ed), 3-49

Hosking KFG, Stanley GJ, and Camm GS (1987) The occurrence, nature and genesis of wood tin in South-west England. Trans Royal Geol Soc Cornwall 21: 153-212

Jackson KJ and Helgeson HC (1985) Chemical and thermodynamic constraints on the hydrothermal transport and deposition of tin: I. Calculation of the solubility of cassiterite at high pressures and temperatures. Geochim et Cosmochim Acta 49: 1-22

Kelly WC and Turneaure FS (1970) Mineralogy, paragenesis and geothermometry of the tin and tungsten deposits of the Eastern Andes, Bolivia. Econ Geol 65: 609-680

Kontak DJ and Clark AH (1988) Exploration criteria for tin and tungsten mineralisation in the Cordillera Oriental of southeastern Peru. *In:* Recent Advances in the Geology of Granite-Related Mineral Deposits, Taylor RP and Strong DF (eds), Can Inst Mining and Metall, Spec Vol 39: 157-169

Kontak DJ and Clark AH (2002) Genesis of the giant, bonanza San Rafael lode tin deposit, Peru: origin and significance of pervasive alteration. Econ Geol 97: 1741-1777

Lehmann B (1982) Metallogeny of tin: magmatic differentiation versus geochemical heritage. Econ Geol 77: 50-59

Lehmann B (1990) Metallogeny of tin. Lecture Notes in Earth Sciences 32, Springer-Verlag, Berlin, 211 p

Menzie WD, Reed BL, and Singer DA (1988) Models of grades and tonnages of some lode tin deposits. *In:* Geology of tin deposits in Asia and the Pacific - selected papers from the International Symposium on the Geology of Tin Deposits, Nanning, China, October 1984, Hutchison CS (ed), 73-88

Müller B and Seward TM (2001) Spectrophotometric determination of the stability of tin (II) chloride complexes in aqueous solution up to 300°C. Geochim et Cosmochim Acta 65: 4187-4199

Pabalan RT (1986) Solubility of cassiterite (SnO_2) in NaCl solutions from 200°C - 350°C, with geologic applications. Unpub PhD thesis, Pennsylvania State University, U.S.A., 141 p

Palma VV (1981) The San Rafael tin-copper deposit, Puno, SE Peru. Unpub M.Sc. thesis, Queen's University, Kingston, Ontario, Canada, 235 p

Pirajno F (1992) Hydrothermal mineral deposits: principles and fundamental concepts for the exploration geologist. Springer-Verlag, 709 p

Primmer TJ (1985) Discussion on the possible contribution of metamorphic water to the mineralising fluid of south-west England: preliminary stable isotope evidence. Proc Ussher Soc 6: 224-228

Rivas S (1979) Geology of the principal tin deposits of Bolivia. Geol Soc Malaysia Bull 11: 161-180

Sheppard SMF (1994) Stable isotope and fluid inclusion evidence for the origin and evolution of hercynian mineralizing fluids. *In:* Metallogeny of collisional orogens; Seltmann R, Kämpf H, and Möller P (eds.), Czech Geological Survey, Prague, 49-60

Sillitoe RH, Halls C, and Grant JN (1975) Porphyry tin deposits in Bolivia. Econ Geol 70: 913-927

Sinclair WD (1995) Vein-stockwork tin, tungsten. In: Eckstrand OR, Sinclair WD, Thorpe RI (eds) Geology of Canadian Mineral Deposit Types. Geol Surv Canada, Geology of Canada 8: 409-420

Singer DA, Mosier DL, and Menzie DW (1993) Digital Grade and Tonnage Data for 50 Types of Mineral Deposits, Macintosh version. USGS open-file report 93-0280, USGS, Reston, VA

Taylor RG (1979) Geology of tin deposits. Developments in Economic Geology 11, Elsevier, 543 p

Taylor JR and Wall VJ (1993) Cassiterite solubility, tin speciation and transport in a magmatic aqueous phase. Econ Geol 88: 437-460

Turneaure FS (1971) The Bolivian tin-silver province. Econ Geol 66: 215-225

Urquidi-Barrau F (1989) Tin and tungsten deposits of the Bolivian tin belt. *In:* Geology of the Andes and its relation to hydrocarbon and mineral resources. Circum-Pacific

Council for Energy and Mineral Resources Earth Science Series 11, Ericksen GE, Cañas Pinochet MT, and Reinemund JA, (eds), V Houston, Texas, 313-323

Wilkinson JJ, Jenkin GRT, Fallick AE, and Foster RP (1995) Oxygen and hydrogen isotopic evolution of Variscan crustal fluids, south Cornwall, U.K. Chem Geol 123: 239-254

CHAPTER II

San Rafael, Peru: geology and structure
of the worlds richest tin lode

M.S.J. Mlynarczyk, R.L. Sherlock and A.E. Williams-Jones

ABSTRACT

The San Rafael mine exploits an unusually high grade, lode-type Sn-Cu deposit in the Eastern Cordillera of the Peruvian Central Andes. The lode is centered on a shallow-level, Late Oligocene granitoid stock, which was emplaced into early Paleozoic metasedimentary rocks. It has a known vertical extent exceeding 1,200 m and displays marked vertical primary metal-zoning, with copper overlying tin. The tin mineralization occurs mainly as cassiterite-quartz-chlorite veins and as cassiterite in breccias. The bulk of it is hosted by a K-feldspar megacrystic, biotite- and cordierite-bearing leucomonzogranite, which is the most distinctive phase of the pluton. Copper mineralization occurs predominantly in the veins that straddle the metasedimentary rock-intrusion contact or are hosted entirely by slates. Both tin and copper mineralization are associated with strong chloritic alteration, which is superimposed on an earlier episode of sericitization and tourmaline-quartz veining.

Based on the distribution of alteration and ore mineralogy, cassiterite deposition and subsequent chalcopyrite precipitation are believed to have been the result of a single, prolonged hydrothermal event. The source of the metals is inferred to be a highly evolved, peraluminous magma, related to the leucomonzogranitic phase of the San Rafael pluton. Sulfur may have been derived from the surrounding metasedimentary rocks. Preliminary fluid inclusion microthermometry suggests that ore deposition took place during the mixing of moderate and low salinity fluids, which were introduced in a series of pulses. Several large fault-jogs, created by sinistral-normal, strike-slip movement, are interpreted to have focused synkinematic magmatic fluids and permitted their effective mixing with meteoric waters. It is proposed that this mixing led to rapid oxidation of Sn (II) chloride species and caused supersaturation of the fluids in cassiterite, resulting in the development of localized, high-grade ore shoots. A favourable structural regime that promoted large-scale mixing of two fluids originating under very different physico-chemical conditions appears to have been the key factor responsible for the unusual richness of the deposit.
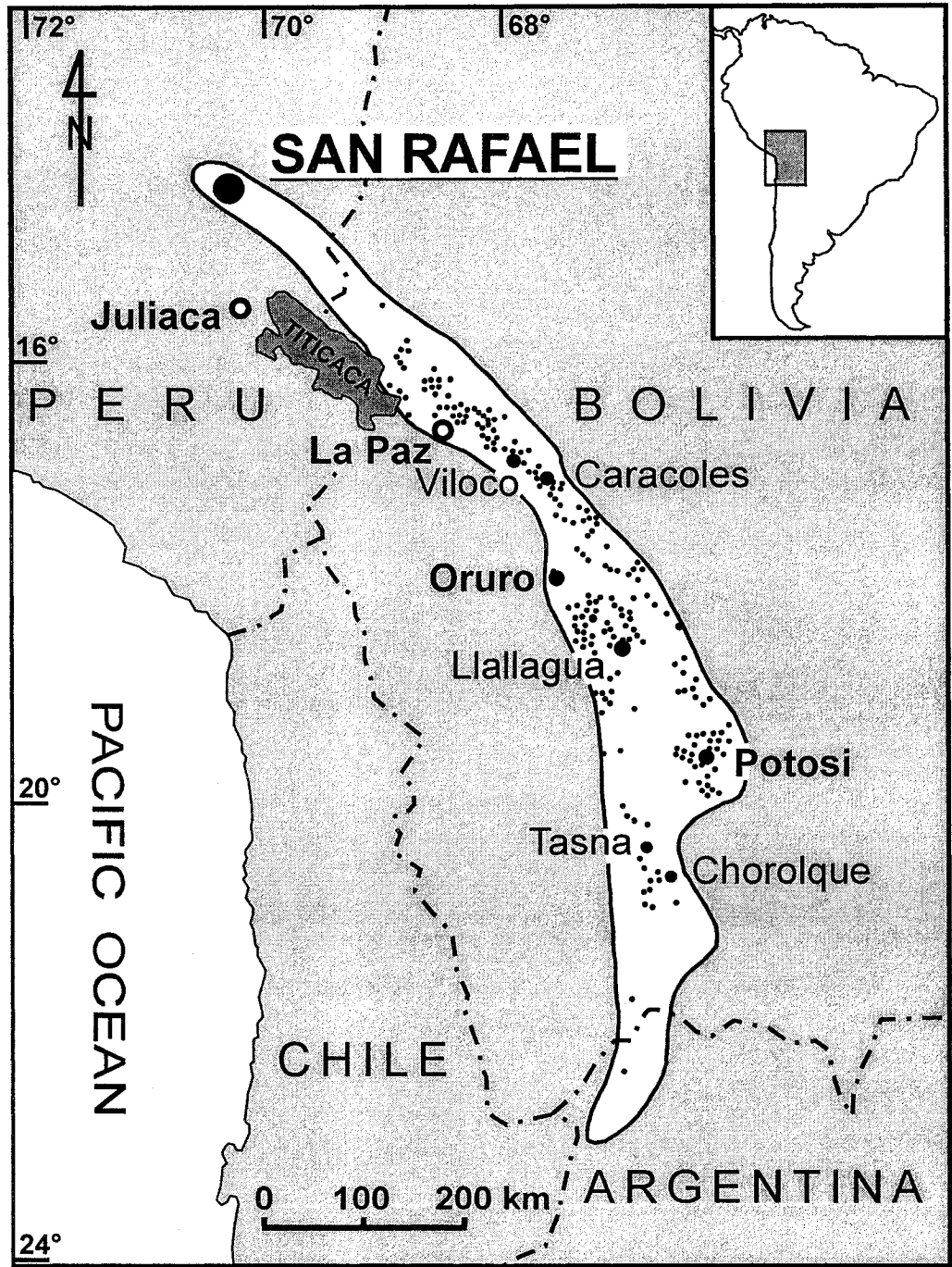
INTRODUCTION

San Rafael is a lode-type cassiterite-sulfide deposit, located in the northernmost extension of the Central Andean tin belt, in the department of Puno, southeastern Peru (Fig. 1). It crops out at elevations between 4,500 and 5,100 m, on the flanks of the glacier-capped Quenamari mountain (Fig. 2a, b). The mine is owned and operated by Minsur S.A., and has been worked for more than 40 years.

The deposit occurs in a NW-trending and NE-dipping composite vein system, spatially associated with a Late Oligocene (~25 Ma) granitoid intrusion. Although there are numerous subparallel veins in the district, a single complex vein, the San Rafael lode, hosts the bulk of the known mineralization, which is of unusually high grade. It is estimated that, prior to mining activity, the deposit had an average tin grade of 4.7 wt. %, and a total resource of ~1 million tonnes Sn (metal), making it the highest grade primary tin deposit in the world (Fig. 3). Proven and probable reserves are estimated at 13.9 million tonnes ore, grading 5.27 wt.% Sn and 0.16 wt.% Cu (Minsur, unpub. data, December 2000). Mining and processing of the ores has increased steadily from 500 tonnes/day in 1980 to 2,500 tonnes/day in 1999. Present production of 27,000 tonnes/year of tin metal represents ~13 % of the annual hard-rock production of tin globally (J. Carlin, USGS, written comm. 2000).

EXPLORATION AND MINING HISTORY

The exploration history of the San Rafael area dates back to 1913, when a German-Chilean company discovered copper mineralization on the northwestern slopes of the Quenamari mountain, which at the time was mainly covered by glaciers (Arenas 1980a, 1999). In 1947, prospector Rafael Avendaño outlined a copper deposit, which was subsequently named the San Rafael lode. Development of the near surface, high-grade copper mineralization commenced in 1958 when Lampa Mining Co. used the copper ore to blend with copper-silver ore from the nearby Berenguela deposit. In 1966, W.R. Grace & Co. purchased 67 % of Lampa Mining Co. and formed Minsur Sociedad de Responsabilidad Ltda. The company operated the deposit until 1977, when the Brescia

14

FIGURE 1. Location of the San Rafael Sn-Cu deposit in the Central Andean tin belt (outline and dots representing the major deposits are modified after Lehmann 1979; Claure and Minaya 1979).

SAN RAFAEL

72°   70°   68°

N

Juliaca

16°

TITICACA

P E R U   B O L I V I A

La Paz

Viloco   Caracoles

Oruro

Llallagua

20°

Potosi

Tasna

Chorolque

PACIFIC OCEAN

CHILE

0   100   200 km

A R G E N T I N A

24°

**FIGURE 2.** Geological setting: alteration and vein styles. **a** - View of the San Rafael mine. Glacier fields in the background are *on the left*: Nevado San Bartolome de Quenamari (5299 m) and *on the right*: Nevado San Francisco de Quenamari (5297 m). The present entrance to the mine (at 4533 m) and the mine plant are in the *lower right part* of the photograph, beside the Chocñacota lake (4500 m). Old waste dumps can be seen in the *middle left part* of the photograph. **b** - The San Rafael lode at the entrance of the 4820 adit. **c** - Porphyritic granitoid on the 4200 level, containing large, flow-oriented alkali-feldspar megacrysts. The scale is in cm. **d** - Strong, pervasive chloritization of the granitic wallrock on the 4225 level of the Ore Shoot. The only primary mineral remaining is quartz, visible as small white patches in the green groundmass. The scale is in cm. **e** - Barren, quartz-cemented "breccia-dyke" of angular wallrock fragments, hosted by tourmalinized wallrock on the 4225 level of the Ore Shoot. The scale is in cm. **f** - The Jorge vein as seen in the roof of the 4050 level. After an early stage of sericitization (best seen in the *upper part* of the photograph) and tourmalinization (along the vein margins), the vein was repeatedly opened and filled with quartz, chlorite and sulfides (mostly pyrite, see arrow). The vein width is ~25 cm (including the tourmalinization envelope). **g** - Subvertical cassiterite-quartz-chlorite vein crosscutting early tourmaline-quartz veins on the 4310 level of the Ore Shoot. Note the intense chloritic haloes around the quartz veins in the *lower central part* of the photograph. The scale is in cm. **h** - Late, barren quartz vein crosscutting the subvertical cassiterite-quartz-chlorite vein shown in g. The scale is in cm. **i** - Botryoidal tin ore from the mined-out zone of wood tin ores at an elevation of ~ 4450-4500 m. The scale is in cm. The wood tin ores at San Rafael represent the bulk of the wood tin known in the world (A.H. Clark, pers. comm.).

16

strong chlorite alteration of metasedimentary rocks

hangingwall

footwall

py
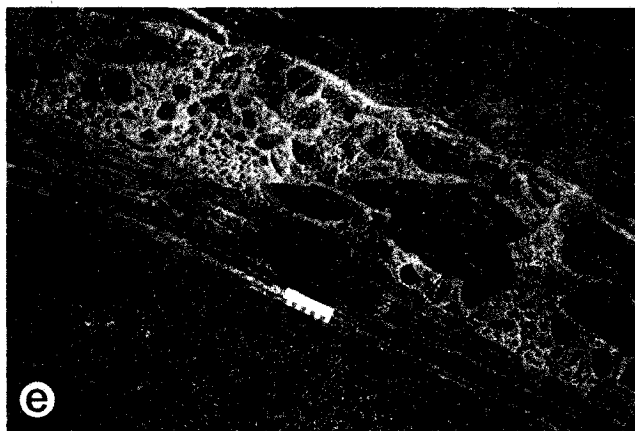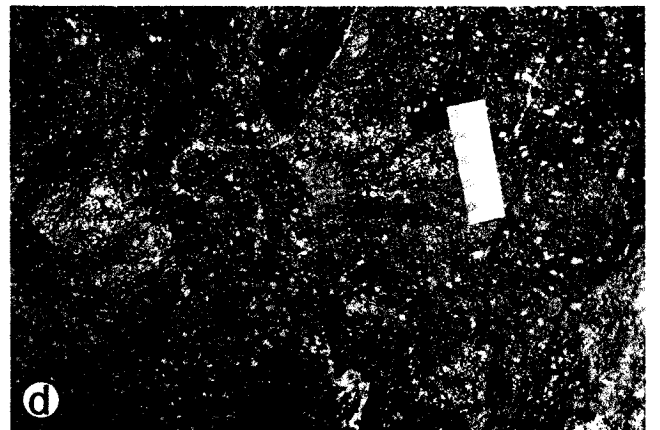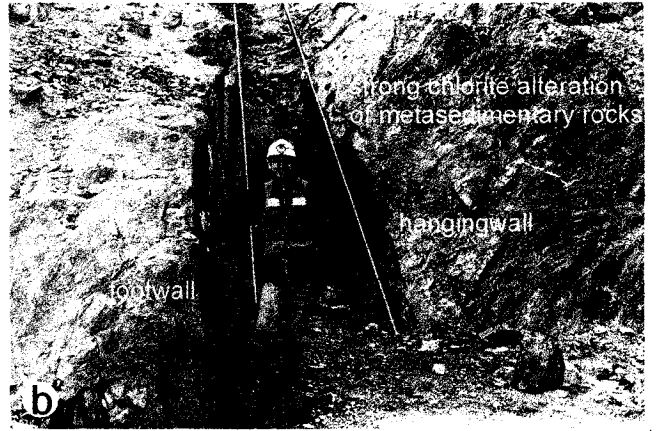
FIGURE 3. Grade versus tonnage for selected, large and high-grade, primary tin deposits. The deposit types are: 1 = lode, 2 = carbonate replacement, 3 = skarn, 4 = porphyry, 5 = greisen, 6 = rhyolite-hosted (Mexican type), 7 = VMS. Some deposits belong to more than one class. The outline of the circles is schematic. Data compiled from: Evans 1993; Singer et al. 1993; Sinclair 1995; Kirkham and Sinclair 1995; P Laznicka, pers. comm. 2000; Minsur, unpub. data.
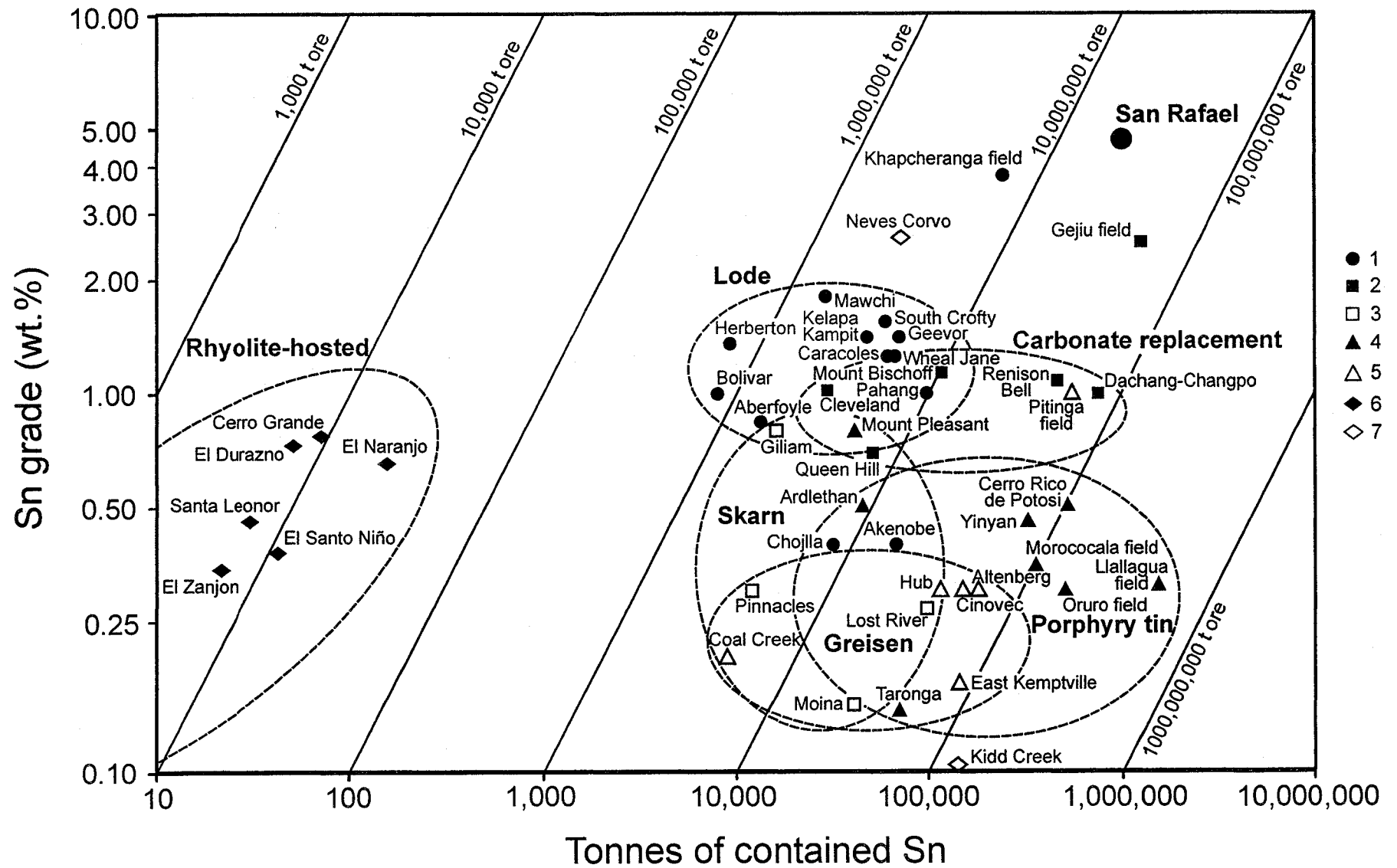
Group purchased Minsur and Lampa's shares, becoming 100 % owners and operators of San Rafael, as Minsur Sociedad Anonima.

During the initial period of development, mining was focused mainly on the near-surface copper orebody, as the underlying tin ore had not been discovered. In the late 1970s, copper grades were decreasing and the known mineralization was thought to terminate at about the 4533 m level (Arenas 1999). However, exploration and development work undertaken by Minsur S.A. in 1980 led to the discovery of several large tin orebodies grading as much as 15 wt.% Sn, below the 4533 m elevation. Continuing exploration has demonstrated the presence of high-grade tin ore down to the 3950 m level.

REGIONAL GEOLOGICAL SETTING

The San Rafael property lies within the Cordillera Carabaya of Peru, part of the Eastern Cordillera, which consists mainly of a thick sequence of marine sedimentary rocks. Throughout the Phanerozoic, this region underwent convergent plate interaction, orogeny and intermittent, mixed, mantle- and crust-derived bimodal magmatism (Clark et al. 1990). The stratigraphy of the area, described in detail by Laubacher (1978) and Kontak and Clark (1988), is shown schematically in Figure 4. The lower 10 - 15 km of the sequence is composed of early Paleozoic pelites and psammites (the San José, Sandía and Ananea Formations), which are inferred to overlie unexposed Precambrian gneissic basement. The early Paleozoic strata were deformed and metamorphosed to sub-greenschist facies in a Late Devonian - Early Carboniferous orogeny.

These rocks are unconformably overlain by a 3- to 4-km-thick succession of late Paleozoic psammites and carbonates (Mississippian Ambo Group, Pennsylvanian Tarma Group, and Permian Copacabana Group). Following a weak episode of deformation that lacked accompanying regional metamorphism, there was further sedimentation and intermittent alkaline volcanism from mid-Permian to Triassic times, which led to the accumulation of approximately 3 km of red beds and intercalated volcanic rocks (Mitu Group). The sequence is unconformably capped by a 1-km-thick sequence of Cretaceous psammites and carbonates (Cotacucho Group) and approximately 800 m of Miocene-

18

FIGURE 4. Schematic lithostratigraphic column for the Cordillera Carabaya, with indication of the major metallogenic episodes (modified after: Clark et al. 1983; Kontak et al. 1986; Kontak and Clark 1988; Kontak et al. 1990; Clark et al. 1990; Sandeman et al. 1995; Sandeman et al. 1996). Time scale from Okulitch 1999. The size of the symbols representing the intrusions, as well as the font of the corresponding mineralization (BM refers to base metals), are proportional to the importance of the magmatic / metallogenic event.

	Age (Ma)	System	Cordillera Carabaya	Ore event	Formation (Fm.) / Group (Gr.), lithology and thickness
CENOZOIC	1.6	Quaternary	Hiatus		Glacial and alluvial deposits, areally restricted mafic volcanic rocks
CENOZOIC	65	Tertiary		U Sn-W Ag-BM	Quenamari Gr. felsic volcanic rocks, red beds } Crucero Supergroup Picotani Gr. mafic-felsic volcanic rocks, red beds } (< 800 m)
MESOZOIC	145	Cretaceous		Ag-BM	Vilquechico Fm. shales Cotacucho Gr. sandstones, shales, dolomites (< 1,100 m)
MESOZOIC		Jurassic	Hiatus	Ag-Cu	Allinccapác Gr. peralkaline volcanic rocks
MESOZOIC	200 / 251	Triassic		W-Sn Mo-Cu	
PALEOZOIC		Permian			Mitu Gr. alkaline volcanic rocks and red beds (< 3,000 m)
PALEOZOIC	300	Carboniferous			Tarma-Copacabana Gr. limestones, sandstones, shales (< 3,000 m) Ambo Gr. sandstones and shales (> 1,500 m)
PALEOZOIC	355	Devonian	Hiatus	Sn-W	Ananea Fm. shales (> 2,500 m)
PALEOZOIC	418	Silurian	Hiatus		
PALEOZOIC	441	Ordovician			Sandía Fm. shales and quartzites (~ 3,500 m) San José Fm. shales (> 3,500 m)

Precambrian gneissic basement - not exposed

Pliocene felsic ignimbrites and red beds of the Crucero Supergroup (Clark et al. 1983; Kontak et al. 1995; Sandeman et al. 1996).

Plutonic rocks were emplaced repeatedly from the Late Devonian to the late Tertiary. These intrusions can be broadly subdivided into: Late Devonian-Early Carboniferous granitoids with minor Sn-W mineralization; large Permo-Triassic granitoid batholiths with significant Sn-Cu-W-Mo mineralization; small Late Cretaceous granodiorite stocks with minor silver and base metal mineralization; and, finally, stocks of middle to late Tertiary granitic rocks, which host the bulk of the Sn-W-Ag-base metal mineralization in the area, including the San Rafael deposit (Kontak and Clark 1988).

The Late Oligocene (~25 Ma; Clark et al. 1983) granitoid intrusion, with which the San Rafael deposit is associated, is part of the Picotani intrusive suite, belonging to the Crucero Supergroup (Sandeman et al. 1995, 1996). Sandeman et al. (1995, 1996) suggested that the Nazca plate ruptured in the vicinity of the Peru-Chile trench at about 38 Ma, and the foundering of the downgoing slab resulted in the formation of a slab window. This, in turn, caused an episode of anomalous asthenospheric upflow, which was responsible for the emplacement of rocks of the Picotani Group between 25 and 22 Ma. A local transtensional stress regime permitted the ascent of voluminous, mantle-derived mafic melts into the middle crust, which induced dehydration, partial melting of metasedimentary rocks (metapelites) and generation of water-undersaturated peraluminous felsic melts. The mixing and comingling of parental and daughter melts in shallow magma chambers gave rise to a diversified igneous suite, comprising mantle-derived shoshonites, minettes, absarokites, high-K calc-alkaline basalts, and peraluminous rhyodacites and monzogranites (Sandeman et al. 1995). Tin mineralization is spatially associated with strongly peraluminous leucomonzogranites, which crop out in only a few localities, such as San Rafael and the nearby Santo Domingo tin prospect.

GEOLOGY OF THE SAN RAFAEL DISTRICT

The San Rafael area is underlain mainly by slates and subordinate quartzites of the Late Ordovician Sandía Formation, which were intruded in the Late Oligocene by a small (<

15 km^2) plug of K-feldspar megacrystic granitoid porphyry (Fig. 2c). The pluton is elongated to the northeast, and although its core corresponds to a prominent topographic high (5300 m), much of the pluton remains unroofed. The surface exposure of the intrusion is limited to two stocks, each a few hundred meters in diameter, which converge at a depth of less than 1 km below the surface. Numerous NW-trending dykes of granitoid porphyry, and several that are semi-annular, crop out in the area surrounding the two stocks.
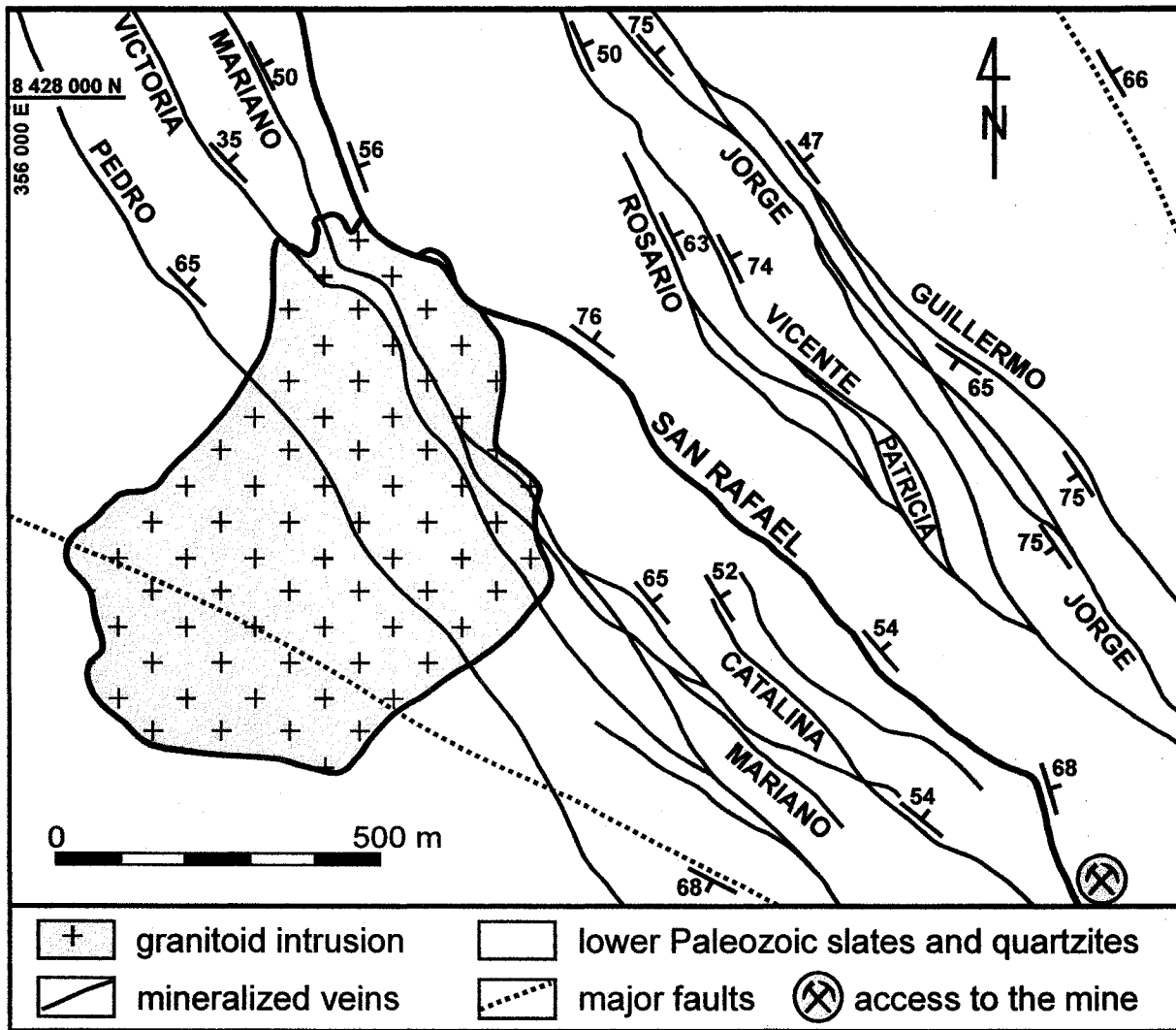
The metasedimentary rocks hosting the intrusion form a structural dome, which consists of a core of early Paleozoic rocks belonging to the Sandía, San José and Ananea Formations, surrounded by late Paleozoic rocks of the Ambo, Tarma and Copacabana Groups. Strata of the Sandía Formation are marked by a strong penetrative foliation, generally parallel to bedding, and are strongly deformed in a series of recumbent to upright folds and associated thrust faults. The early Paleozoic metasedimentary rocks immediately surrounding and overlying the intrusion have undergone contact metamorphism, indurating and locally converting them to hornfels.

Granitic rocks forming the San Rafael pluton can be subdivided into two major phases: a white-gray, porphyritic leucomonzogranite, and a dark-gray, fine-grained to porphyritic granodiorite. The most distinctive phase is a coarse-grained, biotite- and cordierite-bearing subsolvus leucomonzogranite with abundant alkali feldspar megacrysts, $\leq$ 10 cm in length. This phase has a strongly peraluminous character, as indicated by the presence of cordierite, and may be classified as an S-type granite, as defined by Chappell and White (1974). Granodiorites, which contain cordierite, garnet and minor sillimanite, are also S-type and increase in volume at depth. Finally, some tonalite enclaves occur locally in the granodiorites and leucogranites.

The San Rafael area hosts a number of subparallel, generally NW-trending and moderately to steeply dipping, planar veins (Fig. 5). These veins cut the intrusion-metasedimentary rock contacts without any appreciable deflection, and can be traced on surface for > 3 km. Within the slates of the Sandía Formation, the vein traces are commonly marked by zones a few meters in width of anastomosing milky quartz veinlets containing minor amounts of sulfide minerals and surrounded by chloritization haloes. Locally, the veinlets coalesce into quartz-sulfide lenses that are tens of centimeters wide

FIGURE 5. Bedrock geology of the southwestern part of the San Rafael district (modified after Arenas 1980b; Sherlock 1999). The stock shown is composed of granite and granodiorite and is one of the two exposures of the San Rafael pluton (the other lies outside the map area, in the northeastern part of the district).

Map labels and annotations:

8 428 000 N

356 000 E

VICTORIA

MARIANO

PEDRO

50

35

56

65

75

50

47

JORGE

ROSARIO

63

74

76

VICENTE

PATRICIA

SAN RAFAEL

GUILLERMO

65

75

75

JORGE

66

N

65

52

54

CATALINA

MARIANO

54

68

68

0   500 m

granitoid intrusion

mineralized veins

lower Paleozoic slates and quartzites

major faults

access to the mine

and several meters or tens of meters long. At depth, within the granitoid porphyry, the veins are more regular in form and average from 0.5 to 1.5 m in width.
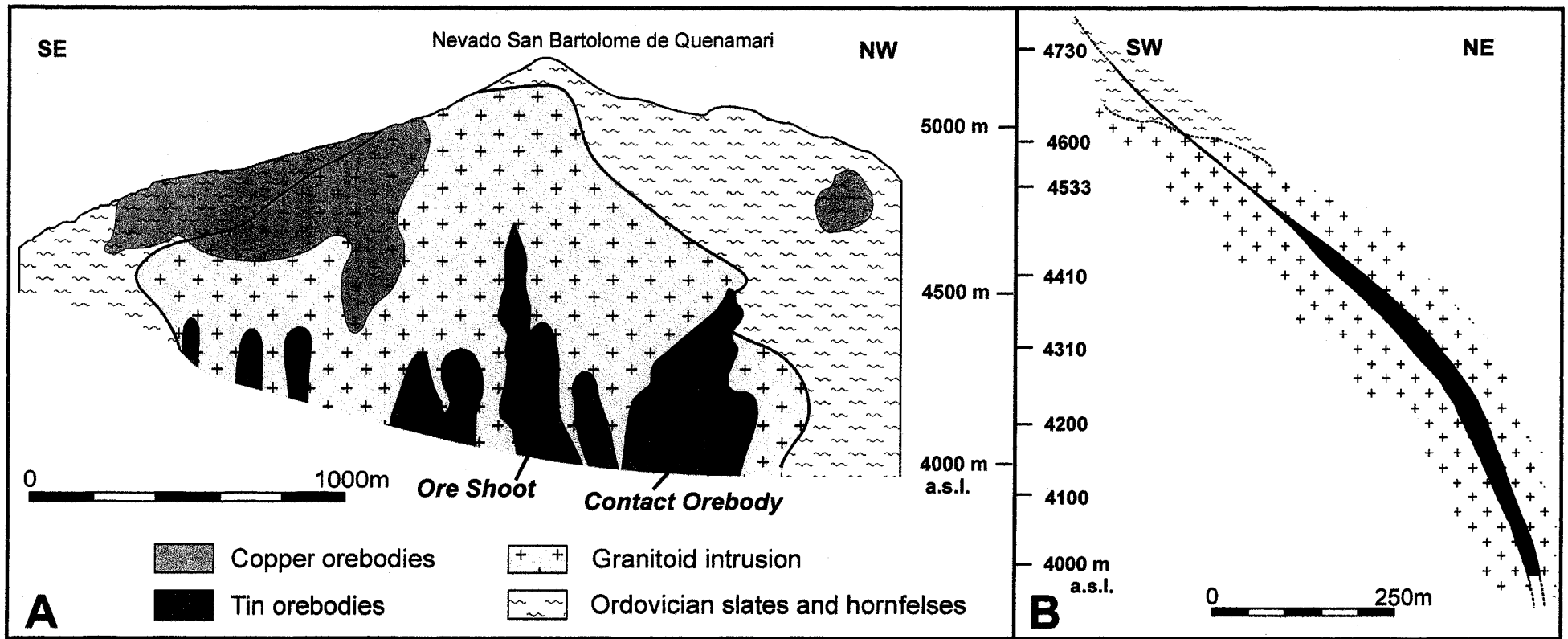
GEOLOGY AND STRUCTURE OF THE SAN RAFAEL LODE

Structural geology

The San Rafael vein, referred to as lode because of its structural complexity, on average, strikes ~330°, dips 40 to 75° to the northeast and can be traced on surface for a distance of ~3.5 km. It is mineralized over an unusually large vertical extent, exceeding 1,200 m (from 5100 to 3900 m above sea level), and hosts ~98 % of the tin reserves of the San Rafael deposit (Minsur, unpub. data 1999). The width of the vein is < 2 m in the upper part of the deposit (Fig. 2b), but, at depth, the structure dilates into a series of subvertical shoots, some of which are as much as 50-m-wide (Figs. 6 and 7). Field observations show that there was movement along the San Rafael fault synchronous with vein filling. Kinematic indicators, such as fault-vein relationships, drag folds, and stratigraphic offsets, consistently indicate a normal-sinistral sense of displacement (Sherlock 1999). Slickensides are poorly developed, but where seen are steeply plunging.
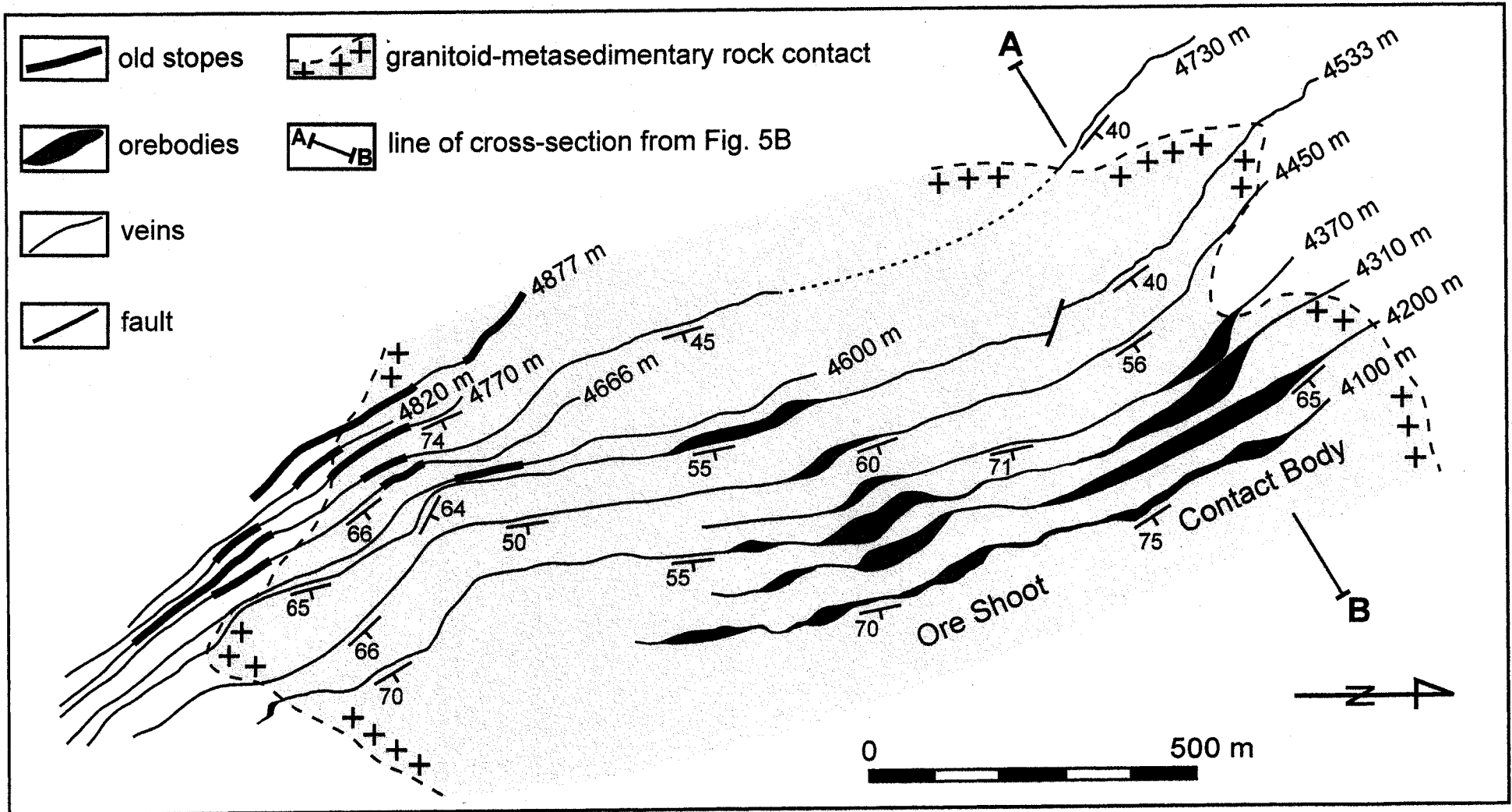
The surface expression of the San Rafael lode consists of a 1- to 2-m-wide network of anastomosing quartz veinlets and quartz-cemented breccias, surrounded on both sides by a zone of chloritization that is ~20-m-wide. The lode is planar (striking 328° and dipping 65°, on average; Fig. 8a) and its hangingwall and footwall contacts are delimited by narrow (~2 cm), gouge-filled fault breccias. Mineralization consists of narrow, semi-continuous bands of massive chalcopyrite, generally developed along the hangingwall and footwall contacts.

The lode continues to be planar and narrow (<2 m) down to the 4600 m level (striking 332° and dipping 68°, on average; Fig. 8b), and displays a geometry identical to that of the surface exposures. It generally has sharp contacts with the adjacent unmineralized wallrock, is commonly brecciated, and exhibits extensive textural evidence of open-space filling. The mineralization consists of narrow zones (~20-cm-wide) of massive to semi-massive chalcopyrite with minor cassiterite.

FIGURE 6. A. Longitudinal section of the San Rafael lode (modified after Minsur, unpub. data). Mine levels correspond to the elevation. B. Cross-section of the San Rafael lode through the Contact Orebody (N 58 E).

A

SE   Nevado San Bartolome de Quenamari   NW

5000 m

4500 m

4000 m
a.s.l.

0   1000m

Ore Shoot   **Contact Orebody**

Copper orebodies   Granitoid intrusion

Tin orebodies   Ordovician slates and hornfelses

B

SW   NE

4730

4600

4533

4410

4310

4200

4100

4000 m
a.s.l.

0   250m

FIGURE 7. Structural contours on the San Rafael lode and intrusion-metasedimentary rock contact (modified after Sherlock 1999 and Minsur, unpub. data).

Legend:
- old stopes
- orebodies
- veins
- fault
- granitoid-metasedimentary rock contact
- line of cross-section from Fig. 5B

A

B

4730 m
4533 m
4450 m
4370 m
4310 m
4200 m
4100 m
4877 m
4820 m
4770 m
4666 m
4600 m

40
40
45
56
74
64
50
55
60
71
65
66
65
66
70
55
55
75
70

Ore Shoot

Contact Body

N

0   500 m

FIGURE 8. Stereonet plots of the main- and late-stage veins composing the San Rafael lode, as exposed: A. On the surface (n=33), B. Between the surface and the 4600 level (n=108), C. Between the 4533 and the 4050 levels (n=301). The data are plotted on the lower hemisphere, as poles to the plane in an equal area projection.
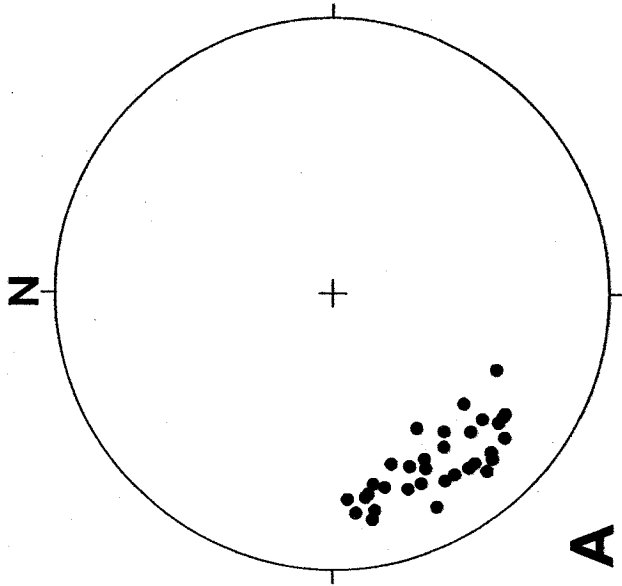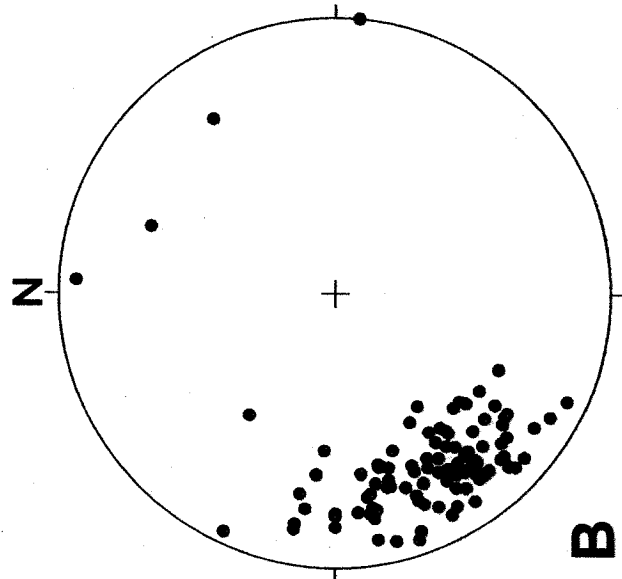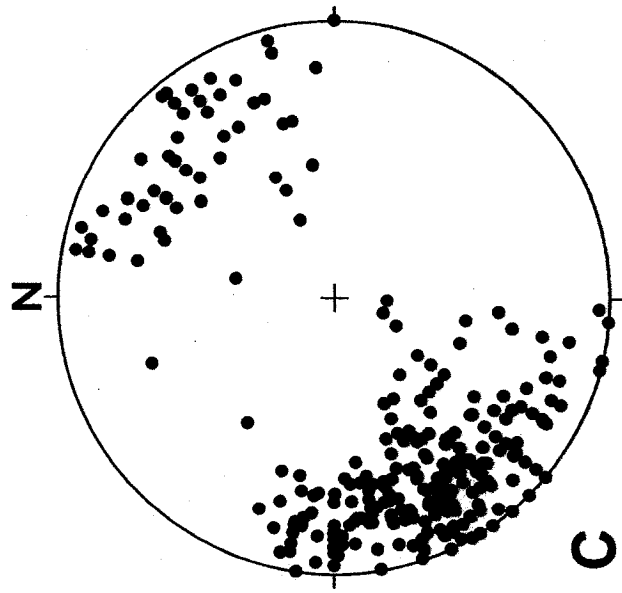
Below the 4533 m level, two major fault jogs are developed, producing a major change in the style of mineralization (Figs. 6 and 7). These jogs localize dilational zones, where the sinistral-normal San Rafael fault has stepped to the west and steepened (Fig. 9). The jogs widen considerably at depth (up to ~50 m) and form the Ore Shoot and Contact orebodies, elongated sinuous zones, marked by sharp hangingwall and footwall contacts, and characterized by an abundance of NW-striking (Fig. 8c), cassiterite-mineralized quartz veins and breccia zones. The two orebodies display a similar style of mineralization and host the highest concentration of cassiterite in the deposit. There are also several smaller orebodies at depth, which include the South Contact, Breccia 150-S, Ramp 410, 150, 310-S and 250-S orebodies. Significantly, all the orebodies in the lower part of the lode are confined to the granitoid intrusion (Figs. 6 and 7), and the veins become irregular where they are hosted by the sedimentary rocks.

Cassiterite associated with quartz and chlorite dominates the lower part of the lode. It occurs mainly as open fracture-filling, breccia and replacement bodies (Figs. 2g-i and 10a-e), as well as disseminations in strongly chloritized wallrock (Fig. 2d). Repeated opening of the veins, evident from crack and fill textures, as well as multiple episodes of brecciation, produced a very complex lode morphology (Fig. 2e, f). Cassiterite is most abundant where veins branch and intersect or where they deflect in strike or dip. The highest ore grades (as much as 45 wt.% Sn) occur in breccias that form zones several meters wide, and in the major veins in the footwall and hangingwall of the lode structure.

The veins composing the San Rafael lode have been subdivided, based on their mineralogy (Fig. 11). Crosscutting relationships among the different vein types clearly demonstrate that the oldest veins are tourmaline- and quartz-bearing (Fig. 2f, g). These veins form a conjugate set (one set striking ~330° and NE-dipping, the other striking ~295° and SW-dipping). By contrast, all main- (ore) and late-stage (post-ore) veins have the same general orientation (strike ~330° and NE-dipping).

Geological mapping on the surface identified tourmaline-quartz veins orthogonal to the San Rafael lode, occupying dilational zones in thrust faults that have been subsequently cut and offset by the lode. These tourmaline-quartz veins are, therefore, very early and may be unrelated to the tin-copper mineralization. However, underground mapping showed that there are major tourmaline-quartz veins, and volumetrically

FIGURE 9. Schematic diagram of the Contact Orebody, showing the relative position of the fault/vein traces, hangingwall and footwall contacts, and the geometry of the vein/breccia system that comprises the orebody in relation to the sinistral normal displacement on the fault. A. Plan view on the 4370 level. B. Vertical section (not to scale).

A

Hangingwall

**Dilational zone
Sinistral shear**

Tension
fractures

⌐70

limit of mine workings

N

Footwall

Fault/vein trace

0   100 m

B

SW

Fault/vein trace

**Fault deflection
and steepening**

NE

Hangingwall

Footwall

Vein/breccias
local dilational features
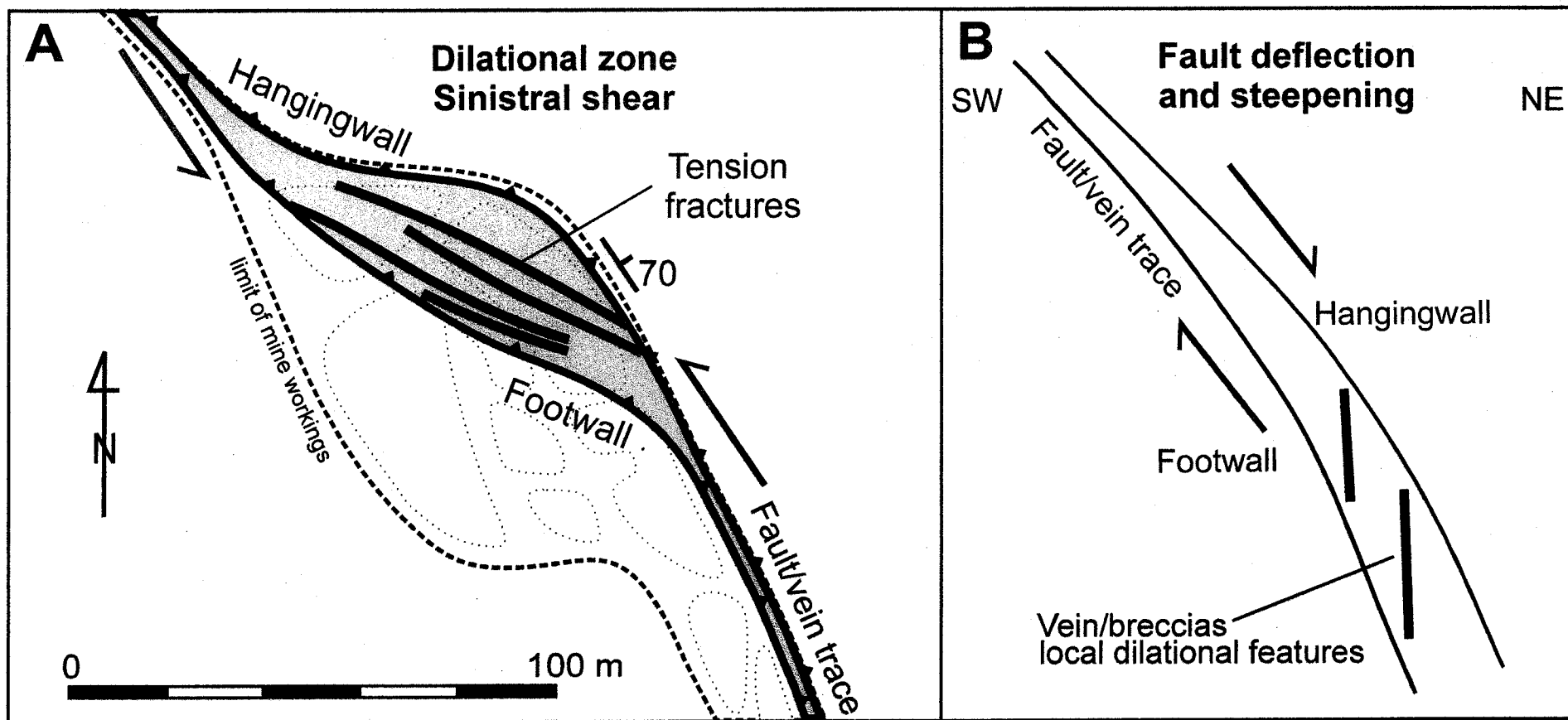
FIGURE 10. Ore textures and paragenetic relationships. **a** - Cassiterite-bearing breccia in the roof of the 4225 level of the Contact orebody. Sub-angular fragments of chloritized wallrock are overgrown by quartz, cassiterite and chlorite and the remaining space is filled with milky quartz, locally forming quartz vugs. Vein width is ~ 40 cm. **b** - Fragments of broken layers of wood tin (yellow-brown) and chlorite (green) in a wallrock composed mostly of massive cassiterite (dark brown), quartz and chlorite. Ore Shoot, 4330 level. **c** - Cassiterite-quartz-chlorite vein on level 4270 of the Contact orebody. Note the cockscomb structure and the alternating layers of quartz, chlorite and cassiterite. The scale is in cm. **d** - Fragment of a composite cassiterite-quartz-chlorite-sulfide vein from the 4310 level of the Contact orebody. The massive cassiterite (cas), associated with quartz (qtz) and chlorite (chl) is close to the vein selvage, whereas the sulfides, i.e., chalcopyrite (cpy) and minor pyrite form the center of the vein (Sample SAR-R103). The scale is in cm. **e** - Banded veins of massive cassiterite (cas), crosscut by quartz veins (qtz) bearing chalcopyrite (cpy). The sample was taken on level 4100 of the "150" orebody (Sample SAR-A4). The scale is in cm. **f** - Botryoidal cassiterite ore (of the type shown in Figure 2i) in thin section, plane polarized light. The sequence starts with quartz (qtz), which is overgrown by minor chlorite (chl) and cassiterite (cas) displaying color zoning from dark brown to yellow (Sample SAR-D5). Width of photo: 2 mm. **g** - Needle tin ore in a doubly polished section (40 μ), plane polarized light. The square habit of the cassiterite crystals (cas) is apparent and arises from their being viewed in a section perpendicular to their elongation. Fibrous aggregates of chlorite (chl) and quartz grains (qtz) are interstitial to the cassiterite (sample SAR-R85). Width of photo: 2 mm. **h** - Needle tin ore in a doubly polished section (200 μ), showing acicular crystals of cassiterite (cas), pale green chlorite (chl) and quartz (qtz) in plane polarized light (Sample SAR-R119). Width of photo: 2 mm.

29
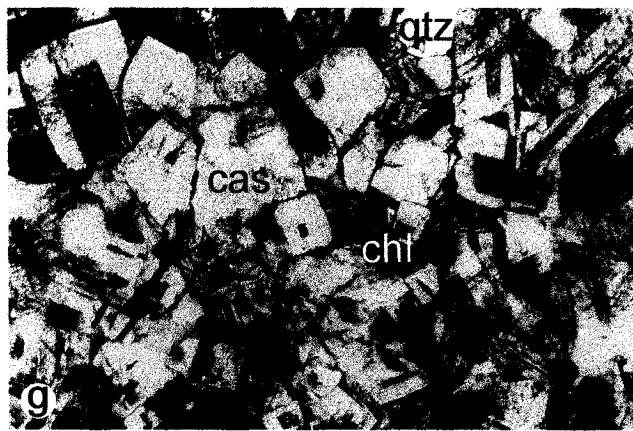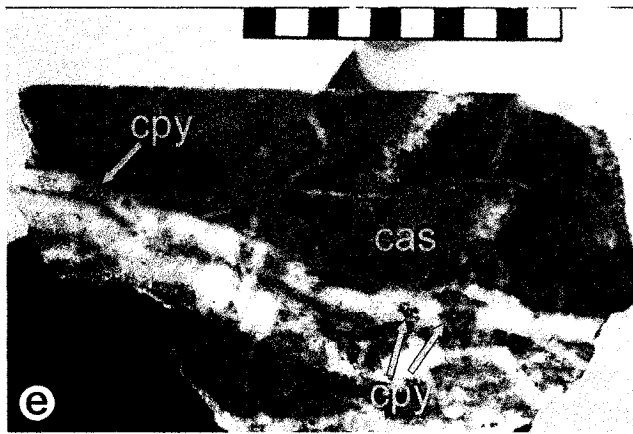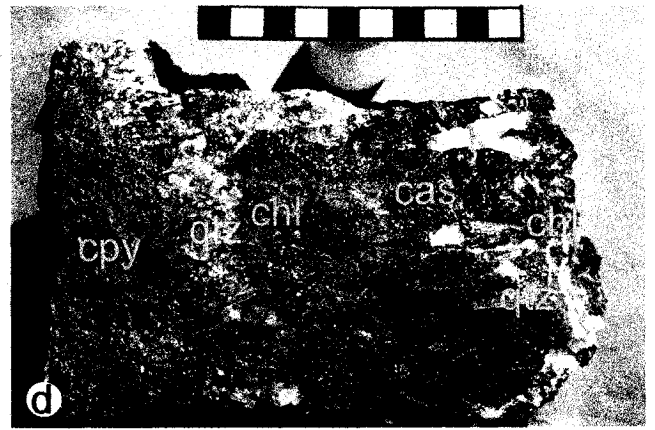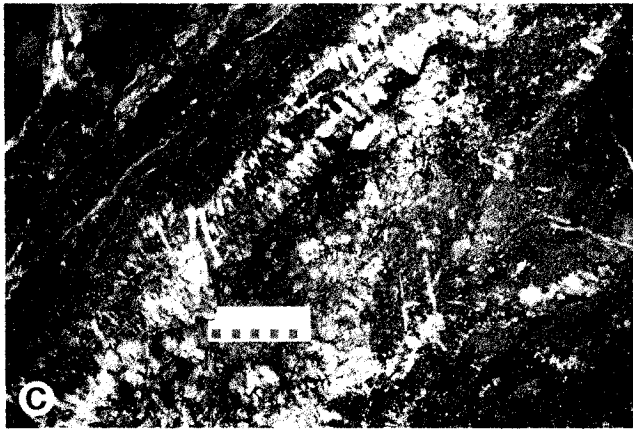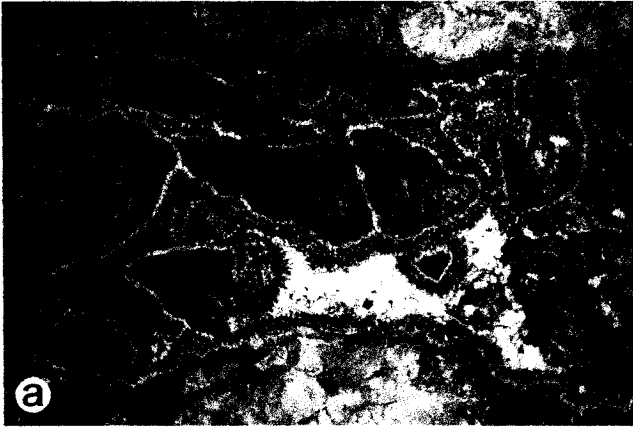
FIGURE 11. Simplified paragenesis for the San Rafael deposit.

	STAGE:	I - EARLY	II MAIN III	IV - LATE
VEIN TYPES:				
Tourmaline-quartz +/- arsenopyrite		▬▬▬		
Cassiterite ("wood tin")-chlorite			▬▬▬	
Cassiterite-quartz-chlorite +/- sulfides			▬▬▬▬▬▬	
Chalcopyrite-"needle tin"-quartz-chlorite			▬▬▬	
Quartz-chlorite-chalcopyrite-other sulfides			▬▬▬	
Quartz-chlorite				▬▬▬
Quartz-calcite				▬▬▬
Quartz-fluorite				▬▬
ALTERATION TYPES:				
Na or K metasomatism		▬▬		
Sericitization		▬▬▬		
Tourmalinization		▬▬▬		
Chloritization		▪	▬▬▬▬▬▬▬▬▬▬▬▬▬	
Silification		▬ ▬	▬ ▬ ▬ ▬ ▬ ▬	▬▬▬
BRECCIAS:				
Tourmaline-cemented		▬▬		
Chlorite-cemented			▬▬▬	
Cassiterite-cemented			▬▬▬	
Quartz-cemented			▬▬▬	
Sulfide-cemented			▬▬▬	

important tourmaline-quartz breccia dykes (described below), which are concordant with the strike of the San Rafael vein-breccia system. Some of these veins were subsequently reopened and filled by the main- and late-stage veins (Fig. 2f). It is thus possible that there was more than one generation of tourmaline-bearing veins and tourmaline crystallization could have partly overlapped tin deposition. Tourmaline-quartz veins and breccias have, therefore, been included in the early paragenesis of the lode, and a genetic link between these and the younger tin- and copper-bearing veins is tentatively inferred.

Alteration and veining

Several distinct stages of alteration and veining accompanied the development of the San Rafael lode and are briefly described below, in chronological order, as inferred from paragenetic relationships. They have been grouped into four broad stages, following the subdivision proposed by Palma (1981):

STAGE I (early, pre-ore)

The earliest alteration is sodic-potassic and is manifested by conspicuous overgrowths of hydrothermal albite or orthoclase on pre-existing feldspars (referred to as pseudo-rapakivi textures by Kontak and Clark 1988). This early alteration is observed only locally within the granitoid intrusion and its irregular distribution is further obscured by the overprint of subsequent alteration. In contrast to sodic-potassic metasomatism, all other pre-ore alteration is clearly associated with tourmaline-quartz veins. These early veins are very common and, in addition to schörl-dravite tourmaline and quartz, also contain arsenopyrite, but are in general barren of cassiterite. They typically are surrounded by envelopes of pervasive sericitization that are 1- to 30-cm-wide (Fig. 2f, g). Where these veins form denser stockworks, sericitic alteration occurs over a width of many meters, but its original extent is commonly obscured by main-stage alteration. In addition to the ubiquitous sericitic haloes, the alteration envelopes of some tourmaline-quartz veins also display an outer zone of very weak, early chloritization and a 0.5- to 5-cm-wide inner zone of tourmalinization.

Fracture-controlled, pervasive tourmalinization of the wallrock post-dated sericitization and is commonly associated with silicification. This alteration can attain a

31

width of tens of centimeters and normally preserves only relics of the quartz phenocrysts from the original granitoid (Fig. 2e) and, in places, the outlines of tourmalinized K-feldspar phenocrysts.

Finally, much and perhaps the bulk of the tourmaline in the San Rafael lode occurs within numerous, subvertical, tourmaline-quartz breccia dykes, which locally are many meters in width and follow the lode along strike for hundreds of meters. These extremely fine-grained microbreccias are composed mainly of fragments of quartz or tourmalinized wallrock, embedded in a matrix of pervasively tourmalinized rock flour. Generally, they are heavily veined by quartz.

STAGE II (main ore stage-A)

The bulk of the tin at San Rafael was deposited as botryoidal wood tin (Figs. 2i and 10b, f) and as veins or breccias consisting almost entirely of quartz, chlorite and cassiterite (Figs. 2g, h and 10a, c). Strong and pervasive, texturally destructive chloritization accompanied the tin mineralization and affected the entire lode structure for distances varying from <1 to >10 m on either side of the vein system, in both the intrusion and the surrounding metasedimentary rocks. Chlorite completely replaced cordierite, biotite and feldspars (leaving only the quartz phenocrysts), and produced a dark green rock with scattered patches of clear to milky quartz (Fig. 2d, g). Rocks previously sericitized were also converted to chlorite, but tourmalinized rocks were left unaffected.

STAGE III (main ore stage-B)

Sulfide mineral deposition occurred mainly during Stage III and is represented by quartz-chlorite-chalcopyrite-sphalerite-galena-cassiterite (± other sulfides) veins. Cassiterite is present as fine-grained needles and prisms (Fig. 10g, h), in contrast to its massive or botryoidal form in Stage II. Wallrock alteration is extensive and similar to that of stage II, with a chloritic halo extending for as much as several m from the surface expression of the copper-bearing veins. The distinction between Stage II and III veins is based on crosscutting relationships (Fig. 10e), mineralogy and metal content.

STAGE IV (late, post-ore)

The large (as wide as 1 m), post-ore, quartz (± calcite, siderite or fluorite) veins of Stage IV are essentially barren and contain only traces of chalcopyrite and other sulfide

minerals (Fig. 2h). They are bordered by narrow zones of intense chloritic alteration, which macroscopically resembles that of the main ore stages. Locally, the chloritized wallrock has undergone weak, diffuse silicification, however, it is not known whether the latter alteration was coeval with the chloritization or superimposed on it at a later time.
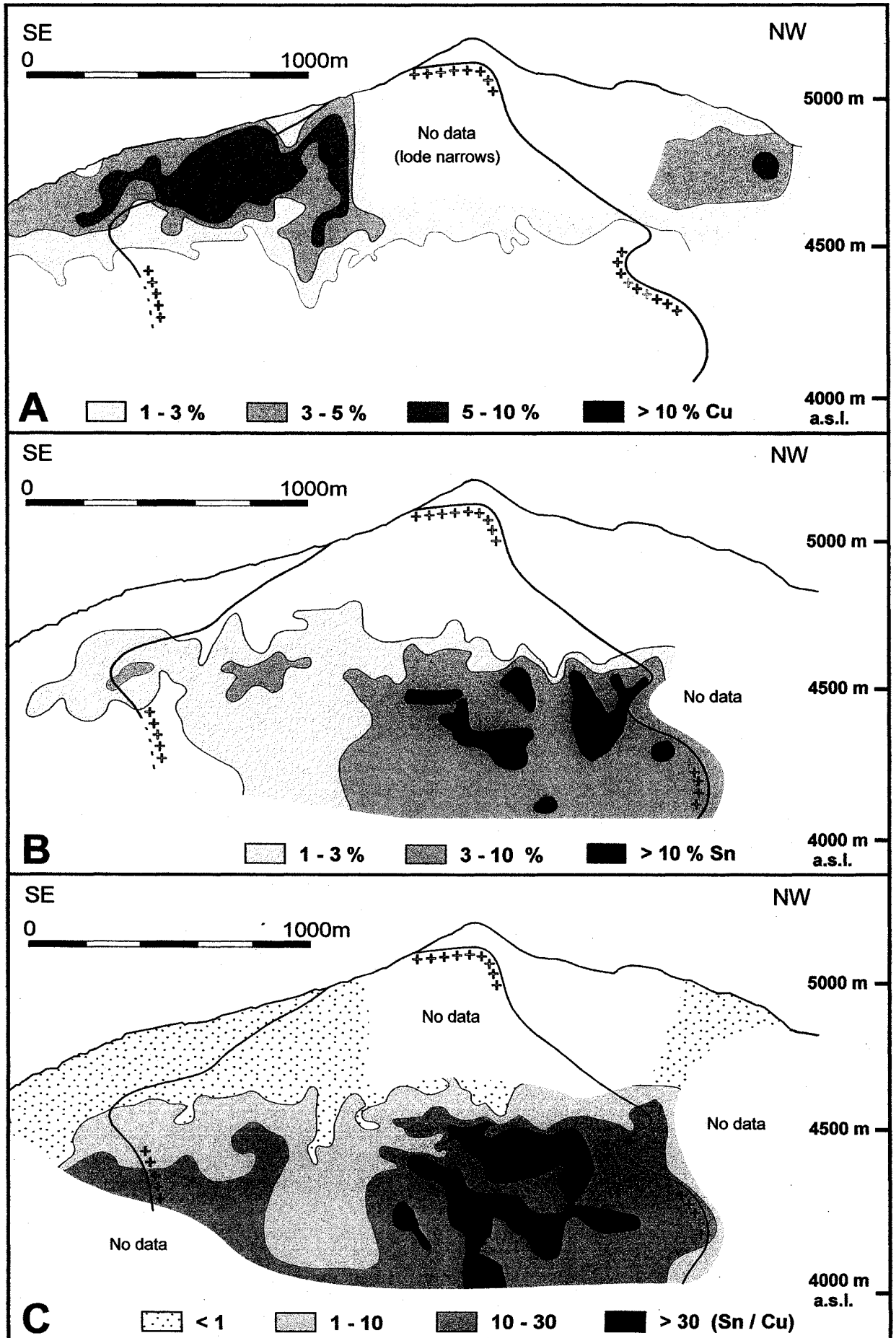
Mineralization and metal zoning

One of the most remarkable features of the San Rafael lode is the pronounced vertical zonation of the metals, copper being concentrated in the near surface parts of the deposit and tin dominantly at depth (Fig. 12). Above 4975 m (i.e., near the surface), the lode averages < 1% Sn and > 8% Cu. This changes to about 1% Sn and 4% Cu at the 4600 m elevation and 1.5% Sn and 1.5% Cu at the 4533 m elevation. Below the 4533 m level, the average metal contents are 5% Sn and 0.2% Cu (Minsur, unpub. data). This zonation is very similar to that described from the Cornish tin deposits, such as the Dolcoath Main Lode (Taylor 1979; Clark et al. 1995). A vertical zonation is also evident in the style of mineralization at San Rafael. In the deepest parts of the deposit (3900-4450 m), the tin ore consists mainly of massive cassiterite; at higher levels (4450-4550 m), there is an interval of botryoidal wood tin; and in the massive chalcopyrite above the 4550 m elevation, cassiterite occurs as the so-called needle tin variety.

Ores in the lower parts of the lode (below 4533 m) generally have a simple mineralogy (quartz-chlorite-cassiterite, with minor wolframite and local chalcopyrite – Figure 10d), whereas in the upper parts (above 4533 m) they contain more diverse mineral associations involving quartz, chlorite, chalcopyrite, cassiterite, pyrrhotite, arsenopyrite, pyrite, marcasite, sphalerite, galena, stannite, bismuthinite, native bismuth, calcite and siderite. It is important to note that, whereas the tin orebodies are confined to the granitoid intrusion, copper orebodies straddle the contact between granitoid and slate or are located entirely within the metasedimentary rocks (Fig. 6a).

Figure 11 provides a simplified paragenesis for the San Rafael lode based on crosscutting relationships between different vein types. In chronological order, the principal vein types are:

1. early, essentially barren tourmaline-quartz veins (with minor arsenopyrite);

FIGURE 12. Geochemical zoning in the San Rafael Lode (longitudinal section): A. Copper grades. B. Tin grades. C. Tin-copper ratios. (All figures modified after Arenas 1999 and Minsur, unpub. data). The line with crosses indicates the limits of the granitoid stock.

A

SE · NW

0 — 1000m

5000 m

4500 m

No data
(lode narrows)

☐ 1 - 3 %   ▨ 3 - 5 %   ■ 5 - 10 %   ■ > 10 % Cu

4000 m
a.s.l.

B

SE · NW

0 — 1000m

5000 m

4500 m

No data

☐ 1 - 3 %   ▨ 3 - 10 %   ■ > 10 % Sn

4000 m
a.s.l.

C

SE · NW

0 — 1000m

5000 m

No data

No data

No data

⬚ < 1   ☐ 1 - 10   ▨ 10 - 30   ■ > 30 (Sn / Cu)

4000 m
a.s.l.

2. cassiterite (wood tin)-chlorite banded veins, veinlets and encrustations;

3. cassiterite (massive)-quartz-chlorite banded veins, some of which have cores comprising a late infill of quartz-chalcopyrite (with minor proportions of other sulfide minerals);

4. chalcopyrite-cassiterite (needle tin)-quartz-chlorite veins (restricted to the upper part of the lode);

5. quartz-chlorite-chalcopyrite-other sulfide minerals (e.g., pyrrhotite, pyrite, marcasite, sphalerite, galena) ± siderite veins;

6. late, barren quartz-chlorite veins; and

7. late, barren carbonate- or fluorite-bearing veins (both types are relatively rare).

The different vein types listed above are associated with a variety of barren or mineralized breccias, which are cemented by tourmaline, chlorite, cassiterite, quartz or sulfide minerals (Figure 11). The breccias range from clast- to matrix-supported, and their clasts, which are angular or rounded, consist of fragments of chloritized, sericitized or tourmalinized wallrock, as well as fragments of earlier veins and breccias. The lack of any fault gouge or tectonic fabrics suggests that these breccias are dominantly of hydrothermal origin.

PRELIMINARY FLUID INCLUSION STUDIES

Microthermometric measurements have been conducted on fluid inclusions in quartz from a quartz-tourmaline vein (Stage I), and in cassiterite and quartz from a banded cassiterite-chlorite-quartz vein (Stage II). Primary fluid inclusions in the first sample generally contain liquid, vapour and a halite crystal. They homogenize in the temperature range 240-535°C, by disappearance of the vapour bubble or halite dissolution, and their salinity ranges from 34-62 wt.% NaCl eq. Further studies of this and other similar samples are in progress (Mlynarczyk and Williams-Jones, in prep.).

The second sample is characterized by alternating layers (on a scale of millimeters) of cassiterite, chlorite and quartz. Primary and pseudosecondary fluid inclusions in cassiterite and primary inclusions in quartz are generally liquid-rich and in

some cases contain an unidentified, tabular, birefringent solid, which does not dissolve on being heated. This mineral is interpreted to be a trapped phase, possibly a phengitic mica. In addition, the quartz-hosted inclusions generally contain a tiny, opaque, nonmagnetic mineral, which is interpreted to be a daughter phase. Cassiterite-hosted primary and pseudosecondary inclusions homogenize at a temperature of 355-360°C, and, on the basis of the final ice melting temperature, are interpreted to have a salinity of 18-21 wt.% NaCl eq. A temperature of initial ice melting (T_e) between -50 and -60°C indicates that the fluid has a significant concentration of divalent cations. Quartz-hosted fluid inclusions homogenize at a temperature of 260-310°C and have a salinity of 1-16 wt.% NaCl eq.; T_e values are > - 45°C.

DISCUSSION

Field relations at the San Rafael deposit indicate a strong structural control on tin mineralization. The bulk of the cassiterite ore is confined to large, high-grade orebodies, which are present only in the lower half of the San Rafael lode and are hosted entirely in granitoid rocks. The distribution of the tin orebodies was clearly controlled by several major fault jogs, which developed at depth in the lode during westward stepping of the sinistral-normal San Rafael fault. The creation of the fault jogs was limited to the mechanically competent granitoid host rock (as opposed to the incompetent slates that surround the pluton) and these dilational zones localized the formation of dense networks of tension fractures. The textures and the geometry of the spatially associated mineralized veins indicate that the hydrothermal activity was synkinematic and that the ore fluids were focused into these dilational sites.

Geologic evidence suggests that the ore veins were emplaced after the host intrusion had cooled appreciably and under a regional tectonic regime, as they are planar and cut straight across the granitoid contact (Sherlock 1999). This is consistent with geochronological data that indicate mineralization may have taken place 1-2 m.y. after emplacement of the intrusion. The latter was dated at 24.7 ± 0.3 Ma (Clark, oral comm., 1997) by the U-Pb method on zircon and at 24.5 ± 0.7 Ma by the K-Ar method on biotite

(Clark et al. 1983). By contrast, K-Ar dates of 23.6 ± 0.6 Ma and 22.6 ± 0.5 Ma were obtained for hydrothermal muscovite (Kontak et al. 1987) and hydrothermal adularia (Clark et al. 1983), respectively. Similar brief time lags between cooling of igneous host rocks and tin deposition, have been reported from Bolivia (Grant et al. 1979), Cornwall and Southern Thailand (Lehmann 1990).

The earliest hydrothermal event (Stage I) recorded in the San Rafael deposit is represented by numerous and volumetrically important tourmaline-quartz veins and breccia dykes, which clearly pre-dated ore deposition. On the basis of preliminary fluid inclusion data, the fluids which produced the above veins and caused pervasive, fracture-controlled sericitization and tourmalinization of the granitoids, were high temperature, hypersaline brines (460-510°C, 44-48 wt.% NaCl eq.). This early, barren tourmaline-quartz stage was marked by repetitive intense brecciation and, based on textural relationships, appears to have established the early framework of the San Rafael vein-breccia system, which was subsequently reactivated during the tin-copper event.

The main stages (II and III) of the hydrothermal system, during which tin and copper ores were deposited, were both characterized by strong chloritization, which overprinted the earlier alteration assemblages. This observation, the intimate association of needle tin cassiterite with chalcopyrite ores and the uniform kinematics of the San Rafael lode throughout its history, all suggest that both tin and copper mineralization were introduced during a single, protracted hydrothermal event, albeit with copper being paragenetically later than tin. Petrographic relationships indicate that deposition of massive and wood tin cassiterite preceded that of chalcopyrite (and other sulfide minerals) and needle tin cassiterite.

It is still premature to propose a model that satisfactorily explains the genesis of the San Rafael deposit. However, some insights are provided by the preliminary fluid inclusion microthermometric data reported above for a banded vein of cassiterite, chlorite and quartz. These data indicate that the fluid trapped during the growth of cassiterite was of moderate salinity and at relatively high temperature (18-21 wt.% NaCl eq., T_h ~355-360°C), whereas that trapped by quartz had a lower, but much broader range in salinity and was at lower temperature (1-16 wt.% NaCl eq., T_h ~260-310°C). The trapping of two

different fluids in separate cassiterite- and quartz-rich layers, millimeters in thickness, within the same vein implies that open fractures were periodically filled by one and then the other fluid. However, the broad range of salinity displayed by the quartz-hosted fluid inclusions also suggests that the two fluids mixed, which, considering their contrasts in temperature and composition, would have produced sharp gradients in physicochemical conditions, potentially favourable for cassiterite deposition.

Experimental studies have shown that in most hydrothermal solutions tin is transported in its reduced form, Sn (II), as the species $SnCl_2^{\circ}$ and $SnCl^+$, and that cassiterite precipitation is induced by decreases in temperature and ligand ion activity (chloride) and increases in pH and fO_2 (Eugster and Wilson 1985; Pabalan 1986; Wilson and Eugster 1990; Taylor and Wall 1993; Müller and Seward 2001). The fluid trapped in cassiterite at San Rafael, therefore, quite clearly has the characteristics needed to make it an ideal ore fluid. The high temperature and salinity suggest that it was magmatic, which, considering the S-type character of the San Rafael pluton, implies that it was probably also reducing. Thus, the combination of high temperature, high salinity and low fO_2 would have made it a suitable fluid for tin transport. The second fluid, i.e., that trapped by quartz, which may have had a salinity as low as 1 wt.% NaCl eq., was likely of meteoric origin and, therefore, probably quite oxidizing, assuming a short residence time in the overlying strata. Mixing of the ore fluid with cool, dilute and relatively oxidizing meteoric water would have produced sharp decreases in temperature and ligand activity (Cl^-) and a sharp increase in fO_2, all of which would have favoured cassiterite precipitation. The rapidity with which these changes would have occurred in a mixing regime, characterized by repeated dominance of one fluid and then the other, would also have promoted supersaturation of SnO_2, which could explain the high grade of the San Rafael ores. It would also explain the formation of the wood tin ores, which display colloform textures akin to those interpreted by Roedder (1968) and Hosking et al. (1987) as having formed in response to high nucleation rates, resulting from extreme supersaturation of the ore solutions.

Although more data need to be collected and geochemical modelling has to be undertaken in order to evaluate alternative hypotheses for the genesis of the San Rafael deposit (e.g., boiling, fluid-rock interaction, redox-coupled precipitation), the available

information suggests a tentative working model, which explains many features of the orebodies. This model envisages that reducing fluids of dominantly magmatic origin extracted tin from the magma and transported it as Sn(II) chloride complexes to the site of deposition. Dilational zones created along the San Rafael fault by tectonic activity, synchronous with the hydrothermal processes, provided an effective mechanism for mixing these fluids with cooler, oxidized fluids of shallow meteoric origin. The ensuing rapid oxidation, cooling and dilution of ligand concentration in the ore fluid resulted in destabilization of the tin complexes and massive deposition of cassiterite in the open spaces provided by the fault jogs.

An additional and striking feature of the San Rafael deposit, which needs to be explained by any viable genetic model, is its marked, vertical primary metal-zoning. The vast majority of the oxide (Sn) ores are hosted by fault jogs located at depth in the lode and confined to the intrusion. On the other hand, the sulfide (Cu-Zn-Pb) orebodies are mainly located on the upper flanks of the San Rafael vein-breccia system, where they straddle the metasedimentary rock-intrusion contacts or are contained entirely within metasedimentary rocks (Fig. 6). This apparent lithological control has also been documented for lode tin deposits elsewhere, e.g., the South Crofty deposit in Cornwall, where the mineralogy of the No. 9 lode "changes from tin- to copper-rich in a space of inches as it leaves the granite and enters the overlying slates" (Taylor 1979). Although stable isotope, bulk chemical and more detailed fluid inclusion studies will be needed to quantitatively assess the controls of sulfide mineral precipitation, it is tentatively proposed that the copper ores at San Rafael formed in response to an increase in sulfur activity and/or decrease in fO_2, which occurred when the orthomagmatic and/or meteoric fluids interacted with the surrounding slates. The vertical metal zonation of the deposit is, therefore, thought to reflect early tin mineralization, localized proximally to source by a favourable structural regime (fault jogs), and later, distal copper mineralization, localized by a gradient in physicochemical conditions at the interface of the intrusion with metasedimentary host rocks.

REFERENCES

Arenas MJ (1980a) El distrito minero San Rafael, Puno - Estaño en el Peru. Boletin Sociedad Geologica del Peru 66: 1-11

Arenas MJ (1980b) Mapa geologico superficial del Distrito Minero San Rafael, Puno. MINSUR Archives

Arenas MJ (1999) Exploracion y geologia de la mina San Rafael, Puno. Mineria 260: 10-31

Chappell BW, White AJR (1974) Two contrasting granite types. Pacific Geology 8: 173-174

Clark AH, Palma VV, Archibald DA, Farrar E, Arenas MJ, Robertson RCR (1983) Occurrence and age of tin mineralization in the Cordillera Oriental, Southern Peru. Econ Geol 78: 514-520

Clark AH, Farrar E, Kontak DJ, Langridge RJ, Arenas Figueroa MJ, France LJ, McBride SL, Woodman PL, Wasteneys HA, Sandeman HA, Archibald DA (1990) Geologic and geochronologic constraints on the metallogenic evolution of the Andes of southeastern Peru. Econ Geol 85: 1520-1583

Clark AH, Chen Y, Sandeman HA, Farrar E, Hodgson MJ, Kontak DJ, Arenas MJ (1995) Two giants and their lairs: The South Crofty, Cornwall and San Rafael, Peru, tin (-copper) deposits. 34th Annual Conference of the Ussher Society, Cornwall: 6-7

Claure HV, Minaya ER (1979) Mineralizacion de los Andes Bolivianos en relacion con la Placa de Nazca. Program E.R.T.S. Servicio Geologico de Bolivia, Sensores Remotes 4, La Paz, 50 pp

Eugster HP, Wilson GA (1985) Transport and deposition of ore-forming elements in hydrothermal systems associated with granites. In: Halls C (chairman) High heat production (HHP) granites, hydrothermal circulation and ore genesis. Inst Mining and Metall Conference, London, 87-98

Evans AM (1993) Ore Geology and Industrial Minerals - an Introduction. Blackwell Scientific Publications, Oxford, 390 pp

Grant JN, Halls C, Avila Salinas W, Snelling NJ (1979) K-Ar ages of igneous rocks and mineralization in part of the Bolivian tin belt. Econ Geol 74: 838-851

Hosking KFG, Stanley GJ, Camm GS (1987) The occurrence, nature and genesis of wood tin in South-west England. Trans Royal Geol Soc Cornwall 21(4): 153-212

Kirkham RV, Sinclair WD (1995) Porphyry copper, gold, molybdenum, tungsten, tin, silver. In: Eckstrand OR, Sinclair WD, Thorpe RI (eds) Geology of Canadian Mineral Deposit Types. Geol Surv Canada, Geology of Canada 8: 421-446

Kontak DJ, Clark AH (1988) Exploration criteria for tin and tungsten mineralization in the Cordillera Oriental of southeastern Peru. In: Taylor RP, Strong DF (eds) Recent Advances in the Geology of Granite-Related Mineral Deposits. Proc CIM Conference on Granite-Related Mineral Deposits, Can Inst Mining and Metall, Spec Vol 39: 157-169

Kontak DJ, Clark AH, Farrar E, Pearce TH, Strong DF, Baadsgaard H (1986) Petrogenesis of a Neogene shoshonite suite, Cerro Moromoroni, Puno, Southeastern Peru. Can Mineral 24: 117-135

Kontak DJ, Clark AH, Farrar E, Archibald DA, Baadsgaard H (1987) Geochronological data for Tertiary granites of the southeast Peru segment of the Central Andean Tin Belt. Econ Geol 82: 1611-1618

Kontak DJ, Cumming GL, Krstic D, Clark AH, Farrar E (1990) Isotopic composition of lead in ore deposits of the Cordillera Oriental, Southeastern Peru. Econ Geol 85: 1584-1603

Kontak DJ, Clark AH, Halter W, Williams-Jones A (1995) Metal concentration versus dispersal in the magmatic-hydrothermal environment: a case study contrasting low-grade (East Kemptville, Nova Scotia) and high-grade (San Rafael, Peru) Sn-base metal deposits. Proc 2nd Giant Ore Deposits Workshop, Kingston, Ontario, Canada, Vol. 2: 347-413

Laubacher G (1978) Estudio geologico de la region norte del Lago Titicaca. Inst Geol Mineria (Peru) 5, 120 pp

Lehmann B (1979) Schichtgebundene Sn-Lagerstätten in der Cordillera Real, Bolivien. Berlin Geowiss Abh, A(14), 135 pp

Lehmann B (1990) Metallogeny of tin. Lecture Notes in Earth Sciences, 32, Springer-Verlag, 211 pp

Müller B, Seward TM (2001) Spectrophotometric determination of the stability of tin (II) chloride complexes in aqueous solution up to 300°C. Geochim et Cosmochim Acta, 65, 4187-4199

Okulitch AV (1999) Geological Time Chart, The National Earth Science Series Geological Atlas, Geol Surv Canada, Open File 3040

Pabalan RT (1986) Solubility of cassiterite (SnO_2) in NaCl solutions from 200°C - 350°C, with geologic applications. Unpub PhD thesis, Pennsylvania State University, U.S.A., 141 pp

Palma VV (1981) The San Rafael tin-copper deposit, Puno, SE Peru. Unpub MSc thesis, Queen's University, Kingston, Ontario, Canada, 235 pp

Roedder E (1968) The noncolloidal origin of "colloform" textures in sphalerite ores. Econ Geol 63: 451-471

Sandeman HA, Clark AH, Farrar E (1995) An integrated tectono-magmatic model for the evolution of the Southern Peruvian Andes (13-20°S) since 55 Ma. Int Geol Rev 37: 1039-1073

Sandeman HA, Clark AH, Farrar E, Arroyo-Pauca G (1996) A critical appraisal of the Cayconi Formation, Crucero Basin, southeastern Peru. Jour South Amer Earth Sci 9: 381-392

Sherlock RL (1999) Structural framework of the San Rafael tin-copper deposit, Peru. Unpublished report for Inca Pacific Resources Inc. 29 pp

Sinclair WD (1995) Vein-stockwork tin, tungsten. In: Eckstrand OR, Sinclair WD, Thorpe RI (eds) Geology of Canadian Mineral Deposit Types. Geol Surv Canada, Geology of Canada 8: 409-420

Singer DA, Mosier DL, Menzie DW (1993) Digital Grade and Tonnage Data for 50 Types of Mineral Deposits, Macintosh version. USGS open-file report 93-0280, USGS, Reston, VA

Taylor RG (1979) Geology of tin deposits. Developments in Economic Geology 11, Elsevier, 543 pp

Taylor JR, Wall VJ (1993) Cassiterite solubility, tin speciation and transport in a magmatic aqueous phase. Econ Geol 88: 437-460

Wilson GA, Eugster HP (1990) Cassiterite solubility and tin speciation in supercritical chloride solutions. In: Spencer RJ, Chou-I-Ming (eds) Fluid-mineral interactions; a tribute to H.P. Eugster. Geochem Soc Spec Publ, 2, 179-195

INTRODUCTION TO CHAPTER III

In Chapter II, I presented a general characterization of the San Rafael deposit, focusing on the structural geology and its relationship to mineralization. I showed that the different stages in the deposit paragenesis are associated with specific styles of wall-rock alteration. In the following chapter, I examine the hydrothermal alteration in detail and make quantitative estimates of mass-transfer associated with the different alteration stages. I also use these data to constrain the physicochemical conditions responsible for alteration and mineralization.

CHAPTER III

Geology and geochemistry of alteration
at the San Rafael Sn-Cu deposit, SE Peru

M.S.J. Mlynarczyk, A.E. Williams-Jones and D. Dolejš

ABSTRACT

San Rafael, located in the Eastern Cordillera of the Peruvian Central Andes, is a world-class hydrothermal tin lode, which hosts a total resource of ~1 million tonnes tin (metal), and has an average grade of 4.7 wt.% Sn. The mineralization is of the cassiterite-sulfide type and occurs in a vertically extensive vein-breccia system, centered on a shallow-level, Late Oligocene granitoid stock. Two distinct stages of pervasive alteration are developed throughout the 1,200 m-high vertical extent of the deposit, and are interpreted to represent the interaction of the granitic host rocks with fluids of contrasting composition.

An early, pre-ore alteration consisting of weak incipient sericitization and chloritization, was followed by strong sericitization and strong tourmalinization. The former developed at the margins of early, barren, tourmaline-quartz veins, and is attributed to hot magmatic brines (400-530°C and 34-62 wt.% NaCl eq.), which circulated in the early stages of the hydrothermal system. Where brought to completion, this alteration sequence produced a marked enrichment of the rocks in B, Mg and Fe, and a strong depletion of alkalis and alkali-earth elements, which resulted in a total mass gain of ≤ 6 % and a volume increase of ≥ 6 %.

The ore stage alteration, which surrounds cassiterite-quartz-chlorite-($\pm$ sulfide)-bearing veins and breccias, consisted of pervasive chloritization. It was caused by fluids of intermediate temperature and salinity (~380°C and ~20 wt.% NaCl eq.), and strongly overprinted all earlier alteration, apart from tourmalinization. These fluids introduced large amounts of Fe, Mn, Sn, W and In, and largely removed alkalis and alkali-earth elements from the rocks, producing a mass increase of ~ 4 % and a volume decrease of 3-4 %.

The early and later ore-stage fluids either represent separate pulses, exsolved from discrete injections of granitic magma, or the latter fluid was the product of mixing of the early hypersaline (magmatic) brine with later meteoric waters. The second hypothesis is favoured, based on evidence that onset of the ore-stage coincided with opening of the vein system and a marked decrease in fluid salinity and temperature (down to 0 wt.% NaCl eq. and ~ 230°C). A substantial dilution of the early hypersaline fluid, coupled with

moderate cooling, would also explain very well the massive precipitation of Fe-rich chlorite and tourmaline, characteristic of the ore stage, because it would strongly depress the solubility of Fe in the hydrothermal solution.

On the basis of mineral stability relationships during main-stage chloritization, the accompanying deposition of cassiterite took place at an fO_2 between 10^{-35} and 10^{-30} and an (aFe^{2+}/a^2H^+) ratio between $10^{3.8}$ and $10^{4.6}$, from fluids which became progressively cooler and more oxidizing. Fluid-rock interaction did not favor tin deposition, as chloritic alteration of granitic rocks increases the fluid acidity, and this in turn increases Sn solubility. This explains why the bulk of cassiterite in the deposit is restricted to veins and breccias, as opposed to being disseminated in the chloritic alteration.

INTRODUCTION

Hydrothermal alteration, an important feature of many ore deposits, is a product of direct interaction between the fluids circulating in the geological environment and their host rocks, and commonly reflects the physical and chemical conditions of mineralization. Although such alteration is widespread in tin-mineralized systems and takes many forms (e.g., tourmalinization, greisenization, sericitization, chloritization, albitization, microclinization, and silicification; Hosking, 1951; Taylor, 1979; Stemprok, 1987) very few studies have fully taken advantage of its potential to quantitatively constrain the chemistry of the ore fluids and the conditions of ore genesis.

The San Rafael deposit in Peru, the world's largest hydrothermal tin lode, containing ~ 1 million tonnes of metal at an average ore grade of ~ 4.7 wt.% Sn (Minsur, unpubl. data, 2002) is encased in a broad envelope of intense wall-rock alteration that displays a complex evolution from early pre-ore sericitization and tourmalinization in the early barren stage, to strong ore stage chloritization. The deposit thus affords an outstanding oportunity to use this record of fluid-rock interaction to reconstruct the changing physicochemical conditions of the hydrothermal system and identify some of the important controls of ore formation.

In this paper, we characterize in detail the distinctive types of hydrothermal alteration at San Rafael, relate them to specific episodes of veining and mineralization,

and establish a general sequence of alteration. We then use the alteration to estimate quantitatively the physico-chemical conditions and the mass transfer associated with the formation of the deposit. This allows us to place constraints on the fluid evolution in this hydrothermal system, required to develop a comprehensive genetic model for this world-class example of lode-style tin mineralization.

GEOLOGIC SETTING

The San Rafael deposit is located in the Cordillera Carabaya, a sub-unit of the Eastern Cordillera of the Peruvian Central Andes, which is composed of a ~15-km-thick sequence of (mostly) Lower Paleozoic marine sedimentary rocks. This region is the interface between the Brazilian craton and the Main Arc of the Andean orogen, and has been marked by episodic, mixed, mantle- and crust-derived magmatism (Kontak et al., 1986; Clark et al., 1990). The Andean orogenic cycle was initiated in the Triassic, with the onset of eastward subduction of the Nazca plate beneath the South American plate, however, the modern Central Andes have been forming since the Late Oligocene, when the convergence rate between the two plates increased significantly (Sempere et al., 1990). The stratigraphy of the area is built on a basement of Precambrian gneisses, and begins with ~10 km of early Paleozoic pelites and psammites (the San José, Sandía and Ananea Formations), which were deformed and metamorphosed to sub-greenschist facies during the Late Devonian to Early Carboniferous. These strata are overlain unconformably by 3-4 km of late Paleozoic psammites and carbonates (Mississippian Ambo Group, Pennsylvanian Tarma Group, and Permian Copacabana Group), and ~3 km of red beds and intercalated volcanic rocks (Mitu Group) deposited from mid-Permian to Triassic times. The sequence ends with 1 km of Cretaceous psammites and carbonates (Cotacucho Group) and ~800 m of Miocene-Pliocene felsic ignimbrites and red beds of the Crucero Supergroup (Laubacher, 1978; Clark et al. 1983; 1990; Sandeman et al., 1996).

There were several Late Devonian to late Tertiary episodes of felsic magmatism in the Cordillera Carabaya, which were associated with metallic mineralization. The earliest of these, from Late Devonian to Early Carboniferous, produced granitoid plutons with

minor Sn-W mineralization. This was followed by the emplacement of large Permo-Triassic granitoid batholiths containing substantial Sn-Cu-W-Mo mineralization, and later by small (Late Cretaceous) granodiorite stocks with minor Ag and base-metal mineralization. However, the bulk of the economic mineralization (Sn, W, Ag and base metals) accompanied intrusion of middle to late Tertiary granitic stocks (Kontak and Clark, 1988).

San Rafael is part of the northwestern extension of the Central Andean tin belt, a regionally extensive metallogenic province, stretching some 1,400 km through Bolivia, to northern Argentina, and hosting over 400 tin-tungsten-base metal deposits. These deposits, generally of the hydrothermal-vein or porphyry-tin type, are associated with felsic to intermediate, plutonic and subvolcanic rocks, and are either of Late Triassic-Early Jurassic or Late Oligocene to Miocene age (Ahlfeld and Schneider-Scherbina, 1964; Kelly and Turneaure, 1970; Turneaure, 1971; Sillitoe et al., 1975; Grant et al., 1980; Urquidi-Barrau, 1989). The tin and tungsten deposits of the Eastern Cordillera of Peru are few in number compared to those in neighbouring Bolivia, and are associated with very small igneous centers. Nevertheless, some of these deposits, which include San Rafael and Palca XI (~ 1.5 Mt ore at an average grade of 1.3 % WO_3; Farrar et al., 1990) host ores that are among the richest in the World.

GEOLOGY OF THE DEPOSIT

San Rafael is a lode-type tin-copper deposit, located at latitude 14°13'00"S and longitude 70°19'30"W, ~150 km NNW of the city Juliaca in SE Peru (Fig. 1). The deposit crops out at elevations between 4,500 and 5,100 m, on the flanks of the glacier-capped Nevado Quenamari, and is estimated to have contained (prior to mining activity) ~21 million tonnes of ore, with an average tin grade of 4.7 wt. %. Currently, after over 45 years of mining activity, the reserves are ~14 million tonnes of ore, grading 5.3 wt.% Sn (Minsur, unpubl. data, 2002). Despite its world-class character, the deposit is still poorly known and research on it has been limited to preliminary studies in the 1980's (Arenas, 1980; Palma, 1981; Clark et al., 1983; Kontak and Clark, 1988) and the more recent work of Kontak and Clark (2002) and Mlynarczyk et al. (2003).

49

FIGURE 1. Geological map of the southwestern part of the San Rafael district (modified after Arenas et al., 1980). The granitic stocks are the exposure of a composite granitoid pluton of Late Oligocene age, which underlies the area shown on the map. Hornfelses and quartzites are contact metamorphosed shales and sandstones of the Sandía Formation (Upper Ordovician). The small area in black, on the western flank of the stock, corresponds to a localized zone of pervasive boron metasomatism.

PERU

PACIFIC OCEAN

Lima

SAN RAFAEL ☆

Juliaca○

0   500 km

MARIANO

JORGE

VICENTE

SAN RAFAEL

GUILLERMO

PEDRO

Tourmalinized granite
Coarse-grained granitoids
Fine-grained granitoids
Quartzite (Sandía Fm.)
Hornfels (Sandía Fm.)
Mineralized veins

N

0   500 m

access to mine

50 75 50
35 56 62 43 47 73
70
65 63 74
76 51 85 65
78 52 75
75 80
60 65 52 47 68 54 75
64 64 71 68 54 65 68
65 66 85 54
68
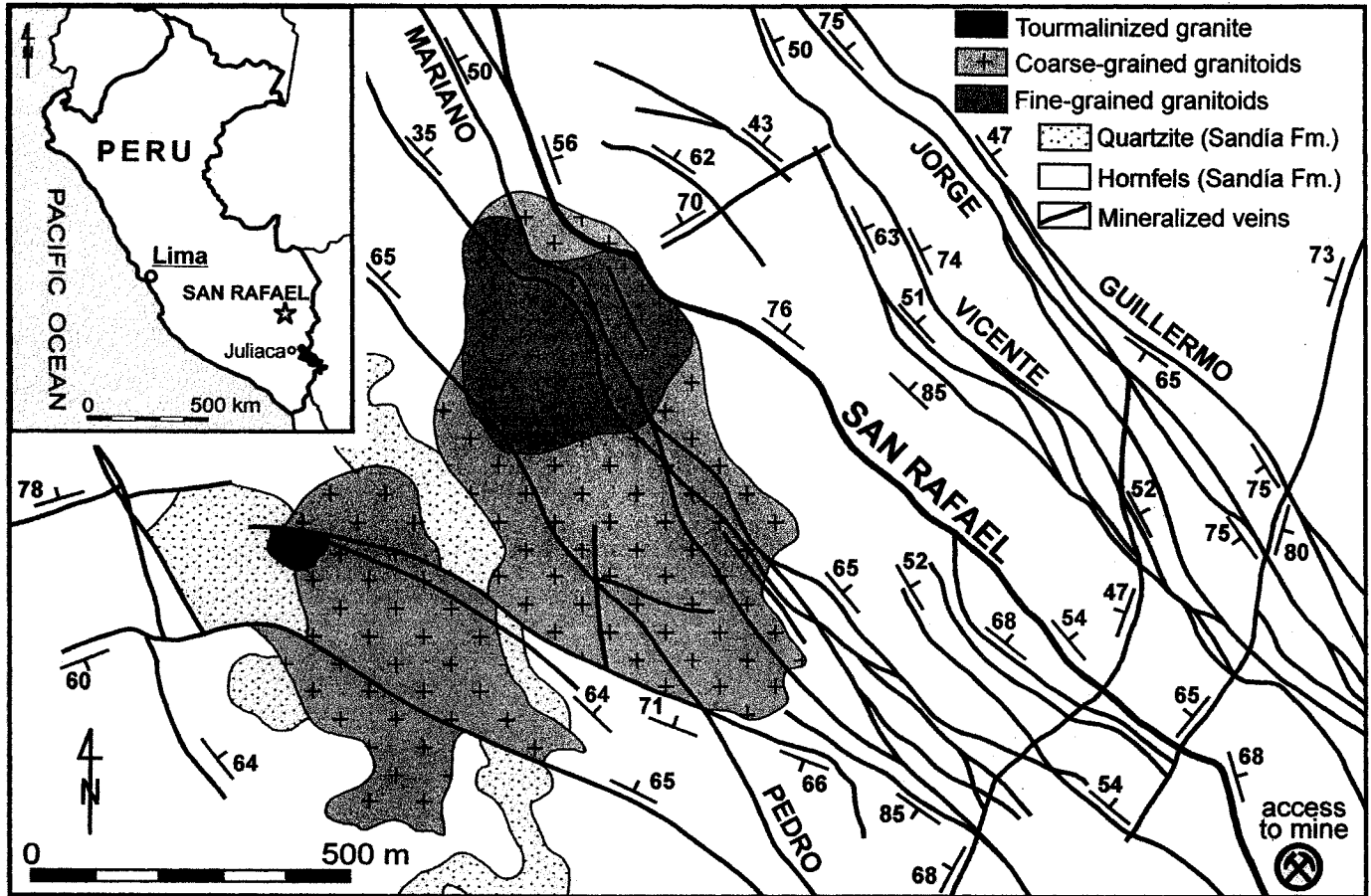
The mining area of San Rafael hosts a large number of sub-parallel veins, most of which are 2-3 km long, trend NW and dip moderately to steeply to the NE (Fig. 1). This composite vein system is centered on a small granitoid pluton ($<$ 15 km^2 surface area) of Late Oligocene age ($\sim$25 Ma), emplaced in slates and subordinate quartzites of the Late Ordovician Sandía Formation. The intrusion, which is elongated to the northeast, crops out only at its extremities, and in the central part is covered by a structural dome of metasedimentary rocks (5300 m above sea level), which were indurated and locally converted to hornfels. The pluton consists of porphyritic, cordierite- and biotite-bearing, subsolvus granites and granodiorites, which are strongly peraluminous and host abundant alkali-feldspar megacrysts, up to 10 cm in length. In addition, there are numerous dykes of granitoid porphyry and quartz-feldspar-phyric rhyolite, which cut the pluton and adjacent metasedimentary rocks.

Despite the large number of veins in the district, about 98 % of the known tin reserves are hosted by a single complex vein-breccia structure, the San Rafael lode (Minsur, unpubl. data, 1999). This structure is located in the southwestern part of the mining area, has an average strike of $\sim$330°, dips 40 to 75° to the NE and can be traced on surface for a distance of $\sim$3.5 km (Fig. 1). A feature that makes the San Rafael lode exceptional, is that it is mineralized over a vertical extent exceeding 1,200 m (from 5100 to 3900 m above sea level), and hosts ores of unusually high grade, locally attaining 45 wt.% Sn.

In its upper part (down to the 4600 m level), the lode is narrow ($<$ 2 m), planar and contains 4 to 8 wt.% Cu and $<$ 1 wt.% Sn (Minsur, unpubl. data, 2000). The copper orebodies occur where the lode is hosted by slates or cuts the outer parts of the pluton and, therefore, straddles the granitoid-metasedimentary rock contact (Fig. 2). Brecciation and open-space filling are common textural features of the ores, which consist of massive to semi-massive chalcopyrite, with quartz and chlorite, as well as minor cassiterite (needle-tin), pyrite, marcasite, sphalerite, galena, pyrrhotite, arsenopyrite, fluorite, calcite and siderite.

In the lower parts of the deposit, where it is hosted by the intrusion, the San Rafael lode dilates into a series of nine subvertical shoots, which attain widths of up to 50 m and extend up to 700 m downdip (Fig. 2). These shoots are fault-jogs created during sinistral-

FIGURE 2. A. Cross-section of the San Rafael lode through the Contact Orebody (N 58 E). **B.** Longitudinal section of the San Rafael lode (modified after Minsur, unpub. data and Mlynarczyk et al., 2003).

A

4730 — SW   NE

4600

4533

4410

4310

4200

4100

4000 m a.s.l.

0   250m

B   SE   Nevado Quenamari   NW

5000 m

4500 m

4000 m a.s.l.

0   1000m

Ore Shoot   *Contact Orebody*

Ordovician slates and hornfelses   Copper orebodies

Granitoid intrusion   Tin orebodies
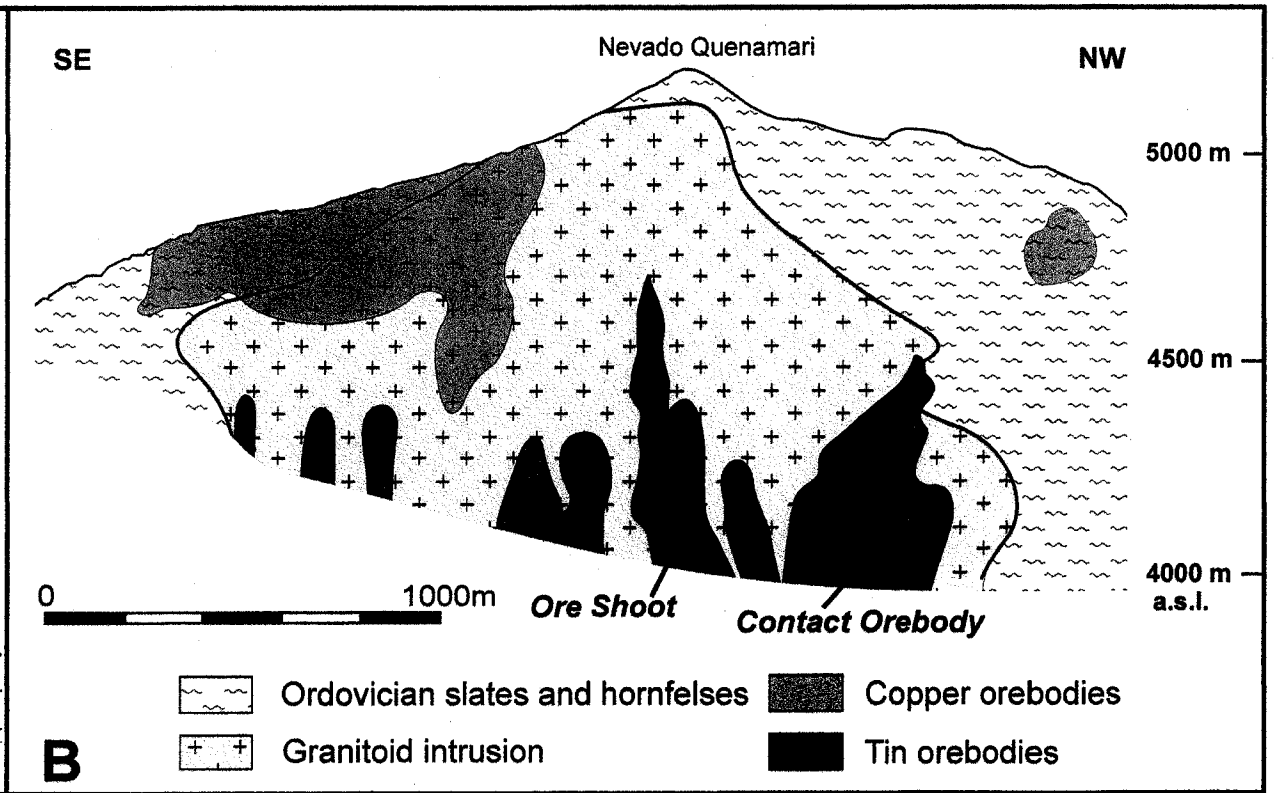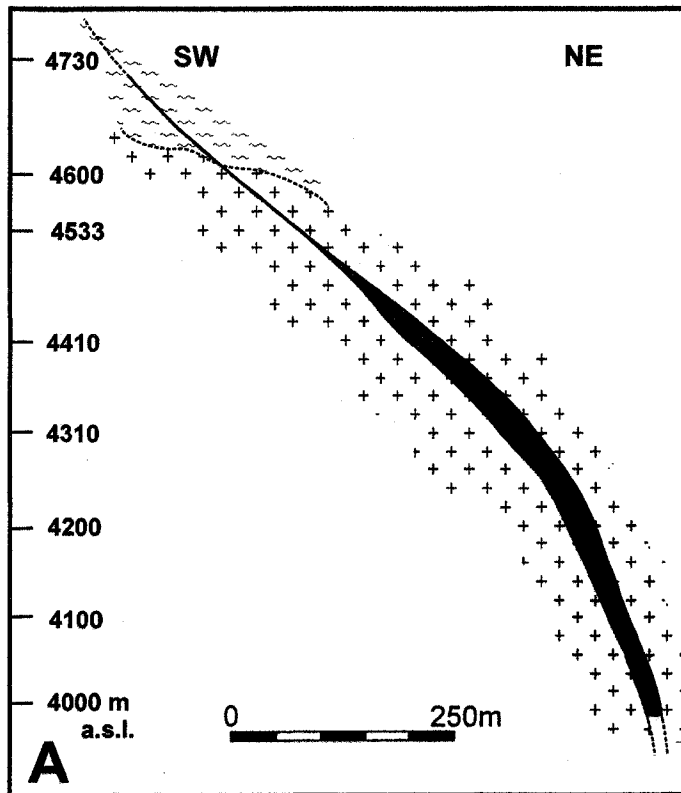
normal strike slip movement, which took place along the San Rafael fault (Mlynarczyk et al., 2003). They localize dilational zones, filled with rich tin ores, that contain an average of > 5 wt.% Sn but only ~0.2 wt.% Cu (Minsur, unpubl. data, 2000). The mineralization occurs in the form of veins and breccia zones, and is dominated by cassiterite (massive cassiterite, wood-tin or needle-tin), quartz and chlorite, with locally minor wolframite, hematite and chalcopyrite. Cross-cutting relationships among veins and multiple episodes of vein reopening, brecciation and open fracture-filling led to a complex lode structure (Fig. 3). The proportion of cassiterite in the ore was clearly controlled by the abundance of veins and veinlets, and increases where they branch or intersect, and where they deflect in strike or dip. Tin grades are the highest in the large (1-2 m wide) footwall and hangingwall veins, as well as in the zones of brecciation, which commonly are several meters wide. Where they are hosted by the granitoid pluton, cassiterite-bearing veins have sharp contacts and are easily traced, but within metasedimentary rocks they are very irregular.

HOST ROCKS

The pluton, which hosts the San Rafael deposit, is composed of a variety of S-type, ilmenite-series granitoids (Chappell and White, 1974; Ishihara, 1981), most of which have a markedly porphyritic texture (Fig.4E). According to the criteria of Frost et al. (2001), the granitoid suite can be classified as magnesian, alkali-calcic and peraluminous (Alumina saturation index, ASI[1] ~ 0.96-1.11). The principal intrusive phases are: (1) a coarse-grained K-feldspar-megacrystic, cordierite-biotite leucogranite; (2) a medium-grained, grey, K-feldspar-megacrystic, cordierite-biotite granite; and (3) a coarse- to fine-grained, grey to dark-brown, biotite granodiorite, which varies from K-feldspar-megacrystic, and cordierite- and garnet-bearing (3a) to equigranular, biotite-rich, and cordierite- and garnet-absent (3b). In addition, small (5-30 cm) enclaves of tonalitic composition (4) occur locally in the darker (more mafic) phases of the intrusion.

Spatial relationships among the granitoid phases suggest that the leucogranite may be slightly younger than the other intrusive phases, as it locally contains enclaves of the

---

[1] The formula of Frost et al. (2001) for ASI was modified to be: Al / [2 x (Ca − 1.67 P) + Na + K]

FIGURE 3. Schematic plan views of the San Rafael lode on the 4050 m level (modified after unpublished Minsur mine data). Section A - between stations 18 and 14 (south); section B - between stations 13 and 9 (south); section C - between stations 1 (south) and 4 (north). Strike and dip measurements are given for the footwall and hangingwall veins.

A
75̄ 70̄ 65̄
60̄ 70̄ 70̄
65̄

B
70̄ 65̄
65̄ 70̄ 75̄

C
77̄
70̄
70̄ 75̄
65̄

0   20m

☐ Extent of chloritic alteration envelope

▨ Cassiterite veins with brecciation

▨ Cassiterite veinlets in chloritized wallrock

■ Principal cassiterite veins
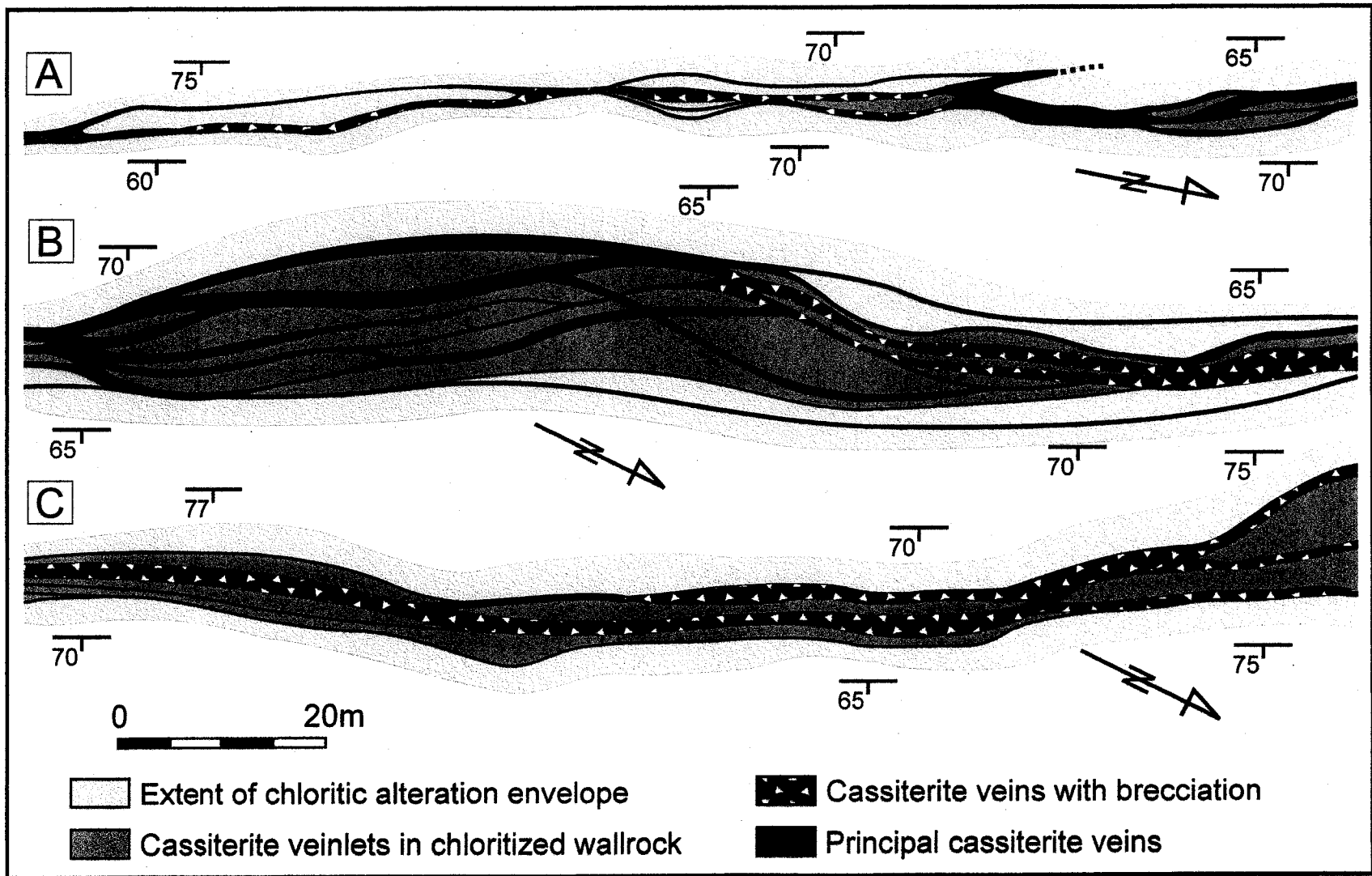
FIGURE 4. Alteration in hand samples. **A** - Multiply reopened quartz vein with adjacent zones of strong sericitization and tourmalinization of alkali-feldspar granite. Jorge vein (North), level 4050, between stations 1 and 2. (Sample SAR-J26). Capitals indicate the slabs (discussed in the text) for which whole-rock compositions were analysed. The arrow indicates the vein leader. Scale bar divisions are in cm. **B** - Zoned alteration halo surrounding a tourmaline-quartz vein in tonalite (see text for discussion). In order inward: incipient sericitization *(yellow)*, chloritization *(green)*, sericitization *(pinkish)* and tourmalinization *(dark brown)*. Drill hole no. 4, from the Jorge vein to the San Rafael lode, 68.6 m. Capitals indicate the slabs for which whole-rock compositions were analysed. The arrow indicates the vein leader. Scale bar divisions are in cm. **C** - Zoned alteration halo surrounding a tourmaline-quartz vein in granite. In order inward: incipient sericitization *(whitish)*, chloritization *(green)*, sericitization *(yellow)* and tourmalinization *(dark brown)*. Drill hole no. 4, from the Jorge vein to the San Rafael lode, 61.8 m. The arrow indicates the vein leader. Scale bar divisions are in cm. **D** - Tourmaline veinlets surrounded by diffuse alteration haloes in a mildly sericitized and chloritized granite. The preferential tourmalinization of the alkali-feldspar megacryst is conspicuous. Upper part of the San Rafael lode. (Sample SAR-D7). Scale bar divisions are in cm. **E** - Fresh, porphyritic granitoid, with large, flow-oriented alkali-feldspar megacrysts. Level 4200. Scale bar divisions are in cm. **F** - Strong chloritization of the granitic wallrock on the 4225 level of the Ore Shoot. The only primary mineral remaining is quartz, visible as white patches in the green groundmass. Scale bar divisions are in cm. **G** - Contact between an early dyke of tourmaline-quartz microbreccia *(dark-brown, upper part of image)* and strongly chloritized granitic wallrock *(green, lower part of image)*, both crosscut by numerous late quartz veins. Contact orebody, level 4270, front A. Hammer for scale. **H** - Late, barren quartz vein crosscutting a cassiterite-quartz-chlorite vein in strongly chloritized granitic wallrock on the 4310 level of the Ore Shoot. Scale bar divisions are in cm.
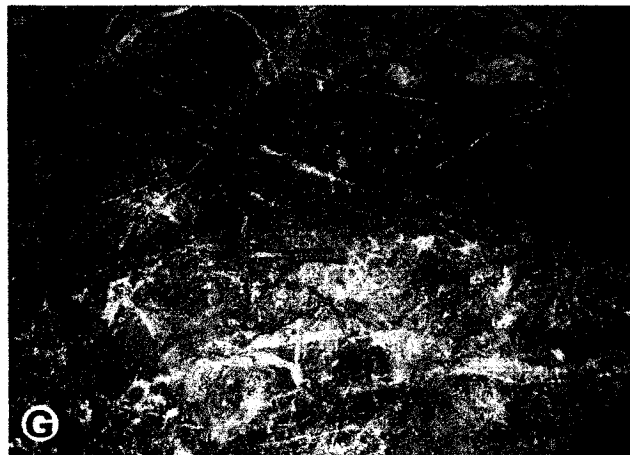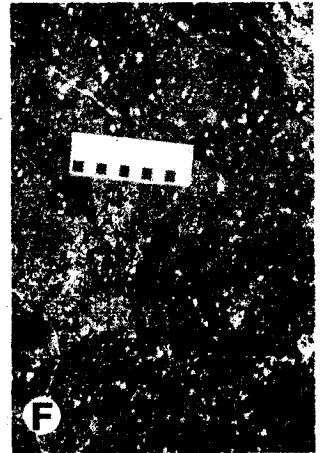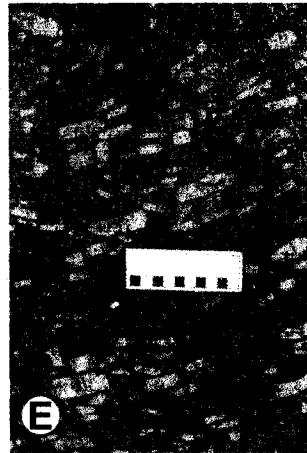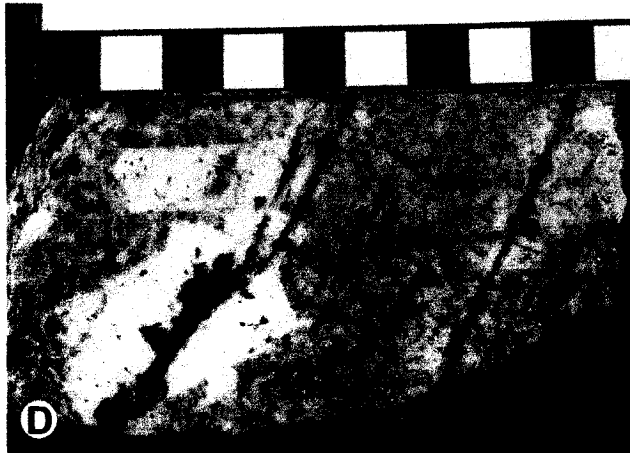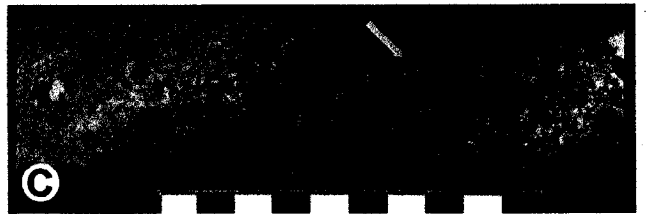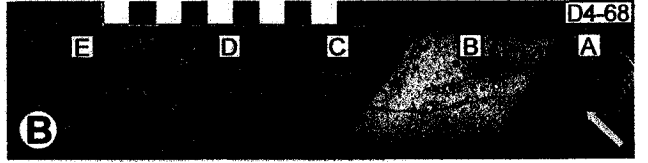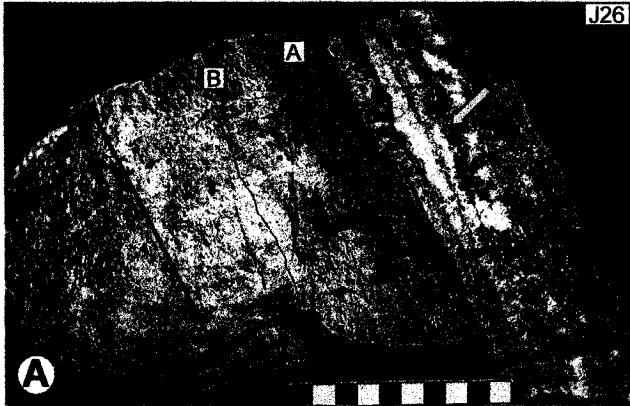
biotite-granodiorite and tonalite, measuring 1-3 m, and forms apophyses, which penetrate between them. Nevertheless, the rather diffuse contacts between the lighter- and darker-colored phases, as well as the local occurrence of K-feldspar megacrysts along these contacts indicate that, with the exception of the tonalitic enclaves, the other phases were essentially coeval.

Abundant highly-aluminous and/or ferromagnesian minerals (biotite, cordierite, garnet, sillimanite or andalusite) in the granitoids indicate that the suite originated by partial melting of metasediments and experienced only a short evolutionary history, with very incomplete restite separation. Petrographic and bulk rock geochemical studies of the granitoids (Mlynarczyk et al., in prep.) suggest that the San Rafael granites are not geochemically evolved, and do not represent a fractional crystallization series. Rather, the different phases are related to one another by various mechanisms of crystal accumulation, and represent restite-rich crystal mushes.

The metasedimentary rocks, surrounding the San Rafael pluton consist mostly of indurated slates, hornfelses, and subordinate quartzites, which correspond mostly to the Late Ordovician Sandía Formation (Palma, 1981). These rocks experienced deformation and regional metamorphism in the sub-greenschist to upper-greenschist facies during a Late Devonian-Early Carboniferous orogeny, prior to the emplacement of the San Rafael pluton.

VEIN TYPES AND ASSOCIATED ALTERATION

The granitic rocks, which host the San Rafael lode, are commonly altered, even at considerable distance from the veins, albeit weakly, as indicated by ubiquitous *pinitization* of cordierite and local, weak sericitization of calcic plagioclase and chloritization of biotite. These features represent incipient, regional, post-magmatic alteration. The main hydrothermal alteration is clearly fracture-controlled, and the bulk of it is confined to the vicinity of the vein-breccia system.

In addition to irregularly distributed, late-magmatic (or early post-magmatic), sodic or potassic metasomatism of feldspars, two distinct stages of alteration and veining are evident. Early, pre-ore alteration shows a broad evolution from incipient, weak

sericitization and chloritization to strong sericitization, and then intense tourmalinization. This alteration is associated with early, barren, tourmaline-quartz (± arsenopyrite) veins and veinlets, and extends for tens of centimeters on either side of them, commonly affecting large areas of the intrusion.

The main ore-stage alteration consists of strong, pervasive chloritization, which envelops the entire vein-breccia system, and overprints all earlier alteration types, with the exception of tourmalinization (Figs. 4F,G,H). Chloritic alteration is associated with tin- and copper-bearing quartz veins, and is texturally destructive, transforming the precursor granitic rocks into a dark green rock, in which the quartz phenocrysts are the only remaining evidence of its igneous origin. The presence of rare tourmaline-cassiterite-chlorite-arsenopyrite veins indicates that the early tourmalinization and main-stage chloritization were separated by a relatively short interval of time. The uppermost part of the deposit (above elevation 4730 m) subsequently experienced supergene alteration, which produced characteristic secondary minerals, such as covellite, chalcocite, goethite and limonite.

Whereas the nature of the alteration changed with time, there is no evidence of a spatial control on its distribution. Tourmaline-quartz veins with wide sericitic haloes are present in both the upper and the lower parts of the San Rafael lode, as is pervasive chloritization. There does not seem to have been a host-rock control on the alteration type either, as both the granitoids and metasedimentary rocks have undergone the different types of alteration and appear equally affected by strong chloritization.

Partly for ease of study and partly because the deposit is hosted mainly by the intrusion, this study focuses on the hydrothermal alteration of granitic rocks rather than that of hardened slates and hornfelses. The latter are much less suitable for alteration studies because of compositional heterogeneity and the effects of contact metamorphism.

In total, 15 vein types and associated alteration have been recognized and ordered chronologically, based on crosscutting relationships and mineralogy (Tab. 1). Vein types 1 and 2 formed during the early barren stage, type 3 - at the onset of the main ore stage, during which types 4 to 13 developed, and finally, types 14 and 15 formed during the closing stages of the hydrothermal system. Summary descriptions of these vein types are

TABLE 1. Vein types at San Rafael (in chronological order) and associated alteration.

Vein type	Alteration (in sequence inwards)	Shape and size Special features	Position in paragenesis Crosscutting relationships and occurrence
Quartz-arsenopyrite ± tourmaline	Strong sericitization	Planar, 1-4 mm wide. Alteration halo > 15 mm wide.	Earliest veinlets (?). Rare.
Tourmaline-quartz ± arsenopyrite	(Mild sericitization) → (chloritization) → strong sericitization → strong tourmalinization ± silicification	Planar, locally irregular, ≤ 3 cm wide. Parallel veinlets are common. Halo 1-25 cm wide.	Very early. Crosscut vein types 1, 2. Very common. Multiple generations and evidence of vein reopening are common. Blue tourmaline veinlets crosscut brown tourmaline veinlets.
Tourmaline-cassiterite-chlorite-arsenopyrite	Strong chloritization	Planar, ≤ 15 cm wide. Alteration halo > 10 cm wide. Quartz is absent.	Tourmaline last, and cassiterite and chlorite are first to appear in the paragenesis. Very rare.
Chlorite-cassiterite (wood-tin)-quartz	Strong chloritization	Irregular, 1-15 cm wide. Generally composed of alternating lighter and darker cassiterite-rich layers. Occur in pervasively chloritized zones.	Early tin ore stage ? Crosscut / reopen type 2 veins. Common, especially at elevations of 4350-4533 m. Commonly associated with multiple episodes of brecciation
Chlorite-cassiterite-hematite ± quartz	Strong chloritization	Irregular, > 6 cm wide. Occur in pervasively chloritized zones. Quartz is present only locally and may be a later infill (?).	Assumed to belong to the main ore stage, based on the abundance of cassiterite. Very rare.
Cassiterite (massive)-quartz-chlorite	Strong chloritization	Planar, typically 1-30 cm wide. Alteration halo ≤ 15 cm wide. Occur in pervasively chloritized zones. Open-space filling, with most of the quartz in the center of the vein.	Main (tin) ore stage. Crosscut vein types 2, 4, 6. Very common. Multiple generations and evidence of vein reopening (crack and fill or cookscomb textures) are common.
Cassiterite (massive)-quartz-chlorite - wolframite-sulfides (mainly: chalcopyrite or arsenopyrite, with minor pyrite and sphalerite)	Strong chloritization	Planar, typically 1-40 cm wide. Alteration halo ≤ 15 cm wide. Occur in pervasively chloritized zones. The sulfides invariably fill the center of the vein, together with or on top of late quartz.	Late (tin-copper) ore stage. Crosscut vein types 2, 4, 6. Some type 7 veins may be broadly coeval with type 6 veins, except that they remained open until the onset of sulfide deposition. Moderately common.
Chlorite	Strong chloritization	Planar, 1-3 mm wide. Alteration halo ≤ 3 mm wide.	Crosscut type 2 veinlets. Occur in the vicinity of vein types 6-7-13, therefore assumed coeval with them.
Cassiterite (as needle-tin)-chlorite-quartz-chalcopyrite-pyrite	Strong chloritization	Irregular, 1-15 cm wide. Occur in pervasively chloritized zones.	Late (tin-copper) ore stage. Common, though mostly restricted to elevations of 4533-4750 m.
Quartz-sulfides (mainly: sphalerite, galena, chalcopyrite, pyrite, marcasite, arsenopyrite, siderite)	Chloritization	Planar, 1-30 cm wide.	Late (sulfide) ore stage. Reopen type 2 veins. Moderately common. Vein reopening / brecciation observed.
Pyrrhotite-chalcopyrite-quartz (± pyrite-marcasite-siderite)	Chloritization	Planar, ≤ 30 cm in width. Pyrite, marcasite, siderite are secondary. Vugs in massive pyrrhotite contain euhedral pyrite crystals ≤ 3 cm long	Late (sulfide) ore stage. Moderately common in the lower part of the deposit (below 4533 m).
Chalcopyrite-quartz-chlorite-pyrite ± fluorite-siderite	Strong chloritization	Planar or irregular, 1 to > 50 cm wide. The alteration halo can exceed a width of 30 cm. Occur in pervasively chloritized zones.	Late (sulfide) ore stage. Crosscut vein types 2,6,7. Very common in the upper part of the deposit (above 4533 m).
Quartz (± very minor chlorite or traces of sulfides)	Strong chloritization	Planar, 1-30 cm wide. Alteration halo commonly several-cm wide, but can exceed 1 m in width. Open-space filling with quartz vugs in the center.	Crosscut veins type 2, 4, 6, 7, 8, 10, 13, hence are very late in the paragenesis. Ubiquitous. Multiple generations and evidence of vein reopening are common.
Quartz-calcite	Weak chloritization (unless the host rock is tourmalinized, then no overprint is visible)	Planar or irregular, 2-20 mm wide with rather narrow halo. The white calcite is subhedral w.r.t. quartz and has a peculiar flaky habit.	Crosscut or reopen vein types 2, 8, 13. Moderately common
Quartz	No alteration halo	Planar, 1 to > 25 cm wide. A central zone of amethystine quartz is sometimes observed.	Latest in the paragenetic sequence ? (no alteration associated). Common.

presented in Table 1 and the associated alteration types are described in more detail below.

Very early, sodic and potassic alteration of feldspars

Evidence of the earliest post-solidus modification of the San Rafael granitoid suite can be observed only locally and may be inconspicuous in hand specimen. It is represented either by albitic overgrowths on alkali felspar phenocrysts (Fig. 5A), observed in the southwestern part of the intrusion, or by K-feldspar overgrowths on plagioclase crystals (Fig. 5B), encountered in the northeastern (Quenamari) part of the pluton. This sodic or potassic alteration has an irregular distribution within the intrusion and does not show any clear spatial relationship to the San Rafael vein-breccia system. Also, while it affects the composition of the feldspars, it does not much influence the bulk rock geochemistry, i.e., it was a closed system (isochemical) phenomenon. Although Kontak and Clark (2002) reported trends of marked Na or K enrichment in altered granitoids collected from surface exposures and the uppermost part of the San Rafael pluton (Fig. 6A, op. cit.), such trends were not observed in the present study, which was based mainly on samples from the central and lower part of the intrusion. All the granitoids representative of the San Rafael suite display a general trend of Na and K depletion with respect to fresh rocks, independent of alteration type (see below). The Na-K alteration of feldspars is, therefore, interpreted to reflect local, fluid-mediated, late-magmatic or early post-magmatic reequilibration of the cooling pluton. It does not appear to be related to any of the alteration types present in the deposit (either pre-ore, or associated with ore deposition) and did not contribute to the overall metasomatic mass change.

Early, barren stage

The earliest veins in the San Rafael deposit are associated with the barren, pre-ore stage and consist of tourmaline and subordinate quartz. They are very common, both in the vicinity of the lode and farther away and, typically, are surrounded by haloes of strong sericitization tens of centimeters-wide with a much narrower (several mm - several cm) inner envelope of tourmalinization (Fig. 4A). In some cases, disseminated arsenopyrite is

FIGURE 5. Alteration in thin sections. **A** - Rim of sodic plagioclase around a K-feldspar phenocryst. (Sample SAR-I42). Crossed polarisers. Length of photo: 2 mm. **B** - Twinned K-feldspar overgrowing a plagioclase phenocryst. (Sample SAR-I36). Crossed polarisers. Length of photo: 1.5 mm. **C** - Radiating aggregates of tourmaline crystals in altered granite. (Sample SAR-J26C). Crossed polarisers. Length of photo: 2 mm. **D** - Aggregate of dumortierite crystals *(yellow)* in strongly tourmalinized granitoid. (Sample SAR-I46). Crossed polarisers. Length of photo: 1 mm. **E** - Tourmaline crystals displaying marked color zoning. (Sample SAR-D1-276). Plane polarised light. Length of photo: 2 mm. **F** - Green, acicular crystals of late, iron-rich tourmaline, growing in a quartz-filled fracture in yellow tourmaline. (Sample SAR-D4-68A). Plane polarised light. Length of photo: 0.3 mm. **G** - Quartz-cassiterite veinlet crosscutting strongly chloritized wallrock. Note the absence of disseminated cassiterite. (Sample SAR-D1-444). Plane polarised light. Width of photo: 1 mm. **H** - Sheets of sericite growing beside a plate of chloritized biotite, containing minor carbonate and titanite *(small dark crystals)*. (Sample SAR-R432-B). Crossed polarisers. Width of photo: 1 mm. **I** - Plate of pervasively tourmalinized biotite with euhedral inclusions of rutile (Sample SAR-D4-68B). Plane polarised light. Length of photo: 1 mm. **J** - Plate of pervasively chloritized biotite with prismatic inclusions of rutile and pleochroic halos (Sample SAR-R432A). Plane polarised light. Length of photo: 2 mm. **K** - Alternating layers of chlorite and cassiterite in a complex cassiterite-quartz-chlorite vein (Sample SAR-A4-3). Plane polarised light. Length of photo: 2 mm. **L** - Simultaneous growth of chlorite, hematite and cassiterite in a chlorite-cassiterite vein (Sample SAR-R143). Plane polarised light. Length of photo: 1 mm. **M** - Cassiterite intergrown with chlorite (both replacing a plate of biotite) in strongly chloritized and mineralized wallrock. (Sample SAR-D1-444). Plane polarised light. Width of photo: 2 mm.
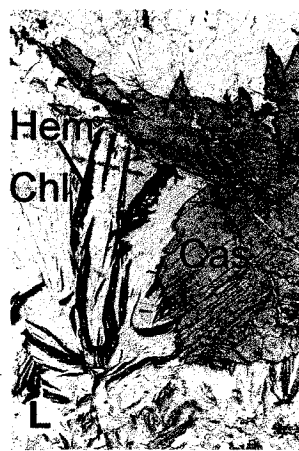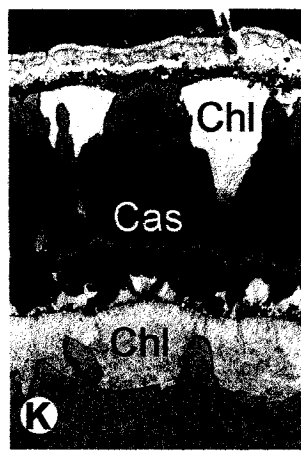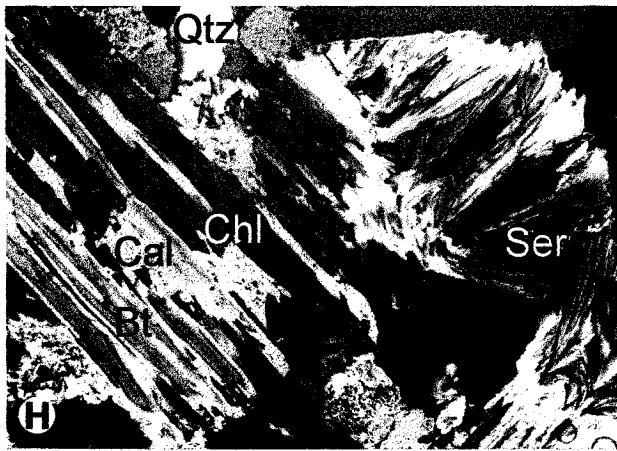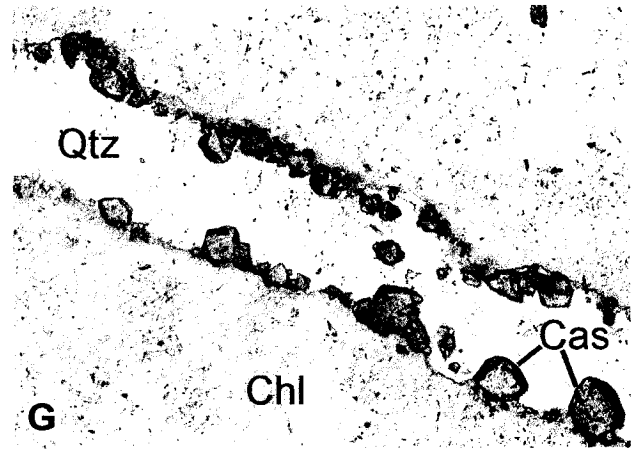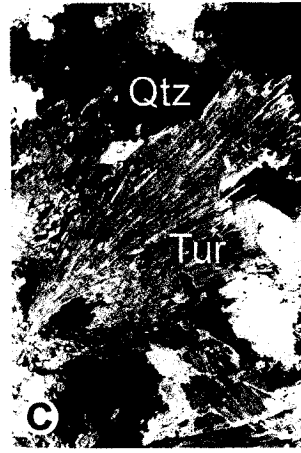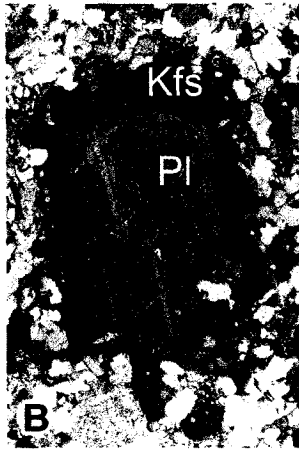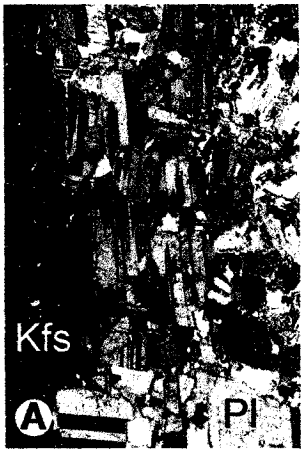
present in the alteration halo or occurs in the vein itself, and silicification accompanies tourmalinization. The tourmaline-quartz veins or veinlets commonly occur as a series of parallel structures, cutting through large parts of the intrusion (Fig. 6), and may form denser stockworks, characterized by multiple vein generations and vein reopening. In such cases the associated sericitic alteration encompasses a width of many meters. Generally, the tourmaline-quartz veins are planar, and appear to form a conjugate set, with some veins striking ~330° and dipping NE (concordant with the strike of the San Rafael lode), and others striking ~295° and dipping SW. Some of the larger veins of the first set were reopened during the subsequent ore stage and filled by the main- and late-stage veins.

The alteration associated with the early, tourmaline-quartz veins can be fairly complex (Fig. 4A,B,C) and is described below, based on the veins where it is the most complete. The process was initiated by sericitization and minor chloritization of cordierite, moderate chloritization and subordinate sericitization of biotite, moderate sericitization of plagioclase (especially of its more calcic zones) and lesser sericitization of K-feldspar. This commonly imparted a bleached appearance to the rock (yellowish coloration in the case of tonalite). Rarely, local tourmalinization of cordierite, biotite and feldspars is also observed.

This incipient alteration was followed by *strong chloritization*, which produced a distinctive dark green color in the rock. Biotite was completely chloritized, plagioclase strongly sericitized and/or chloritized and K-feldspar moderately chloritized and sericitized. The next alteration phase is evident as a broad halo of *strong sericitization and subordinate tourmalinization,* which gives the host rock a whitish or yellowish coloration. In some cases, a greater abundance of tourmaline can produce a pinkish coloration of the rock. During this phase, previously chloritized biotite was partly or completely sericitized. Cordierite and feldspars were variably sericitized and these minerals, together with biotite, were locally replaced by tourmaline. Locally, the host rock displays a marked yellow coloration from pervasive or semi-pervasive iron-oxide staining, due to the decomposition of ferromagnesian minerals.

The last phase of early alteration comprised *strong tourmalinization and subordinate silicification,* and produced relatively narrow, dark brown haloes. In this

FIGURE 6. Core log # 5, from the Jorge vein (310-07 H-14 N) to the San Rafael Lode, showing the relationship between veins and the different styles of alteration and mineralization.

Host Rock | Principal alteration | Tourmaline breccias and veins | Ore veins | Tin grades (wt.%)

Jorge vein

Vicente vein
Split of the Vicente vein

Split of the San Rafael lode

San Rafael lode

Granodiorite   Sericitization   Sulfide-bearing veins

Leucogranite   Chloritization   Cassiterite-bearing veins

Fresh rocks
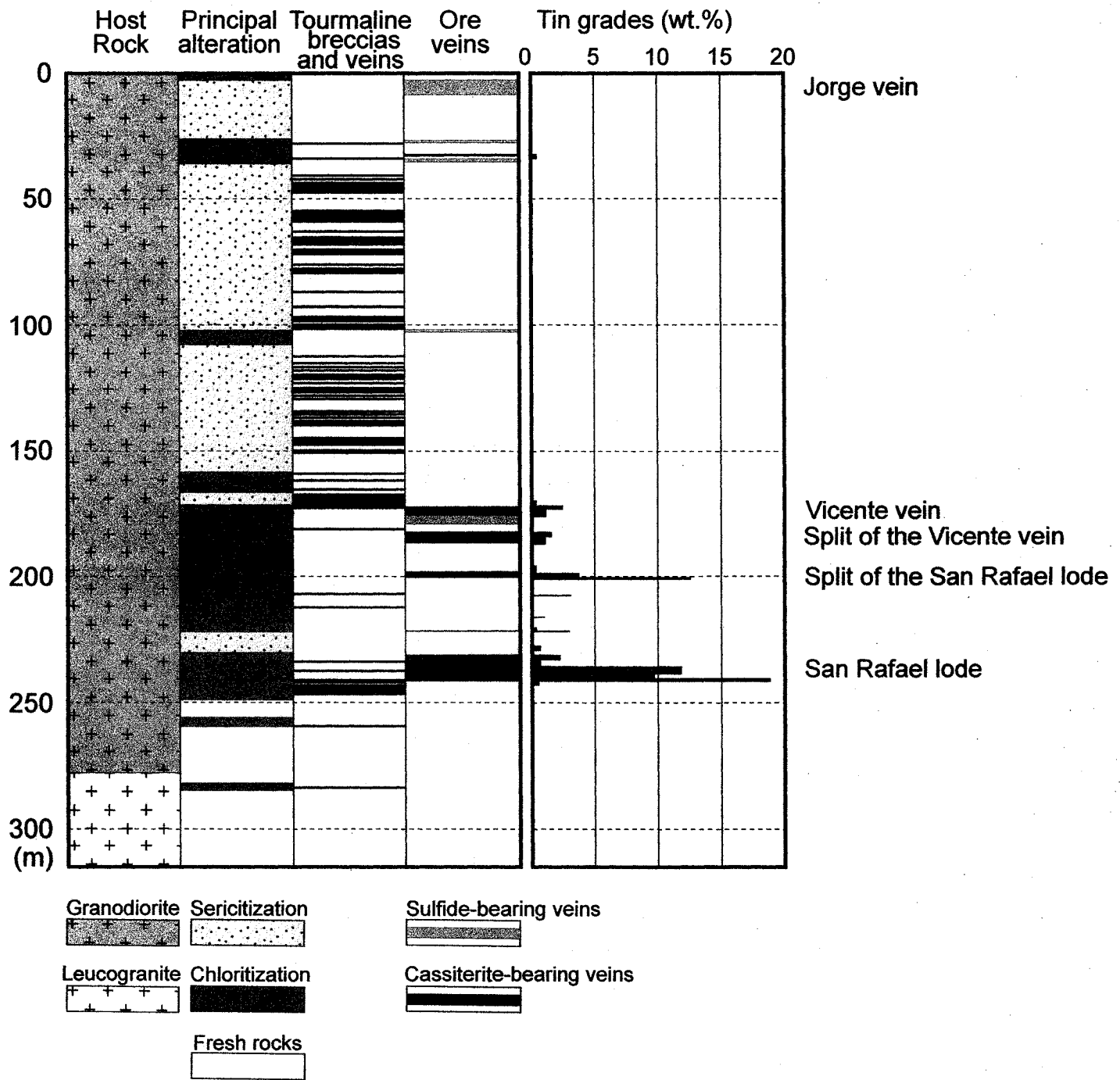
zone, the amount of tourmaline gradually increases inwards, until all former biotite, plagioclase, K-feldspar, cordierite, as well as secondary chlorite and sericite are replaced by tourmaline and quartz, which account for the bulk of the rock (Fig. 5C). The only relics of the original granitoid are the quartz phenocrysts, the accessory minerals (zircon, monazite ± apatite) and, in some cases, the outlines of tourmalinized K-feldspar phenocrysts. The proportions of tourmaline and quartz are quite variable, depending on the precursor and, more importantly, the relative importance of tourmalinization and silicification. Narrow haloes (< 3 cm), bordering tourmaline veins and veinlets generally contain appreciable tourmaline (40-50 vol. %), whereas wider haloes (> 30 cm) contain less tourmaline (15-30 vol. %) and more quartz. These latter zones display conspicuous porosity, in the form of abundant, 1 to 4-mm-wide vugs, which commonly host a second generation of euhedral, finely prismatic crystals of light-brown tourmaline.

An interesting and potentially important observation is that the outlines of tourmalinized biotite plates are commonly preserved and enclose numerous, euhedral, equant crystals of rutile (Fig. 5I). It is inferred that these rutile crystals formed as a result of small-scale redistribution of titanium, which was initially contained in the biotite. In some cases, lesser numbers of euhedral cassiterite crystals accompany the inclusions of rutile, but it is not clear whether the tin was also derived from the biotite or was introduced by late infiltration of ore-stage fluids.

Despite the ubiquitous occurrence of early tourmaline-quartz veins and associated tourmalinization, the bulk of the tourmaline is concentrated in hydrothermal microbreccia dykes, which locally are several meters in width and follow the lode along strike for hundreds of meters. These dykes, which are very common and frequently form swarms, are inferred to be broadly coeval with the tourmaline-quartz veins. They are composed mainly of fragments of quartz or tourmalinized wall rock, embedded in a matrix of pervasively tourmalinized rock flour and, commonly, are heavily veined by quartz (Fig. 4G). In general, they are very fine-grained and exhibit evidence of multiple episodes of brecciation.

Transition between the early, barren stage and the mineralized stage

In general, the tourmaline-quartz veins were closed prior to the ore event, creating the impression that the early, barren stage and ore deposition were separated in time. Thus, Clark et al. (2000) and Kontak and Clark (2002) suggest a ~2 Ma time gap between them. Nevertheless, a continuous transition between the deposition of barren tourmaline (identical to that of "common" tourmaline-quartz veins) and massive deposition of cassiterite and chlorite can be observed in rare tourmaline-cassiterite-chlorite-arsenopyrite veins, found in the lower part of the deposit. These veins are surrounded by haloes of intense chloritization and record a marked change, in both the nature and composition of their minerals. From the vein selvage to the center of the vein, the color of tourmaline (as seen in plane polarised light) changes abruptly from very pale or orange to dark green and then khaki-green. Cassiterite and chlorite (the principal minerals of the main ore event) co-precipitated with the khaki-green tourmaline. This, and especially the evidence of coeval growth of cassiterite and tourmaline suggest that the main, tin-ore stage followed immediately after the early, barren stage, but that this coincided with a major change in the physicochemical conditions of hydrothermal activity.

Main, tin-copper stage

All main- and late-stage veins in the San Rafael deposit, both tin- and copper-bearing, are associated with strong, pervasive chloritic alteration. This is the principal alteration in the deposit, and it affected the lode structure throughout its entire vertical extent, and for distances locally exceeding 10 m on either side of the vein system. Both the granitic rocks and the surrounding slates underwent strong chloritization, which is also well developed in the neighbouring veins of the mining district. Where carried to completion, this alteration resulted in the complete replacement of cordierite, biotite and feldspars by chlorite, and produced a dark green rock, which only preserved quartz phenocrysts from the protolith (Fig. 4F). In many places, chloritization also overprinted the earlier sericitic alteration, obscuring former textural relationships, though it did not pervasively affect tourmalinized rocks or tourmaline-quartz microbreccia dykes (Fig. 4G). Locally, strong silicification is observed together with ore-stage chloritic alteration. It is considered,

however, that this silicification generally represents a late overprint, coeval with the formation of thick, barren quartz veins, during the waning stages of the hydrothermal system.

The San Rafael lode hosts as many as 12 types of ore and post-ore veins associated with strong chloritic alteration (Tab. 1). The most common are cassiterite-quartz-chlorite veins, chlorite-wood tin (cassiterite)-quartz veins, cassiterite-quartz-chlorite-wolframite-sulfides veins, chalcopyrite-chlorite-quartz-pyrite-fluorite-siderite veins and barren quartz veins. All of these vein types have the same general orientation (strike ~330° and are NE-dipping), and are characterized by open-space filling, frequent reopening and, locally, brecciation. It should be emphasized that, as is the case for tourmaline, chlorite occurs both in the wall rocks as an alteration mineral and in the ore veins, where it commonly alternates with layers of cassiterite and quartz (Fig. 5K) or accompanies chalcopyrite.

Thin section examination of chloritized granitic rocks reveals that, in addition to the conversion of primary rock-forming minerals to chlorite, there was also formation of abundant sericite at the start of main stage chloritic alteration. Also, minor amounts of rutile, epidote, allanite, carbonates, titanite, amorphous iron oxides, and tourmaline (usually as fine overgrowths on earlier tourmaline) are locally developed.

The first mineral to undergo alteration in granitic rocks was *cordierite*, which was converted to a mixture of sericite and chlorite, giving it a green color in hand specimen. Unaltered cordierite can be observed only in the freshest rocks, in the cores of crystals. The next minerals to alter were biotite and plagioclase (especially calcic plagioclase).

Biotite altered directly to chlorite, but initially some sericite may also have formed. The chlorite commonly contains inclusions of rutile formed by the redistribution of titanium released from the biotite lattice during alteration. It is worth noting that, in contrast to some tourmalinized biotite, cassiterite was not observed in the chloritized biotite. This suggests that during the process of chloritization of biotite tin (if any) was released from the biotite lattice and remobilized, a process which may have had a positive impact on the ore potential of the deposit.

In addition to the features described above, several samples also display an initial decoloration of biotite (which can be colorless in plane polarised light). This

phenomenon, termed *baueritization*, is caused by the hydrothermal leaching of cations from the interlayer site of micas (Rinne, 1912). At San Rafael, it is generally associated with the presence of sulfide grains (such as pyrrhotite), rutile, fluorite, sericite, chlorite, carbonate, epidote or tourmaline.

Plagioclase in the San Rafael granitoids varies in composition between An_0 and An_{50} (on average, An_{23-27}), and usually displays marked compositional zoning. The zones which are the most calcium-rich (commonly the cores of plagioclase phenocrysts) were invariably the first to alter. They were initially sericitized, and were subsequently replaced by chlorite, which ultimately became the only alteration mineral. Locally, where more significant amounts of calcium were released during the destruction of plagioclase, minor amounts of carbonates, titanite and epidote formed (Fig. 5H). In comparison to other rock-forming minerals, *K-feldspar* appears to have altered relatively late, initially undergoing sericitization and only later chloritization.

After cordierite, biotite and the feldspars were completely chloritized, the only primary minerals to remain in the granitic precursor were quartz, apatite, zircon, monazite, rutile and tourmaline (as a relict of pre-ore alteration). *Tourmaline* was completely unaffected by chloritic alteration, as can be inferred from the undisturbed color zoning of its crystals. However, there was minor growth of a greenish to bluish (plane polarised light) variety of tourmaline. This late tourmaline occurs as ubiquitous, tiny overgrowths on the tips and edges of early tourmaline crystals (generally yellow in color), but also occurs as separate, acicular crystals, growing freely in the fractures, which crosscut earlier tourmaline and were later filled with quartz (Fig. 5F). Locally, extremely fine needles of late tourmaline are also intergrown with chlorite. Even though tourmaline growth was volumetrically insignificant after the early, pre-ore stage alteration, this greenish-bluish late variety of tourmaline was not only stable during the tin ore event, but apparently coexisted in equilibrium with chlorite and sericite.

A very important feature of the chloritic alteration is that the altered wall rock does not contain disseminated cassiterite and the concentrations of tin are clearly vein- and veinlet-controlled (Fig. 5G) or hosted by hydrothermal breccias. The notable exception is a strongly chloritized rock, in which cassiterite and chlorite preferentially replaced biotite, as well as filled pores and vugs (Fig. 5M). Generally, there is little

porosity associated with chloritic alteration and, where present, the pores are either empty or host small crystals of late quartz.

SERICITE, CHLORITE AND TOURMALINE MINERALOGY

A total of 65 polished thin sections of the different types of alteration were made and studied petrographically. Electron microprobe WDS analyses (43 analyses on 19 individual sericite grains, 350 analyses on 67 individual chlorite grains, and 535 analyses on 71 individual tourmaline zones/grains) were conducted at the Department of Earth and Planetary Sciences of McGill University in Montreal (JEOL JXA-8900L). The analytical conditions were an accelerating voltage of 15 kV, a beam current of 20 nA, and a spot size of 5 µm. The standards used were natural or synthetic albite (Na), diopside (Si, Ca, Mg), orthoclase (K, Al), hematite (Fe), spessartine (Mn), TiO_2 (Ti), chromite (Cr), fluorite (F), vanadinite (Cl).

Sericite

The bulk of the sericite is associated with early, pre-ore alteration and occurs mainly as aggregates of 20 to 300 µm-long flakes, replacing the feldspars, cordierite and biotite. Pervasively sericitized feldspar phenocrysts also occur locally in rocks, which experienced moderate chloritic alteration during the main ore stage. The results of microprobe analyses of sericite are listed in Table 2 and illustrated in Figure 7A,B. The sericite is generally a potassium-deficient phengite, which can be described as a solid solution of muscovite (dominant), aluminoceladonite and hydromuscovite (illite). It contains 0.39 to 0.78 a.p.f.u. of Fe+Mg+Mn, has a $Al_{iv}/(Al_{iv}+Si)$ ratio between 0.20 and 0.22, and a Fe/(Fe+Mg) ratio between 0.04 and 0.56. A second sericite, which occurs together with abundant tourmaline, has a composition much closer to that of illite (Fig. 7B) and a very low K content (~6 wt.% K_2O, compared to ~10.5 wt.% K_2O for the more common sericite, Table 2). This trend parallels closely the strong loss of alkalis produced by tourmaline alteration.

TABLE 2. Average composition of sericite from San Rafael.

Elevation (m)	4245	4245	4245	4245	4250	4050	4310	4200
Associated minerals	qtz,plag,bt Kfs,ap,rt	qtz,chl ap,rt	qtz,chl ap,rt	qtz,tur chl,ap,rt	qtz,tur,ap,rt chl,plag,Kfs	qtz,tur ap,rt	qtz,chl tur,ap,rt	qtz,chl,ap,rt plag,Kfs,tur
Sample	D4-68E	D4-68DE	D4-68CD	D4-68B	D4-62A	J26B	R502	R432B
SiO_2 (wt.%)	47.93	48.02	47.88	49.05	48.89	50.09	47.38	46.30
TiO_2	0.00	0.06	0.16	0.27	0.20	0.14	0.15	0.16
Al_2O_3	33.22	32.88	34.43	34.11	33.15	35.40	33.83	31.66
FeO	1.63	2.90	1.97	0.14	1.26	0.17	3.09	3.49
MnO	0.03	0.03	0.04	0.00	0.04	0.01	0.02	0.02
MgO	2.49	2.18	0.89	1.96	2.06	1.23	1.20	1.89
CaO	0.00	0.00	0.00	0.00	0.00	0.00	0.00	0.00
Na_2O	0.14	0.15	0.21	0.38	0.19	0.09	0.28	0.27
K_2O	10.46	10.25	10.54	10.58	9.96	6.02	10.19	10.37
F	0.49	0.43	0.31	0.60	0.62	0.34	0.42	0.37
Cl	0.00	0.00	0.00	0.00	0.00	0.01	0.01	0.05
O=F,Cl	-0.21	-0.18	-0.13	-0.25	-0.26	-0.15	-0.18	-0.16
Total	96.17	96.74	96.30	96.86	96.13	93.38	96.40	94.42

Stoichiometric coefficients based on 22 O

Si $(a.p.f.u.)$	6.33	6.34	6.32	6.39	6.42	6.52	6.28	6.31
Al iv	1.67	1.66	1.68	1.61	1.58	1.48	1.72	1.69
Al vi	3.51	3.45	3.67	3.62	3.56	3.96	3.57	3.39
Ti	0.00	0.01	0.02	0.03	0.02	0.01	0.02	0.02
Fe	0.18	0.32	0.22	0.02	0.14	0.02	0.34	0.40
Mn	0.00	0.00	0.00	0.00	0.00	0.00	0.00	0.00
Mg	0.49	0.43	0.17	0.38	0.40	0.24	0.24	0.38
Ca	0.00	0.00	0.00	0.00	0.00	0.00	0.00	0.00
Na	0.04	0.04	0.05	0.10	0.05	0.02	0.07	0.07
K	1.76	1.73	1.77	1.76	1.67	1.00	1.72	1.80
OH*	3.79	3.82	3.87	3.75	3.74	3.86	3.82	3.83
F	0.20	0.18	0.13	0.25	0.26	0.14	0.17	0.16
Cl	0.00	0.00	0.00	0.00	0.00	0.00	0.00	0.01
Cation total	17.98	17.98	17.91	17.90	17.85	17.26	17.96	18.07
Y total	4.18	4.21	4.08	4.04	4.13	4.23	4.17	4.20
X total	1.80	1.77	1.83	1.85	1.72	1.02	1.79	1.87
Al total	5.17	5.12	5.35	5.23	5.13	5.43	5.29	5.08
Fe/(Fe+Mg)	0.27	0.44	0.55	0.04	0.27	0.12	0.56	0.49
Al iv / (Al iv + Si)	0.21	0.21	0.21	0.20	0.20	0.19	0.22	0.21
No. of analyses	2	9	2	6	11	4	8	5

* Calculated by the difference OH=4-F-Cl

Abbreviations: qtz - quartz, chl - chlorite, tur - tourmaline, plag - plagioclase, Kfs - K feldspar, rt - rutile, ap - apatite.

FIGURE 7. A,B. Composition of sericite from San Rafael (n=43)

A

Muscovite
$KAl^{VI}_2[Al^{IV}Si_3O_{10}](OH)_2$

$Al^{VI}Al^{IV}- MgSi$

Phengites

$KFeAl^{VI}[Si_4O_{10}](OH)_2$
Ferro-aluminoceladonite

$\longleftarrow$ Fe - Mg $\longrightarrow$

$KMgAl^{VI}[Si_4O_{10}](OH)_2$
Aluminoceladonite

B

Aluminoceladonite
$KMgAl^{VI}[Si_4O_{10}](OH)_2$

Muscovite
$KAl^{VI}_2[Al^{IV}Si_3O_{10}](OH)_2$

1

K

0

Al^{IV}

1

$\square Al^{VI}_2[Si_4O_{10}](OH)_2$
Pyrophyllite

$(H_3O^+)Al^{VI}_2[Al^{IV}Si_3O_{10}](OH)_2$
Illite
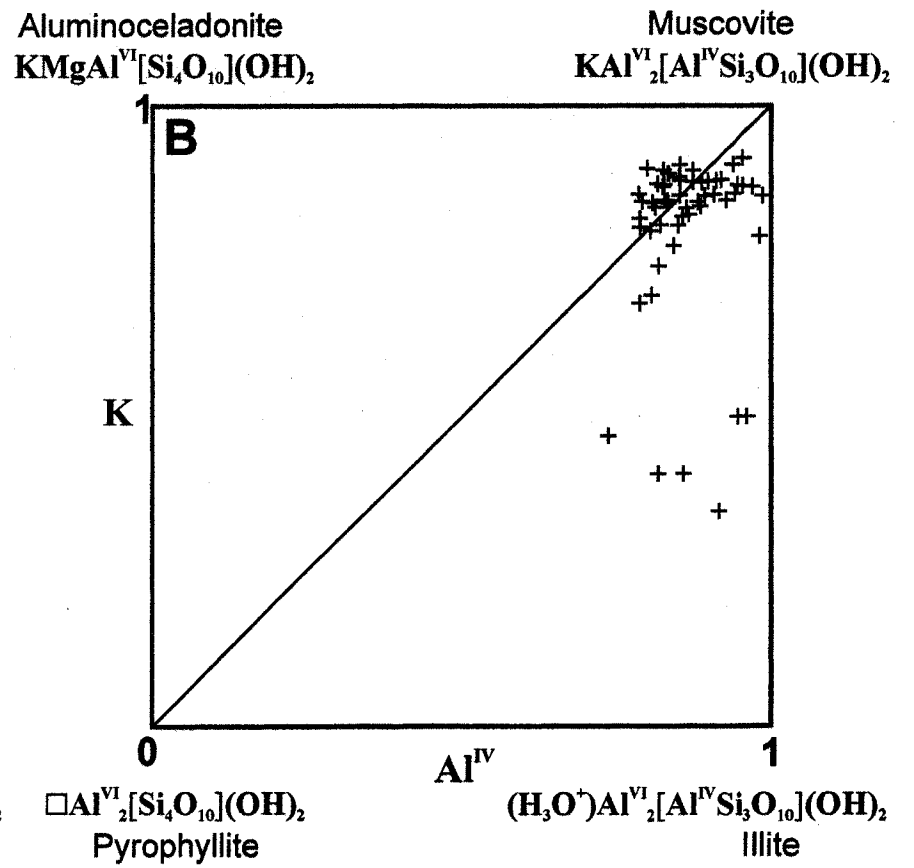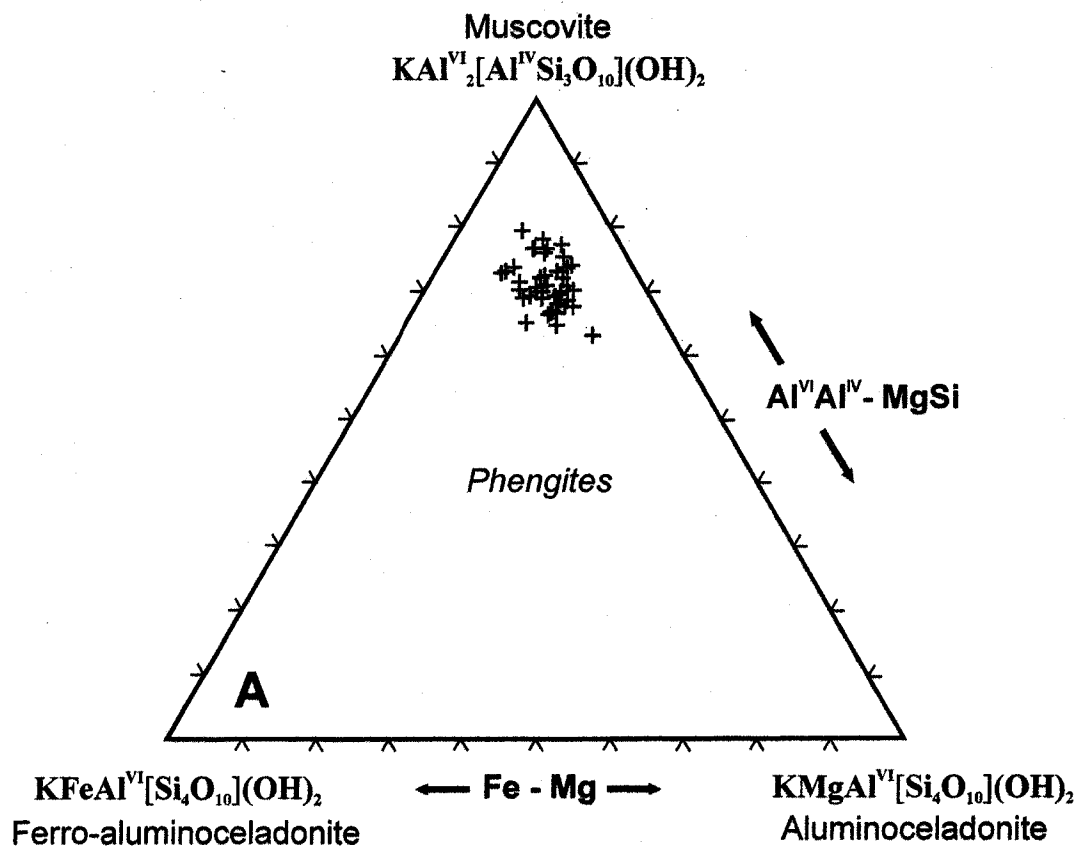
Chlorite

The chlorite in this study was subdivided based on its mode of occurrence (vein versus alteration chlorite) and position in the paragenesis (early / transitional / main-stage chlorite). This classification yielded four paragenetically distinct varieties of chlorite, i.e., early alteration chlorite, transitional vein chlorite, main-stage alteration chlorite, and main-stage vein chlorite (discussed below).

In thin section, chlorite is typically light- to medium-green (plane polarised light) and strongly pleochroic. With crossed polarisers, it is yellow, grey, or light- to medium-blue, however, green, brown, berlin blue and white anomalous colors have also been observed. In addition, some chloritic veinlets also display fine-scale color zoning.

The mineral assemblage, which accompanies alteration chlorite is commonly quite complex. It may include relict feldspars and ferromagnesian minerals (in proportions depending on alteration intensity), chloritization-resistant minerals (e.g., quartz, apatite, rutile, zircon), as well as other alteration minerals, such as tourmaline, sericite, epidote, allanite or carbonates. By contrast, the majority of chlorite-bearing veins are composed only of quartz, chlorite and cassiterite. Sulfides (mainly chalcopyrite) are generally restricted to centers of veins and occur rather late in the main-stage paragenesis. Wolframite and hematite occur only very locally (Fig. 5L). Most chlorite-bearing veins consist of alternating layers of chlorite, cassiterite and quartz (Fig. 5K), suggesting episodic precipitation from an ore fluid, which experienced temporal physicochemical fluctuations.

Figure 8 shows chlorite compositions based on results of ~350 microprobe analyses of 67 individual chlorite crystals. Average compositions and recalculated stoichiometries are listed in Table 3. As indicated by octahedral vacancies, typically < 0.15 and a sum of Na+K+Ca < 0.03 a.p.f.u., the chlorite from San Rafael is very pure. Chlorite analyses form a single population, which falls into the ripidolite and daphnite fields in the classification scheme of Hey (1954) - (Fig. 8). Nevertheless, the composition varies significantly within individual thin sections, particularly those, in which the chlorite is color-zoned or there are multiple generations of chlorite. From Figure 9A,C it can be seen that the extent of Fe ⇔ Mg substitution was quite large, especially in the alteration chlorite. This is not surprising as chlorite formed by the alteration of

TABLE 3. Average composition of chlorite from San Rafael (selected samples) and calculated formation temperature.

	D4-68CD 1st gen.	D4-68CD 2nd gen.	D4-62A (rim)	D4-62A (core)	D3-182C	D3-182A	D1-444	A5	R432A	R577 1st gen.	R577 2nd gen.	R119 1st gen.	R119 4th gen.	R121A	R143	R701
Stage	Early	Early	Early	Early	Transitional		Main					vein	vein	vein	vein	vein
Chlorite type	alt	alt	alt	alt	vein	vein	alt / vein	vein	alt	alt	alt	vein	vein	vein	vein	vein
Elevation (m)	4245	4245	4250	4250	3967	3967	3881	4100	4200	4225	4225	4310	4310	4310	4430	4820
Associated minerals	qtz,ser rt,ap	qtz,ser rt,ap	qtz,ser tur,rt,ap	qtz,ser tur,rt,ap	cas,apy tur	cas,tur apy	qtz,cas ap,rt,tur	cas	qtz,ap,rt	qtz,tur ap,rt,py	qtz,tur ap,rt,py	qtz,cas	qtz,cas	qtz,cas	hem,cas qtz	qtz,cas cpy,sd
SiO_2 (wt.%)	25.16	23.08	24.49	22.90	23.66	24.32	22.84	24.77	23.27	22.66	25.12	23.09	24.67	25.11	23.47	24.44
TiO_2	0.07	0.06	0.04	0.08	0.04	0.02	0.05	0.01	0.06	0.03	0.03	0.01	0.02	0.01	0.01	0.01
Al_2O_3	22.01	22.16	22.07	22.04	21.20	20.86	21.84	19.18	22.18	22.06	22.12	20.63	20.38	19.79	21.56	19.84
Cr_2O_3	0.03	0.00	0.08	0.06	0.00	0.00	0.00	0.00	0.02	0.01	0.01	0.00	0.00	0.01	0.00	0.00
FeO	28.20	37.94	30.70	37.80	39.77	35.35	39.57	38.52	36.96	40.27	26.69	39.70	34.82	33.89	35.98	37.53
MnO	0.55	0.33	0.74	0.38	0.20	0.20	0.40	0.36	0.67	0.38	0.72	0.30	0.24	0.27	0.28	0.46
MgO	12.12	4.89	10.11	4.98	3.85	6.59	3.91	5.99	5.16	3.31	13.44	4.26	8.33	9.45	6.80	6.32
CaO	0.01	0.02	0.01	0.01	0.01	0.02	0.01	0.02	0.01	0.00	0.01	0.02	0.01	0.02	0.01	0.01
Na_2O	0.01	0.01	0.02	0.01	0.00	0.01	0.00	0.01	0.01	0.01	0.01	0.00	0.01	0.01	0.01	0.01
K_2O	0.02	0.02	0.03	0.02	0.02	0.03	0.02	0.05	0.04	0.03	0.02	0.00	0.06	0.06	0.00	0.02
F	0.14	0.00	0.01	0.00	0.00	0.02	0.00	0.00	0.01	0.01	0.16	0.00	0.06	0.01	0.01	0.02
Cl	0.00	0.01	0.01	0.01	0.02	0.01	0.01	0.02	0.01	0.02	0.01	0.02	0.01	0.01	0.00	0.01
O=F,Cl	-0.06	0.00	0.00	0.00	0.00	-0.01	0.00	-0.01	-0.01	-0.01	-0.07	0.00	-0.03	-0.03	0.00	-0.01
Total	88.26	88.51	88.33	88.28	88.77	87.43	88.65	88.92	88.38	88.78	88.27	88.05	88.53	88.62	88.15	88.67

Stoichiometric coefficients based on 28 O

	D4-68CD 1st gen.	D4-68CD 2nd gen.	D4-62A (rim)	D4-62A (core)	D3-182C	D3-182A	D1-444	A5	R432A	R577 1st gen.	R577 2nd gen.	R119 1st gen.	R119 4th gen.	R121A	R143	R701
Si (a.p.f.u.)	5.36	5.18	5.29	5.16	5.34	5.44	5.17	5.55	5.21	5.14	5.31	5.28	5.43	5.50	5.23	5.46
Al iv	2.64	2.82	2.71	2.84	2.66	2.56	2.83	2.45	2.79	2.86	2.69	2.72	2.57	2.50	2.77	2.54
Al vi	2.88	3.04	2.91	3.01	2.98	2.94	3.00	2.61	3.06	3.05	2.83	2.83	2.72	2.60	2.90	2.70
Ti	0.01	0.01	0.01	0.01	0.01	0.00	0.01	0.00	0.01	0.01	0.00	0.00	0.00	0.00	0.00	0.00
Cr	0.00	0.00	0.01	0.01	0.00	0.00	0.00	0.00	0.00	0.00	0.00	0.00	0.00	0.00	0.00	0.00
Fe(II)	5.03	7.12	5.55	7.12	7.51	6.62	7.49	7.22	6.93	7.65	4.72	7.57	6.42	6.21	6.71	7.02
Mn	0.10	0.06	0.14	0.07	0.04	0.04	0.08	0.07	0.13	0.07	0.13	0.06	0.04	0.05	0.05	0.09
Mg	3.84	1.64	3.26	1.67	1.29	2.19	1.32	2.00	1.71	1.12	4.24	1.45	2.73	3.08	2.26	2.10
Ca	0.00	0.00	0.00	0.00	0.00	0.01	0.00	0.01	0.00	0.00	0.00	0.00	0.00	0.00	0.00	0.00
Na	0.00	0.00	0.01	0.00	0.00	0.00	0.00	0.00	0.00	0.00	0.00	0.00	0.00	0.00	0.01	0.00
K	0.01	0.01	0.01	0.00	0.01	0.01	0.01	0.01	0.01	0.01	0.00	0.01	0.01	0.01	0.01	0.00
F	0.09	0.00	0.00	0.00	0.00	0.01	0.00	0.00	0.01	0.00	0.11	0.00	0.04	0.04	0.00	0.02
Cl	0.00	0.00	0.00	0.01	0.01	0.01	0.00	0.01	0.00	0.01	0.00	0.01	0.00	0.00	0.00	0.00
OH	15.91	16.00	15.99	15.99	15.99	15.98	16.00	15.99	15.99	15.99	15.89	15.99	15.96	15.95	16.00	15.98
Cation total	19.87	19.88	19.89	19.90	19.84	19.81	19.91	19.93	19.86	19.91	19.93	19.94	19.93	19.95	19.94	19.92
Al total	5.52	5.86	5.62	5.85	5.64	5.50	5.83	5.07	5.85	5.90	5.51	5.56	5.29	5.11	5.67	5.23
Fe/(Fe+Mg)	0.57	0.81	0.63	0.81	0.85	0.75	0.85	0.78	0.80	0.87	0.53	0.84	0.70	0.67	0.75	0.77
T (J)	369	407	383	410	383	363	409	347	402	414	376	392	363	352	396	360
T (C)	362	392	374	396	366	350	394	333	387	398	371	377	352	341	383	346
T (W)	293	314	303	318	–	–	315	–	308	319	311	–	–	–	310	–
log fO_2 (W)	-32.9	-32.3	-32.2	-31.8	–	–	-32.4	–	-32.0	-32.1	-30.5	–	–	–	-32	–
# of analyses	9	7	3	3	10	14	12	29	30	5	3	15	9	11	6	17

Abbreviations: alt - alteration, vein - vein mineral, qtz - quartz, ser - sericite, rt - rutile, ap - apatite, tur - tourmaline, cas - cassiterite, apy - arsenopyrite, py - pyrite, cpy - chalcopyrite, sd - siderite, hem - hematite.
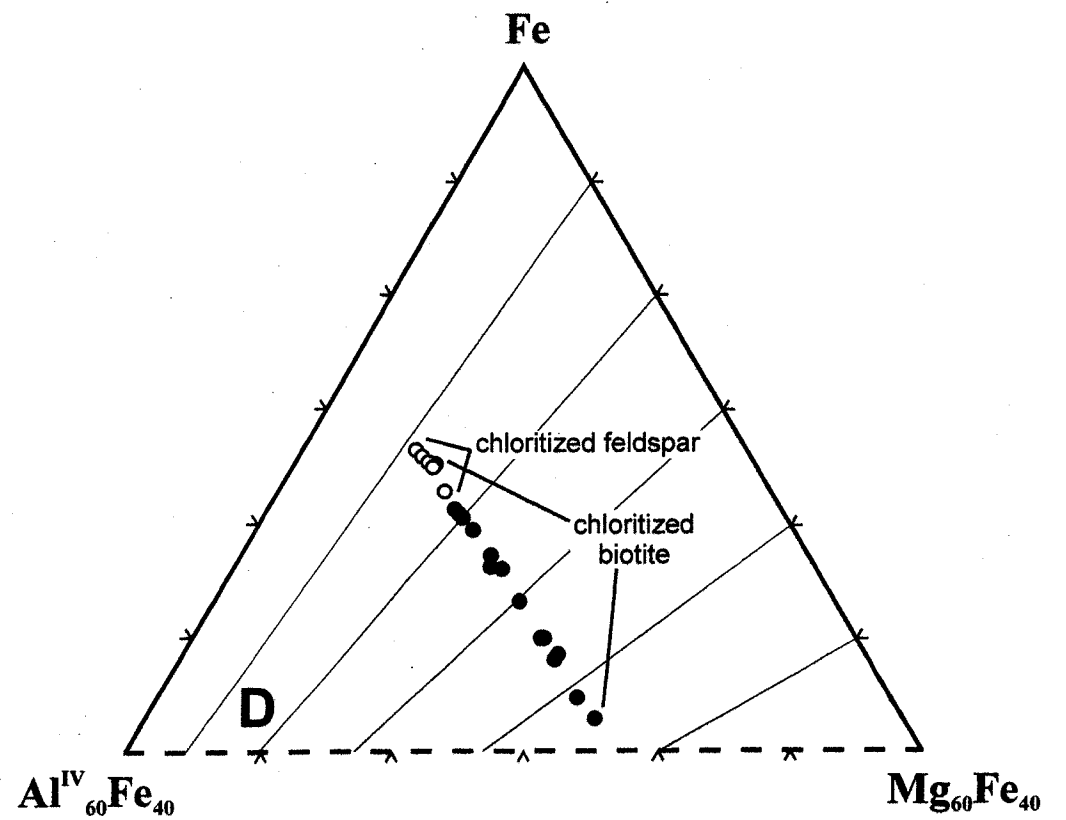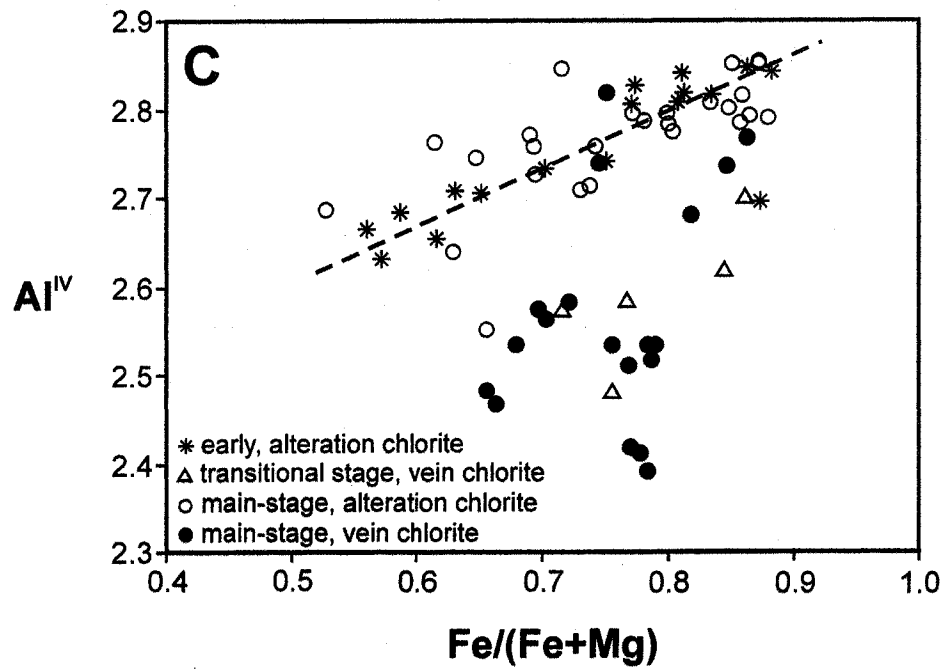
FIGURE 8. Composition of chlorite from San Rafael (n=350).

$Mg_8Al^{VI}_4Al^{IV}_4Si_4O_{20}(OH)_{16}$ $Fe_8Al^{VI}_4Al^{IV}_4Si_4O_{20}(OH)_{16}$

$Al^{VI}Al^{IV}$- FeSi

Corundophilite

Pseudothuringite

9-6-5

9-6-5

Sheridanite

Ripidolite

Daphnite

Clinochlore

Clinochlore

Pycnochlorite

Brunsvigite

Chamosite

Penninite

Diabantite

Talc-chlorite

$Mg_{12}Si_8O_{20}(OH)_{16}$ ⟵ Mg - Fe ⟶ $Fe_{12}Si_8O_{20}(OH)_{16}$
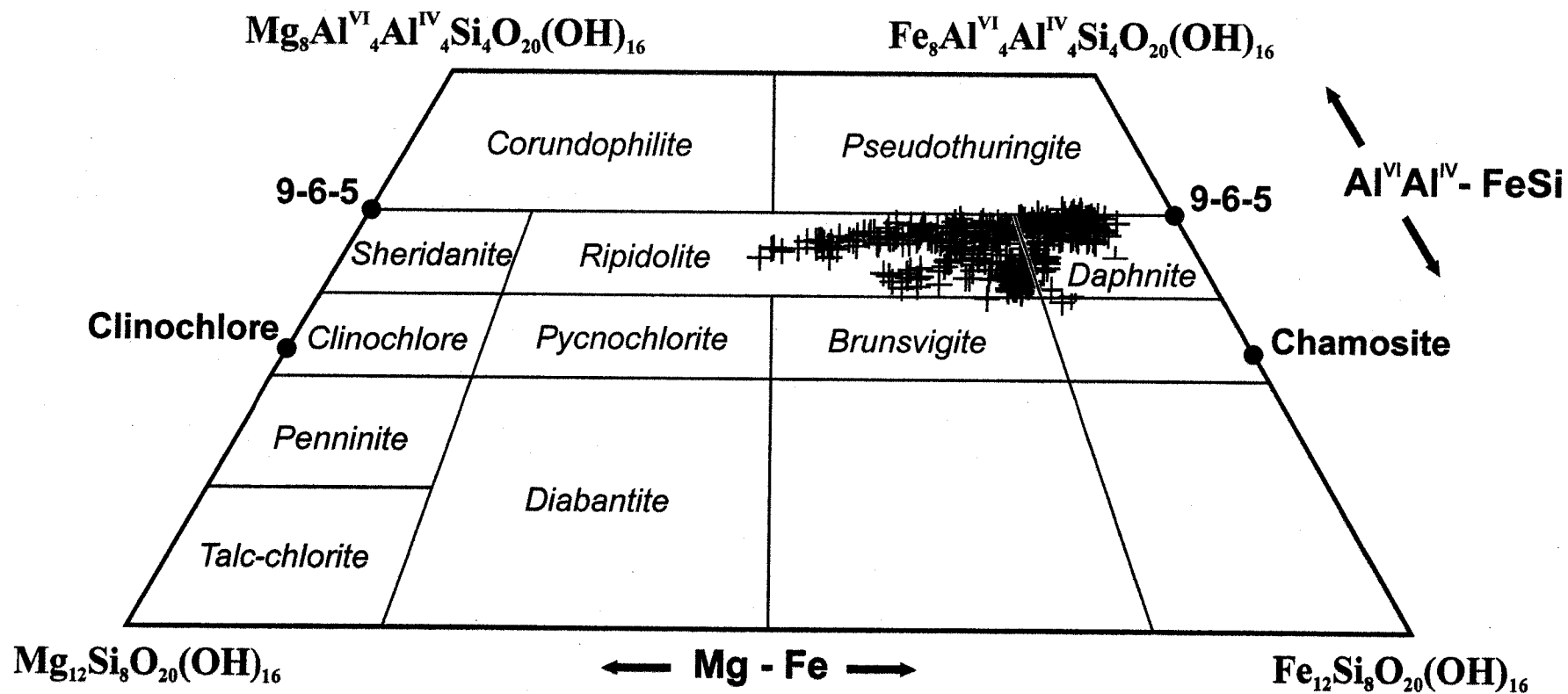
FIGURE 9. A. Composition of chlorite from different vein and alteration types at San Rafael (n=67). The solid lines correspond to constant values of the Fe/(Fe+Mg) ratio. **B.** Plot of Al^{IV} versus Al^{VI} (in a.p.f.u.) for the chlorite types. **C.** Plot of Fe/(Fe+Mg) versus Al^{IV} for the chlorite types. **D.** Dependence of the composition of alteration chlorite on the nature of the precursor mineral (n=21).

Fe

* early, alteration chlorite
△ transitional stage, vein chlorite
○ main-stage, alteration chlorite
● main-stage, vein chlorite

A

$Al^{VI}_{70}Fe_{30}$

$Mg_{70}Fe_{30}$

B

Al^{VI}

1:1

* early, alteration chlorite
△ transitional stage, vein chlorite
○ main-stage, alteration chlorite
● main-stage, vein chlorite

Al^{IV}

C (plot)

Al^{IV} (vertical axis) vs Fe/(Fe+Mg) (horizontal axis)

Vertical axis values: 2.3, 2.4, 2.5, 2.6, 2.7, 2.8, 2.9
Horizontal axis values: 0.4, 0.5, 0.6, 0.7, 0.8, 0.9, 1.0

* * early, alteration chlorite
* △ transitional stage, vein chlorite
* ○ main-stage, alteration chlorite
* ● main-stage, vein chlorite

D (ternary diagram)

Fe

chloritized feldspar

chloritized biotite

Al$^{IV}_{60}$Fe$_{40}$ Mg$_{60}$Fe$_{40}$

ferromagnesian minerals (biotite, cordierite) is expected to have a different Fe/(Fe+Mg) ratio from that formed by the alteration of feldspars. Indeed, Figure 9A shows that the most magnesian compositions are restricted to alteration chlorite and Figure 9D, that chlorite formed by the alteration of biotite has a higher content of Mg than chlorite formed at the expense of feldpars (the Fe/(Fe+Mg) ratio is ~0.72 for the former and ~0.86 for the latter). These observations suggest that the fluid, which produced chloritic alteration was relatively Fe-rich.

Although vein chlorite has a higher content of iron than alteration chlorite, it is characterized by a considerably larger range of $(Fe,Mg)Si \Leftrightarrow Al^{VI}Al^{IV}$, substitution (i.e., Tschermak's) and has higher (Fe+Mg) and Si^{IV}, but is poorer in Al^{IV} and, especially Al^{VI} (Fig. 9A,B,C). Thus, as the vein chlorite crystallized directly from the ore fluid and in the absence of any other Al-bearing phases, it is alumina-poor, compared to alteration chlorite, which grew in the presence of several aluminosilicates and displays clear enrichment in alumina (Fig. 9A,C). This observation suggests also that Al was relatively immobile in the ore fluids. With an increase of Fe/(Fe+Mg) ratio from ~0.5 to ~0.9, the Al^{IV} of alteration chlorite increases from 2.63 to 2.86 and Al^{VI} from 2.83 to 3.12. It is also interesting to note that chlorite formed by the alteration of feldspars has a slightly higher proportion of Al^{IV} (avg. ~2.82) than that formed by the replacement of biotite (avg. ~2.73). The overall ratio of Al^{VI} to Al^{IV} is quite variable and generally >1, which implies the substitution of *other* R^{3+} for R^{2+} in the octahedral site. Fe^{3+} is a likely candidate for this, and its appreciable content can be deduced from chemical analyses. Thus, assuming that in pervasively chloritized wall rocks (composed almost exclusively of quartz, chlorite and accessory minerals) the bulk of the iron is contained in chlorite, it is estimated that up to 9 wt.% of the iron in chlorite occurs as Fe^{3+}.

Tourmaline

Three major types of tourmaline have been identified (Tab. 4). *Magmatic* tourmaline is observed in relatively rare dykes and plugs of tourmaline-bearing leucogranite, which occur on the margins of the intrusion, and are inferred to represent the latest and most evolved phase of igneous activity. This magmatic tourmaline is present as numerous,

TABLE 4. Average composition of tourmaline from San Rafael (selected samples).

	magmatic	very early alteration	very early alteration	very early alteration	very early alteration	early alteration	early alteration	early alteration	early alteration	early vein	very early alteration	transitional alteration	early vein	late-early vein	transitional vein
Stage	magmatic	very early alteration	very early alteration	very early alteration	very early alteration	early alteration	early alteration	early alteration	early alteration	early vein	very early alteration	transitional alteration	early vein	late-early vein	transitional vein
Type	magmatic	replacement of cordierite	radiating, columnar xls	color zoned, irregular xls	color zoned, irregular xls	color zoned, columnar xls	aggregates, columnar xls	replacement of cordierite	radiating, columnar xls	veinlet	irregular xls, aggregates	late overgrowths	clasts in breccia	matrix of breccia	late overgrowths
Description	disseminated, isometric xls														
Color (PPL)	dark yellow	light blue	colorless	dark yellow	blue	yellow	yellow	blue	yellow	pale yellow	orange	green	pale yellow	greish	greenish
Elevation (m)	5100	4280	4950	4950	4950	4220	4050	4050	4250	4250	4225	4225	4207	4207	4207
Associated minerals	qtz,plag,Kfs rt, bauer. bt	qtz,ser,plag Kfs,bt,ap,rt	qtz,ser,rt dum,tur	qtz,ser,rt dum,tur	qtz,ser,rt dum,tur	qtz,rt,ap	qtz,rt	qtz,rt	qtz,ser,rt,ap chl,plag,Kfs	qtz	chl,qtz ap,rt	chl,qtz ap,rt	qtz	qtz	qtz
Sample	I36	D5-37	I46	I46	I46	D4-94	J26A	J26A	D4/62A (1st gen)	D4/62A (2nd gen)	R577 (1st gen)	R577 (2nd gen)	D5-100 (1st gen)	D5-100 (2nd gen)	D5-100 (3rd gen)
SiO$_2$ (wt.%)	34.53	35.69	37.07	35.33	36.08	36.34	36.25	36.58	35.96	36.48	36.72	35.74	36.49	36.85	34.89
TiO$_2$	0.51	0.01	0.11	1.33	0.32	0.42	1.31	0.00	0.22	0.12	0.68	0.31	0.19	0.17	0.15
Al$_2$O$_3$	35.11	34.38	38.66	32.07	32.82	35.29	30.82	33.41	35.51	33.53	32.61	32.03	36.89	36.05	29.81
Cr$_2$O$_3$	0.00	0.00	0.03	0.04	0.01	0.01	0.04	0.00	0.00	0.00	0.02	0.00	0.00	0.00	0.00
FeO	10.84	10.53	0.29	9.15	7.81	5.92	5.90	4.70	5.57	7.57	5.81	14.20	1.48	4.22	13.92
MnO	0.06	0.01	0.01	0.07	0.04	0.01	0.01	0.01	0.01	0.03	0.02	0.05	0.01	0.02	0.02
MgO	2.26	3.23	7.07	4.87	5.75	5.29	7.53	7.38	5.66	5.30	7.03	1.80	7.11	5.50	3.17
CaO	0.15	0.24	0.19	0.66	0.33	0.35	0.93	0.49	0.57	0.26	0.51	0.18	0.45	0.07	0.32
Na$_2$O	1.96	1.80	1.67	2.05	2.14	1.82	2.08	2.17	1.81	1.74	2.03	1.77	1.99	1.51	2.22
K$_2$O	0.05	0.02	0.02	0.06	0.05	0.03	0.04	0.03	0.41	0.03	0.05	0.04	0.00	0.01	0.02
F	0.37	0.11	0.24	0.60	0.65	0.29	0.20	0.24	0.41	0.19	0.31	0.09	0.23	0.05	0.37
Cl	0.00	0.00	0.00	0.01	0.01	0.00	0.00	0.01	0.00	0.01	0.02	0.01	0.00	0.00	0.00
O=F,Cl	-0.16	-0.04	-0.10	-0.25	-0.28	-0.12	-0.09	-0.10	-0.17	-0.08	-0.14	-0.04	-0.10	-0.02	-0.16
Total	83.51	84.11	85.27	85.98	85.75	85.65	85.03	84.93	85.59	85.18	85.68	86.17	82.62	82.91	82.29

Stoichiometric coefficients (a.p.f.u.) based on T+Z+Y=15

		magmatic	very early	very early	very early	very early	early	early	early	early	early vein	very early	transitional	early vein	late-early	transitional
T	Si	5.83	5.96	5.94	5.95	6.00	5.98	6.06	6.04	5.92	6.06	6.05	6.07	5.95	6.06	6.05
	Al	0.17	0.04	0.06	0.05	0.02	0.03	0.00	0.00	0.08	0.00	0.00	0.00	0.05	0.01	0.00
B		3.00	3.00	3.00	3.00	3.00	3.00	3.00	3.00	3.00	3.00	3.00	3.00	3.00	3.00	3.00
Z	Al	6.00	6.00	6.00	6.00	6.00	6.00	5.92	6.00	6.00	6.00	6.00	6.00	6.00	6.00	6.00
	Cr	0.00	0.00	0.00	0.00	0.00	0.00	0.00	0.00	0.00	0.00	0.00	0.00	0.00	0.00	0.00
	Mg	0.00	0.00	0.00	0.00	0.00	0.00	0.08	0.00	0.00	0.00	0.00	0.00	0.00	0.00	0.00
Y	Al	0.83	0.72	1.25	0.31	0.42	0.82	0.15	0.50	0.81	0.56	0.33	0.41	1.05	0.98	0.09
	Cr	0.00	0.00	0.00	0.01	0.00	0.00	0.00	0.00	0.00	0.00	0.00	0.00	0.00	0.00	0.00
	Ti	0.06	0.00	0.01	0.17	0.04	0.05	0.17	0.00	0.03	0.01	0.08	0.04	0.02	0.02	0.02
	Mg	0.57	0.81	1.69	1.22	1.43	1.30	1.80	1.82	1.39	1.31	1.73	0.45	1.73	1.35	0.82
	Mn	0.01	0.00	0.00	0.01	0.01	0.00	0.00	0.00	0.00	0.00	0.00	0.01	0.00	0.00	0.00
	Fe	1.53	1.47	0.04	1.29	1.09	0.82	0.82	0.65	0.77	1.05	0.80	2.02	0.20	0.58	2.02
X	Ca	0.03	0.04	0.03	0.12	0.06	0.06	0.17	0.09	0.10	0.05	0.09	0.03	0.08	0.01	0.06
	Na	0.64	0.58	0.52	0.67	0.69	0.58	0.67	0.70	0.58	0.56	0.65	0.58	0.63	0.48	0.75
	K	0.01	0.00	0.00	0.01	0.01	0.01	0.01	0.01	0.01	0.01	0.01	0.01	0.00	0.00	0.00
	Vac	0.32	0.37	0.44	0.20	0.24	0.35	0.15	0.21	0.31	0.39	0.25	0.38	0.29	0.50	0.19
Sum cations		15.68	15.63	15.56	15.80	15.76	15.65	15.85	15.79	15.69	15.61	15.75	15.62	15.71	15.50	15.81
O*		27.12	27.09	27.20	27.13	27.09	27.16	27.13	27.11	27.14	27.09	27.11	27.07	27.21	27.16	27.03
Oxy*		0.25	0.18	0.41	0.26	0.17	0.31	0.27	0.22	0.29	0.18	0.22	0.14	0.42	0.33	0.05
OH		3.55	3.77	3.47	3.42	3.48	3.54	3.62	3.65	3.50	3.72	3.61	3.81	3.47	3.64	3.75
F		0.20	0.06	0.12	0.32	0.34	0.15	0.11	0.12	0.21	0.10	0.16	0.05	0.12	0.03	0.20
Cl		0.00	0.00	0.00	0.00	0.00	0.00	0.00	0.00	0.00	0.00	0.01	0.00	0.00	0.00	0.00
Fe/(Fe+Mg)		0.73	0.65	0.02	0.51	0.43	0.39	0.31	0.26	0.36	0.44	0.32	0.82	0.10	0.30	0.71
# of analyses		7	3	8	8	11	10	5	5	5	5	5	9	3	8	2

(*) - assuming all Fe=Fe2+

... rutile, tur - tourmaline, dum - dumortierite, cas - cassiterite, apy - arsenopyrite, plag - plagioclase, Kfs - K feldspar, chl - chlorite.

small (40-400 μm), yellow, prismatic crystals, disseminated in the groundmass of the leucogranite. In addition, a late-magmatic (or early postmagmatic) variety of bluish tourmaline commonly replaced parts of cordierite phenocrysts hosted by the other granitic phases of the pluton.

The bulk of tourmaline, however, is of *hydrothermal* origin and occurs either as an *alteration* phase or as a *vein* mineral, both restricted mostly to the earliest, barren stage of the deposit paragenesis, for which they are characteristic. In general, tourmaline is the only boron-bearing phase in the early alteration and is present in large amounts, replacing both ferromagnesian minerals and feldspars. However, extreme boron metasomatism at a location on the southwestern flank of the pluton also produced dumortierite, which coexists with colorless (pure dravite) and brown (Fe-rich dravite) tourmaline.

Vein tourmaline displays a wider compositional and optical range than alteration tourmaline and several generations are commonly observed. Early vein tourmaline is yellow (or bluish/colorless) in thin section, whereas later generations are successively colorless or orange, blue, and finally, green. The last of these tourmaline generations coexists with chlorite and, locally, also cassiterite. Tourmaline occurs also in the hydrothermal microbreccia dykes, where it is typically yellow (in thin section) and is present both as fine clasts and as a very fine matrix.

The composition of 71 tourmaline grains from the deposit is shown in Figure 10 and demonstrates extensive solid-solution among dravite, alkali-free dravite and schorl, with most compositions falling in the dravite field (i.e., with Mg > Fe). With the exception of (very early ?) magmatic tourmaline, which is iron rich, a marked trend of progressive iron enrichment is observed in the paragenesis. Thus, while the earliest hydrothermal tourmaline is Mg-rich and locally approaches the composition of pure dravite, late tourmaline is strongly Fe-rich and typically has a Fe/(Fe+Mg) ratio between 0.70 and 0.83. Wet chemical analyses have shown that most of the iron in tourmaline is ferrous (Mlynarczyk and Williams-Jones, in preparation), an observation in good agreement with the reduced, S-type nature of the host granitic pluton (*cf* London and Manning, 1995; Slack, 1996).

The concentration of Na and Ca in tourmaline from San Rafael is very uniform, and that of F is relatively low (<1 wt.%, avg. ~0.28 wt.%). Tourmaline was not analysed

FIGURE 10. Composition of different types of tourmaline from the San Rafael deposit (n=71).
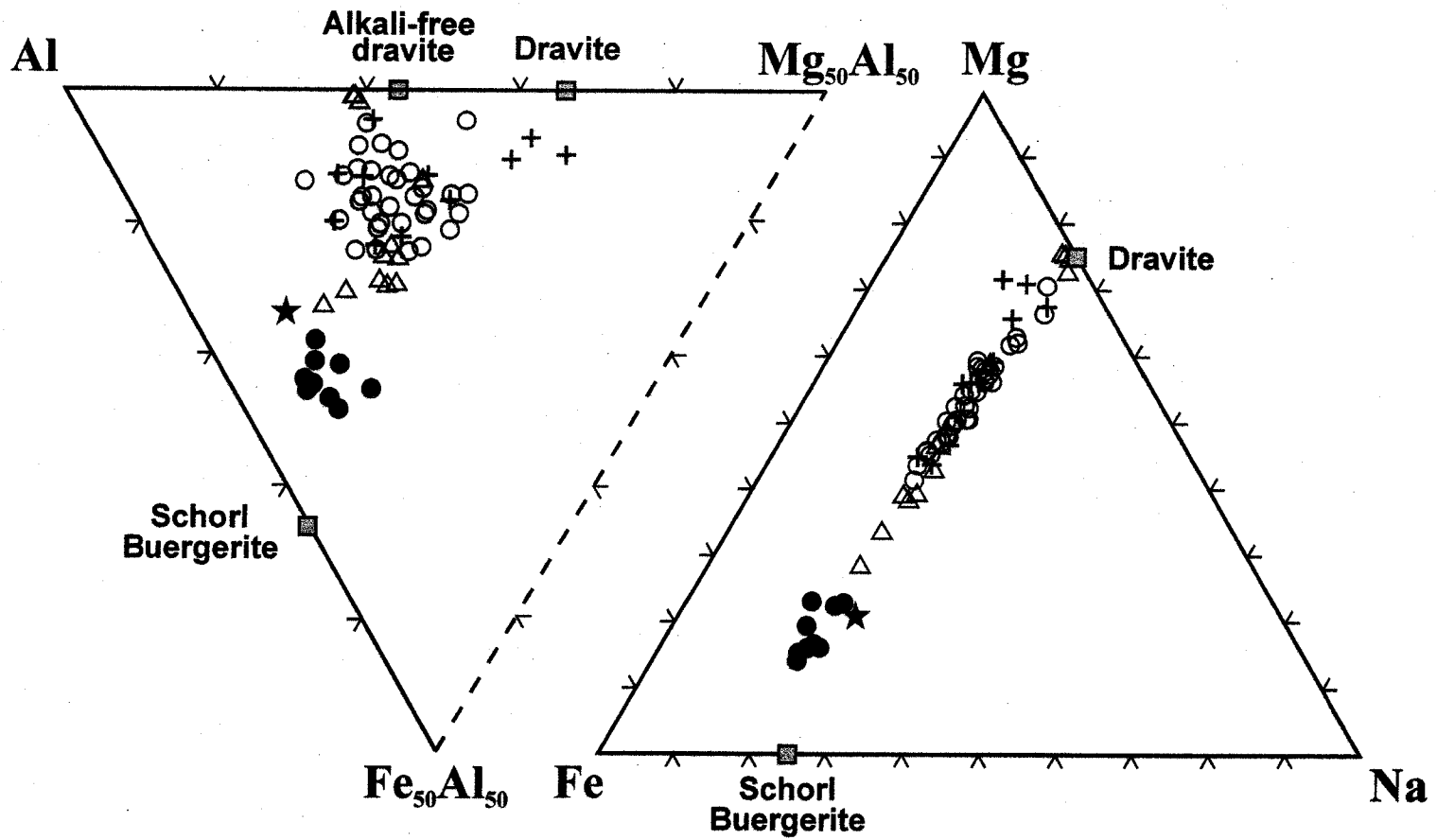
★ magmatic tourmaline

△ very early, alteration tourmaline

○ early alteration tourmaline

+ vein tourmaline

● late overgrowths on earlier tourmaline

for Li, however, bulk-rock analyses of strongly tourmalinized wall rock indicate that Li contents are typically very low (60-100 ppm Li, Tab. 5). As can be deduced from Figure 11A, there is an excellent negative correlation between Fe+Mg+Mn+Ti and Al in the Y site, which indicates that the bulk of these divalent cations occupy the Y site. The only exception is the last generation of tourmaline, which is so Fe-rich that the divalent cations fill the Y site completely, leaving no space for Al, while excess Fe is located in the Z site.

There is also a relatively clear correlation between pleochroic color ($\varpi \gg \varepsilon$) and the chemistry of tourmaline (Fig. 11B). Tourmaline, which is closest in composition to pure dravite (i.e., contains the least Fe and low Ti) is colorless. With the increase of Fe, the color changes to bluish, and at high Fe contents (Fe/(Fe+Mg) ~0.8) is dark green. On the other hand, yellow and orange tourmaline is characterized by elevated Ti (> 0.05 a.p.f.u.) and has a moderate Fe content. Similar correlations between composition and color have been reported for tourmaline from the Seagull batholith (Sinclair and Richardson, 1992).

Figure 12 shows consistent partitioning of Fe and Mg between coexisting chlorite and late tourmaline, which supports the observation that these minerals formed coevally and attained chemical equilibrium. The average $K_{D(chlorite/tourmaline)}$ value obtained is ~0.701 ± 0.071. This value is only slightly higher than the 0.579 ± 0.08 obtained by Henry and Guidotti (1985) for the K_D between chlorite and tourmaline in metapelites, which suggests $(Mg/Fe)_{tourmaline} > (Mg/Fe)_{chlorite}$ is an equilibrium Fe-Mg distribution.

CHLORITE GEOTHERMOMETRY

A number of studies have attempted to relate the composition of chlorite to its temperature of formation, producing several potentially useful geothermometers, including those of Cathelineau (1988) and Jowett (1991), based on calibrations from active geothermal fields, and the geothermometer of Walshe (1986), based on a thermodynamic model of a six-component chlorite solid-solution (see De Caritat, 1993, for review). As chlorite at San Rafael occurs almost invariably in equilibrium with quartz, these geothermometers were tested and the results are listed at the bottom of Table 3.

TABLE 5. Whole-rock composition of fresh and altered granitoids from the San Rafael deposit.

Alteration	Fresh Granite	Fresh Granite	Fresh Granite	Fresh Granite	Fresh Granite	Strong Chloritic	Strong Chloritic	Moderate Chloritic	V. weak Chloritic	Chlorite-rich material	Strong Chloritic	Incipient Chloritic
Sample	I 20 *	R 566	D4-443	I 8	I 51	R 80	R432 A	R432 B	R432 C	D1M-61 A	D1M-61 B	D1M-61 C
wt. %												
SiO_2	68.61	66.54	68.03	66.56	68.21	59.06	63.63	65.76	68.06	33.89	65.05	65.31
TiO_2	0.346	0.360	0.442	0.440	0.411	0.430	0.307	0.346	0.348	0.507	0.425	0.445
Al_2O_3	15.98	17.34	15.97	16.38	15.76	14.39	12.41	14.83	15.97	17.86	12.85	15.71
Fe_2O_3 total	2.63	2.30	2.47	3.09	2.92	18.62	15.56	10.50	3.35	36.86	14.25	4.95
FeO	2.25	2.07	2.26	2.67	2.54	15.52	13.89	9.01	3.01	32.60	12.17	4.08
Fe_2O_3	0.13	< d.l.	< d.l.	0.12	0.10	1.37	0.13	0.49	< d.l.	0.63	0.73	0.42
MnO	0.051	0.026	0.029	0.037	0.034	0.145	0.231	0.140	0.059	0.368	0.203	0.090
MgO	1.25	1.33	1.28	1.65	1.51	1.98	1.38	1.36	1.14	3.20	2.28	2.88
CaO	1.71	1.79	1.52	1.99	1.68	0.32	0.98	0.42	0.69	0.39	0.36	0.59
Na_2O	3.28	3.79	3.36	3.20	3.24	0.13	0.15	1.50	2.97	< d.l.	0.04	1.29
K_2O	4.91	5.19	5.36	5.02	4.86	1.74	1.54	2.49	5.40	< d.l.	1.64	4.65
P_2O_5	0.229	0.216	0.249	0.236	0.239	0.232	0.224	0.232	0.232	0.300	0.240	0.249
LOI	1.22	1.25	1.13	1.23	1.17	3.51	3.12	2.62	1.67	5.55	3.18	3.76
F	0.16	0.14	0.20	0.12	0.15	0.10	0.07	0.11	0.15	0.02	0.11	0.14
Cl	0.02	0.04	0.03	0.04	0.04	0.01	0.01	< d.l.	0.01	0.01	< d.l.	0.01
S	< d.l.	< d.l.	< d.l.	0.02	0.03	< d.l.	< d.l.	< d.l.	< d.l.	0.03	< d.l.	< d.l.
Total	100.20	100.14	99.85	99.84	100.04	100.57	99.58	100.21	99.91	98.96	100.53	99.94
ppm												
B	135	89	126	59	158	159	80	103	129	69	75	128
Li	185	152	264	201	304	314	294	229	174	308	304	264
Ba	560	1190	767	858	651	284	485	612	845	4	594	2160
Rb	317	299	367	285	297	151	130	195	368	9	132	351
Sr	196	297	207	258	215	6	12	27	121	6	13	209
Cs	154	182	93	230	293	16	18	27	61	5	27	158
V	24	31	30	35	32	45	29	26	28	48	57	61
Cr	46	53	44	61	56	78	56	72	53	141	156	154
Co	4	4	4	7	5	15	14	8	5	54	19	12
Ni	16	16	6	21	19	17	473	13	13	159	32	34
Cu	30	40	44	44	27	59	< d.l.	50	42	< d.l.	43	42
Pb	37	40	52	48	36	< d.l.	< d.l.	< d.l.	36	< d.l.	< d.l.	14
Zn	22	< d.l.	20	18	12	46	< d.l.	24	22	189	69	22
Ag	< d.l.	< d.l.	< d.l.	< d.l.	< d.l.	< d.l.	< d.l.	< d.l.	0.7	< d.l.	< d.l.	< d.l.
As	31	< d.l.	104	51	9	< d.l.	< d.l.	< d.l.	25	11	< d.l.	13
Sb	0.5	1.0	0.7	1.0	0.9	1.6	1.6	1.2	1.9	3.2	1.1	3.3
Bi	0.2	0.6	5.0	0.3	0.4	0.2	0.3	0.4	1.5	0.1	0.2	2.6
Sn	12	12	18	11	6	110	164	156	38	> 1000	216	58
W	2.1	1.5	4.3	1.3	1.3	14.7	12.0	12.2	5.6	54.8	33.6	3.2
Ta	2.15	1.62	1.80	1.94	2.10	2.06	2.28	2.40	2.41	3.10	2.66	2.80
Nb	14.9	12.9	13.9	15.7	15.3	14.7	13.7	13.8	14.1	19.1	16.8	16.5
Y	16.7	15.9	16.0	18.1	17.7	16.1	15.6	16.6	16.7	31.6	20.4	23.1
Zr	141	153	195	173	162	159	116	113	135	182	167	164
Hf	3.9	4.1	5.3	4.6	4.3	4.7	3.6	3.6	4.2	5.6	4.8	5.0
Ga	26	26	27	26	26	33	32	29	27	67	27	25
Ge	1.4	1.5	1.8	1.7	1.3	2.8	2.1	2.0	1.9	3.7	1.9	1.9
In	< d.l.	< d.l.	< d.l.	< d.l.	< d.l.	0.77	0.98	0.86	0.18	19.42	0.84	0.19
Tl	1.89	1.77	3.19	2.58	1.66	1.09	0.91	1.44	2.80	0.25	0.77	2.45
U	12.9	7.9	15.1	10.5	12.7	12.2	12.5	12.6	13.2	17.2	14.5	14.7
Th	19.7	20.7	25.7	24.5	21.1	18.2	18.2	18.7	18.7	21.8	17.4	20.8
Mo	< d.l.	< d.l.	< d.l.	< d.l.	< d.l.	< d.l.	< d.l.	< d.l.	< d.l.	< d.l.	< d.l.	< d.l.
Sc	< d.l.	< d.l.	< d.l.	15	11	< d.l.	< d.l.	12	12	< d.l.	15	14
La	37.7	41.6	49.3	48.5	44.8	39.2	35.2	29.4	35.5	86.1	56.8	62.6
Ce	73.3	81.2	100.2	94.1	88.1	76.3	71.0	59.9	70.8	164.6	108.6	118.6
Pr	7.09	7.91	10.12	9.14	8.63	8.20	7.97	6.68	7.86	19.04	12.04	13.16
Nd	28.0	31.3	40.2	35.6	33.9	33.0	31.4	26.5	30.7	80.3	47.7	52.5
Sm	4.93	5.39	6.83	6.20	5.88	5.57	5.34	4.80	5.29	12.75	8.03	8.58
Eu	1.011	1.499	1.140	1.269	1.072	1.263	1.150	1.143	1.179	2.456	1.511	1.798
Gd	3.74	4.02	4.72	4.58	4.24	4.39	3.82	3.73	3.91	9.39	5.94	6.44
Tb	0.58	0.58	0.62	0.67	0.63	0.62	0.58	0.60	0.60	1.24	0.83	0.89
Dy	2.97	2.96	2.97	3.39	3.22	3.19	2.92	3.15	3.10	6.12	3.88	4.42
Ho	0.56	0.55	0.53	0.62	0.59	0.56	0.53	0.58	0.58	1.11	0.71	0.82
Er	1.50	1.46	1.41	1.69	1.63	1.59	1.48	1.57	1.55	2.98	1.93	2.15
Tm	0.234	0.209	0.207	0.256	0.249	0.236	0.220	0.228	0.232	0.392	0.274	0.312
Yb	1.44	1.33	1.34	1.54	1.52	1.53	1.33	1.35	1.49	2.17	1.70	1.96
Lu	0.205	0.192	0.181	0.222	0.215	0.206	0.173	0.186	0.212	0.288	0.224	0.279

* average of two analyses   < d.l. = below detection limit   For detailed descriptions of the samples, see Appendix-I.
n.a. = not analyzed (in tourmaline-bearing samples the ferrous and ferric iron contents could not be determined because of the poor solubility of the mineral in acids)

	Fresh Granodiorite D1M-61 D	Mild Sericitic D5-2	Strong Tourmaline J 26 A	Strong Sericitic J 26 B	Strong Tourmaline D5-138	Sericitic + Tourmaline I 45	Sericitic + Tourmaline D4-68 B	Strong Chloritic D4-68 C	Sericitic + Chloritic D4-68 D	Incipient Sericitic D4-68 E	Tourmaline + Silicic D4-94	Detection limit (ppm)
	65.39	68.31	72.91	73.53	71.78	76.04	74.91	62.98	63.44	65.78	87.13	60
	0.453	0.463	0.421	0.469	0.381	0.345	0.526	0.533	0.571	0.554	0.484	35
	15.86	15.81	15.67	16.18	16.47	16.71	15.71	15.27	16.66	16.08	7.74	120
	4.26	3.05	4.13	2.06	3.54	0.56	0.84	12.31	7.26	3.87	1.50	30
	3.59	2.74	n.a.	n.a.	n.a.	n.a.	n.a.	10.33	5.91	3.35	n.a.	0.01
	0.27	< d.l.	n.a.	n.a.	n.a.	n.a.	n.a.	0.83	0.69	0.15	n.a.	0.01
	0.066	0.044	0.015	0.012	0.015	0.010	0.008	0.201	0.126	0.046	0.014	30
	3.14	1.51	2.60	1.68	2.63	0.89	0.89	2.45	2.37	2.89	1.30	95
	1.62	0.93	0.50	0.49	0.61	0.32	0.38	0.37	0.50	1.51	0.27	15
	2.29	2.10	0.82	0.44	0.89	0.33	0.27	0.11	0.34	2.40	0.43	75
	4.46	5.94	0.06	1.28	0.06	2.36	3.48	2.46	4.09	5.08	0.05	25
	0.250	0.254	0.166	0.252	0.234	0.245	0.274	0.253	0.272	0.261	0.152	35
	2.30	1.71	1.26	2.61	1.34	2.23	2.40	3.58	4.75	1.67	0.71	100
	0.16	0.18	0.15	0.14	0.12	0.11	0.16	0.12	0.14	0.33	0.08	100
	0.03	0.02	0.02	0.01	0.02	0.01	0.01	< d.l.	0.01	0.04	0.01	100
	0.02	0.02	< d.l.	< d.l.	< d.l.	< d.l.	< d.l.	< d.l.	< d.l.	< d.l.	0.01	100
	100.10	*100.13*	*98.57*	*99.00*	*97.95*	*100.04*	*99.69*	*100.53*	*100.39*	*100.15*	*99.79*	
	83	148	9413	5773	9759	3471	1852	75	160	75	5371	2
	257	359	100	100	73	60	112	261	387	393	74	1
	2180	731	6	149	3	198	389	723	719	941	3	3
	341	487	5	80	4	184	192	190	369	492	1	1
	444	163	62	52	43	21	17	14	37	195	20	2
	131	203	3	24	1	26	19	33	352	182	1	0.1
	58	40	41	39	34	22	50	49	51	46	34	5
	149	61	82	66	72	46	146	146	151	141	78	20
	11	14	2	2	1	< d.l.	< d.l.	10	10	11	1	1
	30	51	11	15	11	< d.l.	5	51	34	47	9	3
	34	40	34	27	30	30	29	53	44	36	34	2
	13	35	< d.l.	< d.l.	< d.l.	75	< d.l.	< d.l.	6	15	< d.l.	5
	43	< d.l.	< d.l.	< d.l.	< d.l.	< d.l.	< d.l.	47	21	27	< d.l.	2
	< d.l.	< d.l.	< d.l.	< d.l.	< d.l.	< d.l.	< d.l.	< d.l.	< d.l.	< d.l.	< d.l.	0.5
	19	410	31	43	< d.l.	23	11	< d.l.	9	16	11	5
	2.5	1.8	2.0	10.2	1.0	91.2	3.8	1.2	2.6	0.8	1.2	0.2
	1.5	7.3	0.7	1.1	1.5	0.1	0.3	0.1	1.2	0.2	0.5	0.1
	27	14	81	88	53	21	21	114	56	9	23	1
	1.4	14.3	10.4	11.4	16.9	6.5	32.5	44.1	16.1	2.0	47.7	0.5
	2.71	1.93	1.47	2.05	1.39	3.01	1.80	1.82	1.94	1.73	2.54	0.01
	15.4	14.7	9.5	15.2	10.1	14.7	13.8	13.1	13.9	12.6	18.1	0.2
	21.4	16.8	7.5	17.3	13.3	8.5	15.0	15.8	15.9	14.9	10.4	0.5
	156	184	144	165	141	123	196	183	193	181	178	1
	4.5	5.0	4.5	4.9	3.9	3.4	5.3	5.4	5.9	5.6	4.8	0.1
	24	27	44	34	29	7	19	31	29	27	10	1
	1.5	1.7	6.5	4.9	5.9	2.8	3.5	1.8	3.2	1.2	2.7	0.5
	0.14	< d.l.	0.41	0.40	0.37	< d.l.	0.11	0.62	0.26	< d.l.	0.10	0.1
	2.11	3.68	0.09	0.66	0.11	2.40	0.65	1.68	2.22	2.89	< d.l.	0.05
	12.1	16.0	6.5	11.7	8.2	8.4	9.9	11.2	13.5	10.3	5.6	0.01
	17.4	27.0	19.0	22.4	25.4	17.9	28.6	28.5	28.7	26.9	16.9	0.05
	< d.l.	< d.l.	< d.l.	< d.l.	< d.l.	< d.l.	< d.l.	26.57	< d.l.	< d.l.	< d.l.	2
	11	< d.l.	14	15	14	18	10	11	< d.l.	12	18	10
	55.1	50.2	12.0	28.1	9.3	5.1	55.9	31.7	35.0	46.7	6.7	0.05
	105.0	101.3	23.5	56.4	20.2	10.7	108.7	68.1	75.0	96.4	14.6	0.05
	11.64	10.99	2.61	6.38	2.34	1.21	11.79	7.91	8.78	11.12	1.68	0.01
	46.8	44.2	10.3	25.7	10.2	5.3	47.3	32.1	35.5	44.5	7.4	0.05
	7.68	6.92	1.73	4.43	2.19	1.28	7.32	5.47	5.76	6.74	1.61	0.01
	1.823	1.185	0.397	0.757	0.250	0.246	0.825	0.582	0.612	1.208	0.222	0.005
	5.67	4.88	1.21	3.57	2.14	1.27	5.37	4.02	4.14	4.56	1.54	0.01
	0.84	0.64	0.21	0.56	0.37	0.22	0.61	0.58	0.58	0.59	0.27	0.01
	4.01	3.15	1.20	3.01	2.19	1.31	2.77	3.00	3.03	2.83	1.64	0.01
	0.74	0.57	0.26	0.62	0.45	0.27	0.48	0.57	0.57	0.52	0.34	0.01
	2.03	1.57	0.84	1.67	1.29	0.77	1.38	1.54	1.55	1.43	1.05	0.01
	0.286	0.240	0.147	0.262	0.222	0.132	0.190	0.221	0.237	0.205	0.195	0.005
	1.89	1.50	1.00	1.49	1.39	0.85	1.17	1.23	1.38	1.20	1.29	0.01
	0.249	0.203	0.164	0.224	0.202	0.129	0.170	0.177	0.190	0.169	0.211	0.002

FIGURE 11. Relationship between the color of tourmaline in thin section (plane polarized light) and its composition.

A

B
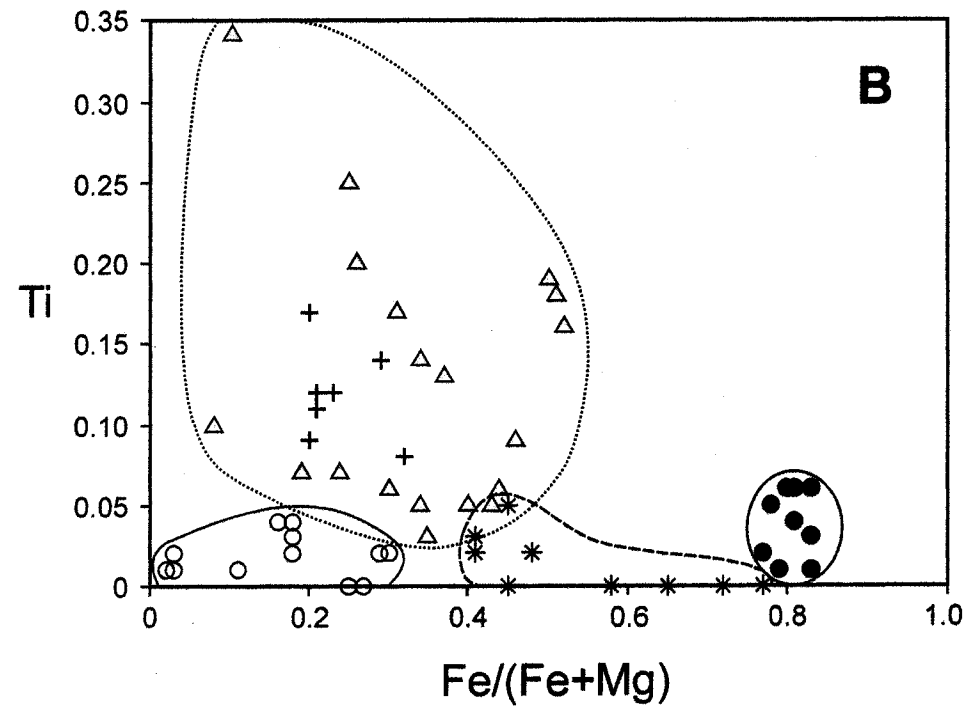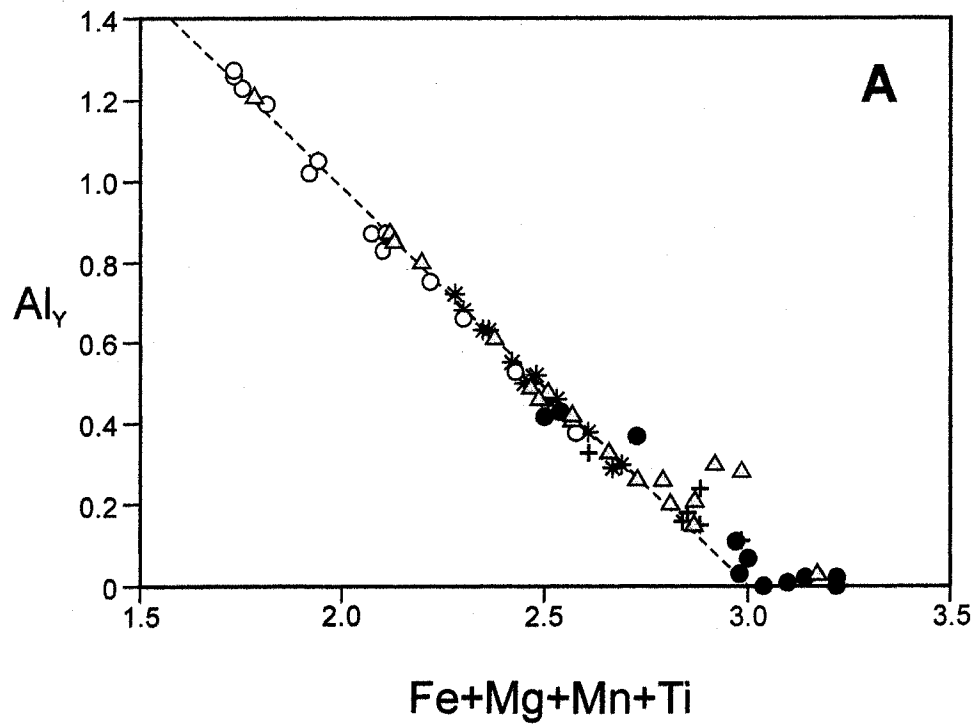
○ colorless △ yellow + orange * blue ● green

FIGURE 12. Partitioning of Mg and Fe between coexisting chlorite and late tourmaline.
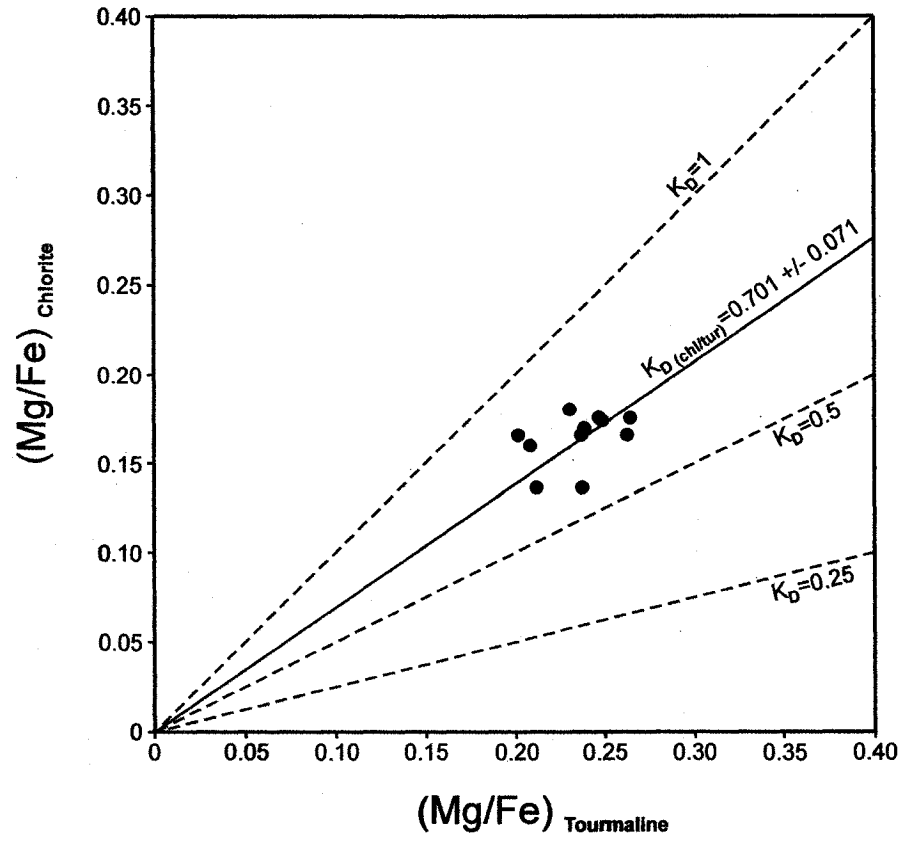
The geothermometers of Cathelineau (1988) and Jowett (1991) predict temperatures for San Rafael in the range 335-415°C, the latter yielding values 5-15°C higher than the former (Tab. 3). The temperature obtained for alteration chlorite is, on average, 50°C higher than that obtained for vein chlorite, which reflects the systematic difference in Al^{IV} contents between these two chlorite groups. Considering the relatively poor precision of the geothermometers, the results compare well with the homogenization temperatures of cassiterite-hosted primary fluid inclusions from the same ores, which typically are in the range 355-360°C (Mlynarczyk et al., 2003).

The geothermometer of Walshe yields temperatures in the range 295 to 320°C for the alteration chlorite (i.e., ~80°C lower than the temperature predicted by the two other geothermometers), and log fO_2 values between -32.9 and -30.5 (Tab. 3). A possible explanation for this disagreement in predicted temperatures is that the geothermometer of Walshe is based on selected components (e.g., it does not take into account Mn-chlorite end-members, whereas San Rafael chlorite contains 0.2-0.7 wt.% MnO). The model also does not incorporate the most recent thermodynamic data for chlorite species.

In conclusion, it is considered that the method of Walshe (1986) likely underestimates the temperature of chlorite formation, whereas the temperature obtained using the empirical geothermometers of Cathelineau (1988) and Jowett (1991) is more accurate. The temperature of chlorite formation at San Rafael is thus considered to lie in the upper part of the 300-400°C range, in good agreement with estimates from fluid inclusion microthermometry.

ALTERATION GEOCHEMISTRY AND MASS TRANSFER

Sampling and analytical methods

A systematic study of alteration at San Rafael involves several challenges. The precursor granitic rocks are chemically inhomogenous, due to their highly porphyritic character and an irregular distribution of the 2 to 10-cm-long K-feldspar megacrysts, especially in the granodiorites. Locally, many enclaves are present, which also contributes to the heterogeneity of the rock. An additional complication is the obliteration of early alteration by main-stage chloritization, which in the vicinity of the ore veins is generally so strong

82

and laterally extensive that no alteration zoning can be observed. Finally, multiple episodes of veining and brecciation produced a great textural complexity of the vein envelopes.

In order to overcome these difficulties, the present study focuses largely on the porphyritic, cordierite-biotite leucogranite, which hosts the bulk of tin mineralization and is the most abundant phase in the southwestern part of the pluton. This leucogranite is characterized by a relatively regular distribution of K-feldspar megacrysts and is generally enclave-free, which makes it a very appropriate host rock for the study of alteration. Careful underground sampling and selection of drill core made it possible to avoid areas with accumulations of K-feldpar megacrysts, texturally complex zones and those with superimposed alteration. Furthermore, to ensure that the samples are representative, several samples of fresh granite and of each alteration type were collected at several different locations. In order to minimize the effect on bulk composition from any heterogeneity in phenocryst distribution, the samples collected were either large fragments of wall rock (20-30 kg) or several-meter-long fragments of drill core. Finally, in order to study the evolution of alteration in more detail, the whole-rock samples were supplemented by several pieces of drill core, exhibiting marked alteration zoning in finer-grained granitoids.

In total, about 100 samples were either broken down into smaller fragments or slabbed and then carefully inspected for any inhomogeneities (e.g., enclaves, veining, alteration). Samples judged to be homogenous (63) were crushed in a case-hardened iron jaw crusher and ground in a pure iron (steel) grinder. Splitting procedures were used to obtain a representative aliquot of the crushed sample (~ 400 g) for subsequent grinding.

Major elements and scandium were analyzed by fusion X-ray fluorescence (XRF), chlorine, fluorine and sulfur by pressed powder pellet X-ray fluorescence (XRF), and ferrous/ferric iron by titration in the Geochemical Laboratories at McGill University. Loss on ignition was established from mass loss after fusion. Trace and rare earth elements were analyzed by inductively coupled plasma-mass spectrometry (ICP-MS) following sample fusion, lithium by total acid digestion inductively coupled plasma (ICP), and boron by prompt gamma neutron activation analysis (PGNAA) at Activation Laboratories, Ancaster, Ontario.

83

Whole-rock geochemistry

The results of selected bulk-rock analyses, together with the detection limits are presented in Table 5 and a detailed description of the samples is provided in Appendix-I. The data presented are raw data, however, the calculations performed in the paper were based on data normalized to 100 %, including the trace elements.
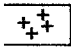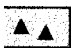
The principal geochemical changes associated with individual alteration types and the mineral assemblages that accompany them are summarized in Figure 13, under the headings: weak sericitic alteration (early), tourmaline alteration (early) and chloritic alteration (dominantly main-stage). An additional single analysis of an uncommon albite-sericite alteration (observed only in an outcrop) was also plotted. Analyses of superimposed alteration, i.e., tourmalinization or chloritization on strong sericitization, plot between the main alteration fields, but are not shown for the purpose of clarity.

The ternary diagrams in Figure 13 show that weak sericitic alteration, which typically preceded extensive tourmalinization and chloritization, did not produce significant bulk chemical changes. Compared to unaltered rocks, mildly sericitized granitoids have only slightly lower contents of Na and Ca, and slightly higher contents of Al. Tourmalinized rocks, however, contain much less Na, K and Ca than their precursors and considerably more Al and Mg. Chloritized rocks also have much lower contents of Na, K and Ca, but differ from tourmalinized rocks in containing less Mg and more Fe. Finally, the single sample of albite-sericite alteration exhibits a marked enrichment in Na and a loss of K, Fe and Mg. This strongly metasomatized granitic rock displays an unusual, strongly positive Eu anomaly (not shown), which suggests that none of the fresh rocks analyzed in this study (typically displaying strongly negative Eu anomalies) could be its precursor. Consequently, the geochemical changes experienced by this rock cannot be estimated accurately.

The boron content of the unaltered rocks ranges from 60 to 250 ppm B, which is within the typical range for granitic rocks (London et al., 1996), but it increases to ~1 wt.% B in strongly tourmalinized wall rocks. Fluorine and lithium concentrations are slightly higher in the unaltered granitoids than is generally reported for such rocks (0.12-0.22 wt.% F, 150-350 ppm Li) and experienced a minor depletion in the altered rocks.

FIGURE 13. Bulk-rock composition of the different alteration types presented on ACF-AKF diagrams, following those of Meyer and Hemley (1967). The compositions are plotted as mole % oxide and n = 30. The field of fresh granite and granodiorite indicates the precursors for all of the altered rocks, except that for albite-sericite alteration, which is inferred to have been different. Arrows indicate the paths of geochemical change. Minerals plotted for reference have end-member compositions, unless indicated otherwise: Kfs - K-feldspar, Ab - albite, Ms - muscovite, Ser - sericite (average composition from microprobe data), Bt - biotite, Chl - chlorite (average composition from microprobe data), Zo - zoisite, Pst - pistacite, Tur - dravite-schorl tourmaline (average composition from microprobe data), Kln - kaolinite, Prl - pyrophyllite, Cal - calcite, Sd - siderite, Ank - ankerite, Py - pyrite.

Top diagram (diamond):

Al$_2$O$_3$ — Kln,Prl

Ms

Kfs,Ab

Ser

K$_2$O+Na$_2$O

Zo

epidote ss.

Pst

Tur

CaO

Cal

Bt

Chl

Ank

Hm,Py,Sd

FeO$_{tot}$+MgO+MnO

Legend:
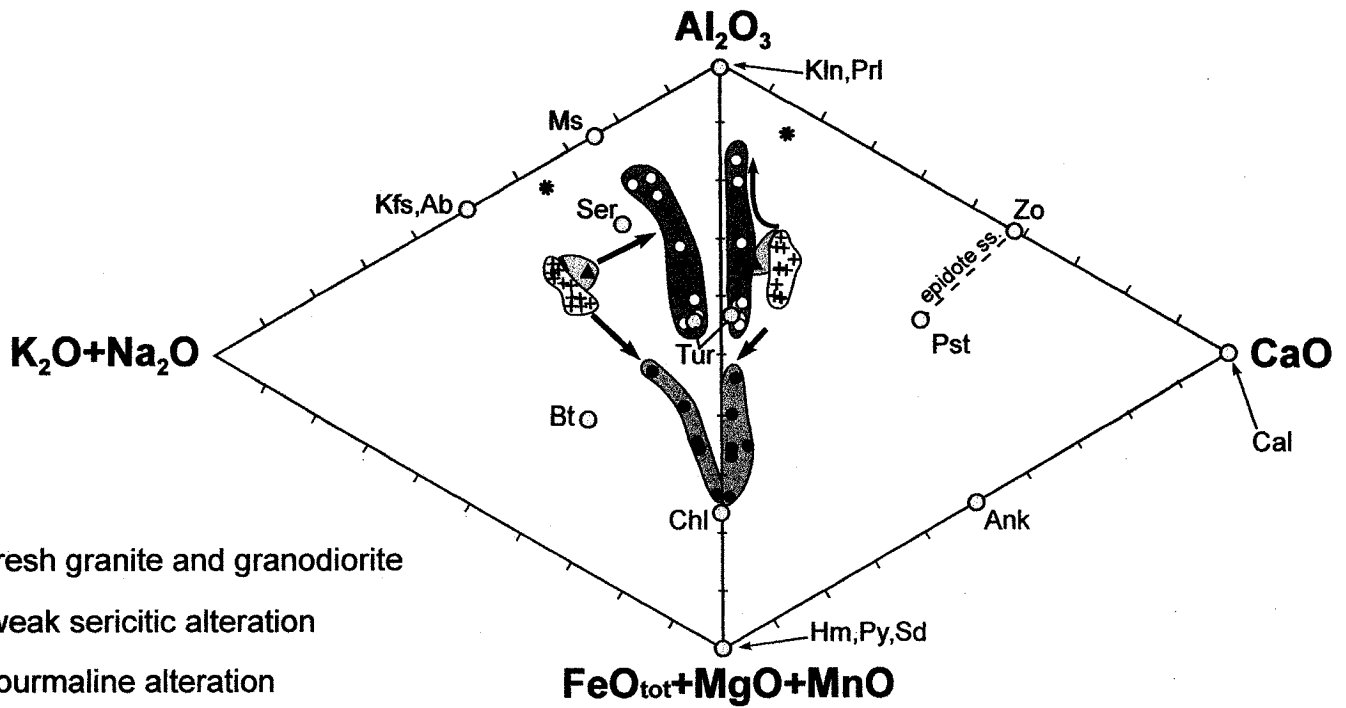
++ fresh granite and granodiorite

▲▲ weak sericitic alteration

●○○ tourmaline alteration

●● chloritic alteration

* albite-sericite alteration

Lower-left diagram (triangle):

K$_2$O+Na$_2$O — Kfs,Ab,Ms,Kln,Prl

*

Ser

Bt

Tur

Chl

Hm,Py,Sd

IgO

FeO$_{tot}$

Lower-right diagram (triangle):

Al$_2$O$_3$ — Chl,Kln

Tur

Mus,Ser

*

Ab

alkali-feldspar ss.

Kfs

Na$_2$O

K$_2$
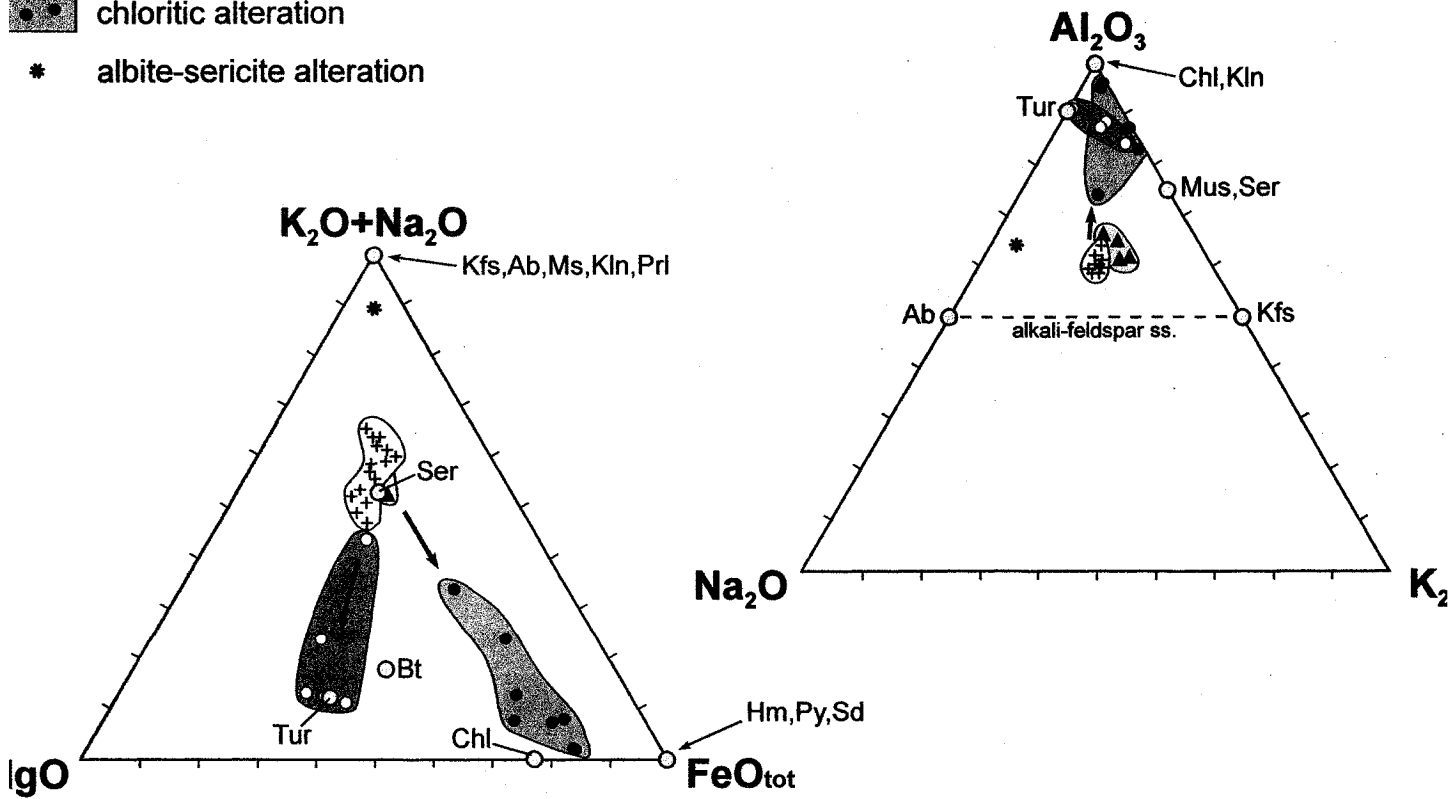
The concentration of copper in the unaltered rocks typically ranges between 30 and 45 ppm, and is only slightly enriched in the chloritized rocks (up to 60 ppm). Tin concentrations, however, are much higher in the altered rocks than in their unaltered equivalents. Thus, while fresh rocks contain 5-12 ppm Sn (values typical of non-specialized granitoids, *cf.* Lehmann, 1990), strongly sericitized and tourmalinized wall rocks generally contain 20-90 ppm Sn, and strongly chloritized rocks >100 ppm (up to 215 ppm). We note, however, that not all of the pervasively chloritized wall rocks have such high tin contents and some do not exceed a threefold tin enrichment with respect to unaltered rocks. Also, due to the strong overprint of main-stage chloritization on earlier alteration types at San Rafael, it is possible that the relatively elevated tin contents of sericitic and tourmaline-altered rocks developed during later alteration. Finally, as was the case for tin, the content of tugsten increased greatly, almost tenfold, from 1-4 ppm in unaltered rocks to 10-48 ppm in tourmalinized or chloritized wall rocks.

Mass changes during alteration

Methodology

The calculation of mass transfer between rock and the fluid during alteration requires that the whole-rock chemical data are corrected for changes in total mass by using immobile elements. In the present study, the isocon method of Grant (1986) was used to identify the elements, which were immobile during alteration. In this method, element concentrations of an unaltered rock are plotted against their concentrations in the corresponding altered rock. The elements, which were immobile during alteration maintain constant ratios, which together define a line of constant mass (isocon). The slope of the isocon determines the mass factor used to adjust element concentrations of the altered rock, which serves to calculate the final mass change (Grant, 1986; Ulrich et al., 2001). It should be emphasized that, in order for the method to yield accurate results, the selected immobile elements must not only have a truly immobile behaviour with respect to the alteration considered, but also occur in a significant concentration in the rock (so that they are more sensitive to the mass changes and easy to analyse) and be homogeneously distributed (to avoid "nugget effects").

The sample pairs of "fresh" vs. "altered" rock, used to construct the isocon diagrams should, ideally, be spatially adjacent. At San Rafael, however, strong chloritic alteration extends for up to 10 meters away from the ore veins and the spatial transition between fresh and altered rock occurs on a scale of several meters. Because of this, it was seldom possible to sample fresh rock directly beside strong alteration, and some sample pairs were "matched" together. When selecting the immobile elements, care was taken, therefore, that in addition to the previously mentioned criteria, these elements also occur in a very narrow range of concentrations in the granitic rock suite, to eliminate any effect of precursor variability.

The large, bulk-rock samples were supplemented by pieces of wall rock and drill core, collected further away from the main zone of chloritization, and displaying zoned, fracture-controlled alteration on a scale of centimeters (Fig. 4A,B,C). A multiple slabbing approach (*cf.* Mountain and Williams-Jones, 1996; Halter et al., 1996) was used on these samples but, because of the porphyritic nature of the host rocks, only a few slabs representative of the rock composition could be made of each sample. One such sample is D4-68 (Fig. 4B and Fig. 16), which displays an unusually well developed sequence of early alteration surrounding a single tourmaline vein. The alteration envelope is ~ 20-cm-wide and progresses (inwards) from a mildly sericitized tonalite, through strong (pre-ore) chloritization, then strong sericitization overlapping with incipient tourmalinization and, finally, to strong tourmalinization with silicification. As this last zone is crosscut by fine tourmaline and quartz veinlets, the chemical analysis of this slab would not have yielded reliable results, and was replaced by a closely matched sample of tonalite tourmalinization (sample D4-94), collected from the same drill core.

Early, pre-ore alteration

Figures 14 and 15 show representative isocon diagrams and calculated histograms of mass change for the principal types of early alteration, i.e., sericitization and tourmalinization, whereas Figure 16 shows the mass changes across a complex alteration halo surrounding a tourmaline vein. The data on which these diagrams are based are presented in Tables 6 and 7. As strong sericitization is invariably accompanied or overprinted by tourmalinization, it cannot be characterized unambiguously and the results

FIGURE 14. Isocon diagrams for sericitic alteration and tourmalinization of granite at the San Rafael deposit. The concentration of selected elements in the precursor is plotted versus that in the corresponding altered rock. Concentrations (expressed in wt.% for the oxides, F, Cl, S, LOI, and in ppm for the other elements) are multiplied by a constant, to fit the common scale of the diagrams. LOI corresponds to H_2O+CO_2. Solid lines, representing the isocons are defined by the constant ratios of TiO_2, assumed to be immobile. Elements above the isocons are enriched in the altered rock, whereas those below are depleted. Grey fields highlight the elements which usually display an immobile behaviour in hydrothermal systems (Ti, Al, P, Ta, Nb, Zr, Hf, Th, and on the diagrams for sericitic alteration also Y and the HREE). Diagrams **A, B, E** are for large samples of wallrock or core that were matched together, based on petrography and location in the deposit. Diagrams **C** and **D** belong to the same sample set, representing progressive tourmalinization of a previously sericitized granite. It is also important to note that the strongly tourmalinized rock plotted on diagram E (D5-138) displays marked porosity, which may explain the mass loss indicated by the isocon, in contrast to the diagrams B and D, which suggest the alteration is related to a mass gain.

A - incipient sericitization of granite

D5-2

D4-443

B - sericitization, tourmalinization and dumortieritization of granite

I 45

I 20

C - sericitization and tourmalinization of granite

J26-B

I 8

D - very strong tourmalinization of granite

J26-A

I 8

E - very strong tourmalinization of granite

D5-138

R566

concentration in altered rock (wt.% or ppm)

concentration in precursor (wt.% or ppm)

FIGURE 15. Gains and losses of major and trace elements during sericitic alteration and tourmalinization. The values have been calculated assuming that titanium is immobile (see also Table 6) and correspond to the isocon diagrams of Fig.14. The third set of histograms (C/D) represents stages of increasing sericitization and tourmalinization (the grey columns correspond to initial, pervasive sericitization and tourmalinization, whereas the thick, black ones represent very strong tourmalinization).

A - incipient sericitization of granite (D4-443 vs D5-2)

B - sericitization, tourmalinization and dumortieritization of granite (I20-I45)

C/D - sericitization and tourmalinization of granite (I8 vs J26-B and J26-A)

E - strong tourmalinization of granite (R566 vs D5-138)
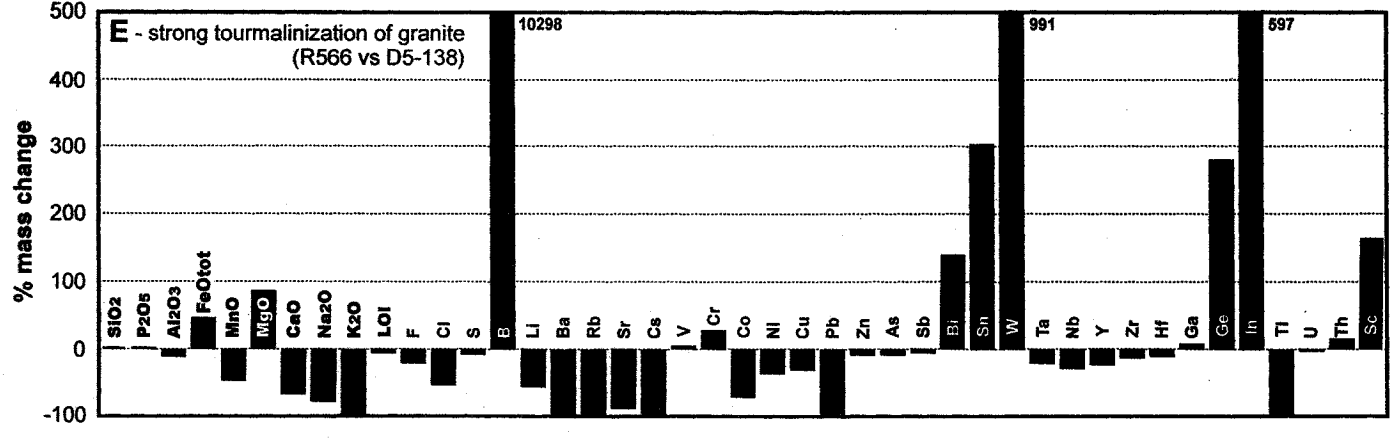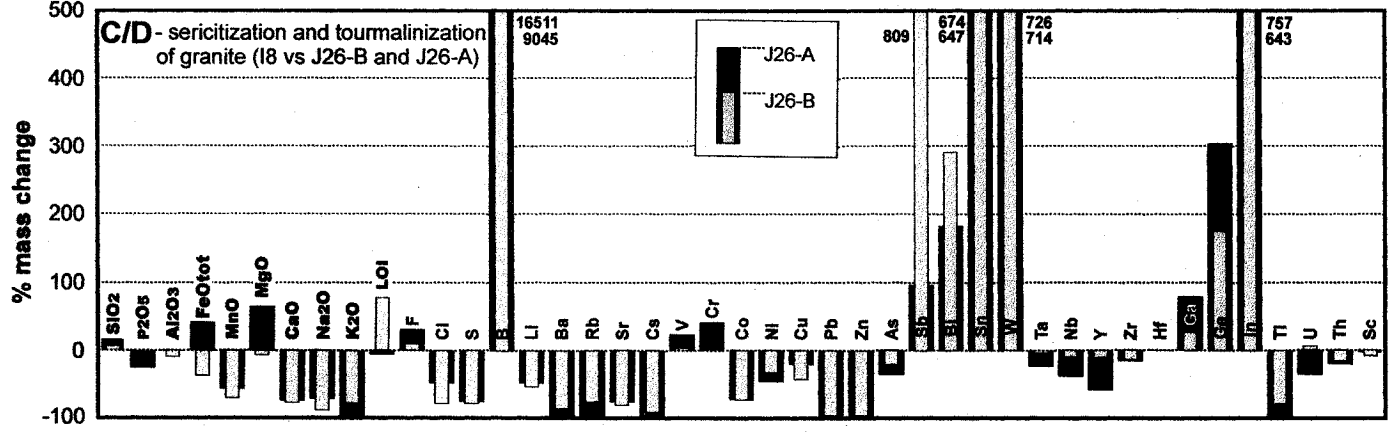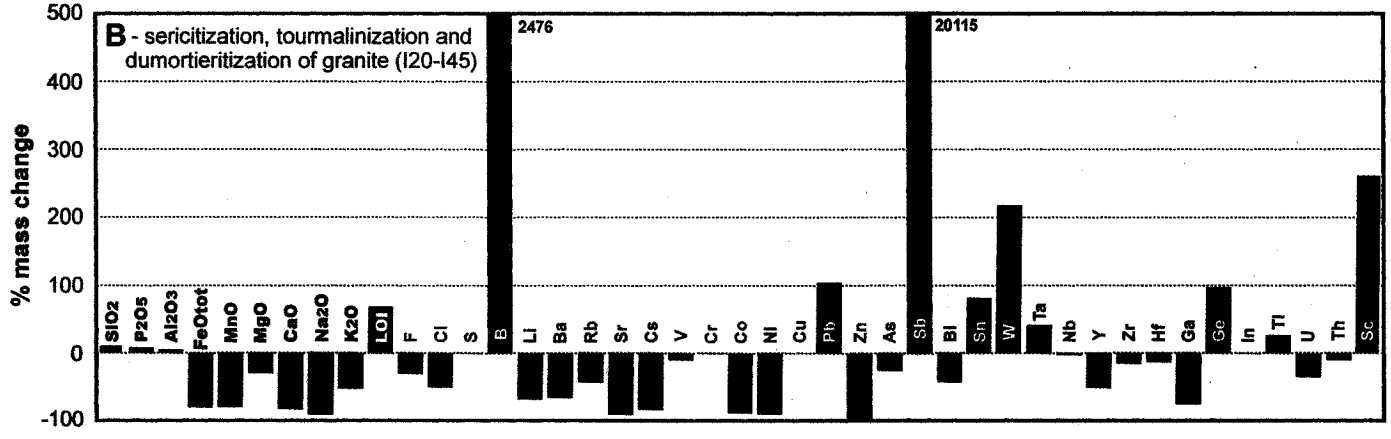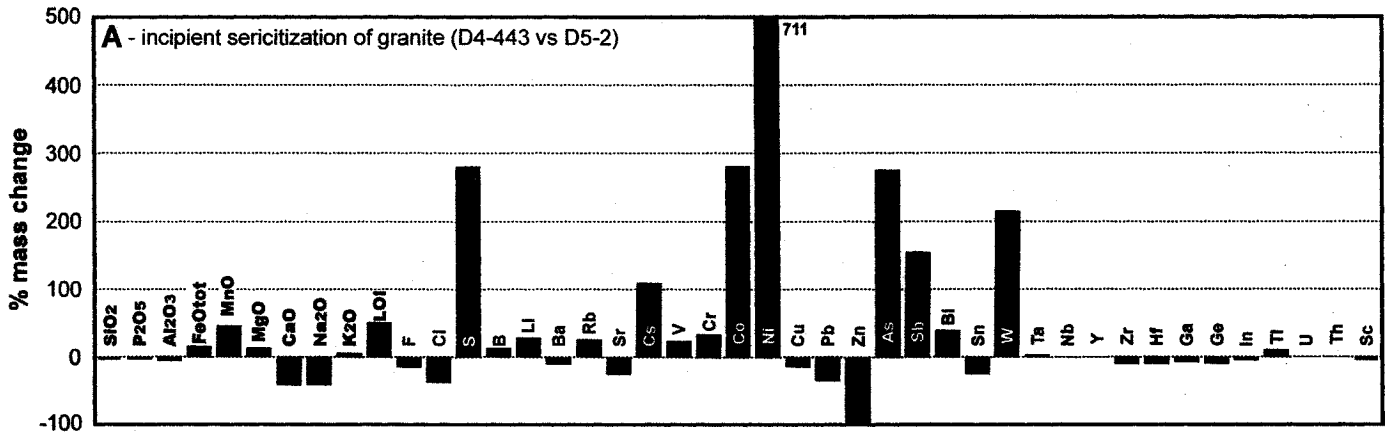
FIGURE 16. Mass change profiles for selected elements across a halo of early, pre-ore alteration surrounding a single tourmaline vein (sample D4-68). The mass changes were calculated assuming immobile Ti, and are reported as grams added/removed per 100 g of rock (i.e., %) for major elements, and grams per 1 ton of rock (i.e., ppm) for trace elements. Percentage changes are relative to the concentration in the precursor, i.e., sample D4-68E (*cf.* Tables 6,7). As it was not possible to analyze slab D4-68A, sample D4-94 (which closely matches the former) is used as a surrogate.
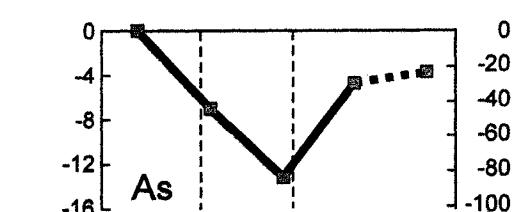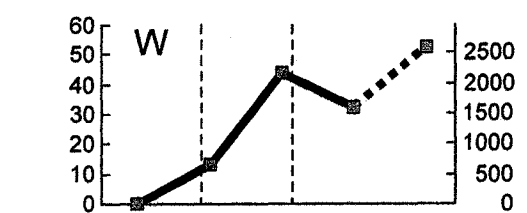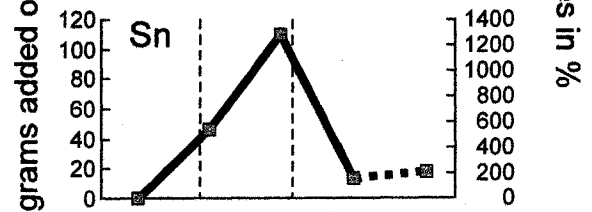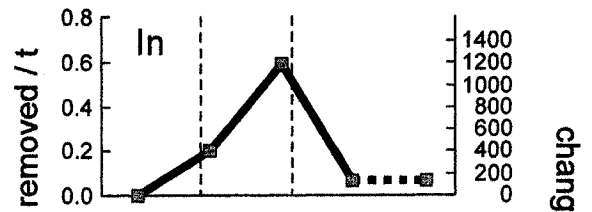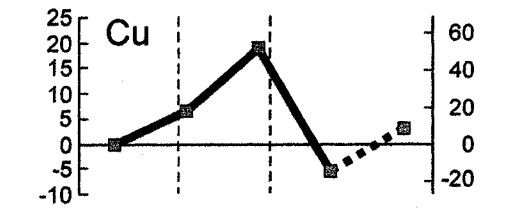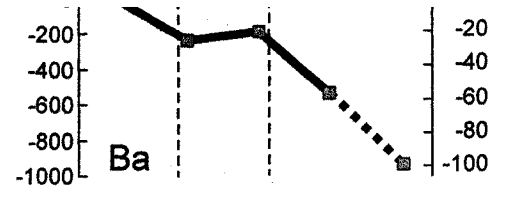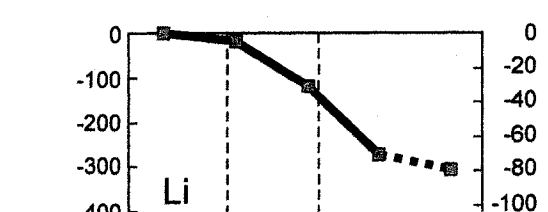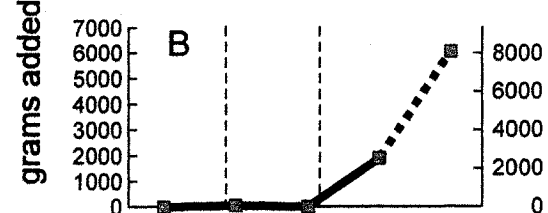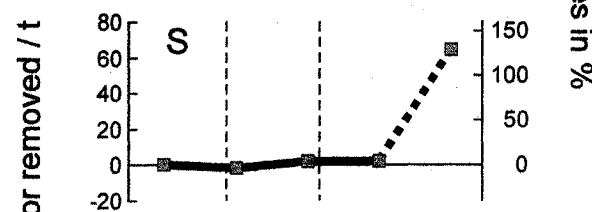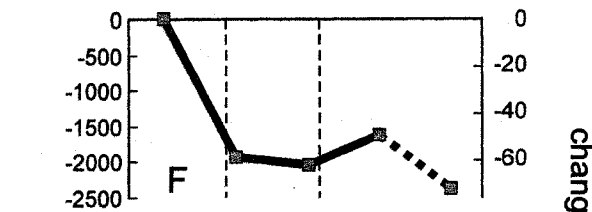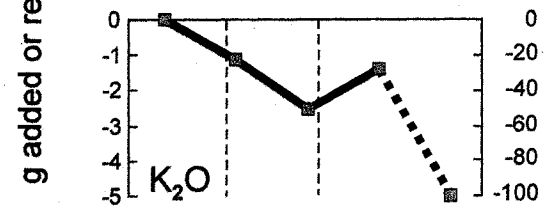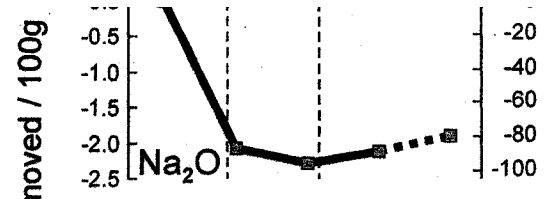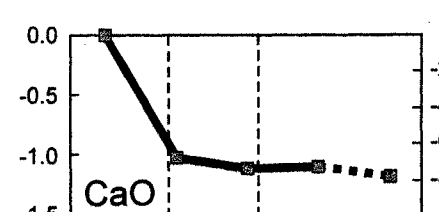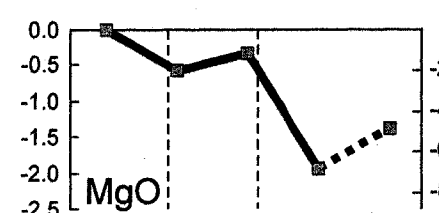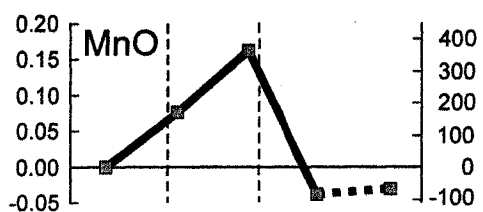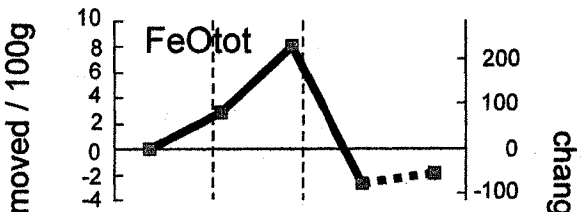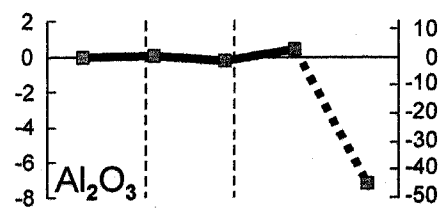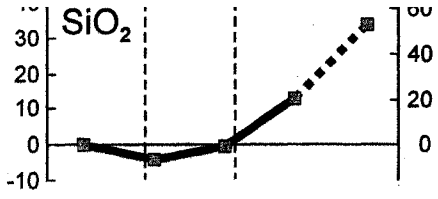
SLABS: E D C B A ///
Alteration: Chloritic   Tourmaline   Tour-Qz

TABLE 6. Elemental and oxide mass gains / losses associated with alteration (expressed as a percentage of the concentration in fresh rock).

iple :	Chloritic					Sericitic	Sericitic & Tourm.	Sericitic & Tourm.	Tourmaline		Sericitic & Chloritic	Strong Chloritic	Sericitic & Tourm.	Tourm. & Silicic
	Strong I51 R80	Moderate R432-C R432-B	Strong R432-C R432-A	Incipient D1M-61D D1M-61C	Strong D1M-61D D1M-61B	Incipient D4-443 D5-2	I20 I45	I8 J26-B	Strong I8 J26-A	Strong R566 D5-138	D4-68E D4-68D	D4-68E D4-68C	D4-68E D4-68B	D4-68E D4-94
?	-11	-3	-3	0	4	-4	11	4	14	2	-6	0	20	52
!	8	-1	-9	-1	-2	0	0	0	0	0	0	0	0	0
l3	-6	-7	-20	-1	-16	-5	5	-7	0	-10	1	-1	3	-45
tot	557	213	380	17	248	16	-79	-37	40	45	82	231	-77	-56
)	339	137	306	37	220	45	-80	-70	-58	-45	166	354	-82	-65
)	35	19	25	-8	-24	13	-29	-5	65	87	-20	-12	-68	-48
)	-80	-39	46	-63	-77	-42	-81	-77	-74	-68	-68	-75	-73	-79
O	-96	-50	-95	-43	-98	-40	-90	-87	-73	-78	-86	-95	-88	-80
	-63	-54	-70	5	-62	6	-52	-76	-99	-99	-22	-50	-28	-99
s	0	0	0	0	0	-3	7	0	-26	2	1	1	11	-33
	328	90	158	64	85	49	68	76	-6	-5	206	187	45	-51
	-31	-27	-52	-12	-28	-14	-29	9	31	-19	-59	-62	-49	-72
	-74	-50	4	-67	-83	-36	-50	-77	-48	-53	-76	-87	-74	-71
	-83	0	4	-75	-74	282	0	-77	-74	-6	-3	4	5	129
	4	-20	-35	55	-6	12	2476	9046	16511	10298	108	5	2514	8138
	6	32	75	3	23	30	-68	-53	-48	-54	-4	-31	-70	-78
	-55	-28	-41	-1	-72	-9	-65	-84	-99	-100	-26	-20	-56	-100
	-48	-47	-63	3	-60	27	-42	-74	-98	-99	-27	-60	-59	-100
	-97	-78	-90	-53	-97	-25	-89	-81	-75	-86	-81	-93	-91	-88
	-94	-56	-69	21	-79	108	-83	-90	-99	-99	88	-81	-89	-99
	45	-7	8	6	3	24	-10	5	22	6	7	10	13	-16
	43	36	9	4	9	34	0	2	40	29	4	8	9	-37
	220	63	178	17	81	282	-87	-72	-73	-71	-15	-5	-95	-88
	-8	0	3668	14	11	711	-91	-33	-45	-35	-30	13	-89	-78
	125	19	-98	24	32	-13	0	-42	-19	-29	19	53	-15	8
	-93	-93	-93	7	-79	-35	105	-95	-95	-94	-61	-83	-83	-81
	295	9	-95	-49	67	-95	-95	-95	-94	-6	-25	81	-96	-96
	-72	-90	-90	-28	-86	275	-25	-20	-35	-6	-44	-84	-30	-24
	76	-38	-13	34	-55	155	20115	809	96	-5	209	50	391	72
	-37	-74	-76	77	-87	39	-43	290	182	139	528	-38	85	218
	1884	312	348	115	741	-24	80	647	674	303	542	1289	155	207
	1090	119	123	124	2340	215	217	714	726	991	669	2155	1586	2590
	1	0	-2	3	2	2	40	-1	-21	-19	9	9	10	68
	-1	-2	1	7	14	1	-1	-9	-37	-26	7	8	15	64
	-6	-1	-3	8	-1	0	-49	-10	-57	-21	3	10	6	-20
	1	-17	-11	5	12	-10	-13	-11	-13	-13	4	5	14	13
	11	-13	-11	10	10	-9	-12	-1	1	-10	3	2	1	-1
	34	8	24	6	19	-7	-74	26	80	8	4	20	-26	-59
	130	6	16	29	34	-9	96	175	304	281	158	58	206	159
	1483	370	455	42	537	-5	0	643	757	597	401	1189	136	134
	-33	-48	-66	17	-62	10	27	-76	-96	-94	-25	-39	-76	-99
	-1	-4	-2	22	25	1	-34	5	-36	-1	27	13	1	-37
	-8	-3	1	20	4	0	-9	-15	-19	16	4	10	12	-28
	-53	0	-57	28	42	-5	261	-6	-2	165	-60	-5	-12	72
	-10	-17	3	14	7	-3	-86	-46	-74	-79	-27	-30	26	-84
	-11	-15	4	13	8	-3	-85	-44	-74	-77	-25	-27	19	-83
	-2	-15	5	14	8	4	-83	-35	-70	-72	-23	-26	12	-83
	0	-14	6	13	6	5	-81	-32	-70	-69	-23	-25	12	-81
	-3	-9	5	12	9	-3	-74	-33	-71	-62	-17	-16	14	-73
	21	-3	1	-1	-14	-1	-76	-44	-67	-84	-51	-50	-28	-79
	7	-5	1	14	9	-1	-66	-27	-73	-50	-12	-8	24	-61
	2	0	1	6	2	-1	-62	-21	-67	-40	-4	2	10	-48
	2	2	-3	11	1	1	-56	-17	-63	-30	4	10	3	-34
	-3	0	-6	12	0	3	-52	-7	-56	-23	7	15	-3	-24
	1	1	-1	6	-1	6	-49	-7	-48	-16	5	11	1	-16
	-2	-2	-2	9	0	11	-43	-4	-40	1	12	12	-2	9
	3	-9	-7	4	-6	7	-41	-9	-32	-1	11	7	3	23
	-1	-12	-16	13	-6	7	-37	-5	-23	0	9	9	6	43

TABLE 7. Mass gains / losses associated with alteration (in g/100g rock or ppm).

	Chloritic					Sericitic	Sericitic	Sericitic	Tourmaline		Sericitic	Strong	Sericitic	Tourm.
ple	Strong I51 R80	Moderate R432-C R432-B	Strong R432-C R432-A	Incipient D1M-61D D1M-61C	Strong D1M-61D D1M-61B	Incipient D4-443 D5-2	& Tourm. I20 I45	& Tourm. I8 J26-B	Strong I8 J26-A	Strong R566 D5-138	& Chloritic D4-68E D4-68D	Chloritic D4-68E D4-68C	& Tourm. D4-68E D4-68B	& Silicic D4-68E D4-94
	-7.35	-2.30	-2.16	0.18	2.36	-2.81	7.51	2.42	9.63	1.28	-4.21	-0.32	13.07	33.82
	0.032	-0.002	-0.030	-0.006	-0.010	0.000	0.000	0.000	0.000	0.000	0.000	0.000	0.000	0.00(
3	-0.93	-1.14	-3.11	-0.09	-2.46	-0.88	0.76	-1.20	-0.01	-1.77	0.08	-0.21	0.46	-7.19
ot	14.59	6.42	11.47	0.64	9.47	0.35	-1.85	-1.04	1.11	0.93	2.84	8.00	-2.68	-1.93
	0.115	0.081	0.180	0.024	0.145	0.013	-0.040	-0.026	-0.021	-0.012	0.076	0.162	-0.037	-0.030
	0.53	0.22	0.29	-0.25	-0.76	0.16	-0.36	-0.08	1.07	1.15	-0.59	-0.34	-1.95	-1.39
	-1.35	-0.27	0.32	-1.02	-1.24	-0.63	-1.38	-1.52	-1.46	-1.21	-1.02	-1.12	-1.11	-1.19
)	-3.10	-1.47	-2.81	-0.99	-2.24	-1.35	-2.93	-2.79	-2.34	-2.94	-2.06	-2.28	-2.11	-1.90
	-3.06	-2.91	-3.80	0.21	-2.74	0.31	-2.53	-3.82	-4.95	-5.11	-1.11	-2.51	-1.41	-5.00
	0.000	0.000	0.000	0.000	0.000	-0.007	0.016	0.000	-0.062	0.005	0.003	0.002	0.027	-0.08
	4.03	1.66	2.90	1.58	2.10	0.57	0.87	1.02	-0.08	-0.06	3.42	3.10	0.74	-0.8
	-468	-399	-774	-193	-452	-281	-447	113	367	-265	-1934	-2045	-1609	-237
	-296	-50	4	-199	-247	-109	-99	-306	-191	-210	-302	-347	-294	-28
	-248	0	2	-149	-147	141	0	-153	-148	-3	-1	2	3	6
	6	-26	-46	45	-5	15	3328	5352	9770	9095	80	3	1869	605
	20	55	130	8	60	79	-124	-107	-96	-82	-17	-121	-273	-30
	-357	-233	-342	-11	-1553	-69	-361	-718	-852	-1182	-242	-188	-529	-93
	-141	-173	-233	11	-203	98	-133	-210	-280	-294	-134	-294	-289	-48
	-209	-94	-109	-232	-428	-51	-174	-209	-193	-255	-158	-179	-176	-17
	-275	-34	-42	27	-103	100	-127	-207	-227	-181	159	-147	-161	-17
	14	-2	2	4	2	7	-3	2	8	2	3	4	6	-
	24	19	5	6	13	15	0	1	25	15	6	11	13	-5
	10	3	9	2	9	10	-3	-5	-5	-3	-2	-1	-11	-1
	-1	0	476	4	3	43	-14	-7	-9	-6	-14	6	-42	-3
	34	8	-41	8	11	-6	0	-19	-8	-12	7	19	-5	
	-33	-33	-33	1	-10	-18	38	-46	-45	-38	-9	-13	-13	-1
	35	2	-21	-21	29	-19	-20	-17	-17	0	-7	22	-26	-2
	-7	-23	-22	-5	-16	287	-8	-10	-18	0	-7	-13	-5	-
	0.7	-0.7	-0.2	0.8	-1.3	1.0	90.5	8.5	1.0	-0.1	1.7	0.4	3.1	0.
	-0.1	-1.1	-1.1	1.1	-1.3	2.0	-0.1	0.8	0.5	0.8	1.0	-0.1	0.2	0.
	107	118	132	31	198	-4	9	71	74	38	46	110	13	1
	13.8	6.6	6.9	1.8	33.4	9.3	4.4	9.4	9.6	14.4	13.5	43.6	32.1	52.
	0.02	-0.01	-0.06	0.09	0.06	0.04	0.86	-0.02	-0.40	-0.30	0.15	0.15	0.17	1.1
	-0.2	-0.3	0.1	1.1	2.1	0.1	-0.2	-1.4	-5.8	-3.4	0.9	1.0	1.9	8.
	-1.1	-0.1	-0.5	1.8	-0.1	0.0	-8.1	-1.8	-10.2	-3.3	0.5	1.5	0.9	-3.
	2	-23	-15	8	18	-19	-18	-18	-23	-20	7	9	25	2
	0.5	-0.6	-0.4	0.5	0.4	-0.5	-0.5	0.0	0.0	-0.4	0.2	0.1	0.0	0.
	9	2	6	1	5	-2	-19	7	21	2	1	5	-7	-1
	1.6	0.1	0.3	0.4	0.5	-0.2	1.4	2.9	5.1	4.1	1.9	0.7	2.5	1.
	0.74	0.68	0.83	0.06	0.73	0.00	0.00	0.32	0.38	0.30	0.20	0.59	0.07	0.0
	-0.54	-1.35	-1.85	0.35	-1.30	0.33	0.51	-1.96	-2.48	-1.66	-0.73	-1.13	-2.19	-2.8
	-0.1	-0.6	-0.2	2.7	3.0	0.2	-4.4	0.5	-3.7	-0.1	2.8	1.3	0.1	-3.
	-1.8	-0.5	0.1	3.5	0.7	0.1	-1.8	-3.6	-4.7	3.3	1.0	2.7	3.2	-7.
	-5.8	0.0	-6.8	3.0	4.6	-0.2	13.0	-0.9	-0.4	8.2	-7.1	-0.6	-1.5	8.
	-4.4	-6.0	1.0	7.7	4.0	-1.4	-32.4	-22.2	-35.9	-32.7	-12.7	-13.8	12.1	-38.
	-9.5	-10.9	2.8	14.0	8.1	-3.5	-62.3	-41.2	-69.5	-61.9	-23.6	-25.5	18.0	-79.
	-0.18	-1.18	0.40	1.57	0.90	0.37	-5.86	-3.15	-6.41	-5.67	-2.59	-2.89	1.29	-9.1
	0.1	-4.2	1.8	5.9	2.8	2.0	-22.6	-11.5	-24.7	-21.6	-10.1	-11.1	5.3	-35.
	-0.15	-0.48	0.25	0.93	0.68	-0.23	-3.63	-2.04	-4.39	-3.30	-1.14	-1.04	0.97	-4.8
	0.229	-0.037	0.011	-0.017	-0.247	-0.009	-0.762	-0.558	-0.853	-1.257	-0.612	-0.601	-0.338	-0.95
	0.28	-0.18	0.05	0.80	0.52	-0.06	-2.46	-1.23	-3.32	-1.99	-0.54	-0.37	1.10	-2.7
	0.01	0.00	0.01	0.05	0.02	-0.01	-0.35	-0.14	-0.45	-0.23	-0.02	0.01	0.06	-0.2
	0.07	0.05	-0.08	0.42	0.03	0.04	-1.66	-0.57	-2.14	-0.89	0.11	0.29	0.09	-0.9
	-0.02	0.00	-0.03	0.09	0.00	0.02	-0.29	-0.04	-0.35	-0.13	0.04	0.08	-0.02	-0.1
	0.02	0.02	-0.02	0.13	-0.02	0.09	-0.73	-0.12	-0.82	-0.24	0.07	0.16	0.02	-0.2
	-0.006	-0.003	-0.004	0.027	0.000	0.022	-0.101	-0.010	-0.102	0.002	0.025	0.025	-0.005	0.01
	0.05	-0.13	-0.11	0.08	-0.11	0.10	-0.58	-0.14	-0.49	-0.01	0.14	0.08	0.03	0.2
	-0.003	-0.026	-0.033	0.031	-0.016	0.013	-0.075	-0.012	-0.050	-0.001	0.015	0.015	0.010	0.07
ss tor:	1.035	1.003	1.032	1.003	1.044	0.958	1.010	0.946	1.061	0.951	0.973	1.043	1.053	1.15

for combined alteration are, therefore, presented (Fig. 14C and 15C). In addition, locally, strong boron metasomatism involved formation of both tourmaline and dumortierite (Fig. 14B and 15B). As can be inferred from the isocon diagrams of Figure 14, most elements experienced strong depletion during boron metasomatism, which made selection of a normalizing immobile element difficult. The silicification and destruction of aluminosilicate minerals, which led to loss of Al, precluded the use of either Al or Si as an immobile element. Zirconium was considered for use as a possible normalizing element, but its concentration in the unaltered rocks is unfortunately highly variable (139-368 ppm). Rare earth elements also could not be used because they occur in very small concentrations and experienced a significant depletion. The only element suitable for use in the mass change calculations is titanium, which is present in appreciable concentrations and appears to be relatively immobile (rutile, which is a breakdown product of biotite, is largely restricted to the confines of altered biotite crystals).

Very early chloritization (a poorly represented alteration type in the deposit), involved a net mass gain of ~ 4.3 % and a marked increase in Fe, Mn, H_2O (LOI), Sn, In, Cu and W, whereas Na, K, Ca, Ba, Rb, Sr, Cs, Li, F, Cl, and As were largely removed from the rock (Fig. 16). The gain in Sn associated with this alteration was very pronounced (~120 ppm Sn, i.e., a 14-fold mass increase).

Sericitic alteration was accompanied by a total mass loss on the order of 5 % (possibly higher for strong sericitization not overprinted by tourmaline alteration). As is evident from Figure 15A, apart from significant depletion in Na and Ca, incipient, mild sericitization involved only minor changes in the chemistry of the granitic rock, e.g., less than 50 % Ba, Sr, F, Cl, Pb, Zn were removed from the rock, whereas Mn, As, Sb, Bi, W, Co, Ni, H_2O (LOI), and possibly also Cs were added. As and Sb are inferred to occur in the form of sulfides, as S also experienced a significant mass gain and disseminated arsenopyrite was observed in some samples.

Tourmaline alteration generally involved a mass gain, of up to 6 % (Fig. 14 and Tab. 7). Locally, however, strong tourmalinization involved significant porosity creation (e.g., sample D5-138, Fig. 14E), and was accompanied by a mass loss of ~5 %. Strong tourmalinization (superimposed or not on strong sericitization) invariably involved the nearly complete removal of many major and trace elements from the precursor, namely

93

Na, K, Ca, Ba, Rb, Sr, Cs, Li, Cl, Mn, Co, Ni, Pb, Zn and Tl. A minor loss of Al was also observed. The principal gains were in B, Mg, Fe, Sn, W, In, Ge, Bi, and to a variable extent Sb and Si (Fig. 15C,D,E). Extreme boron metasomatism involving the formation of dumortierite in addition to tourmaline (Fig. 15B) was also accompanied by near complete leaching of most elements; the only significant additions were in B, Sb, Pb, Sn, W, Ge, Sc, Si and H_2O (LOI). These chemical changes are consistent with the observed destruction and replacement of ferromagnesian minerals and feldspars by a mineral assemblage composed almost entirely of dravite-schorl tourmaline and quartz. It is more difficult to interpret whether the observed increase in Sn (as well as those of In and Ge, which display a very similar geochemical behaviour) is primary or represents an overprint of the main-stage chloritic alteration. Enrichments in Sb, Bi and W are thought to be primary, as they were not repeated during later alteration. Finally, a small enrichment in Si (of the order of 10-15 %, Fig. 15, Tab. 6) confirms the macroscopic observation that, locally, some silicification accompanied tourmalinization. Such Si enrichment is, however, not observed in the slightly porous, tourmalinized sample, D5-138 (Fig. 15E). An alternative possibility is that silicification may have slightly postdated tourmalinization and filled the initial porosity of some but not all of the tourmalinized rocks.

Ore-stage alteration

Since *strong, ore-stage chloritization* is the best developed of the alteration types at San Rafael and is directly related to ore deposition, particular emphasis was placed on its study. Figure 17 presents a selection of representative isocon diagrams: two sets of which (B-C and D-E) are designed to show how intensity of alteration and precursor composition (granite vs. granodiorite) affected mass change. In addition, diagram (A) matches two wall rock samples of a larger size than the others, to verify that the coarsely porphyritic character of the granite does not produce any "nugget effects" in diagrams (B-E). In contrast to the isocon diagrams for tourmalinization, elements typically considered immobile for chloritization plot very close to one another on Figure 17, increasing the reliability of the selected isocon. Among these elements, phosphorus was most consistently closest to the best fit isocon and selected as the basis of normalization in

FIGURE 17. Isocon diagrams for chloritic alteration at the San Rafael deposit. The concentration of selected elements in the precursor is plotted versus that in the corresponding altered rock. Concentrations (expressed in wt.% for the oxides, F, Cl, S, LOI, and in ppm for the other elements) are multiplied by a constant to fit the common scale of the diagrams. LOI corresponds to H_2O + CO_2. Solid lines, representing the isocons are defined by the constant ratios of P_2O_5, assumed immobile. Elements above the isocons are enriched in the chloritized rock, whereas those below are depleted. Grey fields highlight the elements which usually display immobile behaviour in hydrothermal systems (Ti, Al, P, Ta, Nb, Y, Zr, Hf, Th and the HREE). Diagrams are shown for three sample sets. I51 vs R80 (**A**) are very large, matched wallrock samples. The other sets (**B-C** and **D-E**) are based on three adjacent slabs, representing the transition from a fresh precursor (R432-C granite or D1M-61D granodiorite) to an increasingly chloritized rock (R432-B and A, D1M-61C and B, the last samples being the most altered).

95

A - strong chloritization of granite
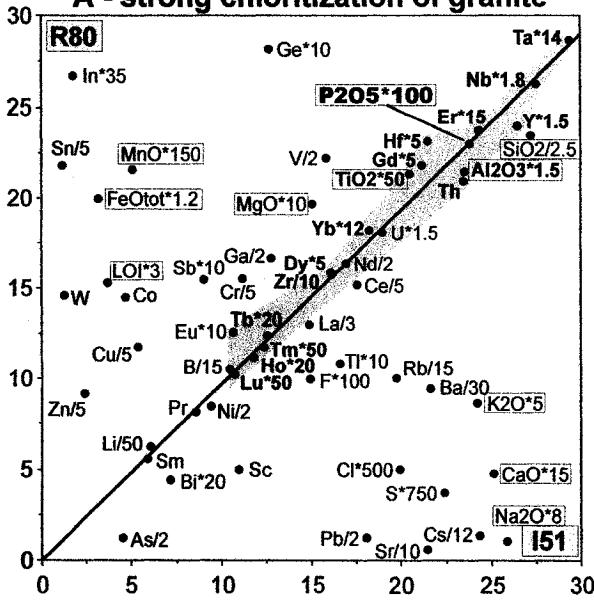
B - incipient chloritization of granite
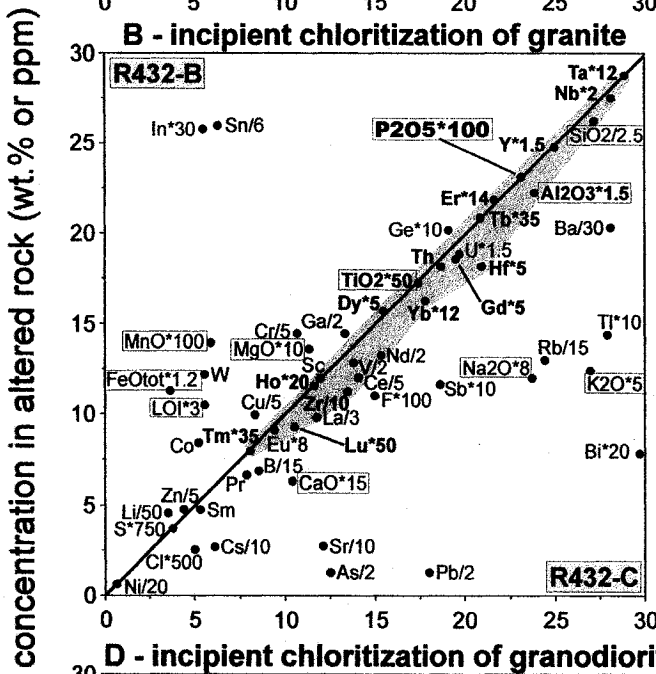
C - strong chloritization of granite
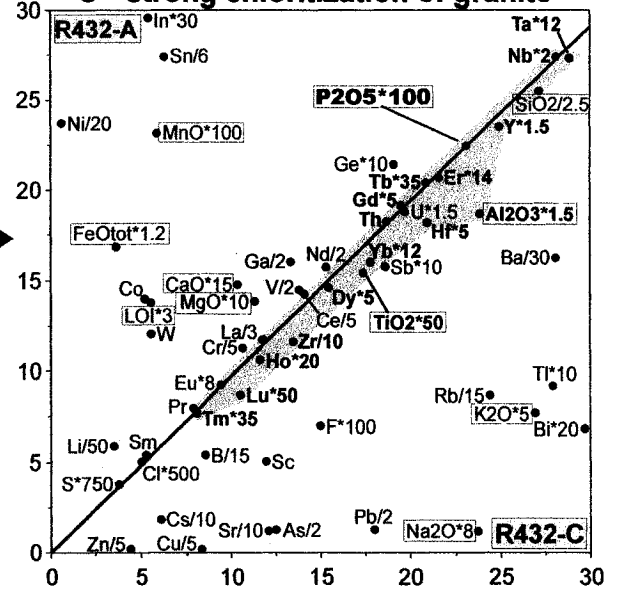
D - incipient chloritization of granodiorite
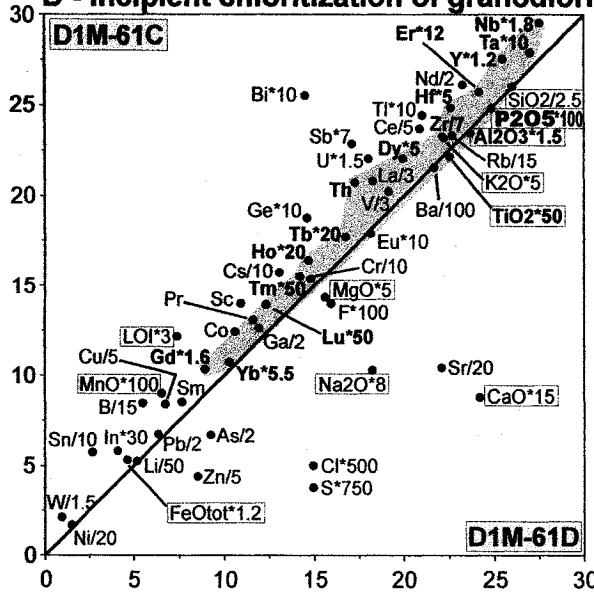
E - strong chloritization of granodiorite

concentration in altered rock (wt.% or ppm)
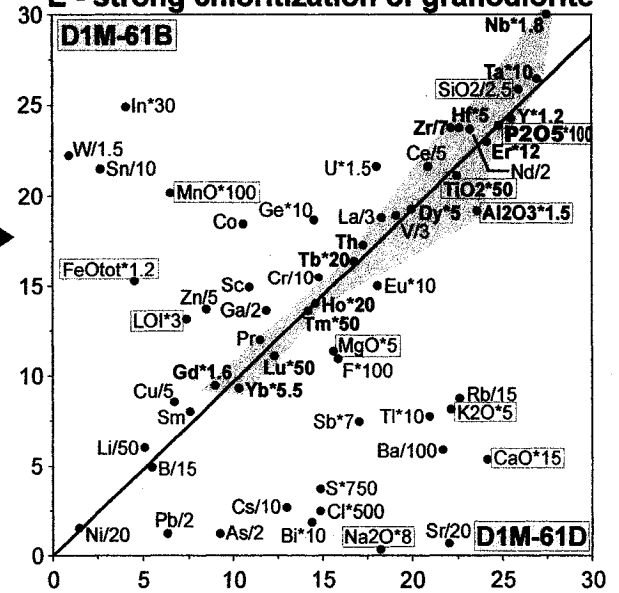
concentration in precursor (wt.% or ppm)

subsequent calculations. Titanium was excluded as there is minor petrographic evidence for its local remobilization during chloritic alteration (chloritized biotite crystals free of rutile and the local presence of interstitial rutile). By contrast, the host of P, apatite, is very well preserved even in strongly chloritized samples. In addition, the concentration range of P in the granitoid suite is very narrow and its values are sufficiently high to allow for an accurate analysis (0.19-0.26 wt.% P_2O_5).

Figure 17 shows that strong, pervasive chloritic alteration is typically associated with a total mass gain of ~ 3.5-4.5 %, due mainly to the addition of Fe, which produced a dark green coloration of the rocks. The gain in iron was of the order of 250-560 % (Fig. 18, Tab. 6), mostly in the ferrous form. In general, the three sample sets analysed predict very similar mass changes; the minor discrepancy shown by Figure 17D is probably related to the smaller size of this sample. It is also clear that granite and granodiorite behaved similarly during chloritic alteration. The elements Si, Ta, Nb, P, Ti, Th, Y, Zr were largely immobile and there was a minor but consistent loss in Al. The elements Na, K, Ca, Ba, Rb, Sr, Cs, F, Cl, S, As, Bi, Tl and Pb were effectively removed from the rock, whereas there were large gains in Fe, Mn, H_2O (LOI), Sn, W and In. It should be noted that the gain in tin was as high as 4 to 20-fold, whereas that of tungsten was 2 to 25-fold and that of indium 5 to 16-fold, suggesting a similar behaviour of these elements during chloritic alteration. By contrast, the concentration of boron (the bulk of which is in disseminated tourmaline from earlier alteration) was not affected by chloritization. Finally, it should be noted that the mass changes associated with main stage chloritization are remarkably similar to those of the early, pre-ore chloritization (recorded by sample D4-68).

Mass changes of REE

Chondrite-normalized plots of rare earth element concentrations (corrected for mass change) for fresh and altered granitic rocks are presented in Figure 19. All but one of the fresh granitoids have very similar, highly fractionated REE profiles, with a small negative europium anomaly. These profiles are similar to those reported by Kontak and Clark (1988, 2002) for mid-Tertiary granitoid rocks of SE Peru. From Figure 19 and Table 6, it is apparent that neither strong chloritic alteration nor weak sericitization produced

FIGURE 18. Gains and losses of major and trace elements during chloritic alteration. The values have been calculated assuming that phosphorus is immobile (see also Table 6) and correspond to the isocon diagrams of Fig. 17. The last two sets of histograms represent two stages of increasing chloritization, the grey columns corresponding to incipient alteration and the thick, black ones to strong chloritization.
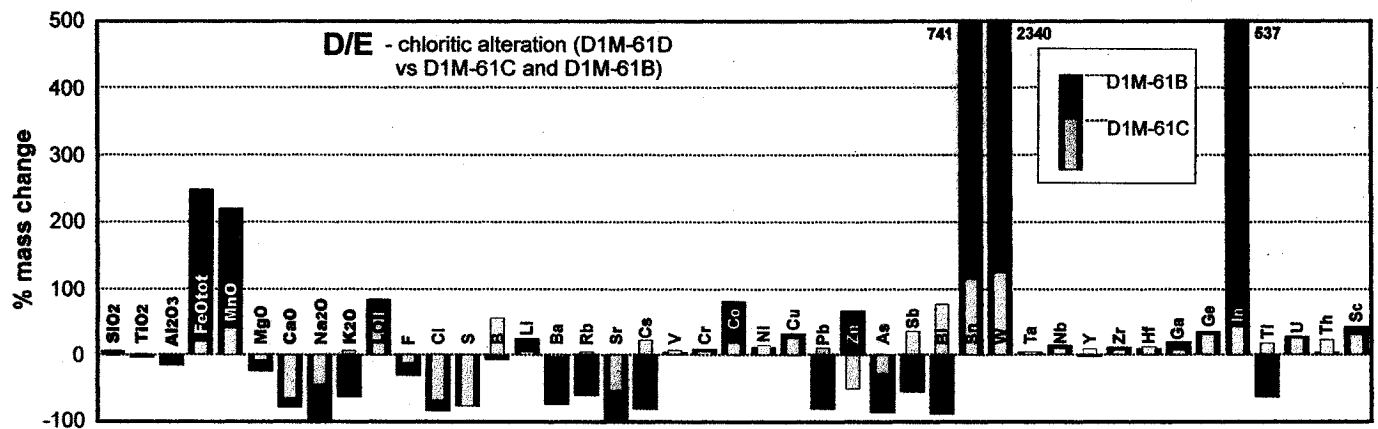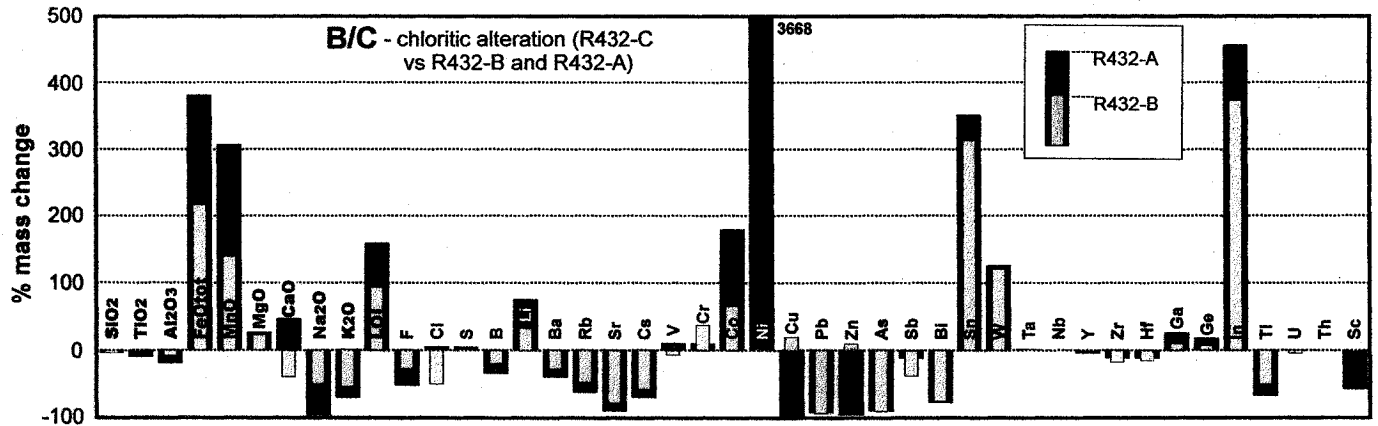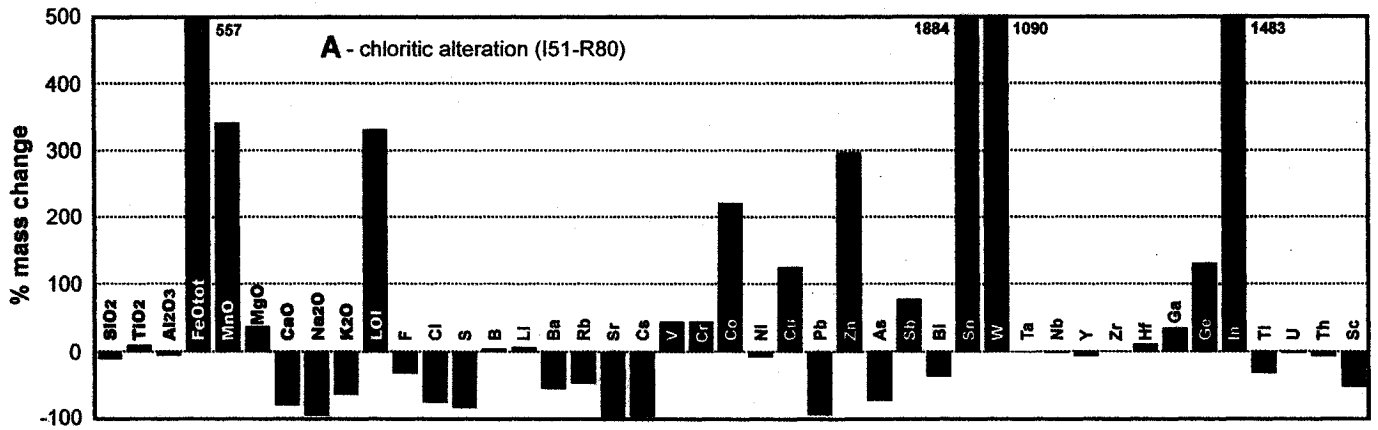
FIGURE 19. Chondrite-normalized plots of REE concentrations (corrected for mass change) for fresh and altered granitic rocks from San Rafael. Chondrite reference values are from Taylor and McLennan (1985).

Fresh granitoids

D1M-61D
D4-443
I8
I51
R566
I20
R432C

A

Sericitized / tourmalinized granitoids

D5-2
J26-B
J26-A
D5-138
I45

B

Chloritized granitoids

D1M-61C
D1M-61B
R80
R432A
R432B

C

La Ce Pr Nd Sm Eu Gd Tb Dy Ho Er Tm Yb Lu

Rock / chondrite
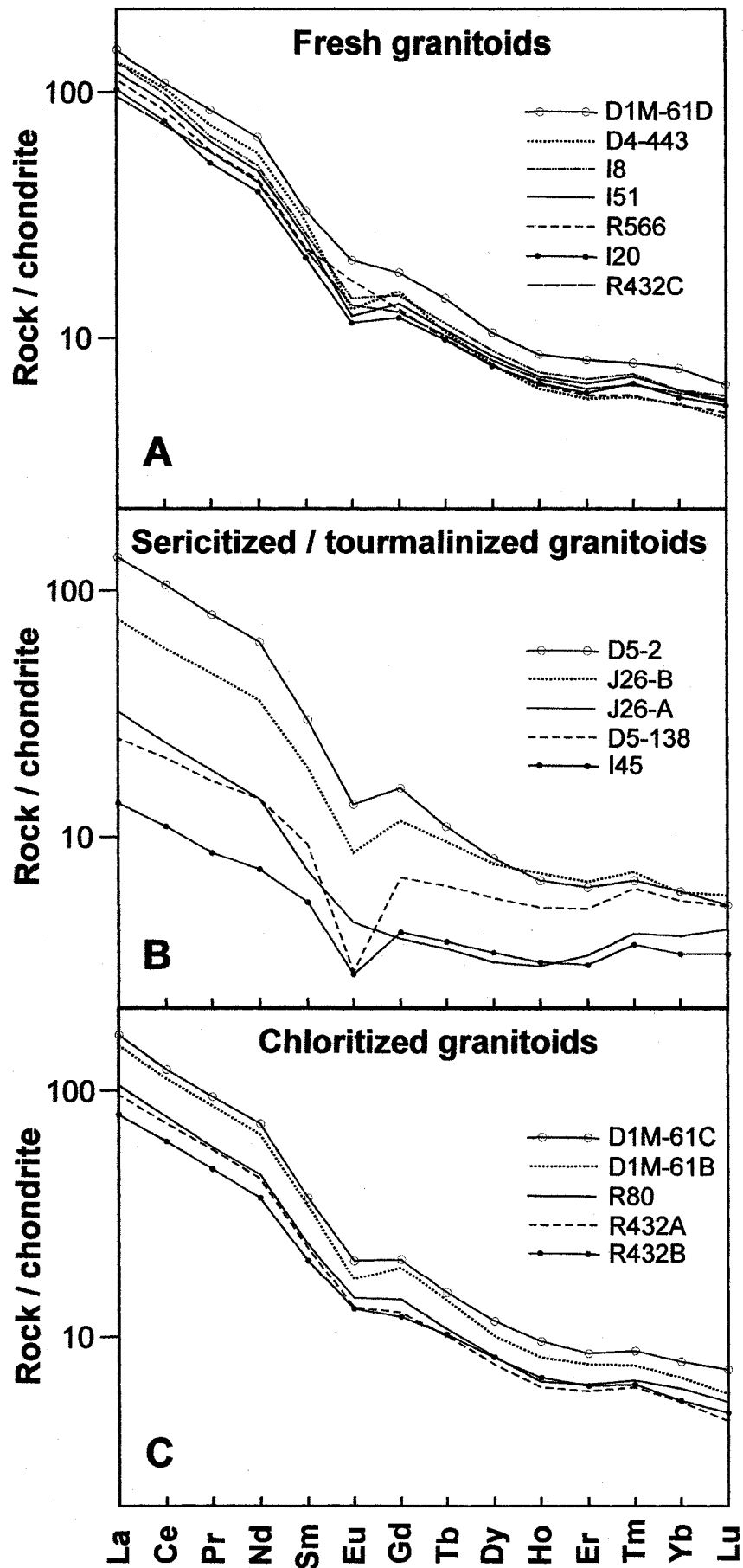
significant mass change of rare earth elements. By contrast, tourmalinization ± strong sericitization led to a major loss of light and medium REE, and strong tourmalinization to a loss of heavy REE as well. In the case of the latter (sample I45) >80 % LREE and >40 % HREE were removed from the rock (Tab. 6). In addition, tourmaline alteration was accompanied by a more pronounced europium anomaly, implying that Eu was largely removed.

Changes in normative mineralogy during alteration

The change in normative mineral composition during alteration was calculated for three sample sets, representing the main alteration types of the deposit: the multiply-zoned alteration envelope of a tourmaline vein (samples D4-68 and D4-94, 5 slabs, Fig. 4B); a pair of matched samples: unaltered granite (sample I8) plus a representative sericite-tourmaline alteration halo of a large quartz-tourmaline vein (sample J26, 2 slabs, Fig. 4A); and the chloritic envelope of a main-stage quartz vein (sample R432, 3 slabs). All the samples were studied in thin section and their mineral assemblages analysed by electron microprobe. It was found that, except for sericite in sample D4-68, there was no significant change in the composition of the minerals across the alteration haloes. The mass changes for the sets of samples are shown in Figures 14-18 and listed in Tables 5-7.

Mineral proportions were calculated for each of the slabs by least-square approximation to an over-determined set of mass-balance equations (Bryan et al. 1969), using our own Pascal code. For each slab, the procedure involves solution of a set of linear equations, $[y]=[A]\cdot[x]$, where $[y]$ is the vector of bulk composition, $[A]$ is a matrix of mineral compositions and $[x]$, the unknown, is the vector of mineral proportions. The mineral compositions used were averages of microprobe analyses, except for the plagioclase, which displays marked chemical zoning. Plagioclase was, therefore, represented by its end-members, albite and anorthite, which were calculated independently. The quality of the fit was evaluated, according to the departure of the mineral total from 100% and from the sum of residual squares between the actual and the calculated whole-rock composition. The calculations yielded whole-rock totals between 97.3-101 wt.%; R^2 = 0.003-2.880. The calculated mineral modes, normalized to 100% are

given in Table 8. The values for fresh granites (R432C and I8) compare very well with the mineral modes of Palma (1981), obtained by staining thin sections of granite. Similarly, the mineral proportions calculated for the altered rocks are in very good agreement with the visual estimates of the proportions from thin section petrography.

The calculated mass changes and the mineral proportions of individual slabs, were used in turn to calculate average rock density and the change in volume associated with alteration. This was achieved assuming a starting mass of 100 g of the precursor rock and adjusting it, together with the masses of the constituent minerals, by the mass change factor calculated for each slab. The masses of the minerals in each slab were divided by their respective densities (derived from molar volume data compiled by Holland and Powell, 1998), in order to calculate their volumes, which added together produced the total volume of the altered slab (Tab. 8). The calculated density (in g/cm^3) is given in Table 8 and the volume change for each slab (expressed as % volume of the fresh rock) is shown in Figure 20.

It can be inferred that the alteration envelopes of early tourmaline ± quartz veins (i.e., samples J26 and D4-68) show a broadly similar evolution, characterized by the massive formation of sericite (30-40 wt.% of the rock), followed by tourmaline (20-45 wt.%). In addition, results for sample D4-68 indicate that, at least locally, strong chloritization (up to 32 wt.% chlorite) preceded sericitization and that silicification (~20 wt.% quartz added) accompanied or was superimposed on tourmalinization. Also, we note that there were two episodes of sericitization: one at the onset of alteration and another following chloritization. However, the early sericite has a significant aluminoceladonite component, whereas the later sericite is closer to muscovite in composition.

The main-stage chloritization had a much simpler evolution. Sericite formation (22 wt.%) accompanied incipient chloritization, and then was replaced by chlorite (~ 43 wt.%), the only alteration mineral apart from quartz. The simplicity of this final alteration assemblage (chlorite + quartz) is remarkably similar to that of the pre-ore alteration (tourmaline + quartz), suggesting that the variance increases with fluid/rock ratio. Thus, a high-variance assemblage (few minerals) is fluid-buffered, i.e., the number of intensive components increases (they are introduced from the fluid), whereas a low-variance

TABLE 8. Calculated mineralogical compositions (in wt.%, normalized to 100 %), rock densities, mass / volume changes (using the mass / volume of the precursor as a reference) for the alteration profiles shown on Fig. 20.

Precursor and alteration	~ Fresh granite	Moderate chloritic	Strong chloritic	Fresh granite	Sericitic & tourmaline	Strong tourmaline	~ Fresh tonalite	Sericitic & chloritic	Strong chloritic	Sericitic & tourmaline	Tourmaline & silicic
Sample	**R432C**	**R432B**	**R432A**	**I 8**	**J26-B**	**J26-A**	**D4-68E**	**D4-68D**	**D4-68C**	**D4-68B**	**D4-94**
Modal mineralogy (wt.%)											
Quartz	**23.94**	40.70	54.98	**23.22**	52.43	55.98	**29.42**	41.51	43.19	53.35	79.11
Apatite	**0.26**	0.67	1.35	**0.53**	0.69	0.41	**0.62**	0.82	0.64	0.63	0.38
Rutile	**0.01**	0.29	0.28	**0.03**	0.37	0.24	**0.00**	0.54	0.48	0.39	0.41
Chlorite	**0.00**	24.91	43.40	**0.00**	0.00	0.00	**0.00**	17.23	32.52	1.52	0.00
Sericite	**0.00**	21.87	0.00	**0.00**	31.67	0.00	**15.47**	39.90	23.18	38.45	0.00
Albite	**17.57**	11.55	0.00	**18.02**	0.00	0.00	**19.88**	0.00	0.00	0.00	0.00
Anorthite	**3.21**	0.00	0.00	**8.62**	0.00	0.00	**5.87**	0.00	0.00	0.00	0.00
Biotite	**10.29**	0.00	0.00	**12.44**	0.00	0.00	**19.51**	0.00	0.00	0.00	0.00
Cordierite	**9.61**	0.00	0.00	**5.49**	0.00	0.00	**0.00**	0.00	0.00	0.00	0.00
K-spar	**35.10**	0.00	0.00	**31.65**	0.00	0.00	**9.24**	0.00	0.00	0.00	0.00
Tourmaline	**0.00**	0.00	0.00	**0.00**	14.84	43.37	**0.00**	0.00	0.00	5.66	20.09
Mineral modes (cm3)											
Quartz	**24.14**	41.17	57.21	**23.58**	50.37	60.33	**30.65**	42.07	46.93	58.52	95.43
Apatite	**0.22**	0.56	1.15	**0.44**	0.54	0.36	**0.52**	0.68	0.57	0.56	0.38
Rutile	**0.01**	0.18	0.18	**0.02**	0.22	0.16	**0.00**	0.34	0.32	0.26	0.31
Chlorite	**0.00**	21.06	37.75	**0.00**	0.00	0.00	**0.00**	14.59	29.53	1.39	0.00
Sericite	**0.00**	20.53	0.00	**0.00**	28.25	0.00	**14.96**	37.54	23.37	39.15	0.00
Albite	**17.78**	11.73	0.00	**18.36**	0.00	0.00	**20.78**	0.00	0.00	0.00	0.00
Anorthite	**3.07**	0.00	0.00	**8.29**	0.00	0.00	**5.79**	0.00	0.00	0.00	0.00
Biotite	**8.91**	0.00	0.00	**10.85**	0.00	0.00	**17.45**	0.00	0.00	0.00	0.00
Cordierite	**9.66**	0.00	0.00	**5.56**	0.00	0.00	**0.00**	0.00	0.00	0.00	0.00
K-spar	**36.22**	0.00	0.00	**32.89**	0.00	0.00	**9.84**	0.00	0.00	0.00	0.00
Tourmaline	**0.00**	0.00	0.00	**0.00**	13.65	44.75	**0.00**	0.00	0.00	5.95	23.21
Total volume (cm3)	**100.00**	95.22	96.28	**100.00**	93.04	105.60	**100.00**	95.23	100.72	105.84	119.33
Total mass (g)	**100.00**	100.30	103.20	**100.00**	94.60	106.10	**100.00**	97.30	104.30	105.30	115.80
Density (g/cm3)	**2.62**	2.76	2.81	**2.64**	2.69	2.66	**2.71**	2.77	2.81	2.70	2.63
Volume change (% vol precursor)		-4.78	-3.72		-6.96	5.60		-4.77	0.72	5.84	19.33

FIGURE 20. Variation in normative mineralogy (vol.%) across the three most representative of the alteration profiles studied. Alteration progresses from left to right (see text for details). Apatite and rutile concentrations are typically < 1 vol.%.

Top figure:

~ Fresh Tonalite → Sericitization (1) →

Chloritization →

Sericitization (2) → Silicification →

Tourmalinization →

Vol. %

- D4-68E: Sericite, Biotite, K-spar, Anorthite, Albite, Quartz
- D4-68D (95.2): Chlorite, Sericite, Quartz
- D4-68C (100.7): Chlorite, Sericite, Quartz
- D4-68B (105.8): Tourmaline, ~Chlorite, Sericite, Quartz
- D4-94 (119.3): Tourmaline, Quartz

Bottom-left figure:

Fresh Granite → Sericitization → Tourmalinization →

Vol. %

- J8: Biotite, Cordierite, K-spar, Anorthite, Albite, Quartz
- J26-B (93.0): Tourmaline, Sericite, Quartz
- J26-A (105.6): Tourmaline, Quartz

Bottom-right figure:

~ Fresh Granite → Chloritization →

Vol. %

- R432C: Biotite, Cordierite, K-spar, Anorthite, Albite, Quartz
- R432B (95.2): Chlorite, Sericite, Albite, Quartz
- R432A (96.3): Chlorite, Quartz

assemblage is rock-buffered (these components are extensive, i.e., they are part of the system).

An important conclusion that can be drawn from the calculations of volume change is that there was significant porosity creation at the onset of both early and main-stage alteration (the rock volume decreased by up to 7 % during the initial sericitic alteration). However, with the progress of alteration this changed and during advanced tourmalinization the volume of the rock actually increased by at least 6 %, with respect to the unaltered rock, in order to accommodate the additional mass (Fig. 20). Strong chloritic alteration was characterized by only a minor volume decrease (~ 3-4 %), with respect to the original rock, an observation supported by the fact that outlines of the replaced rock-forming minerals (alkali-feldspars, plagioclases, cordierite, biotite) commonly retain their original crystal shape. The early creation of porosity is, nevertheless, considered important, as it would have facilitated the progress of alteration, by promoting the flux of metasomatic fluids through the rock and may also have enhanced mineralization, by facilitating fracture porosity.

DISCUSSION

The San Rafael lode is characterized by a uniform development of alteration, for all the 1,200 m of its vertical extent. This indicates that the hydrothermal system, which produced this alteration and the associated tin-copper mineralization was large and relatively homogenous for a protracted period of time. The lode development took place in two major stages, characterized by distinctive alteration types, summarized in Table 9 and discussed in detail below.

Early, sericitic and tourmaline alteration

The early, pre-ore alteration consisted of generally weak chloritization, followed by spatially extensive, strong sericitization and a narrower zone of strong tourmalinization, enveloping tourmaline-quartz veins. This sequence resembles very much the evolution of borosilicate systems reproduced experimentally by Fuchs and Lagache (1994). These

103

TABLE 9. Summary of the paragenetic evolution of the San Rafael deposit, following

the subdivision proposed by Palma (1981).

Alteration stage	I			II	III	IV
Alteration type	(chloritic)	sericitic	tourmaline	chloritic		
Mineral assemblage	chl,qtz ± ser	ser,qtz ± tur	tur,qtz	chl,qtz		
Elements added	Fe,Mn,H_2O,Sn,W,In	Fe,Mn,H_2O,As,Sb,Bi,W	B,Mg,Fe,Sn,W,In,Ge,Bi	Fe,Mn,H_2O,Sn,W,In ± Mg		
Elements removed	Na,K,Ca,Ba,Rb,Sr,Cs,F,Cl	Na,Ca,Ba,Sr,F,Cl	Na,K,Ca,Ba,Rb,Sr,Cs,Li,Cl	Na,K,Ca,Ba,Rb,Sr,Cs,F,Cl		
Cassiterite	traces (?)	absent	traces	very abundant	subordinate	absent
Sulfides	absent	minor (asp)	minor (asp)	absent	very abundant (cpy,po,asp,py)	traces
Temperature	400-530°C			280-380°C		230-280°C
Fluid salinity	34-62 wt.% NaCl eq.			0-21 wt.% NaCl eq.		0-3 wt.% NaCl eq.
Pressure estimate	~700 bars			~300 bars, probably fluctuating		
fO_2 estimate	relatively low			variable, but increasing with time		

authors investigated the influence of boric acid on a mixture of alkali-feldspar and chlorite, contained in sealed gold tubes, in the temperatrure range 400-700°C. They observed that, with progress of the alteration, the mineral assemblage evolves from chlorite + Ca-borosilicates, to phengitic sericite + tourmaline and, finally, dumortierite (± pyrophyllite, andalusite). Similar alteration zoning was also described for a number of U-Mo-Zn and Ag-Au deposits (Fuchs and Lagache, 1994; Fuchs and Maury, 1995).

On the basis of preliminary fluid inclusion data, we interpret the fluids responsible for the early alteration to have been very hot (400-530°C) and highly saline (34-62 wt.% NaCl eq.), thus likely of a magmatic origin. The whole rock chemical data reported earlier indicate that these fluids introduced significant Mg and Fe, in addition to B, and removed large amounts of alkalis and alkali-earth elements.

In order to better constrain the physicochemical conditions that prevailed during this stage, a detailed analysis of the phase equilibria among the alteration minerals is necessary. Figures 21A,B illustrate mineral stability relations on $\log(a\text{K}^+/a\text{H}^+)$ and $\log(a\text{Na}^+/a\text{H}^+)$ versus $\log(a\text{Mg}^{2+}/a^2\text{H}^+)$ diagrams. For their construction, the pressure was taken to be 700 bars, assuming a depth of emplacement of the pluton of ~ 2.5 km and lithostatic conditions. The latter assumption is consistent with the absence of open-fracture filling in the tourmaline veins and with the results of preliminary fluid inclusion microthermometry (Mlynarczyk and Williams-Jones, in prep.). The hydrothermal fluid was assumed to have been saturated in quartz, which is ubiquitous in tourmaline veins and breccias, and Al was considered immobile (as one of the least mobile elements). The activities of all minerals were calculated from microprobe analyses, by using appropriate solid-solution models, except for K-feldspar, which is very close to pure $KAlSi_3O_8$. The details of the thermodynamic calculations are listed in Appendix-II.

The occurrence of muscovite in the alteration assemblage constrains the $a\text{K}^+/a\text{H}^+$ ratio of the sericitizing fluid to between $10^{3.4}$ and $10^{3.7}$, while its coexistence with chlorite indicates that the $a\text{Mg}^{2+}/a^2\text{H}^+$ ratio was close to $10^{4.4}$ at the onset of alteration (Fig. 21A). The subsequent formation of dravite tourmaline (Fig. 21B) was associated with an increase in the activity of H_3BO_3, the predominant borate species at these conditions (Lynch and Ortega, 1997) to above 10^{-3}, which corresponds to a concentration of > 0.01 m. This was accompanied by a slight expansion in the stability field of muscovite, due to

FIGURE 21. Activity-activity diagrams for the early, sericite-tourmaline alteration (**A,B**) and chloritic alteration associated with tin mineralization (**C,D**). The activities of alteration minerals were calculated from microprobe data, except for the feldspars and andalusite, which were assumed to have end-member compositions (Appendix-II). For the purpose of balancing the chemical reactions, Al was considered immobile.

A — T=500°C, P=700 bar, Quartz saturation, aH₂O=0.419 (45 wt.% NaCl eq.)

K-feldspar

Muscovite

a_{Ms}=0.547

a_{Ms}=0.38

Andalusite

Biotite (phl$_{50}$ ann$_{50}$)

Chlorite (clin$_{30}$ daph$_{70}$)

log(aK⁺/aH⁺)

log(aMg²⁺/a²H⁺)

B — T=500°C, P=700 bar, Quartz saturation, aH₂O=0.419 (45 wt.% NaCl eq.), aK⁺/aH⁺=10³·⁴⁴, adravite=0.1

Albite

a_{Ms}=0.38

a_{Ms}=0.547

0.0030 0.0020 0.0013

Dravite

Chlorite (clin$_{30}$ daph$_{70}$)

Muscovite

Biotite (phl$_{50}$ ann$_{50}$)

log(aNa⁺/aH⁺)

log(aMg²⁺/a²H⁺)

C — T=380°C, P=300 bar, Quartz saturation, aH₂O=0.744 (20 wt.% NaCl eq.)

K-feldspar

Muscovite

a_{Ms}=0.517

Andalusite

Biotite (phl$_{50}$ ann$_{50}$)

Chlorite (clin$_{30}$ daph$_{70}$)

log(aK⁺/aH⁺)

log(aFe²⁺/a²H⁺)

D — T=380°C, P=300 bar, Quartz saturation, aH₂O=0.744 (20 wt.% NaCl eq.), aK⁺/aH⁺=10²·⁴, aSchorl=0.4

Albite

0.1 0.2

a_{H3BO3}=0.6

Schorl

Muscovite

a_{Ms}=0.517

Chlorite (clin$_{30}$ daph$_{70}$)

Biotite (phl$_{50}$ ann$_{50}$)

log(aNa⁺/aH⁺)

log(aFe²⁺/a²H⁺)

its depletion in K and resulting activity decrease. However, the more important observation is that the formation of dravite impinges on the stability of albite, muscovite and chlorite at $a\mathrm{Na}^+/a\mathrm{H}^+ \sim 10^{4.2}$ and $a\mathrm{Mg}^{2+}/a^2\mathrm{H}^+ \sim 10^{4.4}$, i.e., with increasing a_{H3BO3} it will replace these minerals, and above $a_{\mathrm{H3BO3}} = 2 \cdot 10^{-3}$ it will replace biotite. If the concentration of boric acid in the fluid is high enough (e.g., > 0.1 m) all the primary minerals in the granite will be tourmalinized, except quartz and certain accessory minerals.

The large amount of tourmaline characteristic of the early paragenesis of the San Rafael deposit raises the obvious question of the source of boron. The peraluminous granitic suite of San Rafael is conspicuous by its lack of magmatic tourmaline and appreciable concentrations of biotite, cordierite, and garnet. Since these latter ferromagnesian minerals convert to tourmaline in boron-rich granitic melts (London 1999), their presence in the intrusion implies that the activity of boron in the melt must have been very low (negligible), and that the granite is unlikely to have been a significant source of boron. These fluids were probably derived from another source. A possible candidate for this could be the magma feeding rare, late-stage dykes of tourmaline leucogranite in the NE part of the district. This evolved melt could have provided the bulk of the boron, whereas most Fe and Mg present in tourmaline was likely derived from igneous phases in the main pluton (Fig. 15).

Mass-balance calculations indicate that early sericite-tourmaline alteration was associated with a substantial (2 to 7-fold) increase in the concentration of Sn, W and In (Fig. 15, Tab. 6). However, the absolute addition of these elements was negligible, e.g., 20-90 ppm in the case of tin. By contrast, some tourmalinites worldwide have very high contents of these elements (e.g., vein tourmalinites from granite-associated polymetallic tin deposits in northern Guangxi province, China, contain 11500-21900 ppm Sn (Jingwen, 1995). In principle, the high salinity of the early fluids at San Rafael should have enabled them to transport high concentrations of tin, as Sn^{2+} forms stable aqueous complexes with Cl^- (Müller and Seward, 2001). It is thus possible that they failed to saturate with cassiterite because temperature was too high and the pH and $f\mathrm{O}_2$ too low.

Chloritic alteration and cassiterite deposition

As indicated by mass-balance calculations, the chloritizing, ore-bearing fluid brought in large amounts of Fe, Mn and H_2O, and removed alkalis and alkali-earth elements from the wall rock. In this respect, it is similar to chloritizing fluids from other deposit types, e.g., those in some unconformity-type uranium deposits (Jabiluka, Australia; Nutt, 1989) or in volcanogenic massive-sulfide deposits (Phelps Dodge, Canada, Kranidiotis and MacLean, 1986; 1987). A significant difference presented by chloritic alteration at San Rafael is, however, the concurrent tin enrichment, as well as the fact that leaching of quartz was very limited and chloritites did not form.

At San Rafael, interestingly, both the very early and the main-stage chloritization were associated with a marked (5 to >20-fold) enrichment in Sn, W and In. These three elements display a geochemical behaviour, which closely matches that of Fe and Mn, and attained their highest concentrations during this alteration (Fig. 16-18, Tab. 5-7). The Sn concentrations (110-215 ppm) are, however, clearly uneconomic and the bulk of cassiterite in the deposit is restricted to breccias, veins, and systems of veinlets, as opposed to being disseminated in the chloritic alteration. This implies a strong structural control on the localization of ore, and suggests that changing conditions in the fluid conduits played a much more important role in tin deposition than the fluid-rock interaction.

The apparent unimportance of fluid-rock interaction in Sn deposition at San Rafael is consistent with the observation that chloritic alteration of granitic wall rock generates H^+, i.e., increases the fluid acidity, and that this in turn increases Sn solubility. The former is illustrated by the irreversible reaction:

$$CaAl_2Si_2O_8 + 7\ NaAlSi_3O_8 + 13\ KAlSi_3O_8 + 2\ Mg_2Al_4Si_5O_{18} + 2\ KFe_3AlSi_3O_{10}(OH)_2 +$$

(anorthite)   (albite)   (K-feldspar)   (cordierite)   (annite)

$$+ 29\ Fe^{2+} + H_4SiO_4{}^0 + 64\ H_2O\ \rightarrow\ 7\ Fe_5Al_2Si_3O_{10}(OH)_8 + 58\ SiO_2 + 15\ K^+ + 7\ Na^+ +$$

(chamosite)   (quartz)

$$+ Ca^{2+} + 4\ Mg^{2+} + 18\ Al(OH)_3{}^0 + 26\ H^+$$
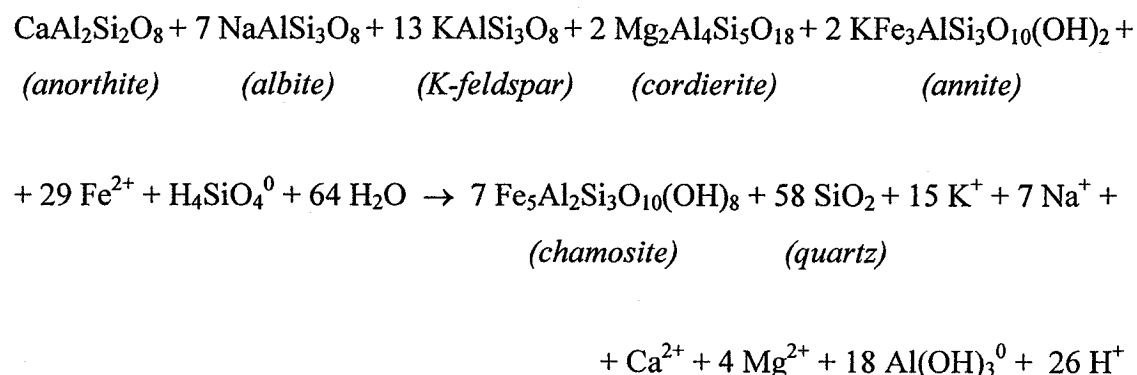
(based on the analysis of unaltered San Rafael granite sample R432C and chloritized granite sample R432A, Table 8), and the latter by the reaction:

$$SnCl_x^{2-x} + 2H_2O = SnO_{2(s)} + 2H^+ + xCl^- + H_2°$$ (Heinrich, 1990)
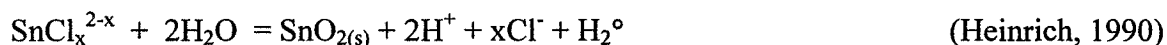
The mineral assemblage characterizing main-stage chloritic alteration is very simple, being composed principally of Fe-rich chlorite and quartz, with trace amounts of (coeval) Fe-rich tourmaline and, locally, epidote, allanite, titanite or carbonates. Figure 21C,D presents the mineral stability relations on $\log(aK^+/aH^+)$ and $\log(aNa^+/aH^+)$ versus $\log(aFe^{2+}/a^2H^+)$ diagrams. The ore fluid temperature was ~380°C, while the salinity was ~ 20 wt.% NaCl eq., based on fluid inclusion microthermometry (Mlynarczyk et al., 2003). The pressure was assumed to be 300 bars, close to hydrostatic conditions, as inferred from the open-fracture filling character of the cassiterite-quartz-chlorite veins. Nevertheless, the ore-fluid pressure is thought to have fluctuated greatly, since crack-and-seal textures are a common feature of the mineralized veins (*cf.* Ramsay, 1980). The ore fluid was assumed to have been saturated in quartz throughout the chloritization, as quartz phenocrysts from the original granitic rocks are typically preserved in the strongly chloritized wall rock and quartz is the principal constituent of the ore veins. Finally, in writing the chemical reactions, Al was assumed to be immobile, and mineral activities were calculated from microprobe analyses, except for the feldspars, which were assumed to have end-member compositions (see Appendix-II).

As can be seen in Figure 21C, the stability field of muscovite is much larger at the lower-temperature conditions of the tin ore stage than during the early alteration, and spans a range of aK^+/aH^+ ratios between $10^{2.2}$ and $10^{3.9}$ (Fig. 21C). The coexistence of chlorite and sericite at the onset of this alteration further implies that aK^+/aH^+ ratios were between $10^{2.2}$-$10^{3.1}$, while aFe^{2+}/a^2H^+ was between $10^{3.8}$ and $10^{3.9}$. The formation of submicroscopic schorl overgrowths on early tourmaline, which coexist with Fe-rich chlorite implies an activity of $H_3BO_3 \geq 10^{-1}$, i.e., a concentration of $5\cdot10^{-1}$ m. Figure 21D indicates also that muscovite and plagioclase are much more prone to alteration by

tourmaline than chlorite, which is consistent with the apparently stable coexistence of the latter two minerals.

Figure 22A overlays contours of cassiterite solubility on the stability fields of the ore stage alteration minerals in log $(a\mathrm{Fe}^{2+}/a^2\mathrm{H}^+)$ – log $f\mathrm{O}_2$ space. The stability fields of Fe-rich chlorite and muscovite, as well as the contours of coexisting schorl for varying values of a_{H3BO3} (dotted lines) are truncated by the saturation boundaries of magnetite and hematite, which, as a rule, are absent from the ore assemblages. For the purpose of constructing the diagram, the pH of the ore fluid was assumed to be ~ 5, as in most chemical reaction-path calculations chlorite forms at a pH between 5 and 5.5 (Reed, 1997). The dominant tin complex at these conditions was determined to be SnCl_3^-, using the UNITHERM database (Shvarov and Bastrakov, 1999) and the data of Ryzhenko (1997), a conclusion in good agreement with the experimental data of Müller and Seward (2001). Calculations using the above information indicate that, in order for cassiterite to precipitate during formation of Fe-rich chlorite, quartz and subordinate schorl, $f\mathrm{O}_2$ needs to range between 10^{-35} and 10^{-30}, and the ratio of $a\mathrm{Fe}^{2+}/a^2\mathrm{H}^+$ between $10^{3.8}$ and $10^{4.6}$ (indicated as a grey ellipse in Figure 22A). It is also apparent that schorl is only stable when $a_{\mathrm{H3BO3}} > 0.2$ (which corresponds to a concentration > 1 m) and has a very narrow stability field, impinging on the fields of muscovite and, to a lesser extent, chlorite. This explains very well the observed paucity of tourmaline in the ore-stage alteration and the abundance of chlorite. On the other hand, the very rarely observed association of cassiterite and chlorite with hematite (Fig. 4L) is best explained by a temperature decrease of the ore fluid, which has already deposited most of its dissolved tin (Fig. 22B). An important conclusion of the latter diagram, when compared to the preceding one, is that with progressive cooling of the ore fluid, the stability field of Fe-rich chlorite expands markedly, which explains why it is the principal alteration mineral of the ore and post-ore stages in the deposit.

Finally, it is interesting to note that the isocon diagrams in Figure 17 indicate that strong, main-stage chloritization was associated with a moderate to strong depletion of sulfur. This suggests that during tin deposition the ore solutions were undersaturated with sulfides, an observation which is consistent with the absence of sulfides in this ore stage. Chalcopyrite, as well as other Cu-Fe-Zn-Pb sulfides precipitated relatively late in the

FIGURE 22. Log $(a\text{Fe}^{2+}/a^2\text{H}^+)$ vs. log $f\text{O}_2$ showing conditions of chloritic alteration, associated with main-stage tin mineralization (**A**) and for the locally observed association of cassiterite with chlorite and hematite (**B**). The activities of alteration minerals were calculated from microprobe data (see Appendix-II for details), except for the iron oxide phases (a=1). The chemical reactions were balanced assuming conservation of Al. The pH value of 5 (diagram A) was chosen as the average pH at which chlorite is present in alteration assemblages, as determined from examples of chemical reaction-path calculations from the literature (e.g., Reed, 1997). For diagram B, a slightly lower value pH of 4 was chosen, assuming that extensive chloritization of the wallrock would have locally acidified the ore fluid. The temperature for which diagram A is drawn was obtained from fluid inclusion microthermometry, whereas that for diagram B was chosen, so as to explain the coexistence between chlorite and hematite. The hashed, grey field in diagram A (superimposed on the fields of muscovite and chlorite) is the stability field of schorl at a_{H3BO3} = 0.6. Thermodynamic data for the tin species were taken from the UNITHERM database and the data of Ryzhenko (1997).

A
T=380°C
P=300 bar
Qtz saturation
$aH_2O=0.744$
(20wt.% NaCl eq.)
pH=5
$aK^+/aH^+=10^{2.4}$
$aNa^+/aH^+=10^3$
$a_{Schorl}=0.4$

Magnetite

Chlorite
(clin$_{30}$ daph$_{70}$)

Schorl

$aH3BO3=0.6$

Hematite

Muscovite
$a_{Ms}=0.517$

SnCl$_3^-$
SnO$_2$

0.1 ppm Sn

B
T=300°C
P=300 bar
Qtz saturation
$aH_2O=0.873$
(20wt.% NaCl eq.)
pH=4
$aK^+/aH^+=10^{1.7}$

Magnetite

Chlorite
(clin$_{30}$ daph$_{70}$)

Hematite

Muscovite
$a_{Ms}=0.517$

SnCl$_3^-$
SnO$_2$

0.01 ppm Sn
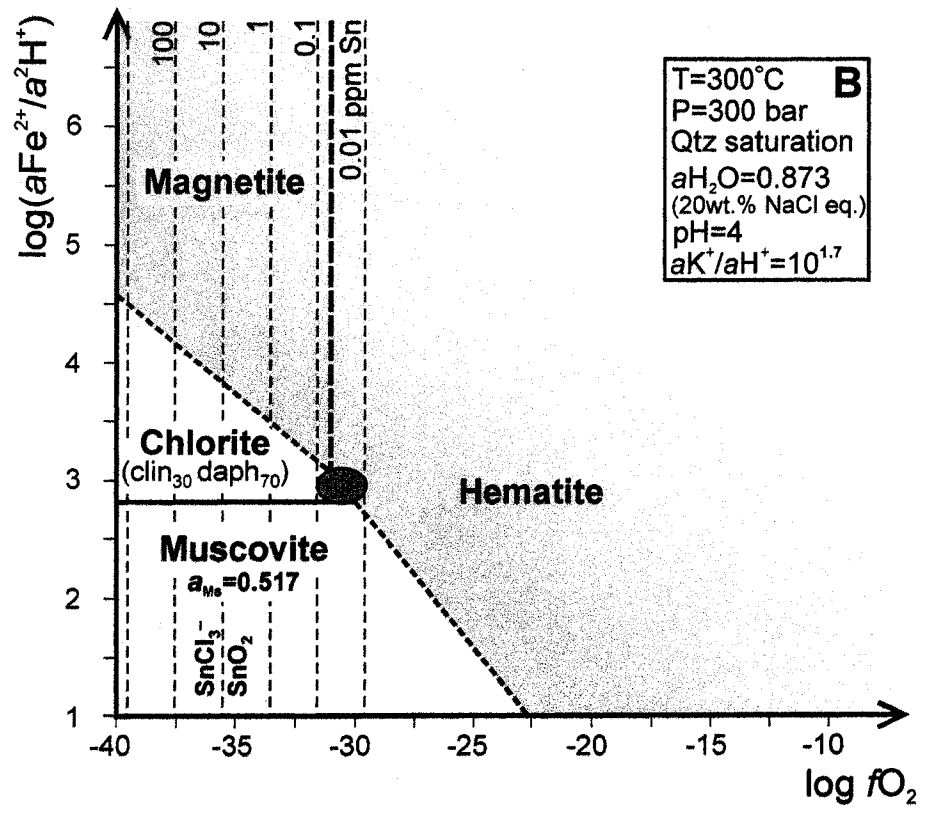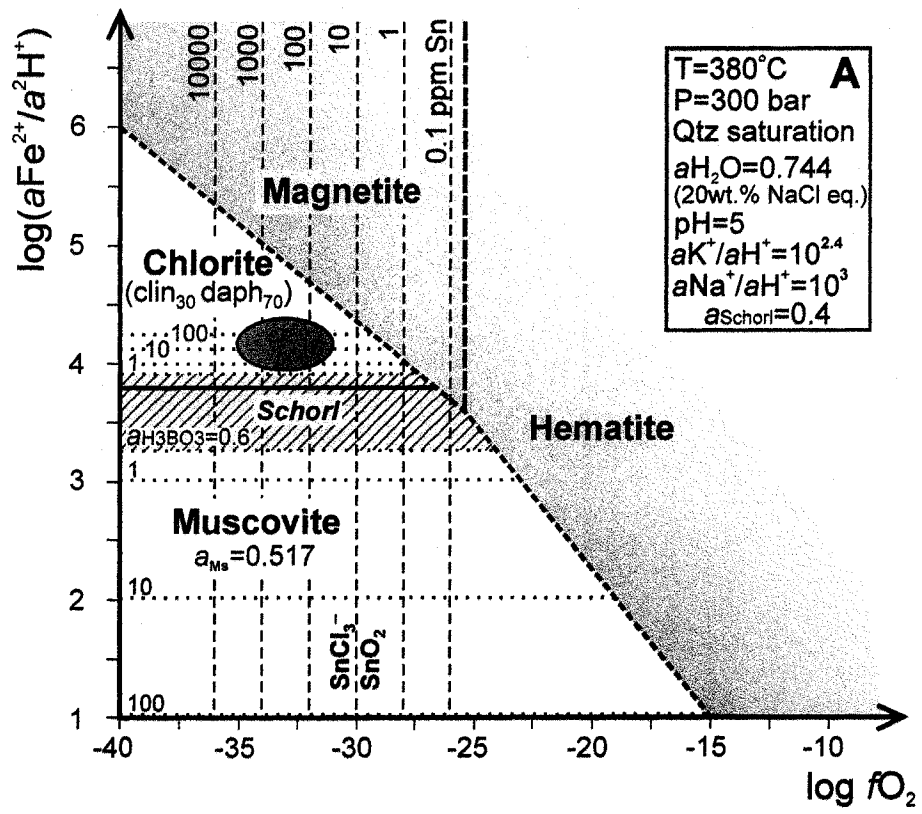
paragenesis (Tab. 9) and are mostly confined to the upper half of the deposit, although they too are associated with abundant chlorite. The temporal and spatial separation of tin and copper ores may reflect to some extent the progressive cooling of the ore fluid, but these two ore types likely formed by markedly different depositional mechanisms (*cf.* Mlynarczyk et al., 2003).

CONCLUDING REMARKS

The fundamental question which remains concerns the origin of the ore fluid. This fluid differed considerably from the hot magmatic brine responsible for the early sericite-tourmaline alteration: it was of moderate temperature and salinity, and produced a very strong Fe-metasomatism of the wall rocks. One possibility is that the ore fluid represented a separate fluid, presumably also magmatic, but derived from a later, highly fractionated granitic melt. Alternatively, the ore fluid could have evolved from the hypersaline magmatic brine by one or a combination of processes such as cooling, boiling, wall rock equilibration, or dilution. An important clue to its origin comes from the structural studies of the deposit, which suggest that the ore stage directly succeeded the early, barren stage, and that its onset coincided with the transition from a closed to an open system. It is, therefore, very likely that, in addition to boiling of the hypersaline brine, expected upon the transition from a lithostatic to a hydrostatic regime, there was also an influx of exotic (possibly meteoric) waters into the vein-breccia system. This last hypothesis is supported by preliminary fluid inclusion microthermometry, which indicates unequivocally that a marked dilution of the ore fluids (down to a salinity of 0 wt.% NaCl eq.) took place between stages II and IV, and was accompanied by moderate cooling (Mlynarczyk et al., 2003). Mixing of the magmatic brine with meteoric waters would also explain the co-precipitation of strongly iron-rich chlorite and tourmaline with cassiterite. Indeed, Kwak et al. (1996) suggest that dilution of a hypersaline, Fe-bearing brine is the most effective mechanism to decrease the solubility of Fe and explain the iron zoning present in many porphyry copper systems. Last but not least, an origin of the ore fluid by mixing of the early brine with dilute meteoric waters would provide a suitable mechanism for depositing the tin contained in the magmatic fluid, since the inherent dilution, cooling,

oxidation and pH increase, all favour cassiterite precipitation (Eugster and Wilson 1985; Pabalan 1986; Taylor and Wall 1993; Müller and Seward 2001).

REFERENCES

Ahlfeld, F., and Schneider-Scherbina, A., 1964, Los yacimientos minerales y de hidrocarburos de Bolivia: Departamento Nacional de Geologia (Bolivia), Boletin, v. 5 (Especial), 388 p.

Arenas, M.J., 1980, El distrito minero San Rafael, Puno - Estaño en el Peru: Boletin de la Sociedad Geologica del Peru, v. 66, p. 1-11.

Beane, R.E., 1994, A graphic view of hydrothermal mineral stabilities, *in* Lentz, D.R., ed., Alteration and alteration processes associated with ore-forming systems: Geological Association of Canada, Short Course Notes, v. 11, p. 1-30.

Bryan, W.B., Finger, L.W., and Chayes, F., 1969, Estimating proportions in petrographic mixing equations by least-square approximation: Science, v. 163, p. 926-927.

Cathelineau, M., 1988, Cation site occupancy in chlorites and illites as a function of temperature: Clay Minerals, v. 23, p. 471-485.

Chappell, B.W., and White, A.J.R., 1974, Two contrasting granite types: Pacific Geology, v. 8, p. 173-174.

Clark, A.H., Palma, V.V., Archibald, D.A., Farrar, E., Arenas, M.J., and Robertson, R.C.R., 1983, Occurrence and age of tin mineralization in the Cordillera Oriental, Southern Peru: ECONOMIC GEOLOGY, v. 78, p. 514-520.

Clark, A.H., Farrar, E., Kontak, D.J., Langridge, R.J., Arenas Figueroa, M.J., France, L.J., McBride, S.L., Woodman, P.L., Wasteneys, H.A., Sandeman, H.A., and Archibald, D.A., 1990, Geologic and geochronologic constraints on the metallogenic evolution of the Andes of southeastern Peru: ECONOMIC GEOLOGY, v. 85, p. 1520-1583.

Clark, A.H., Chen, Y., Grant, J.W., Kontak, D.J., Wasteneys, H.A., Sandeman, H.A., Farrar, E., and Archibald, D.A., 2000, Delayed inception of ore deposition in major lithophile-metal vein systems: The San Rafael tin and Pasto Bueno tungsten

deposits, Peru: Geological Society of America, Abstracts with Program, v. 32, p. 279.

Coggon, R., and Holland, T.J.B., 2002, Mixing properties of phengitic micas and revised garnet-phengite thermobarometers: Journal of Metamorphic Geology, v. 20, p. 683-696.

De Caritat, P., Hutcheon, I., and Walshe, J.L., 1993, Chlorite geothermometry: a review: Clays & Clay Minerals, v. 41, p. 219-239.

Eugster, H.P., and Wilson, G.A., 1985, Transport and deposition of ore-forming elements in hydrothermal systems associated with granites, *in* Halls, C., (chairman), High heat production (HHP) granites, hydrothermal circulation and ore genesis: Institution of Mining & Metallurgy, London, p. 87-98.

Farrar, E., Yamamura, B.K., Clark, A.H., and Taipe, J., 1990, $^{40}Ar/^{39}Ar$ ages of magmatism and tungsten-polymetallic mineralization, Palca 11, Choquene district, Southeastern Peru: ECONOMIC GEOLOGY, v. 85, p. 1669-1676.

Frost, B.R., Barnes, C.G., Collins, W.J., Arculus, R.J., Ellis, D.J., and Frost, C.D., 2001, A geochemical classification for granitic rocks: Journal of Petrology, v. 42, p. 2033-2048.

Fuchs, Y., and Lagache, M., 1994, La transformation chlorite-tourmaline en milieu hydrothermal, exemples naturels et approche expérimentale: Comptes Rendus de l'Académie des Sciences de Paris II, v. 319, p. 907-913.

Fuchs, Y., and Maury, R., 1995, Borosilicate alteration associated with U-Mo-Zn and Ag-Au-Zn deposits in volcanic rocks: Mineralium Deposita, v. 30, p. 449-459.

Fuhrman, M.L., and Lindsley, D.H., 1988, Ternary-feldspar modeling and thermometry: American Mineralogist, v. 73, p. 201-215.

Garofalo, P., Audétat, A., Günther, D., Heinrich, C.A., and Ridley, J., 2000, Estimation and testing of standard molar thermodynamic properties of tourmaline end-members using data of natural samples: American Mineralogist, v. 85, p. 78-88.

Grant, J.A., 1986, The isocon diagram - a simple solution to Gresen's equation for metasomatic alteration: ECONOMIC GEOLOGY, v. 81, p. 1976-1982.

Grant, J.N., Halls, C., Sheppard, S.M.F., and Avila, W., 1980, Evolution of the porphyry tin deposits of Bolivia: Mining Geology, Special Issue 8, p. 151-173.

Halter, W.E., Williams-Jones, A.E., and Kontak, D.J., 1996, The role of greisenization in cassiterite precipitation at the East Kemptville tin deposit, Nova Scotia: ECONOMIC GEOLOGY, v. 91, p. 368-385.

Hawthorne, F.C., 2002, Bond-valence constraints on the chemical composition of tourmaline: Canadian Mineralogist, v. 40, p. 789-797.

Heinrich, C.A., 1990, The chemistry of hydrothermal tin (-tungsten) ore deposition: ECONOMIC GEOLOGY, v. 85, p. 457-481.

Helgeson, H.C., Kirkham, D.H., and Flowers, G.C., 1981, Theoretical prediction of the thermodynamic behavior of aqueous electrolytes at high pressures and temperatures: IV. Calculation of activity coefficients, osmotic coefficients, and apparent molal and standard and relative partial molal properties to 600°C and 5 kb: American Journal of Science, v. 281, p. 1249-1516.

Henry, D.J., and Guidotti, C.V., 1985, Tourmaline as a petrogenetic indicator mineral: an example from the staurolite-grade metapelites of NW Maine: American Mineralogist, v. 70, p. 1-15.

Hey, M.H., 1954, A new review of the chlorites, Mineralogical Magazine, v. 30, p. 277-292.

Holland, T., and Powell, R., 1991, A Compensated Redlich-Kwong (CORK) equation for volumes and fugacities of carbon dioxide and water in the range 1 bar to 50 kbar and 100-1600°C: Contributions to Mineralogy and Petrology, v. 109, p. 265-73.

Holland, T.J.B., and Powell, R., 1998, An internally consistent thermodynamic data set for phases of petrological interest: Journal of Metamorphic Geology, v. 16, p. 309-343.

Holland, T., Baker, J., and Powell, R., 1998, Mixing properties and activity-composition relationships of chlorites in the system $MgO-FeO-Al_2O_3-SiO_2-H_2O$: European Journal of Mineralogy, v. 10, p. 395-406.

Hosking, K.F.G., 1951, Primary ore deposition in Cornwall: Transactions of the Royal Geological Society of Cornwall, v. 18, p. 309-356.

Hosking, K.F.G., Stanley, G.J., and Camm, G.S., 1987, The occurrence, nature and genesis of wood tin in South-West England: Transactions of the Royal Geological Society of Cornwall, v. 21, p. 153-212.

Ishihara, S., 1981, The granitoid series and mineralization: ECONOMIC GEOLOGY, 75th Anniversary Volume, p. 458-484.

Jingwen, M., 1995, Tourmalinite from northern Guangxi, China: Mineralium Deposita, v. 30, p. 235-245.

Johnson, J.W., Oelkers, E.H., and Helgeson, H.C., 1992, SUPCRT 92, a software package for calculating the standard molal thermodynamic properties of minerals, gases, aqueous species and reactions from 1 to 5000 bars and 0 to 1000°C: Computers and Geosciences, v. 17, p. 899-947.

Jowett, E.C., 1991, Fitting iron and magnesium into the hydrothermal chlorite geothermometer: Geological Association of Canada - Mineralogical Association of Canada - Society of Economic Geologists Joint Meeting, Program with Abstracts, v. 16, p. 62.

Kelly, W.C., and Turneaure, F.S., 1970, Mineralogy, paragenesis and geothermometry of the tin and tungsten deposits of the Eastern Andes, Bolivia: ECONOMIC GEOLOGY, v. 65, p. 609-680.

Kontak, D.J., and Clark, A.H., 1988, Exploration criteria for tin and tungsten mineralization in the Cordillera Oriental of southeastern Peru, *in* Taylor, R.P., and Strong, D.F., eds., Recent Advances in the Geology of Granite-Related Mineral Deposits: Canadian Institution of Mining and Metallurgy, Special Volume 39, p. 157-169.

Kontak, D.J., and Clark, A.H., 2002, Genesis of the giant, bonanza San Rafael lode tin deposit, Peru: origin and significance of pervasive alteration: ECONOMIC GEOLOGY, v. 97, p. 1741-1777.

Kontak, D.J., Clark, A.H., Farrar, E., Pearce, T.H., Strong, D.F., and Baadsgaard, H., 1986, Petrogenesis of a Neogene shoshonite suite, Cerro Moromoroni, Puno, Southeastern Peru: Canadian Mineralogist, v. 24, p. 117-135.

Kranidiotis, P., and MacLean, W.H., 1986, Chloritization, element mobility/immobility and mass transfer at the Phelps Dodge massive sulfide deposit: Geological Association of Canada - Mineralogical Association of Canada, Program with Abstracts, v. 11, p. 91.

Kranidiotis, P., and MacLean, W.H., 1987, Systematics of chlorite alteration at the Phelps Dodge massive sulfide deposit, Matagami, Quebec: ECONOMIC GEOLOGY, v. 82, p. 1898-1911.

Kwak, T.A.P., Brown, W.M., Abeysinghe, P.B., and Tan, T.H., 1986, Fe solubilities in very saline hydrothermal fluids: their relation to zoning in some ore deposits: ECONOMIC GEOLOGY, v. 81. p. 447-465.

Laubacher, G., 1978, Estudio geologico de la region norte del Lago Titicaca: Instituto de Geologia y Mineria (Peru) v. 5, 120 p.

Lehmann, B., 1990, Metallogeny of tin: Lecture Notes in Earth Sciences, v. 32, Springer-Verlag, Berlin, 211 p.

London, D., 1999, Stability of tourmaline in peraluminous granitic systems: the boron cycle from anatexis to hydrothermal aureoles: European Journal of Mineralogy, v. 11, p. 253-262.

London, D., and Manning, D.A.C., 1995, Chemical variation and significance of tourmaline from southwest England: ECONOMIC GEOLOGY, v. 90, p. 495-519.

London, D., Morgan, G.B., VI, and Wolf, M.B., 1996, Boron in granitic rocks and their contact aureoles, *in* Grew, E.S., and Anovitz, L.M., eds., Boron: mineralogy, petrology and geochemistry: Reviews in Mineralogy (Mineralogical Society of America), v. 33, p. 299-330.

Lynch, G., and Ortega, J., 1997, Hydrothermal alteration and tourmaline-albite equilibria at the Coxheath porphyry Cu-Mo-Au deposit, Nova Scotia: Canadian Mineralogist, v. 35, p. 79-94.

Meyer, C., and Hemley, J.J., 1967, Wall rock alteration, *in* Barnes, H.L., ed., Geochemistry of Hydrothermal Ore Deposits: Holt, Rinehart and Winston, New York, p. 166-235.

Mlynarczyk, M.S.J., Sherlock, R.L., and Williams-Jones, A.E., 2003, San Rafael, Peru: geology and structure of the worlds richest tin lode: Mineralium Deposita, v. 38, p. 555-567.

Mountain, B.W., and Williams-Jones, A.E., 1996, Mass transfer and the path of metasomatic reactions in mesothermal gold deposits: an example from from Flambeau Lake, Ontario: ECONOMIC GEOLOGY, v. 91, p. 302-321.

Müller, B., and Seward, T.M., 2001, Spectrophotometric determination of the stability of tin (II) chloride complexes in aqueous solution up to 300°C: Geochimica et Cosmochimica Acta, v. 65, p. 4187-4199.

Nutt, C.J., 1989, Chloritization and associated alteration at the Jabiluka unconformity-type uranium deposit, Northern Territory, Australia: Canadian Mineralogist, v. 27, p. 41-58.

Pabalan, R.T., 1986, Solubility of cassiterite (SnO_2) in NaCl solutions from 200°C - 350°C, with geologic applications: Unpublished Ph.D. thesis, Pennsylvania State University, U.S.A., 141 p.

Palma, V.V., 1981, The San Rafael tin-copper deposit, Puno, SE Peru: Unpublished M.Sc. thesis, Queen's University, Kingston, Ontario, Canada, 235 p.

Powell, R., and Holland, T., 1999, Relating formulations of the thermodynamics of mineral solid solutions: Activity modeling of pyroxenes, amphiboles, and micas: American Mineralogist, v. 84, p. 1-14.

Ramsay, J.G., 1980, The crack-seal mechanism of rock deformation: Nature, v. 284, p. 135-139.

Reed, M.H., 1997, Hydrothermal alteration and its relationship to ore fluid composition, *in* Barnes, H.L., ed., Geochemistry of hydrothermal ore deposits (3rd ed.), Wiley & Sons, New York, 972 p.

Rinne, F., 1912, "Baueritizing", a crystallographic disintegration of dark mica: Berichte der königlichen sächsischen Gesellschaft der Wissenschaften Leipzig 63: 441-445

Ryzhenko, B.N., Shvarov, Y.V., and Kovalenko, N.I., 1997, The Sn-Cl-F-C-S-H-O-Na system: Thermodynamic properties of components within the conditions of the Earth's crust: Geochemistry International, v. 35, p. 1016-1020.

Sandeman, H.A., Clark, A.H., Farrar, E., and Arroyo-Pauca, G., 1996, A critical appraisal of the Cayconi Formation, Crucero Basin, southeastern Peru: Journal of South American Earth Sciences, v. 9, p. 381-392.

Sempere, T., Hérail, G., Oller, J., and Bonhomme, M.G., 1990, Late Oligocene - early Miocene major tectonic crisis and related basins in Bolivia: Geology, v. 18, p. 946-949.

Shock, E.L., and Helgeson, H.C., 1988, Calculation of the thermodynamic and transport properties of aqueous species at high pressures and temperatures: Correlation algorithms for ionic species and equation of state predictions to 5 kb and 1000°C: Geochimica et Cosmochimica Acta, v. 52, p. 2009-2036.

Shock, E.L., Helgeson, H.C., and Sverjensky, D.A., 1989, Calculation of the thermodynamic and transport properties of aqueous species at high pressures and temperatures: Standard partial molal properties of inorganic neutral species: Geochimica et Cosmochimica Acta, v. 53, p. 2157-2183.

Shvarov, Yu. V., and Bastrakov, E.N., 1999, HCh: a software package for geochemical equilibrium modelling - User's Guide: Australian Geological Survey Organization Record 1999/25, Canberra, 61 p.

Sillitoe, R.H., Halls, C., and Grant, J.N., 1975, Porphyry tin deposits in Bolivia: ECONOMIC GEOLOGY, v. 70, p. 913-927.

Sinclair, W.D., and Richardson, J.M., 1992, Quartz-tourmaline orbicules in the Seagull batholith, Yukon Territory: Canadian Mineralogist, v. 30, p. 923-935.

Slack, J.F., 1996, Tourmaline associations with hydrothermal ore deposits, *in* Grew, E.S., and Anovitz, L.M., eds., Boron: mineralogy, petrology and geochemistry: Reviews in Mineralogy (Mineralogical Society of America), v. 33, p. 559-643.

Stemprok, M., 1987, Greisenisation (a review): Geologische Rundschau, v. 76, p. 169-175.

Sverjensky, D.A., Hemley, J.J., and D'Angelo, W.M., 1991, Thermodynamic assessment of hydrothermal alkali feldspar-mica-aluminosilicate equilibria: Geochimica et Cosmochimica Acta, v. 55, p. 989-1004.

Tanger, J.C., IV, and Helgeson, H.C., 1988, Calculation of the thermodynamic and transport properties of aqueous species at high pressures and temperatures: Revised equations of state for the standard partial molal properties of ions and electrolytes: American Journal of Science, v. 288, p. 19-98.

Taylor, R.G., 1979, Geology of tin deposits: Developments in Economic Geology, v. 11, Elsevier, 543 p.

Taylor, J.R., and Wall, V.J., 1993, Cassiterite solubility, tin speciation and transport in a magmatic aqueous phase: ECONOMIC GEOLOGY, v. 88, p. 437-460.

Taylor, S.R., and McLennan, S.M., 1985, The continental crust: its composition and evolution, an examination of the geochemical record preserved in sedimentary rocks: Blackwell, Oxford, 312 p.

Turneaure, F.S., 1971, The Bolivian tin-silver province: ECONOMIC GEOLOGY, v. 66, p. 215-225.

Ulrich, T., and Heinrich, C.A., 2001, Geology and alteration geochemistry of the porphyry Cu-Au deposit at Bajo de la Alumbrera, Argentina: ECONOMIC GEOLOGY, v. 96, p. 1719-1742.

Urquidi-Barrau, F., 1989, Tin and tungsten deposits of the Bolivian tin belt, *in* Geology of the Andes and its relation to hydrocarbon and mineral resources: Ericksen, G.E., Cañas Pinochet, M.T., and Reinemund, J.A., eds., Houston, Texas, Circum-Pacific Council for Energy and Mineral Resources Earth Science Series, v. 11, p. 313-323,

Walshe, J.L., 1986, A six-component chlorite solid-solution model and the conditions of chlorite formation in hydrothermal and geothermal systems: ECONOMIC GEOLOGY, v. 81, p. 681-703.

Walther, J.V., 1997, Determination of activity coefficients of neutral species in supercritical H_2O solutions: Geochimica et Cosmochimica Acta, v. 61, p. 3311-3318.

Wen, S., and Nekvasil, H., 1994, SOLVCALC: an interactive graphics program package for calculating the ternary feldspar solvus and for two-feldspar geothermometry: Computers and Geosciences, v. 20, p. 1025-1040.

Wood, S.A., 1998, Calculation of activity-activity and log fO_2-pH diagrams: *in* Richards, J.P., and Larson, P.B., eds., Techniques in hydrothermal ore deposits geology, Littleton, Reviews in Economic Geology, v. 10, p. 81-96.

Zang, W., and Fyfe, W.S., 1995, Chloritization of the hydrothermally altered bedrock at the Igarapé Bahia gold deposit, Carajás, Brazil: Mineralium Deposita, v. 30, p. 30-38.

APPENDIX - I

Description and location of samples referred to in the text

I 20 – San Rafael Vein, Ramp tunnel, 3930 m. Fresh, coarse-grained, biotite- and cordierite-bearing alkali-feldspar megacrystic leucogranite.

R 566 – Transect to the Pedro Vein, 4200 m, (~20 m SW of station T). Fresh, coarse-grained, biotite- and cordierite-bearing leucogranite, rich in alkali-feldspar megacrysts.

D4-443 – Drill hole no. 4, from the Jorge vein to the San Rafael vein, 443 m (elevation ~ 3920 m). Relatively fresh, fine-grained, biotite- and cordierite-bearing, alkali-feldspar megacrystic leucogranite.

I 8 – Transect to the Quenamari mine, 4200 m, close to its end (in 1997). Fresh, coarse-grained, grey, biotite- and cordierite-bearing, alkali feldspar-megacrystic granite.

I 51 – Transect to the Quenamari mine, 4200 m, station B. Relatively fresh, coarse-grained, grey, biotite- and cordierite-bearing, alkali feldspar-megacrystic granite.

R 80 – San Rafael Vein, Ore Shoot, 4390 m. Strongly chloritized granitoid. The only primary minerals remaining in the dark green rock are quartz and altered alkali-feldspar phenocrysts. Very minor sericitization and specks of tourmaline can only be observed locally.

R 432 – San Rafael Vein, Contact Orebody, 4200 m. Quartz vein (1.5 cm-wide), with intense chloritic halo (~5 cm on each side) in a coarse-grained, biotite- and cordierite-bearing, alkali feldspar-megacrystic leucomonzogranite. Three slabs were made of this sample:

A - very strong, dark green chloritization, adjacent to the vein,

B - lesser intensity, pervasive chloritization, further away from the vein,

C - weakly altered leucomonzogranite.

Subordinate sericitization and rare specks of tourmaline are present in all 3 slabs. The quartz vein also crosscuts a tourmaline vein, which indicates that the chloritic alteration belongs to the "main" chloritization event.

D1M-61 – Drill hole no. 1, from the San Rafael vein to the Mariano vein, 61.7 m (elevation ~ 4155 m). Dark-grey, biotite-rich granodiorite, with a 3-cm-wide halo of very strong chloritic alteration, grading into dark-green chlorite. Four slabs were made of this sample:

A - "greasy"-looking , green, vein (?) chlorite,

B - very strong, dark green, chloritic alteration,

C - mild alteration, bleached / yellowish in color,

D - fresh granodiorite.

Rare traces of tourmaline are present in slabs A and B.

D5-2 – Drill hole no. 5, from the Jorge vein to the San Rafael vein, 2 m (elevation ~ 4308 m). Pervasively sericitized, yellow-grey, fine-grained, alkali-feldspar megacrystic granite.

J 26 – Jorge Vein (North), level 4050 m, between stations 1 and 2. Multiply reopened quartz vein (~5-cm-wide), with a halo of tourmaline alteration (~ 3 cm on each side) in a strongly sericitized, alkali-feldspar megacrystic granite. Two slabs were made of this sample:

A - very strong, dark brown tourmalinization (the rock is composed almost entirely of tourmaline and quartz),

B - strong, pervasive sericitization and tourmaliniza-tion.

D5-138 – Drill hole no. 5, from the Jorge vein to the San Rafael vein, 138.2 m (elevation ~ 4175 m). Strongly tourmalinized, alkali-feldspar megacrystic granite. Tourmaline completely replaces feldspar and cordierite phenocrysts and is the only macroscopically recognizable mineral in the rock, in addition to quartz. The rock displays noticeable porosity, with small, euhedral, acicular crystals of brown tourmaline growing in the vugs.

I 45 – Sample from the surface (SW slopes of Nevado San Bartolome de Quenamari, NW of the San Rafael mine plant), elevation ~ 4850 m. Coarse-grained, grey, sericitized and intensely tourmalinized granitoid. Two varieties of tourmaline (light colored and black), as well as dumortierite can be observed macroscopically.

D4-68 – Drill hole no. 4, from the Jorge vein to the San Rafael vein, 68.6 m (elevation ~ 4245 m). Dark-brown tonalite.

A - strong tourmalinization and silicification (brown),

B - sericitization and tourmalinization (pinkish),

C - strong chloritization (green),

D - sericitization and chloritization (yellow),

E - incipient sericitization of tonalite.

D4-94 – Drill hole no. 4, from the Jorge vein to the San Rafael vein, 94 m (elevation ~ 4220 m). Very strongly tourmalinized and silicified tonalite.

APPENDIX - II

Details of the thermodynamic calculations

Activity-activity and activity-fugacity diagrams (Figs. 21 and 22) were calculated by standard thermodynamic techniques (Beane 1994, Wood 1998). Thermodynamic data at elevated temperature and pressure were obtained from the following sources: aqueous species - Johnson et al. (1992), Shock et al. (1988, 1989); end-member solids - Holland and Powell (1998); H_2O, O_2 - Holland and Powell (1991, 1998). Thermodynamic data for dravite and schorl were obtained from Garofalo et al. (2000). Thermodynamic data for aqueous species and minerals are internally consistent to +/- 3 kJ and do not require additional adjustments (*cf.* Sverjensky et al., 1991).

Mixing properties of solid solutions were calculated from the following models: chlorite - Holland et al. (1998); biotite - Powell and Holland (1999); white mica - Powell and Holland (1999), Coggon and Holland (2002); alkali feldspar - Fuhrman and Lindsley (1988), corrected in Wen and Nekvasil (1994); tourmaline - ideal solution with long-range order between Y and W sites (*cf.* Hawthorne 2002). Activity coefficients of charged aqueous solutes were computed using the Debye-Hückel equation with the constant extended term, $b_\gamma = 0.03$ (Walther 1997). The H_2O activity has been corrected for the total solute content (i.e., salinity) and the osmotic coefficient of solvent (Helgeson et al., 1981; Tanger and Helgeson, 1988).

INTRODUCTION TO CHAPTER IV

Chapter IV is a logical continuation of Chapter III, in that it examines in much more detail the mineralogy and composition of successive generations of tourmaline, a common alteration and vein mineral, characteristic of the early, barren stage of hydrothermal activity and the transition to the subsequent ore stage. I use the marked trends in tourmaline composition to make inferences about fluid evolution and the controls on cassiterite precipitation.

CHAPTER IV

Zoned tourmaline associated with cassiterite: implications for fluid evolution and tin mineralization at the San Rafael Sn-Cu deposit, SE Peru

M.S.J. Mlynarczyk and A.E. Williams-Jones

ABSTRACT

The San Rafael lode, located in SE Peru is a world-class tin deposit, associated with a Late Oligocene, shallow-level granitoid intrusion. One of the most characteristic minerals of the deposit is tourmaline, which is ubiquitous in veins and breccias that predate cassiterite mineralization and occurs also in some of the early cassiterite veins. The tourmaline occurs in a wide variety of forms and colors, and spans the compositional range from Mg- to Fe-rich (i.e., most of it represents the dravite-schorl solid solution). The latest generation of tourmaline, associated with the first cassiterite to have formed in the deposit, differs, however, from the other tourmaline types in its unique dark green color and a corresponding trend of strong iron enrichment. Its appearance in the paragenesis coincides with a marked change in the vein style, indicative of an opening of the vein system, and a dramatic change in vein and alteration mineralogy, best evidenced by the precipitation of strongly iron-rich minerals (schorl, Fe-chlorite, and Fe-rich cassiterite). Considering these observations, we suggest that an abrupt change in the plumbing of the hydrothermal system produced strong gradients in physico-chemical conditions, which were reflected in the compositional zoning of tourmaline and culminated with cassiterite deposition. We propose that dilute, relatively oxidizing external waters (presumably of meteoric origin) entered the vein system upon its reactivation, and mixed with the hot magmatic brines, which carried a large amount of dissolved tin and iron. The sudden cooling, dilution, oxidation, and possibly acid neutralization of the ore fluids resulted in the massive precipitation of the metals and formed the world-class tin ores of the deposit.

INTRODUCTION

Tourmaline is a common gangue mineral in a variety of hydrothermal ore deposit types, including granite-related tin lodes, Cu-Mo and Au porphyries, shear-zone hosted gold bonanzas and sediment-hosted massive-sulfide deposits (Slack, 1996). Because it is stable over a wide range of temperature and pressure, and is able to incorporate a great variety of trace elements into its structure (for a review see Henry and Dutrow, 1996), tourmaline

generally preserves a very good record of the composition of the fluid, from which it crystallized. Consequently, tourmaline composition can be used to interpret the origin and evolution of ore fluids and thereby provides a valuable tool for mineral exploration (Taylor and Slack, 1984; Slack and Coad, 1989; Cavaretta and Puxeddu, 1990; London and Manning, 1995; Lynch and Ortega, 1997; Jiang et al., 1998; Pirajno and Smithies, 1992; Griffin et al, 1996; Williamson et al., 2000).

The present paper describes several generations of tourmaline from the San Rafael deposit, a world-class hydrothermal tin lode, located in the Eastern Cordillera of the Peruvian Central Andes. There, tourmaline is very abundant in the early, barren stage, preceding tin mineralization, and occurs in some of the earliest cassiterite-bearing veins. A systematic mineralogical and geochemical study of the successive generations of tourmaline in the deposit revealed strong, consistent variations in tourmaline color, which correlate very well with trends in chemical composition, and are inferred to reflect the evolution of the hydrothermal fluids. In particular, it was observed that the onset of cassiterite precipitation, which coincided with a major reopening of the vein system, was associated with an abrupt change in the composition of tourmaline, that from this point in time became increasingly iron-rich. This observation is very significant, as it allows a direct insight into how changes in the plumbing of the hydrothermal system dramatically modified the physico-chemistry of the ore fluids, triggering such a voluminous deposition of cassiterite that it formed the world's richest primary tin ores.

GEOLOGIC SETTING

San Rafael, which lies in the high mountains of the Eastern Cordillera of SE Peru, is a world class tin-copper deposit. It has an average tin ore grade of ~5 wt.%, hosts a total resource of ~1 million tonnes tin metal (production + reserves), and accounts for over a quarter of world's current mine production of tin (Minsur, unpublished data, 2000; USGS statistics, 2004). The deposit consists of a series of subparallel, NW-trending and NE-dipping veins, up to 3 km in length, centered on a shallow-level, Late Oligocene granitoid pluton (Fig. 1). This intrusion, which has an outcrop area of less than 15 km^2, is largely

FIGURE 1. a. Location of the San Rafael deposit with respect to the Central Andean Sn-W-(Ag) metallogenic province (grey outline, modified after Lehmann, 1979). **b.** Geological map of the southwestern part of the San Rafael district (modified after Arenas et al.,1980).

129

a

BRAZIL

PERU

Lima

SAN RAFAEL

BOLIVIA

Juliaca

La Paz

PACIFIC
OCEAN

CHILE

0   500 km

b

VICTORIA

PEDRO

MARIANO

JORGE

VICENTE

GUILLERMO

SAN RAFAEL

50

75

50

35

56

43

47

62

70

63

74

65

51

73

76

85

65

52

75

75

80

65

52

47

64   71

68   54

65   66   85   54   68

68

Strongly metasomatized granite
Coarse-grained granitoids
Fine-grained granitoids
Quartzites (Sandía Fm.)
Hornfels (Sandía Fm.)
Slates (Sandía Fm.)
Mineralized veins

0   500 m
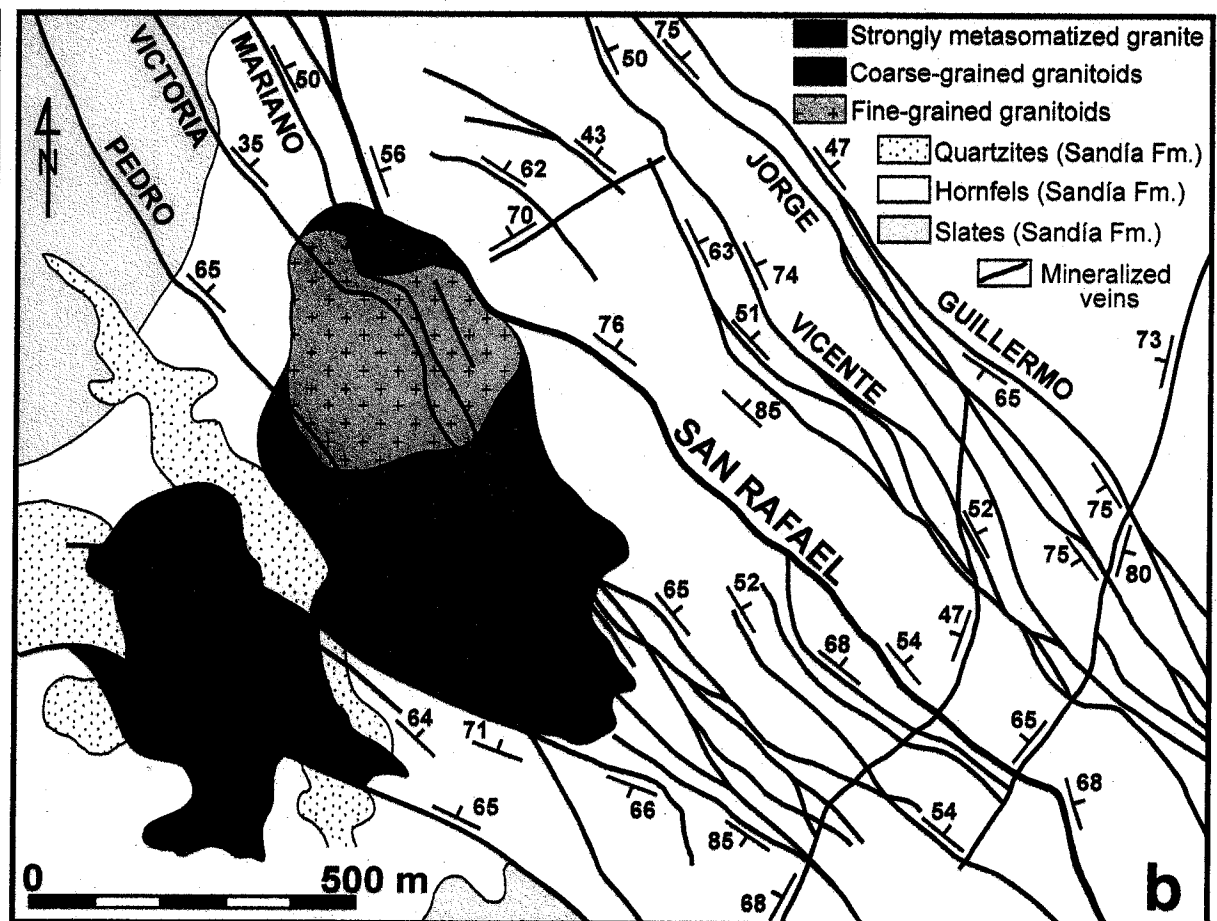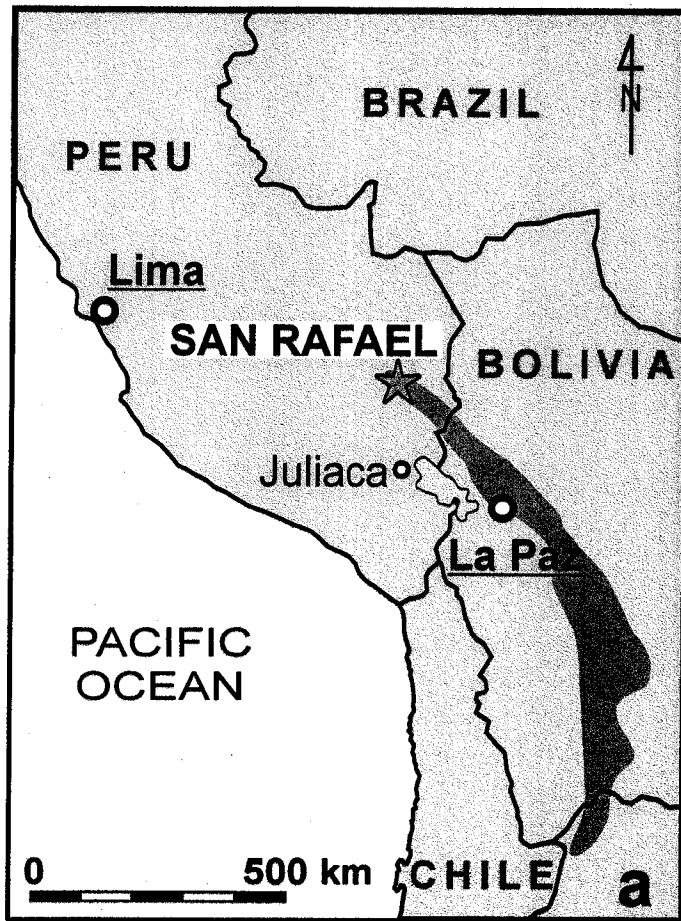
unroofed and only a contact aureole of hornfelsized and indurated Lower Paleozoic slates indicates its substantial extent. The main rock types in the pluton are coarse- to medium-grained, biotite- and cordierite-bearing granites and granodiorites, which typically contain abundant K-feldspar megacrysts. The intrusive suite is strongly peraluminous and belongs to the S-type of Chappell and White (1974).

The bulk of the ore is contained in a single, complex vein-breccia system, the San Rafael lode, which can be traced downdip for more than 1,200 meters and is hosted mainly by granitic rocks. The lode comprises a narrow, chalcopyrite-rich, upper zone, which contains disseminated acicular cassiterite, and dilates at depth into a series of 10-50 m wide fault jogs, which contain the bulk of the tin ore, in the form of cassiterite-quartz-chlorite-bearing veins and breccias. Both ore types are associated with strong chloritic alteration, which forms a 10- to 15-meter-wide envelope around the vein-breccia system.

As indicated by cross-cutting relationships and vein petrography, the sequence of hydrothermal events started with a barren stage, characterized by the formation of abundant tourmaline-quartz ± arsenopyrite veins and tourmaline-quartz microbreccias, associated with intense sericitic and tourmaline alteration. This early stage was followed by strong, laterally extensive chloritization, which overprinted all earlier alteration (except for tourmalinization), and by the massive precipitation of cassiterite, which formed the bulk of the tin ores in the deposit. During a later stage of this protracted mineralizing event, sulfide (mostly chalcopyrite) ores, associated with subordinate "needle tin" cassiterite, were deposited. Hydrothermal activity culminated with the formation of abundant, barren quartz veins, which crosscut the earlier veins and alteration envelopes. A more detailed description of the ores and alteration is given in Chapters II and III.

TOURMALINE PARAGENESIS

Magmatic and post-magmatic tourmaline

Magmatic tourmaline is restricted to subordinate occurrences of late-stage plugs and dykes of tourmaline leucogranite, which crop out along the SW and NE margins of the pluton. This tourmaline occurs as small (40-400 μm), yellow (in thin section), prismatic, euhedral-to-subhedral crystals, which are disseminated throughout the rock (~ 5 vol.%, Fig. 2a). The tourmaline leucogranite represents the latest and most evolved phase of the pluton, but its absolute age has not been determined and, therefore, its genetic relationship to the hydrothermal tourmaline still needs to be established.

Early-postmagmatic tourmaline is observed throughout much of the main granite/granodiorite intrusion and can be distinguished from magmatic tourmaline by its blue color (in thin section) and the fact that it commonly replaces cordierite phenocrysts. Since this tourmaline is not associated with tourmaline veinlets and occurs within rocks that otherwise appear fresh, it is interpreted to have formed very soon after crystallization of the pluton. This conclusion is similar to that of Novák (1998) for the Moldanubicum region, Czech Republic, who proposed that blue dravite, which replaced cordierite in Li-poor granitic pegmatites, formed during the reaction of cordierite with pegmatite-derived, acidic, B-rich fluids during an early stage of subsolidus crystallization.

Early tourmaline

The bulk of tourmaline in the San Rafael deposit is associated with the early, barren stages of the hydrothermal system. Volumetrically, the largest amounts of tourmaline are hosted by dyke-like tourmaline-quartz microbreccias of hydrothermal origin, which follow the tin lode along strike for hundreds of meters and, locally, attain many meters in width. In these rocks, tourmaline has a yellowish color (in thin section) and occurs both in the clasts and in the cement of the breccia, which typically is very fine-grained (Fig. 2b). The clasts are composed of fragments of strongly tourmalinized wallrock and vein tourmaline, as well as fragments of pre-existing tourmaline-quartz microbreccias.

Tourmaline (mostly yellow in thin section) is also very abundant in the early veins and their alteration envelopes. Tourmaline-quartz veins are generally narrow (< 3 cm),

FIGURE 2. a - Subhedral crystals of Fe-rich magmatic tourmaline in a tourmaline leucogranite (sample I36). Plane polarized light. **b** - Hydrothermal microbreccia composed of fragments of quartz, tourmaline and earlier tourmaline-quartz microbreccia, in a cement of tourmalinized rock flour. The microbreccia is cross-cut by quartz veins and veinlets (sample SAR-A7). Plane polarized light. **c** - Tourmalinized biotite laths with enclosed crystals of rutile in a fine-grained, quartz-sericite matrix of an altered granitoid (sample I45). Crossed polars. **d** - Tourmaline-quartz veinlet with kaolinized margins, cross-cutting a tonalite. Rare arsenopyrite crystals are disseminated in the veinlet (sample SAR-D3-47). Plane polarized light. **e** - Color-zoned hydrothermal tourmaline, crosscut by veinlets of later blue tourmaline (center-left). Sample SAR-D1-280. Plane polarized light. **f** - Complex color zoning in vein tourmaline associated with quartz and arsenopyrite (sample SAR-D1M-22). Plane polarized light.
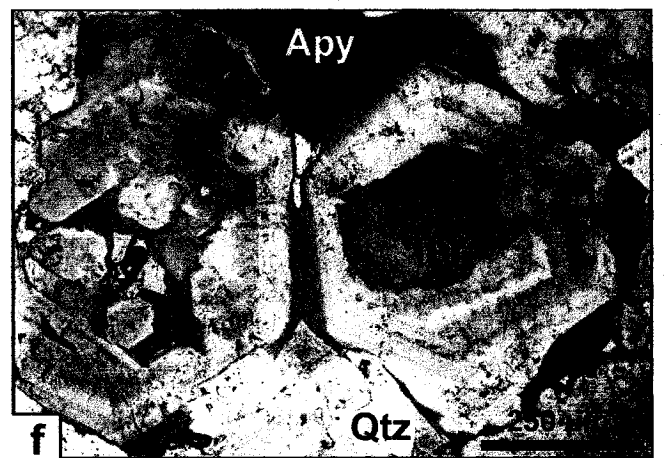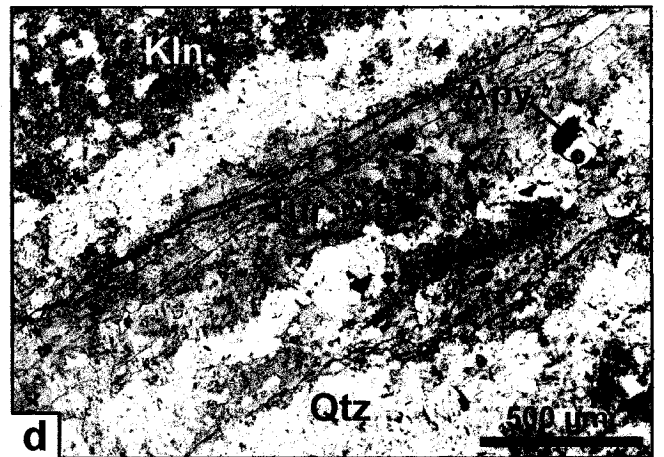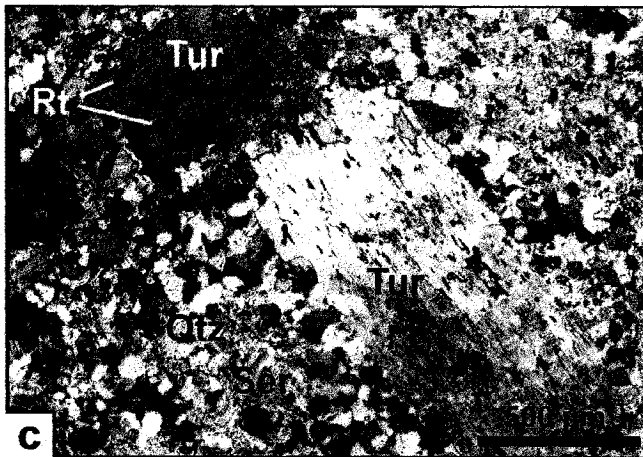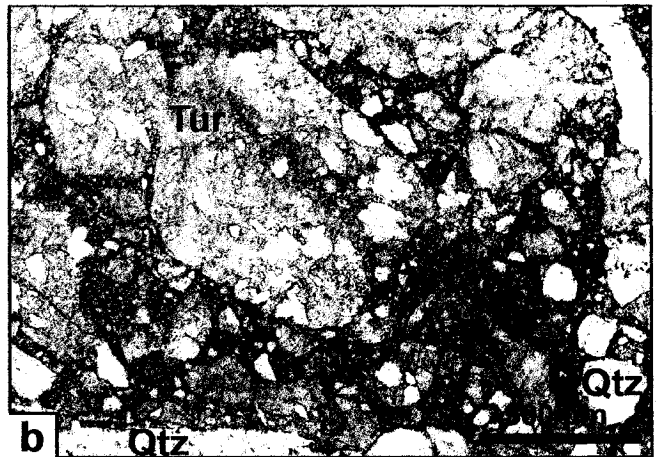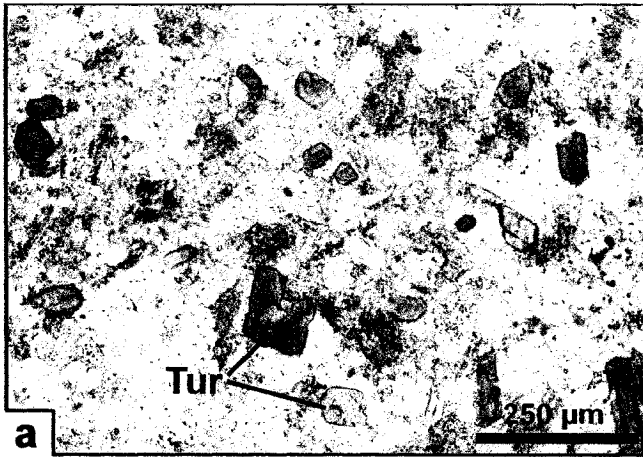
but ubiquitous throughout the pluton, and quite commonly contain arsenopyrite, which is either disseminated in the vein selvages or fills open spaces between tourmaline crystals (Fig. 3a). These barren veins form conjugate sets, one striking ~295° and dipping SW, and the other striking ~330° and dipping NE. The latter set was subsequently reopened and mineralized during the main tin-ore event. Most tourmaline-quartz veins form dense swarms and, locally, denser stockworks, characterized by multiple vein generations and vein reopening. They are commonly bordered by an envelope of strong tourmalinization, which grades outwards into a wider zone of intense sericitic alteration (≤ 25 cm).

Where tourmalinization was particularly intense, tourmaline replaced all the ferromagnesian minerals and feldspars, in a sequence from cordierite and calcic plagioclase, through biotite, sericite and, finally, sodic plagioclase and K-feldspar; so that quartz is the only mineral preserved from the original granitic assemblage. In addition, the outlines of the replaced phenocrysts (such as biotite and feldspars) are also commonly preserved (Fig. 2c). It is noteworthy that the replacement of cordierite phenocrysts invariably produced a tourmaline of bluish color (in thin section), which suggests that the color partly reflects the composition of the parental cordierite.

Vein tourmaline (i.e., tourmaline which precipitated from the hydrothermal fluids, as opposed to having formed by replacement of pre-existing minerals), is generally more varied than alteration tourmaline, in terms of its appearance. Moreover, several generations that can be distinguished optically may be present within the same sample. In hand specimen, vein tourmaline is usually light- to dark-brown, but locally exhibits reddish, creamy or beige tints. In thin section (plane polarized light), it is typically yellowish, colorless or bluish, and commonly is strongly pleochroic, with ω » ε (Fig. 2d,e). The crystal habit varies from short-prismatic to acicular (in vugs) but, unlike magmatic tourmaline, which appears optically homogenous, vein tourmaline crystals commonly display marked color and compositional zoning (Figs. 2f, 3b). Locally, these crystals also display very fine growth lamellae, a feature that has been observed in hydrothermal tourmaline elsewhere (London and Manning, 1995). Based on crosscutting relationships among tourmaline veinlets, we conclude that yellowish tourmaline (plane

133

FIGURE 3. a - Tourmaline intergrown with arsenopyrite (sample SAR-D3-39). Reflected light. **b** - Backscatter electron image of oscillatory zoning in hydrothermal tourmaline (dravite). Sample SAR-D3-182A.
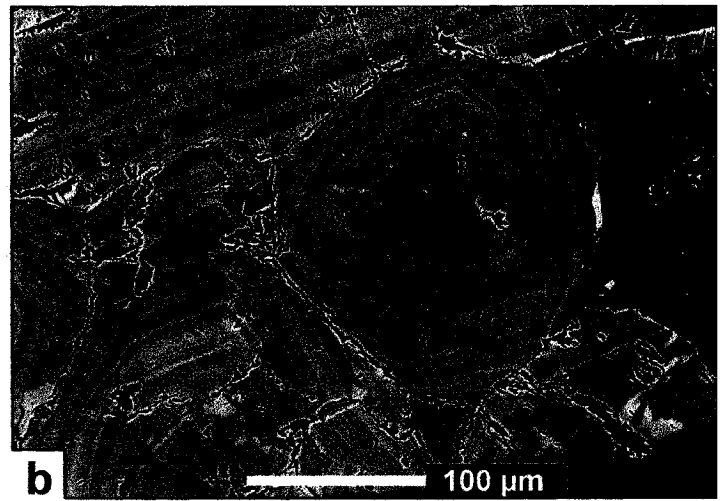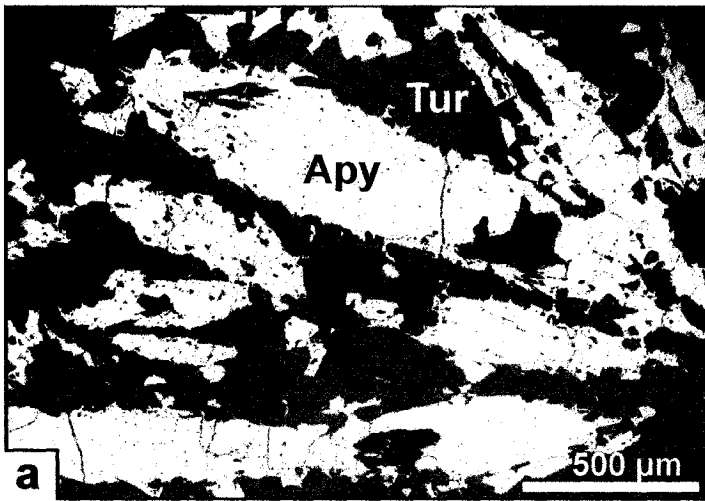
polarized light) was followed by colorless or orange tourmaline, and in turn by dark blue, pale blue or pale green tourmaline (Figs. 4 and 5a,b)

Ore stage tourmaline

The majority of tourmaline-quartz veins were sealed prior to ore deposition, but a few remained open and contain a second generation of tourmaline, which co-precipitated with abundant cassiterite and chlorite. In contrast to the former veins, these veins display evidence of clear open-space filling and are surrounded by haloes of intense chloritization. In cross-section, they typically comprise an outer zone of massive, monomineralic tourmaline, several cm thick, which is colorless or orange in thin section (Fig. 4). This zone is succeeded inwards by a zone of green tourmaline, which rims, replaces and locally cross-cuts the earlier (colorless or orange) tourmaline (Fig. 5c,d). The green tourmaline zone, in turn, is succeeded by a zone containing very fine, radial aggregates of needle cassiterite (Fig. 5e), which were replaced by coarse, euhedral cassiterite crystals, and are intimately intergrown with bundles of acicular khaki-green to dark-green tourmaline (Fig. 5f) and chlorite. This tin-rich zone is relatively porous and lacks any associated quartz. The vein core comprises coarse, monomineralic arsenopyrite, which is commonly euhedral due to its open space deposition.

The complex tourmaline-cassiterite-chlorite-arsenopyrite veins described above record a marked change, both in mineral assemblage and in mineral chemistry. The color of the precipitating tourmaline (as seen in plane polarized light) changes abruptly from colorless and orange to green and subsequently to dark-green. Taken together with the coeval growth of cassiterite and dark green tourmaline, this suggests that the main, tin-ore stage followed immediately after the early, barren stage, and reflects a sudden change in the physicochemical conditions of the hydrothermal fluid.

Late tourmaline

The massive deposition of cassiterite was associated with strong, pervasive chloritization, which largely obliterated earlier sericitic alteration. The pre-existing tourmaline, hosted by the breccias, the early veins and their alteration envelopes, however, was largely

135

FIGURE 4. Drawing of part of a mineralized vein showing the transition from early (orange or pale) tourmaline to late, dark green, iron-rich tourmaline, accompanied by cassiterite and chlorite, and followed by arsenopyrite (sample SAR-D3-182.5, Drill hole nr. 3 to the Mariano vein, 182.5 m, elevation ~ 3967 m a.s.l.).

vein growth

1 cm

coarse crystals of arsenopyrite

chlorite

porous aggregate of coarse cassiterite crystals, intergrown with bundles of acicular, khaki-green to dark-green tourmaline crystals.

chlorite

very fine, radial aggregates of needle-tin cassiterite

very porous aggregate of short-prismatic crystals of green tourmaline

massive aggregate of prismatic crystals of orange (or pale) tourmaline. Where there is porosity, the crystals have thin rims of dark green tourmaline.

FIGURE 5. a - Second generation of zoned, blue, iron-rich tourmaline, as overgrowths on orange, dravitic, vein tourmaline (sample SAR-D1-280). Plane polarized light. **b** - Overgrowths of blue tourmaline on earlier dravite (yellow), in a tourmaline-quartz vein (sample SAR-D4-253). Plane polarized light. **c, d** - Schorl (green) overgrowths on dravite (colorless / yellow / orange) in a hydrothermal vein (sample SAR-D3-182). Plane polarized light. **e** - Finely-crystalline wood tin cassiterite, associated with schorl (green), which replaced and grew on earlier dravite (colorless / yellow). Sample SAR-D3-182). Plane polarized light. **f** - Coarsely-crystalline cassiterite, intimately intergrown with acicular schorl (khaki-green to dark green). White patches represent voids in the sample. Sample SAR-D3-182. Plane polarized light. **g** - Overgrowths of Fe-rich tourmaline (schorl ?) on earlier dravite (orange), coexisting with Fe-rich chlorite (sample SAR-R-577, from a zone of intense, main-stage chloritic alteration). Plane polarized light. **h** - Overgrowths of Fe-rich tourmaline (schorl ?) on earlier dravite (dark yellow), coexisting with quartz and main-stage chlorite (sample SAR-R14, from a zone of intense chloritic alteration). Plane polarized light.

a — Qtz, Tur

b — Qtz, Tur, 25 μm

c — Tur, 250 μm

d — Tur, 250 μm

e — Tur, Cas, 250 μm

f — Cas, Tur, 250 μm

g — Tur, Tur, Chl

h — Qtz, Tur, Chl, 125 μm
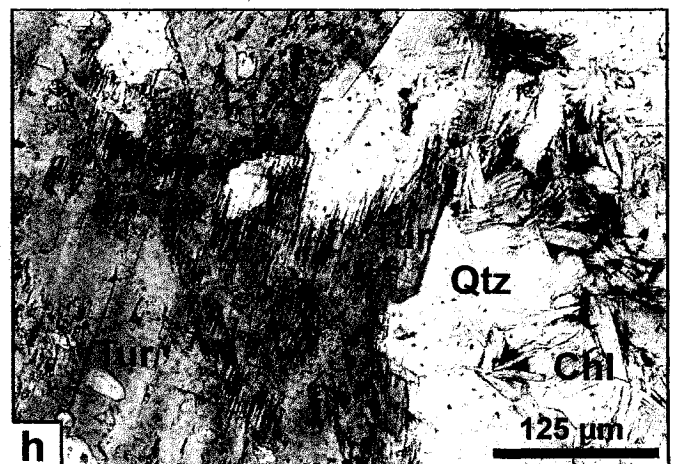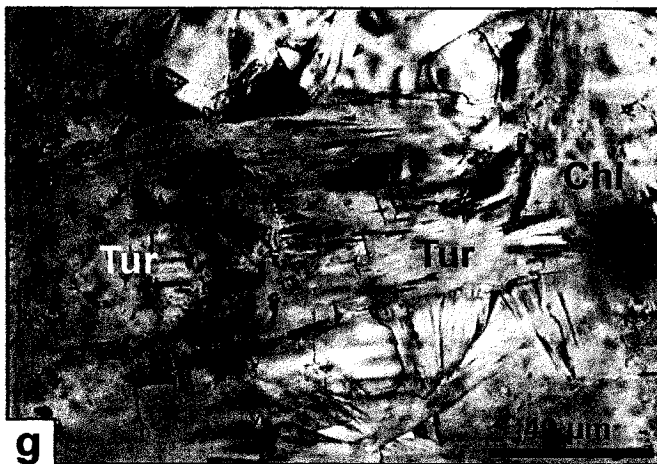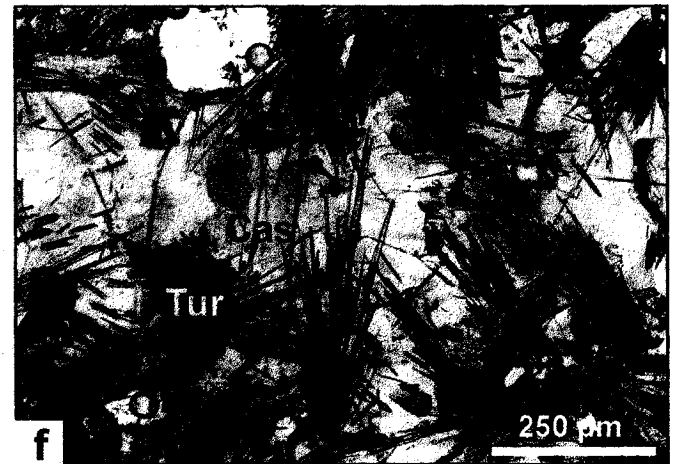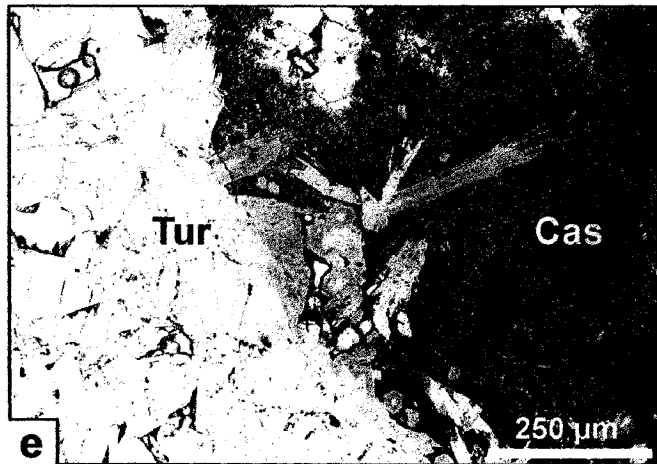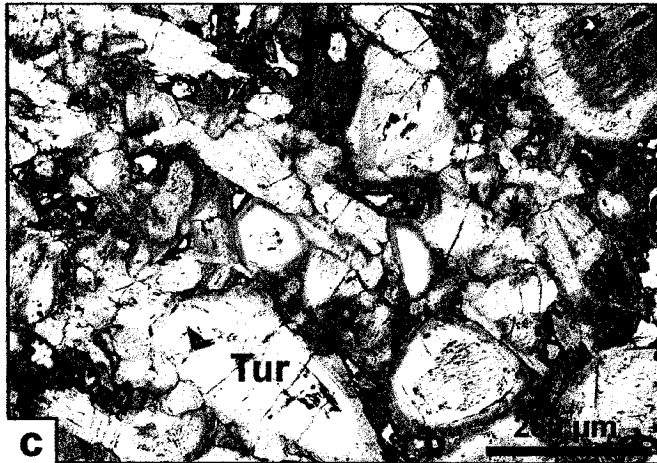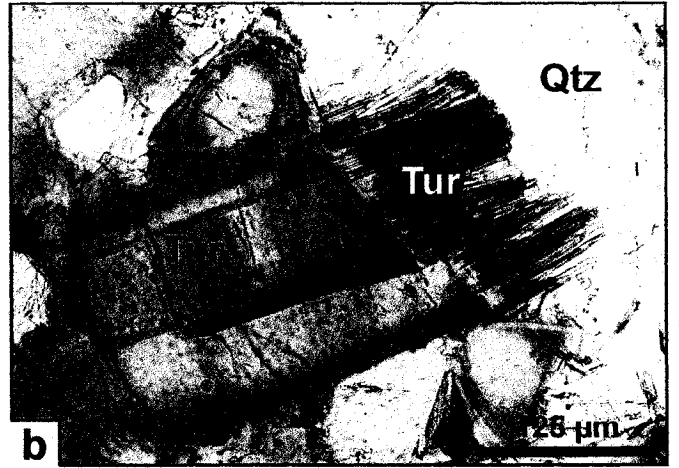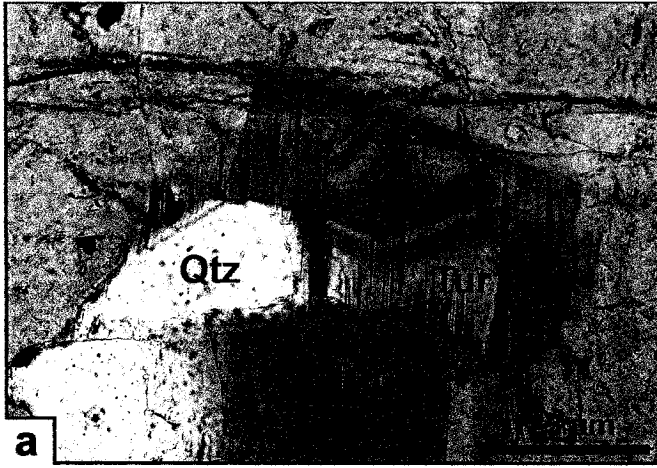
unaffected. Thus, even in wallrock which was so strongly chloritized that it now consists only of chlorite and quartz, tourmaline crystals commonly retain their original color zoning. At high magnification, nonetheless, most tourmaline crystals in rocks affected by chloritic alteration, can be seen to have developed tiny overgrowths of a late, greenish variety of tourmaline (Fig. 5g,h). These overgrowths are optically continuous with the host tourmaline crystal and occur as narrow (5-100 μm) rims on the prism walls or as jagged terminations of the prisms. Owing to their pale-green to blue-green color, they would be easily overlooked were it not for the fact that their interference colors are much higher than those of the surrounding chlorite. In addition to the near ubiquitous green overgrowths, there are also irregular reaction rims of bluish-grey color on some early tourmaline crystals.

The above observations suggest that tourmaline continued to form during chloritic alteration, a conclusion that is supported by the presence in one sample of a complex network of very fine tourmaline needles, which are intimately intergrown with the chloritic groundmass. This interpretation is also consistent with the fact that the vast majority of vein- and breccia-hosted tourmaline samples, even those collected away from zones of chloritization, are crosscut by fine veinlets, containing late, greenish or bluish, tourmaline needles (Fig. 5b), in addition to quartz and, locally, chlorite. The marked difference in color of the late tourmaline suggests that tourmaline composition changed significantly with the evolution of the hydrothermal system from pre-ore to ore stages.

ANALYTICAL METHODS

A total of 46 polished thin sections of tourmaline-bearing samples were prepared and studied petrographically. Electron microprobe WDS analyses (636 analyses on 151 individual tourmaline zones/grains) were carried out at the Department of Earth and Planetary Sciences of McGill University in Montreal (JEOL JXA-8900L), and additional data collected at the Faculty of Geology of the University of Warsaw in Poland (CAMECA SX-100). Detailed X-ray elemental maps of Mg, Fe, Na and Sn were obtained for a late, complexely zoned tourmaline crystal. The analytical conditions were the same

for both electron microprobes: an accelerating voltage of 15 kV, a beam current of 20 nA, and a spot size of 5 μm. The standards used were natural and synthetic materials: albite (Na), diopside (Si, Ca, Mg), orthoclase (K, Al), hematite (Fe), spessartine (Mn), TiO_2 (Ti), chromite (Cr), fluorite (F), vanadinite (Cl) and, for a subset of analyses, cassiterite (Sn) and scheelite (W). The analyses were interpreted using the T+Z+Y=15 scheme (Henry and Dutrow, 1996), assuming all Fe to be ferrous (Table 1).

TOURMALINE CHEMISTRY

Major element composition and crystal chemistry

Tourmaline is a complex borosilicate mineral with the general structural formula: $XY_3Z_6[T_6O_{18}][BO_3]_3V_3W$, where X = Ca, Na, K, □ (vacancy); Y = Li, Mg, Fe^{2+}, Mn^{2+}, Al, Cr^{3+}, V^{3+}, Fe^{3+}, (Ti^{4+}); Z = Mg, Al, Fe^{3+}, V^{3+}, Cr^{3+}, (Fe^{2+}); T = Si, Al, (B); B = B, (□); V = OH^-, O^{2-}; W =OH^-, F^-, O^{2-}. The species in parentheses have not yet been proven to occur in these sites, and the V and W sites are also referred to as the [O(3)]-site and [O(1)]-site, respectively (Hawthorne and Henry, 1999; Henry and Dutrow, 1996). Substitutions in the X, Y, Z, V and W sites are ubiquitous and yield a wide range of tourmaline end-members, 14 of which are recognized (see Hawthorne and Henry, 1999, for review).

Representative microprobe analyses and corresponding sample descriptions of the tourmaline from San Rafael are listed in Table 1. Figure 6 presents ternary plots of Al-Fe-Mg and Ca-^{X}□-(Na+K) for two sets of (averaged) tourmaline analyses. Set A shows the evolution of tourmaline composition in a complex tourmaline-cassiterite-chlorite-arsenopyrite vein of the type described earlier (Fig. 4), in which four successive generations of tourmaline, (colorless, orange, green and dark-green - as seen in plane polarized light) were distinguished. The composition of all the other tourmaline crystals analysed (in total, 110 tourmaline crystals or separate zones within them), are shown in set B and are grouped into the following categories: magmatic, microbreccia-hosted, very early-alteration, early-alteration (barren stage), vein tourmaline and, finally, late (greenish) overgrowths and reaction rims on earlier tourmaline.

TABLE 1. Average composition of tourmaline from San Rafael (selected samples).

	magmatic	very early alteration	very early alteration	very early alteration	early alteration	early alteration	early alteration	early alteration	early vein	transitional ? vein	early alteration
Stage	magmatic	very early alteration	very early alteration	very early alteration	early alteration	early alteration	early alteration	early alteration	early vein	transitional ? vein	early alteration
Tour type / Description	magmatic disseminated, isometric xls	radiating, columnar xls	color zoned, irregular xls	color zoned, irregular xls	color zoned, columnar xls	aggregates, columnar xls	replacement of biotite	radiating, columnar xls	zoned, columnar xls	late overgrowths	replacement of biotite
Color (PPL)	dark yellow	colorless	dark yellow	blue	yellow	yellow	yellow	v. light blue	dark yellow	dark blue	pale yellow
Elevation (m)	5100	4950	4950	4950	4220	4050	4050	4050	4035	4035	4245
Associated minerals	qtz,plag,Kfs rt, bauer. bt	qtz,ser,rt dum,tur	qtz,ser,rt dum,tur	qtz,ser,rt dum,tur	qtz,rt,ap	qtz,rt	qtz,ser,rt	qtz,ser,rt	qtz,ser,chl	qtz,ser,chl	qtz,rt
Sample	I36	I46	I46	I46	D4-94	J26A	J26C	J26C	D1-280	D1-280	D4-68A
SiO_2 (wt.%)	34.526	37.070	35.325	36.080	36.337	36.245	36.233	36.828	35.957	35.647	36.105
TiO_2	0.507	0.112	1.327	0.323	0.420	1.313	1.015	0.008	2.932	0.019	0.210
Al_2O_3	35.113	38.662	32.068	32.819	35.291	30.822	32.996	33.585	29.854	33.214	35.640
Cr_2O_3	n.a.	0.027	0.041	0.009	0.010	0.044	0.041	0.005	n.a.	n.a.	0.017
FeO	10.843	0.295	9.149	7.812	5.923	5.897	6.498	4.864	2.206	13.333	4.075
MnO	0.061	0.011	0.070	0.044	0.012	0.014	0.008	0.023	0.012	0.010	0.006
MgO	2.258	7.074	4.867	5.754	5.294	7.526	6.260	7.251	10.045	1.934	6.353
CaO	0.152	0.191	0.661	0.332	0.353	0.928	0.623	0.402	1.247	0.018	0.523
Na_2O	1.957	1.666	2.054	2.144	1.817	2.079	1.899	2.202	2.208	1.415	1.866
K_2O	0.046	0.022	0.064	0.051	0.027	0.039	0.091	0.026	0.030	0.014	0.032
F	0.372	0.240	0.596	0.649	0.287	0.204	0.507	0.086	0.179	0.038	0.365
Cl	n.a.	0.003	0.007	0.013	0.003	0.002	0.003	0.005	n.a.	n.a.	0.014
O=F,Cl	-0.157	-0.102	-0.253	-0.276	-0.122	-0.086	-0.214	-0.037	-0.075	-0.016	-0.157
Total	85.679	85.269	85.975	85.754	85.652	85.027	85.961	85.245	84.593	85.627	85.050

Stoichiometry (a.p.f.u.), based on T+Z+Y=15

	I36	I46	I46	I46	D4-94	J26A	J26C	J26C	D1-280	D1-280	D4-68A
B	3.000	3.000	3.000	3.000	3.000	3.000	3.000	3.000	3.000	3.000	3.000
Si	5.834	5.944	5.946	6.003	5.983	6.057	5.993	6.050	5.981	6.018	5.941
Al	6.992	7.307	6.382	6.435	6.846	6.070	6.431	6.502	5.852	6.609	6.912
Ti	0.064	0.014	0.168	0.041	0.052	0.165	0.127	0.001	0.368	0.003	0.026
Fe	1.532	0.039	1.288	1.088	0.817	0.825	0.899	0.668	0.307	1.882	0.561
Mn	0.009	0.002	0.010	0.006	0.002	0.002	0.001	0.003	0.002	0.001	0.001
Mg	0.569	1.691	1.221	1.427	1.299	1.875	1.543	1.775	2.491	0.487	1.558
Cr	n.a.	0.004	0.005	0.001	0.001	0.006	0.005	0.001	n.a.	n.a.	0.002
Ca	0.028	0.033	0.119	0.059	0.063	0.166	0.111	0.071	0.223	0.003	0.092
Na	0.641	0.518	0.670	0.692	0.580	0.674	0.609	0.701	0.712	0.464	0.595
K	0.010	0.004	0.014	0.011	0.006	0.008	0.019	0.006	0.007	0.003	0.007
□	0.322	0.445	0.197	0.238	0.352	0.152	0.261	0.223	0.059	0.530	0.306
Sum cations	15.678	15.555	15.803	15.762	15.648	15.848	15.739	15.777	15.941	15.470	15.694
F	0.199	0.122	0.317	0.342	0.150	0.108	0.266	0.045	0.095	0.020	0.190
Cl	n.a.	0.001	0.002	0.004	0.001	0.001	0.001	0.001	n.a.	n.a.	0.004
Fe/(Fe+Mg)	0.729	0.024	0.514	0.432	0.385	0.305	0.368	0.273	0.109	0.795	0.264
Na/(Na+Ca)	0.959	0.940	0.850	0.924	0.906	0.805	0.851	0.908	0.764	0.993	0.866
# of analyses	7	8	8	11	10	5	5	5	14	4	10

Abbreviations: xl(s) - crystal(s), vein - vein mineral, qtz - quartz, ser - sericite, rt - rutile, tur - tourmaline, dum - dumortierite, cas - cassiterite, apy - arsenopyrite, plag - plagioclase, Kfs - K feldspar, chl - chlorite, ap - apatite, ttn - titanite, py - pyrite, bauer. bt - baueritized biotite.
n.a. - not analysed

	early alteration	transitional ? alteration	early ? alteration	transitional ? alteration	very early alteration	transitional ? alteration	transitional ? vein	early vein	early vein	transitional vein	transitional vein
Stage	early	transitional ?	early ?	transitional ?	very early	transitional ?	transitional ?	early	early	transitional	transitional
Tour type	alteration	alteration	alteration	alteration	alteration	alteration	vein	vein	vein	vein	vein
Description	replacement of biotite	late overgrowths	radiating, acicular xls	late overgrowths	irregular xls, aggregates	late overgrowths	late overgrowths	aggregates of prismatic xls	aggregates of prismatic xls	late precipitation	late precipitation
Color (PPL)	dark yellow	brownish	colorless	blue-green	orange	green	greenish	colorless	orange	green	dark green
Elevation (m)	4225	4225	4310	4310	4225	4225	4207	3967	3967	3967	3967
Associated minerals	qtz,ser,rt chl,py	qtz,ser,rt chl,py	qtz,chl,ser rt,ttn,py	qtz,chl,ser rt,ttn,py	chl,qtz ap,rt	chl,qtz ap,rt	qtz	–	–	–	cas,chl,apy
Sample	R 574	R 574	R502	R502	R577 (1st gen)	R577 (2nd gen)	D5-100	D3-182B (1st gen)	D3-182A (2nd gen)	D3-182A (3rd gen)	D3-182A (4th gen)
SiO_2 (wt.%)	35.808	35.027	36.618	35.915	36.720	35.742	34.889	37.265	36.328	35.785	34.106
TiO_2	1.126	0.730	0.110	0.180	0.681	0.310	0.149	0.306	1.108	0.305	0.312
Al_2O_3	31.254	30.595	34.192	31.897	32.610	32.034	29.814	35.123	30.861	33.251	29.298
Cr_2O_3	n.a	n.a	0.008	0.015	0.018	0.002	n.a.	0.005	0.211	0.015	0.005
FeO	6.643	14.958	6.550	13.068	5.814	14.197	13.916	2.787	4.449	12.237	17.120
MnO	0.018	0.026	0.047	0.003	0.018	0.053	0.016	0.001	0.012	0.051	0.031
MgO	7.256	2.129	5.821	2.867	7.031	1.796	3.189	7.409	9.171	2.560	2.035
CaO	0.943	0.139	0.363	0.134	0.511	0.176	0.318	0.240	1.332	0.256	0.516
Na_2O	2.147	2.147	1.969	1.962	2.032	1.767	2.222	1.864	2.002	1.578	2.301
K_2O	0.030	0.030	0.034	0.025	0.053	0.037	0.021	0.014	0.031	0.032	0.060
F	0.267	0.167	0.062	0.030	0.314	0.092	0.372	0.158	0.851	0.177	0.106
Cl	n.a	n.a	0.001	0.005	0.018	0.008	n.a.	0.002	0.003	0.005	0.005
O=F,Cl	-0.112	-0.070	-0.026	-0.014	-0.136	-0.040	-0.156	-0.067	-0.359	-0.076	-0.046
Total	85.380	85.879	85.748	86.086	85.683	86.173	84.727	85.106	85.998	86.176	85.849

Stoichiometry (a.p.f.u.), based on T+Z+Y=15

B	3.000	3.000	3.000	3.000	3.000	3.000	3.000	3.000	3.000	3.000	3.000
Si	5.976	6.016	6.023	6.063	6.050	6.070	6.049	6.058	5.981	6.010	5.931
Al	6.145	6.193	6.628	6.346	6.331	6.412	6.093	6.729	5.987	6.582	6.005
Ti	0.142	0.095	0.014	0.023	0.085	0.040	0.020	0.037	0.137	0.039	0.041
Fe	0.928	2.149	0.902	1.845	0.802	2.016	2.018	0.379	0.613	1.720	2.491
Mn	0.003	0.004	0.007	0.001	0.002	0.008	0.003	0.000	0.002	0.007	0.005
Mg	1.807	0.546	1.426	0.722	1.728	0.454	0.819	1.796	2.251	0.640	0.528
Cr	n.a.	n.a	0.001	0.002	0.002	0.000	n.a.	0.001	0.028	0.002	0.001
Ca	0.169	0.026	0.064	0.025	0.091	0.032	0.059	0.042	0.235	0.046	0.096
Na	0.695	0.715	0.627	0.643	0.650	0.582	0.747	0.588	0.639	0.514	0.776
K	0.006	0.007	0.007	0.006	0.011	0.008	0.005	0.003	0.006	0.007	0.013
□	0.130	0.253	0.302	0.329	0.249	0.378	0.190	0.368	0.119	0.433	0.115
Sum cations	15.871	15.748	15.699	15.672	15.751	15.622	15.811	15.632	15.881	15.567	15.885
F	0.142	0.091	0.032	0.016	0.164	0.049	0.204	0.082	0.444	0.094	0.058
Cl	n.a.	n.a	0.000	0.002	0.005	0.002	n.a.	0.000	0.001	0.002	0.001
Fe/(Fe+Mg)	0.340	0.798	0.387	0.719	0.316	0.818	0.711	0.174	0.214	0.729	0.826
Na/(Na+Ca)	0.809	0.966	0.910	0.964	0.885	0.947	0.927	0.939	0.734	0.919	0.890
# of analyses	8	2	4	2	5	9	2	7	20	8	22

FIGURE 6. A. Evolution of tourmaline composition in a single vein (sample SAR-D3-182), from the early, pre-ore to the main, tin-ore stages (n=41). **B.** Composition (in a.p.f.u.) of different types of tourmaline from the San Rafael deposit (n=110). Each point of the plots represents the average of several microprobe analyses.
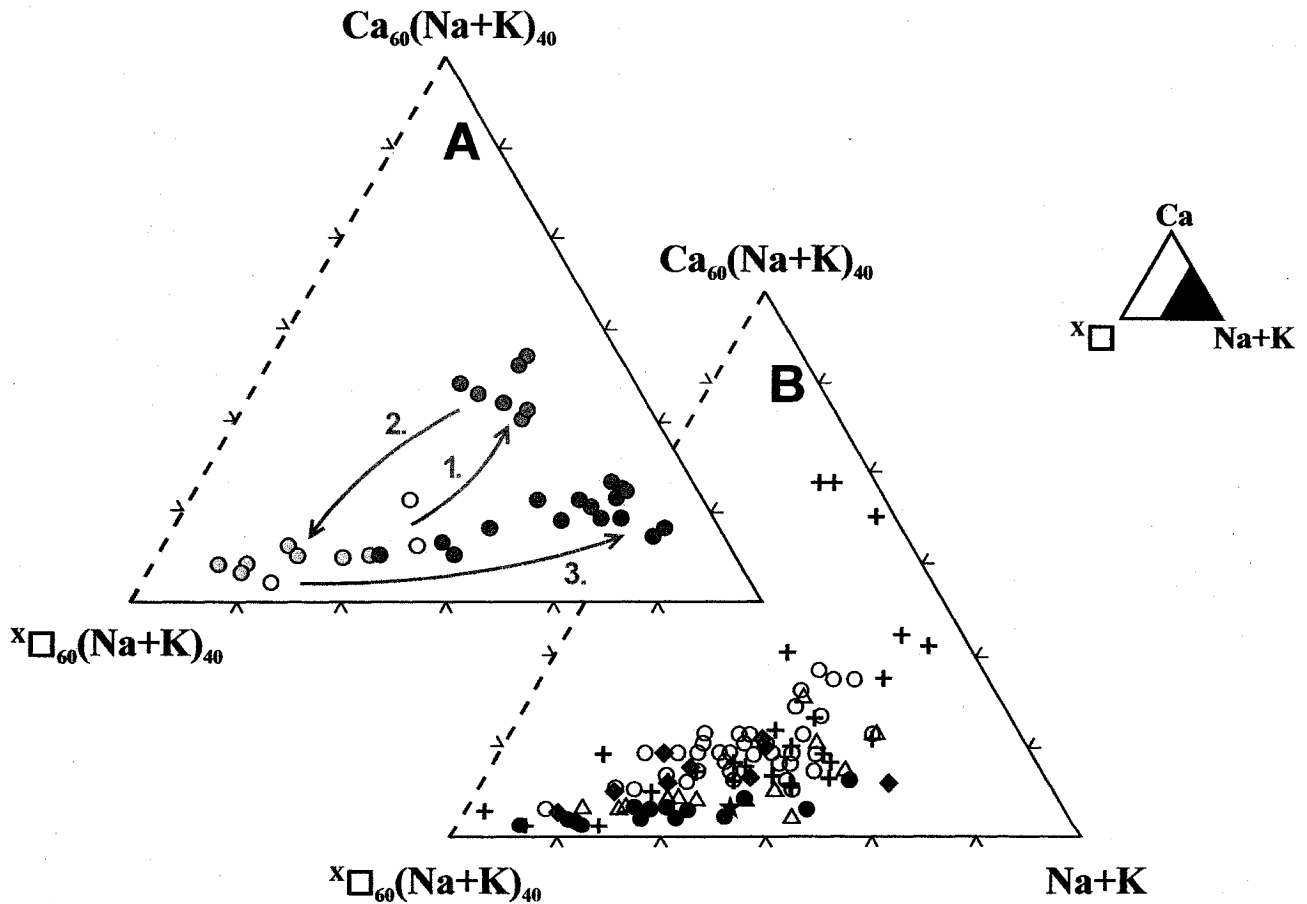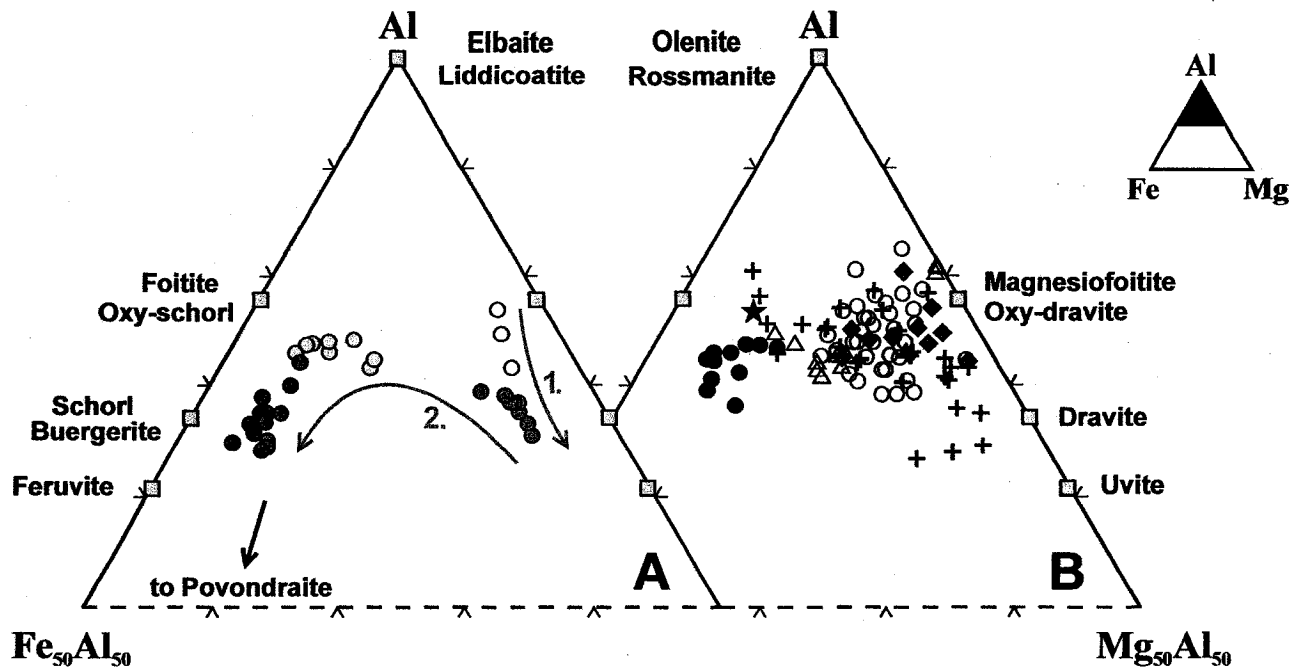
A

- ○ colorless vein tourmaline (1st gen.)
- ● orange vein tourmaline (2nd gen.)
- ◐ green vein tourmaline (3rd gen.)
- ● dark green vein tourmaline (4th gen.)

B

- ★ magmatic tourmaline
- ◆ tourmaline from microbreccia
- △ very early, alteration tourmaline
- ○ early alteration tourmaline
- + vein tourmaline
- ● late overgrowths on earlier tourmaline

The diagrams in Figure 6 reveal that the evolution of tourmaline composition in set A is very similar to that in the deposit-scale set B. Thus, as the sequence of crystallization of the various types of tourmaline in set A is known, the timing relationships of different types of tourmaline elsewhere in the deposit can be determined unequivocally. The composition of most samples corresponds to those of the solid solution series dravite-schorl (see also Fig. 8a), and extends towards the alkali-free counterparts (Mg-foitite and foitite) and oxy-tourmalines (oxy-dravite and oxy-schorl).

Overall, the San Rafael tourmaline is Ca and K-poor: the $Na/(Na+Ca)$ ratio is typically between 0.70 and 0.99 (average: 0.88 a.p.f.u.) and the concentration of $K < 0.01$ a.p.f.u. Following the X-site classification of Hawthorne and Henry (1999), it belongs to the alkali tourmaline group, with the exception of a few samples having a large vacancy in the X-site (Fig. 6). When the Y site is considered, the principal compositional trend is an evolution to systematically higher concentrations of total Fe. Thus, the $Fe/(Fe+Mg)$ ratio increases from as low as 0.02 (nearly pure dravite) to 0.87 a.p.f.u. (schorl), averaging ~0.44, and, whereas the bulk of the early, barren stage tourmaline is Fe-bearing dravite, late tourmaline is Mg-bearing schorl. Interestingly, the magmatic tourmaline is Fe-rich, with a $Fe/(Fe+Mg)$ ratio of ~0.73. There is also a large overlap between the compositions of alteration, microbreccia-hosted, and vein tourmaline. The Li content could not be determined through electron microprobe analysis, but is estimated to be negligible, as bulk-rock analyses of strongly tourmalinized rocks (up to 45 % tourmaline) contain less than 100 ppm Li. Appreciable Li would also be associated with an increased Al content (towards the elbaite-liddicoatite corner) and none of the tourmaline analyses plot in the field of tourmaline from Li-rich granitoids, outlined by Henry and Guidotti (1985).

The pleochroic color of the tourmaline ($\varpi \gg \varepsilon$) correlates well with its major element chemistry. Colorless tourmaline is Ti- and Fe-poor (<0.05 a.p.f.u. Ti and $Fe/(Fe+Mg) < 0.30$), whereas yellow and orange varieties are Ti-rich (0.03-0.35 a.p.f.u. Ti - see Figure 7). Orange tourmaline is also more Ca-rich than yellow tourmaline, with $Na/(Na+Ca)$ values of less than 0.77 versus 0.75-0.95 in yellow tourmaline. On the other hand, blue and green varieties of tourmaline are poor in Ti, but relatively rich in Fe; the $Fe/(Fe+Mg)$ ratio is between 0.40 and 0.75 for blue tourmaline and greater than 0.75 for

FIGURE 7. Relationship between the color of tourmaline in thin section (plane polarized light) and its composition (in a.p.f.u.).
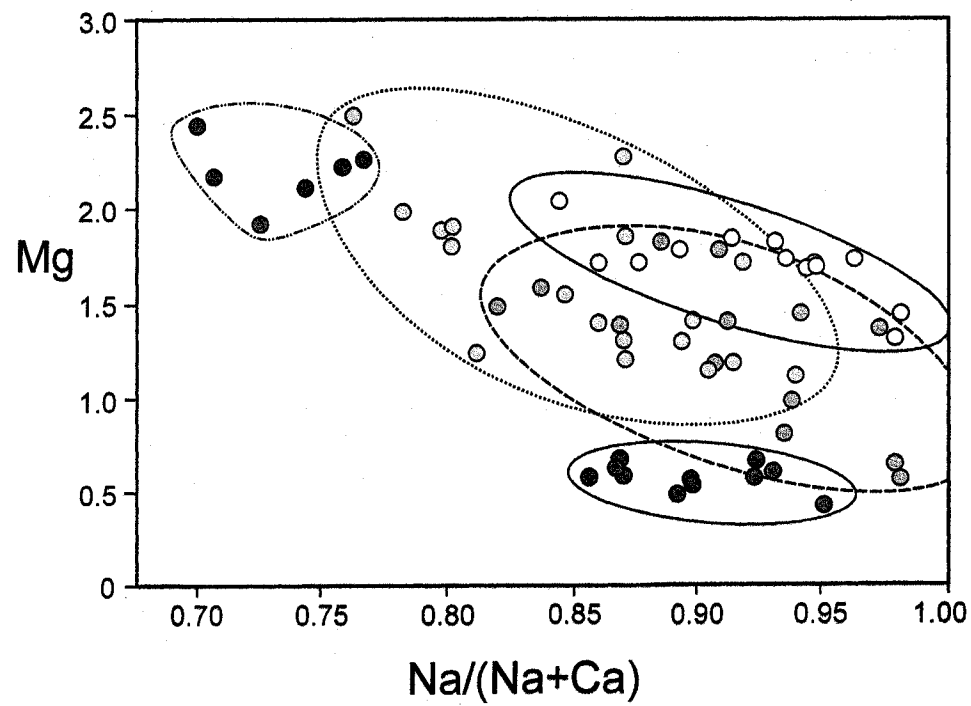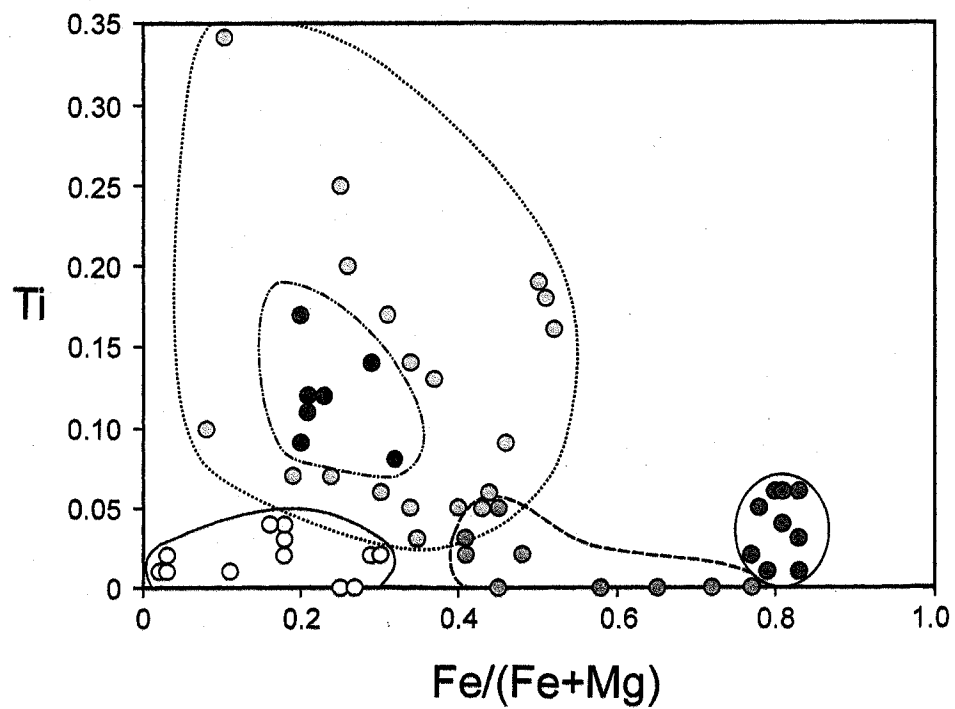
| o colorless | o yellow | ● orange | o blue | ● green |

the green variety. This correlation is very similar to that described from the Ore Knob massive sulfide deposit by Taylor and Slack (1984), who noted that blue and green tourmalines have higher Fe contents than yellow- and brown-colored varieties, which are enriched in Mg. A correlation between the pleochroic color of tourmaline and Ti content, was reported by Sinclair and Richardson (1992) for the Seagull batholith, where orange tourmaline is significantly more Ti-rich than blue tourmaline. Interestingly, however, both varieties of tourmaline from this locality are very Fe-rich (Fe/(Fe+Mg)>0.95), suggesting that factors other than just the proportion of Fe influence the color of tourmaline (*cf.* Faye et al., 1974; Slack and Coad, 1989).

Figure 8 illustrates further compositional variations of the two data sets (A - in a complex tourmaline-cassiterite-chlorite-arsenopyrite vein, and B - on the scale of the deposit). Diagram 8a, in which Fe/(Fe+Mg) is plotted versus $^X\square$/(Na+$^X\square$) confirms the classification of most tourmaline samples as members of the dravite-schorl solid solution series, as opposed to alkali-deficient tourmalines. This can also be observed on diagram 8b (Mg vs. Fe), where the bulk of the San Rafael tourmaline defines a compositional trend, which closely corresponds to the dravite-schorl exchange vector, i.e., $(OH^-)Mg^{2+} \Leftrightarrow$ $(OH^-)Fe^{2+}$ (*cf.* Burt, 1989). There is, however, a systematic departure towards alkali-deficient tourmaline and oxy-tourmaline, which is due to additional elements in the Y site, such as Al. It is noteworthy, that the compositions of the Fe-rich schorl define a trend, which is parallel to the povondraite subsitution vector ($Fe^{3+} \Leftrightarrow Al^{3+}$). This indicates that part of the iron in this tourmaline could actually be Fe^{3+} and substitutes for Al in the Z site, a conclusion reinforced on the diagram 8d by the marked negative correlation between Al and Fe for this tourmaline variety. An accurate determination of Fe^{3+} and Fe^{2+} in tourmaline is, however, problematic, as recalculations based on electron microprobe analyses largely rely on assumptions which cannot be easily verified, whereas the determination of ferric/ferrous iron by wet chemical methods is not possible due to the refractory behaviour of tourmaline in acids. On the other hand, the determination of ferric/ferrous iron in tourmaline by Mössbauer spectroscopy requires pure samples in volumetric amounts that are larger than those typically available in this study.

Diagram 8c, showing the relationship between Al content and $^X\square$ provides information on the relative importance of the exchange mechanisms $\square Al(NaR)_{-1}$ and

144

FIGURE 8. Composition of San Rafael tourmaline (in a.p.f.u.) for: A. tourmaline from a single vein (sample SAR-D3-182), which records the transition from the early, barren to the main, tin-ore stage (n=41). B. other tourmaline from the San Rafael deposit (n=110). Each point represents the average of several microprobe analyses, except for diagram **f**, showing single analyses for a different set of data (n=126). The plots show selected end-member compositions (small boxes) and substitution vectors (arrows). R in diagram **c** represents the sum of Fe(total) + Mg.

a

Mg-foitite — Foitite

Magnesiofoitite | Foitite

$^x\square/(Na+{}^x\square)$

1.0
0.8
0.6
0.4
0.2
0.0

Dravite | Schorl

Dravite — Schorl

Fe/(Fe+Mg)

0   0.2   0.4   0.6   0.8   1.0

b

Schorl
Buergerite

povondraite
$Fe^{3+}Al_{-1}$

uvite
$Ca(Fe,Mg)Na_{-1}Al_{-1}$

Foitite
Oxy-schorl

schorl

dravite

Fe

3.0
2.5
2.0
1.5
1.0
0.5
0.0

Oxy-foitite

Al_Y

Oxy-Mg-foitite

Mg-foitite
Oxy-dravite

Dravite

Mg

0   0.5   1.0   1.5   2.0   2.5   3.0

A

□ colorless vein tourmaline (1st gen.)
● orange vein tourmaline (2nd gen.)
○ green vein tourmaline (3rd gen.)
● dark green vein tourmaline (4th gen.)

B

★ magmatic tourmaline
◆ tourmaline from microbreccia
△ very early, alteration tourmaline
○ early alteration tourmaline
+ vein tourmaline
● late overgrowths on earlier tourmaline

c

$x\square$

$\square Al(NaR)_{-1}$

$FeAl_{-1}$ $AlO(R(OH))_{-1}$

Al

d

inaccessible

Fe

full occupancy of Z by Al

Al

A

□ colorless vein tourmaline (1st gen.)
● orange vein tourmaline (2nd gen.)
○ green vein tourmaline (3rd gen.)
● dark green vein tourmaline (4th gen.)

B
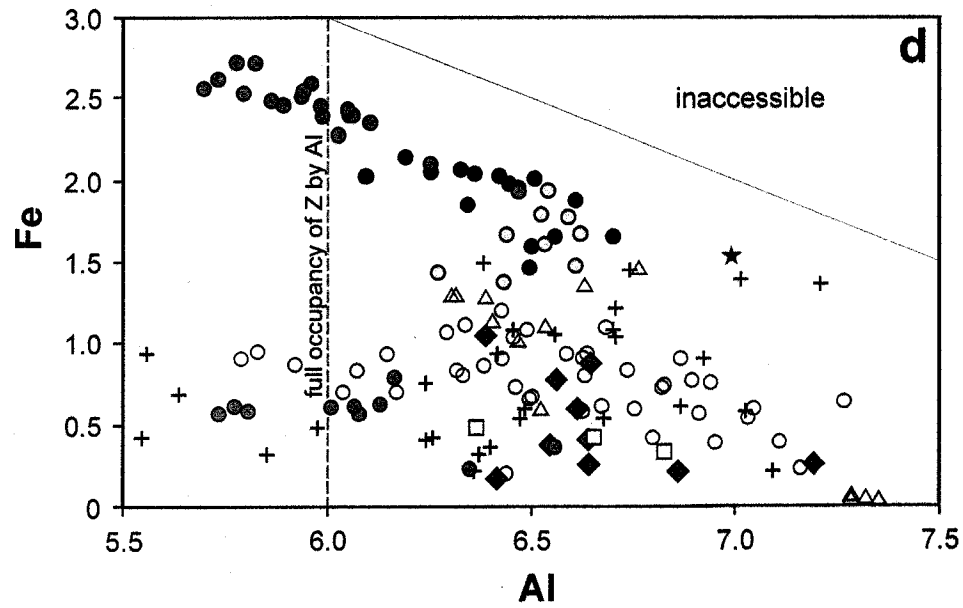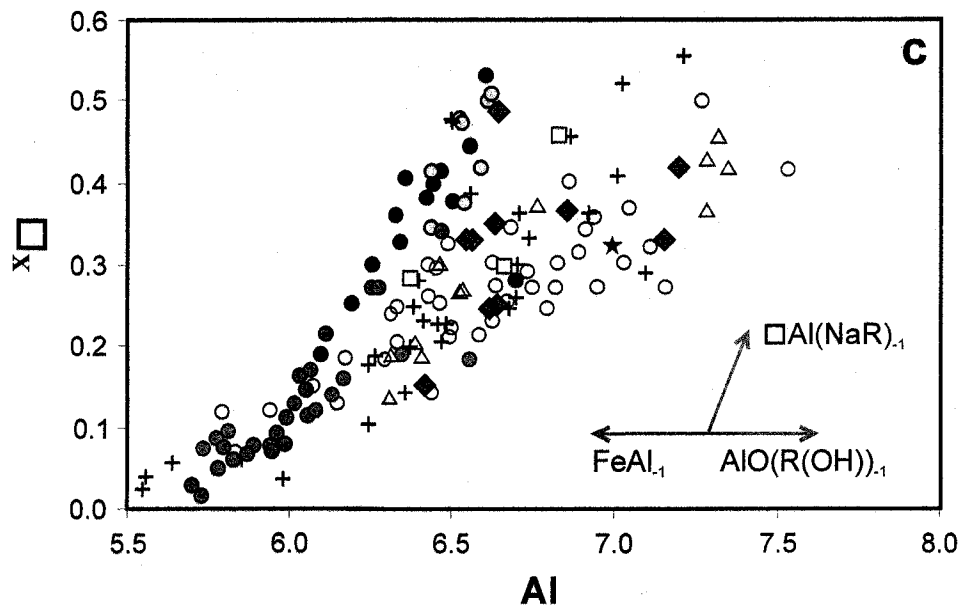
★ magmatic tourmaline
◆ tourmaline from microbreccia
△ very early, alteration tourmaline
○ early alteration tourmaline
+ vein tourmaline
● late overgrowths on earlier tourmaline

A

□ colorless vein tourmaline (1st gen.)
● orange vein tourmaline (2nd gen.)
○ green vein tourmaline (3rd gen.)
● dark green vein tourmaline (4th gen.)

B
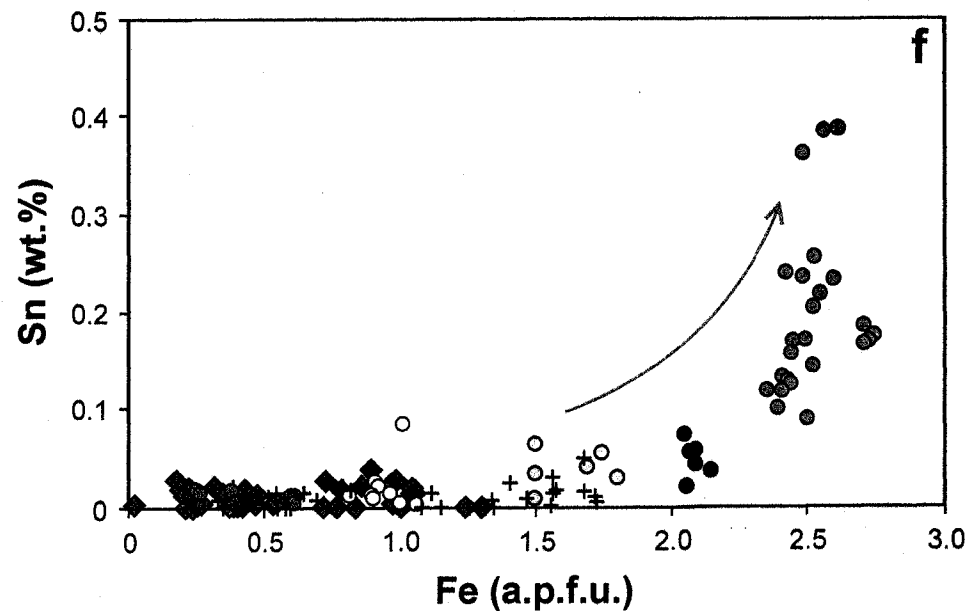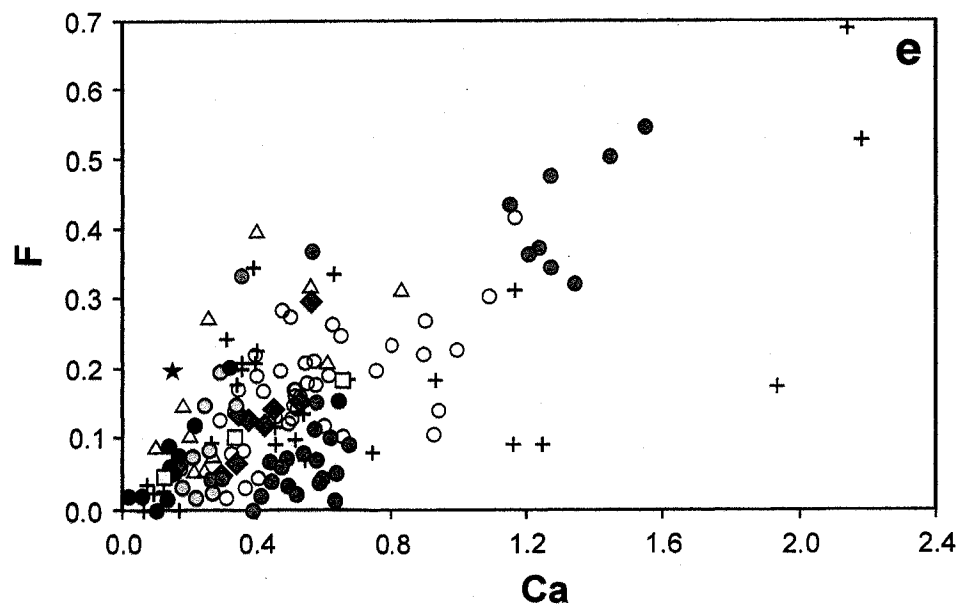
★ magmatic tourmaline
◆ tourmaline from microbreccia
△ very early, alteration tourmaline
○ early alteration tourmaline
+ vein tourmaline
● late overgrowths on earlier tourmaline

AlO(R(OH))$_{-1}$ and FeAl)$_{-1}$. The substitution $\square$Al(NaR)$_{-1}$, which depends strongly on the bulk concentration of Na in the system and on the temperature (von Goerne et al., 2001) clearly dominates, especially in the late, Fe-rich tourmaline varieties. Lastly, diagram 8e suggests a minor uvite component in the colorless and orange tourmaline from the selected vein, which contains higher than average concentrations of Ca, Mg and F.

Tin and tungsten in tourmaline

Tourmaline is a potential host for tin and tungsten through substitution of these elements in the Y site (Power, 1968; Němec, 1973). In view of this, tourmaline from several samples was analysed for Sn (and W) by electron microprobe. The majority of the tourmaline crystals analysed have a very low Sn content (<0.03 wt.% Sn), however, late, Fe-rich tourmaline (schorl) associated with cassiterite contains between 0.20-0.39 wt.% Sn (or up to 0.03 a.p.f.u. Sn, Figure 8f). These values are among the highest recorded for tourmaline anywhere, the others being: 0.46 % Sn (Kidd Creek, Canada; Slack et al., 1999); 0.35 % Sn (Roche, SW England; Williamson et al., 2000), and 0.42 % Sn (Yunlong, China; Yu and Jiang, 2003). Based on the relatively uniform distribution of Sn in the tourmaline, as shown by electron microprobe X-ray maps (Fig. 9), it is concluded that the substantial amount of tin detected is present within the crystal structure of tourmaline (probably in the Y site), and does not represent inclusions of cassiterite. From Figure 8f it is evident that there is a strong correlation between the concentration of Sn and Fe in the tourmaline. We therefore conclude, that Sn and Fe were incorporated into the structure of tourmaline during its crystallization from a Fe-rich, cassiterite-saturated ore fluid. This is consistent with the tendency of tourmaline to incorporate trace elements in proportion to their concentration in the hydrothermal fluid, as documented, for example, for Pb-rich tourmaline coexisting with galena and Cu-rich tourmaline coexisting with chalcopyrite at Black Hawk, Maine (Taylor and Slack, 1984). It is not surprising, therefore, that in contrast to Sn, the W content of the San Rafael tourmaline is very low, typically <0.03 wt.% WO$_3$, with only exceptional analyses as high as 0.14 wt.% W (~0.01 W a.p.f.u.). This reflects the overall character of the San Rafael deposit, i.e., its unusual tin enrichment and the virtual lack of tungsten mineralization.

FIGURE 9. (a) Color zoning in a crystal of hydrothermal tourmaline (center), intergrown with cassiterite. Sample D3-182, plane polarized light. **(b)** Corresponding backscatter electron image. (c-f) X-ray element maps for Mg, Fe, Na and Sn for the same tourmaline crystal.

cas

200 μm

Mg

Fe

Na

Sn

a

b

c

d

e

f
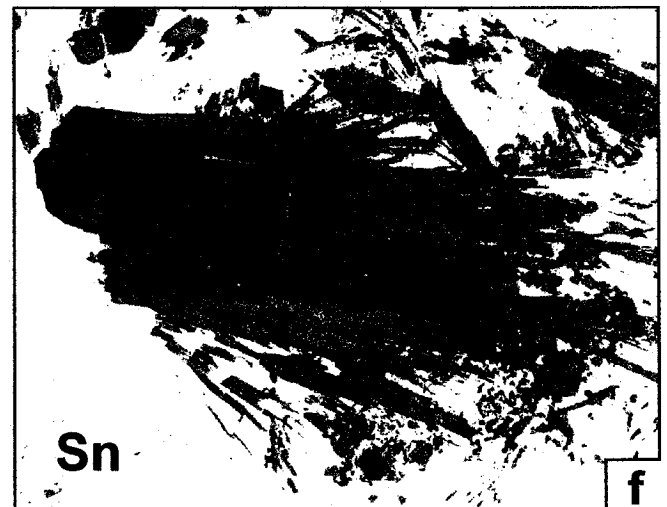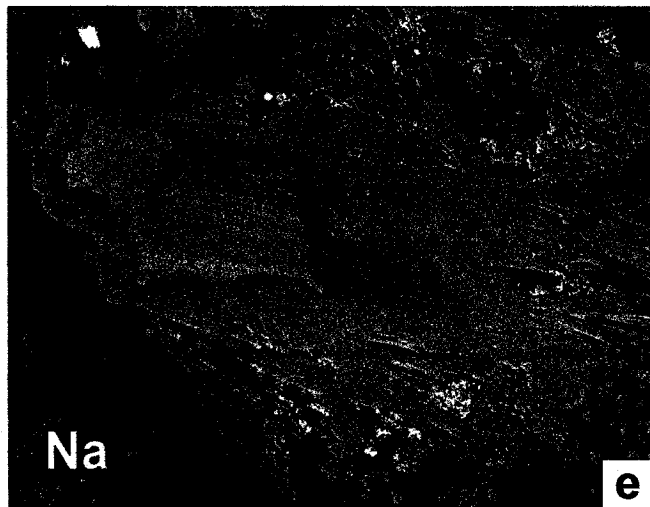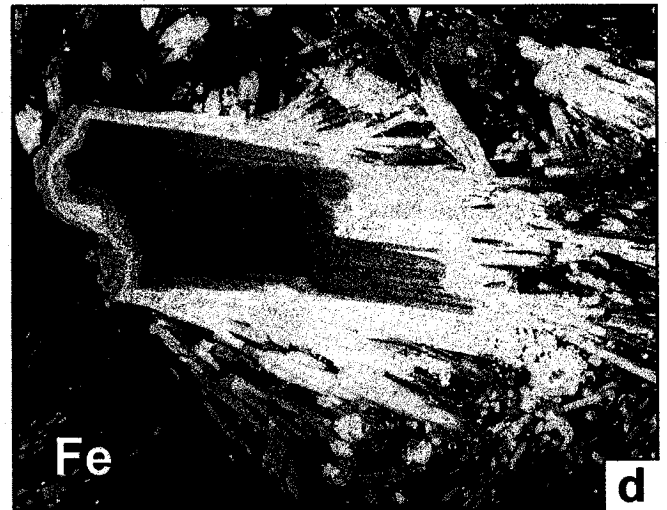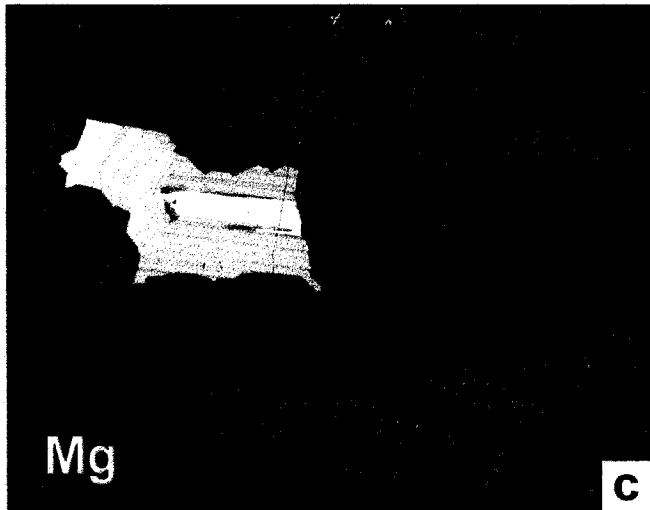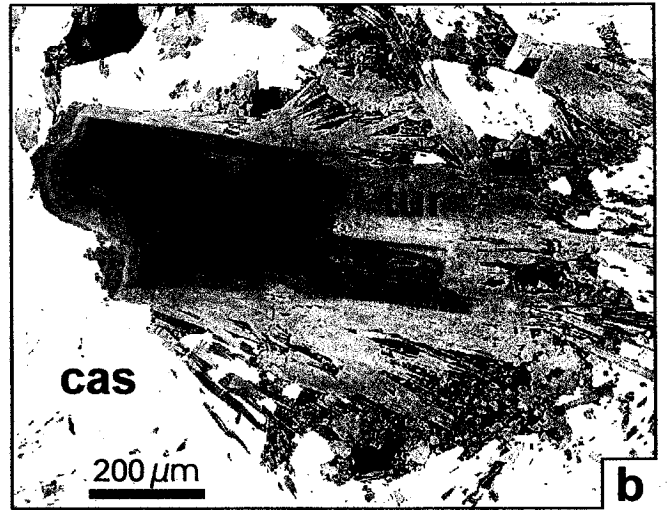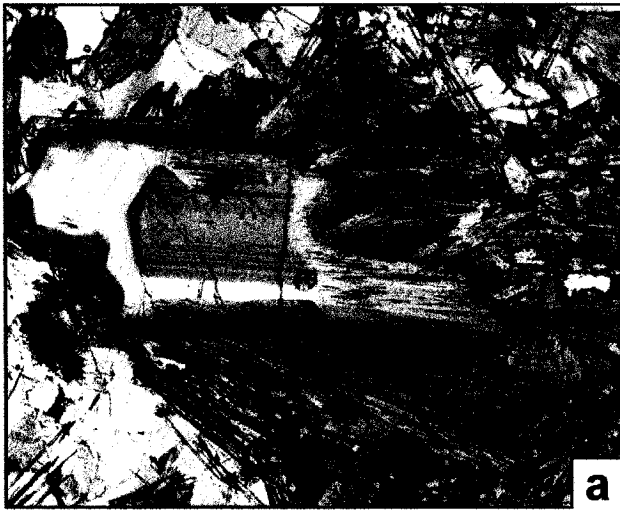
Chemical evolution of zoned crystals of schorl

Investigation of the complex tourmaline-cassiterite-chlorite-arsenopyrite vein depicted in Figure 4, revealed that larger crystals of strongly Fe-rich tourmaline, which coexist with coarse cassiterite, exhibit strong color and compositional zoning. One such crystal, ~1 mm long, was selected for detailed X-ray elemental mapping under the electron microprobe, and another was analyzed along a line profile, traversing the successive zones. The results, shown in Figures 9 and 10 indicate that these crystals have orange-pleochroic, strongly Mg-rich cores, on which, following partial resorption (best seen on Figures 9b,c,d) an increasingly Fe-rich, initially bluish, then dark-green variety of tourmaline precipitated. This sharp enrichment in Fe, corresponds to a change in Fe/(Fe+Mg) from 0.20 to 0.85, and coincided with an enrichment in Sn (up to ~0.4 wt.%) and Na, and a depletion in Ca, F and Ti (Fig. 10). It should be also noted, that the composition of the Mg-rich cores matches closely that of the orange-colored tourmaline, which occurs earlier in the profile of the same vein (Fig. 4). This implies that the zoned tourmaline crystals record a crucial part of the fluid history of the deposit, corresponding to the transition between the early, barren stage and the onset of cassiterite deposition.

DISCUSSION

The association of tourmaline with tin deposits

Tourmaline is a relatively common gangue mineral in many granite-related Sn-W hydrothermal systems, due to the high concentration of boron in peraluminous magmas (Taylor, 1979; Barth, 1988; Manning, 1991; London and Manning, 1995; LeBoutillier, 2002). Pichavant (1981) and Pichavant and Manning (1984) have shown that boron enrichment of silicate melts increases H_2O solubility, thereby lowering solidus temperatures and allowing more time for differentiation. The prolonged crystal fractionation, in turn, favors the concentration of high field strength elements, notably tin, in the residual melt. In addition, the greater solubility of water in B-rich magmas delays vapor separation until the ascent of magma to shallower levels and, therefore, lower confining pressures. The resulting greater volume expansion during the degassing of the

FIGURE 10. Compositional zoning in a single tourmaline crystal, recording the evolution from early, pre-ore to ore stage tourmaline at San Rafael.
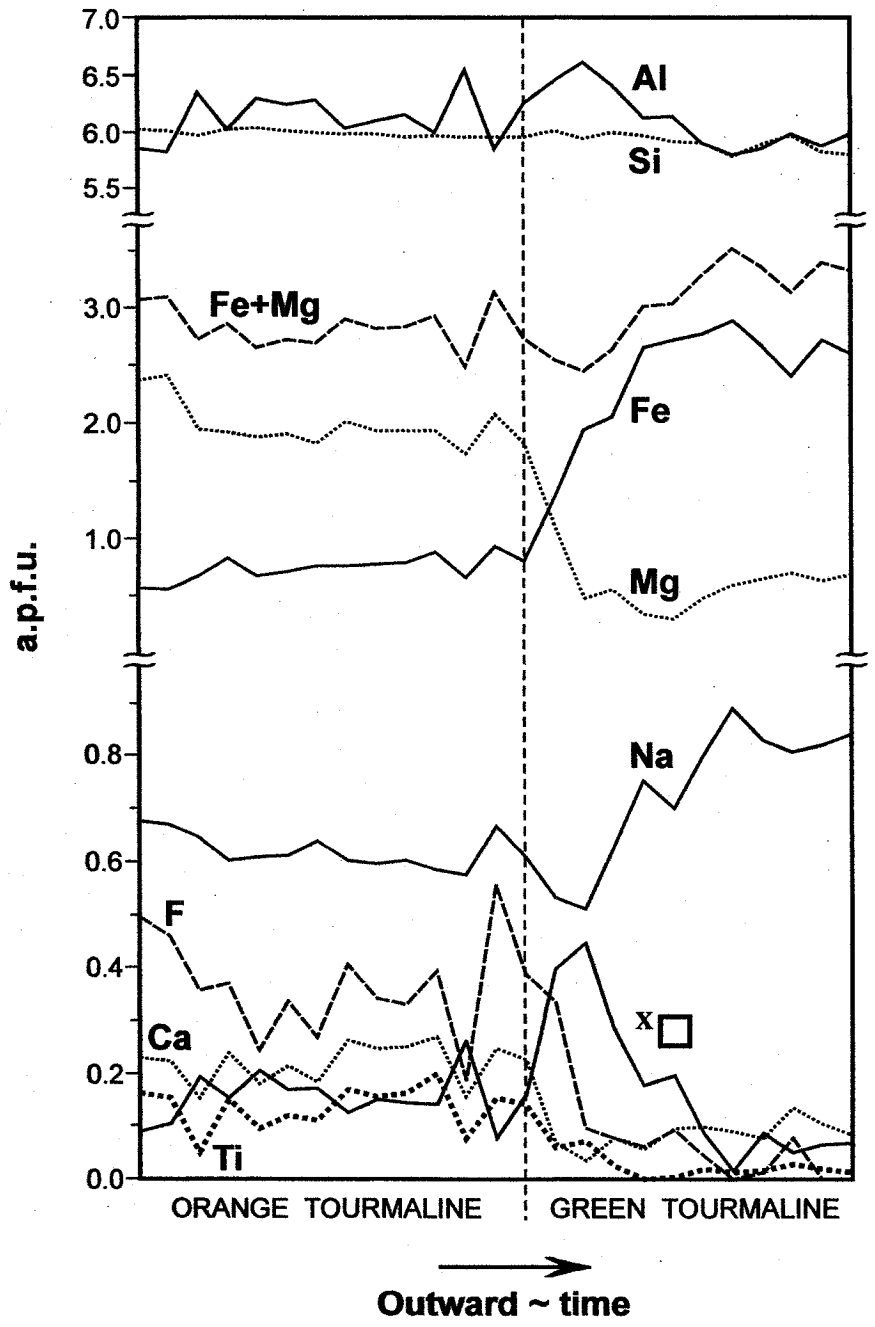
residual melts produces large fluid overpressures and the release of a great amount of mechanical energy. This, in turn, produces intense fracturing and brecciation, which lead to a greater focusing of the ore fluids and concentration of mineralization, as opposed, e.g, to F-rich, greisen-style systems, which are characterized by a more passive crystallization and a more disseminated style of mineralization (Pollard et al., 1987; Halls, 1994). These effects are very obvious at San Rafael, where the early, barren tourmaline-quartz veins established the primary framework of the vein-breccia system, which was subsequently reopened and mineralized with Sn.

Compositional trends in San Rafael tourmaline

The tourmaline at San Rafael bears some similarities to hydrothermal tourmaline in granite-related Sn systems elsewhere. These include its ubiquitous color zoning, a relatively wide range of Fe and Mg contents, and a low F content (*cf.* London and Manning, 1995). Like tourmaline in other tin deposits, San Rafael tourmaline is also rich in Al (*cf.* Fig. 8d), especially where it is an alteration product. We interpret this high Al content to be related to the strongly peraluminous mineralogy of the host granitoids which it replaced, as is also the case, e.g., in SW England (Manning, 1991). The most outstanding feature of the San Rafael tourmaline is, however, the strong increase in Fe content exhibited by the latest generation of schorl. In this respect, the schorl from San Rafael evokes some of the late tourmaline described from Cornish tin deposits, and commonly referred to as "blue peach" (Farmer and Halls, 1993). Thus, Power (1968) described the occurrence of zoned acicular crystals of blue-green tourmaline, which locally grew on corroded nuclei of an earlier, yellow-brown generation of tourmaline (*cf.* Fig. 9a, this paper). More recently, Williamson et al. (2000) described overgrowths of a blue, Fe- and Sn-rich tourmaline on an earlier, light-brown, Mg- and F-rich tourmaline, from fault breccias at Roche, SW England. The remarkable feature of the Fe-rich schorl at San Rafael is, however, that its appearance in the paragenesis is quite abrupt and directly preceded the massive precipitation of cassiterite, with which it is finely intergrown. As this compositional trend undoubtely reflects a change in physicochemical conditions favorable for ore deposition, it is considered in more detail below.

Significance of iron in tourmaline from granitic systems

Whereas tourmaline associated with sedimentary and metamorphic rocks is commonly rich in Mg, tourmaline from granitic environments is typically Fe-rich (Henry and Guidotti, 1985), in particular tourmaline associated with tin mineralization. For example, Pirajno and Smithies (1992) noted that in the case of granite-related Sn-W deposits in South Africa, Namibia and New Zealand, the Fe/(Fe+Mg) ratio of tourmaline increases from < 0.6 for distal deposits to ~1 for proximal and endogranitic deposits. Significantly, as is the case at San Rafael, the early, pre-ore tourmaline in these deposits (e.g., Cornwall and Tasmania) is typically Mg-rich, whereas ore-stage tourmaline is Fe-rich and commonly contains elevated concentrations of Sn (Emond, 1985; Barth, 1988; Griffin et al., 1996; Williamson et al., 2000; LeBoutillier et al., 2002). The opposite trend, i.e., Mg-rich tourmaline associated with cassiterite ores is observed only very rarely, in distal deposits restricted to unusual settings (e.g., the metamorphic Yunlong tin deposit, China - Yu and Jiang, 2003).

The presence of Fe-rich tourmaline in tin deposits is likely related to the fact that in many granites and granitic pegmatites, the bulk rock iron content increases with the degree of melt fractionation (Power, 1968; Neiva, 1974; Manning, 1982; Broska et al., 1998), as does the concentration of tin (Power, 1968; Sinclair and Richardson, 1992). Tin and iron also have a similar geochemical behaviour in hydrothermal fluids, as both are effectively transported in the form of chloride complexes by hot, reducing, relatively acidic and saline solutions (Goldschmidt, 1958; Eugster and Wilson, 1985; Pabalan, 1986; Wood and Samson, 1998). Therefore, the magmatic fluids responsible for the formation of tin deposits, which are typically exsolved from highly-evolved, fractionated magmas (Lehmann, 1990), are likely to be very iron rich.

Tourmaline zoning and cassiterite deposition at San Rafael

The hydrothermal system at San Rafael clearly experienced two different stages of fluid evolution, which were expressed by contrasting styles of veining, alteration and mineralogy. Whereas the early, barren tourmaline-quartz veins are invariably narrow, sealed, and typically discontinuous, indicating that they formed under lithostatic

151

conditions, the ore veins are of the open fracture-filling type, with ubiquitous vugs, and must have formed under largely hydrostatic conditions. This conspicuous difference in vein character is parallelled by a marked change in alteration style (from sericitization and tourmalinization to strong chloritization) and a change in the physicochemical conditions of the ore fluids. Thus, the fluids characterizing the early, barren stage were high temperature, hypersaline brines (>340-535°C, 34-62 wt.% NaCl eq., see Chapters III and V). These brines leached the bulk of alkalis and alkali-earth elements from the granitic precursors, and produced a gain of B of >10,000 % relative to its concentration in the fresh rock (i.e., >100-fold), as well as gains in MgO of 75 % and Fe of ~40 %. Conversely, the ore stage fluids were of only moderate temperature and salinity (>230-360°C, 0-21 wt.% NaCl eq.). While they too caused a strong leaching of alkalis and alkali-earth elements from the wall-rocks, they also produced a much larger gain of Fe than the tourmalinizing fluids, typically between 2-5 fold (200-500 %). In addition, chloritic alteration was accompanied by a 300-2,000 % mass gain in Sn, a 100-2,300 % mass gain in W, a 220-350 % mass gain in Mn, a 100-330 % mass gain in H_2O, and a mass gain of up to 35 % of MgO, relative to their concentrations in the fresh rocks. The obvious question which arises, therefore, is whether these two genetic stages were related, and if it was so, what caused the transition between them.

In this respect, the observations made on the tourmaline-cassiterite-chlorite-arsenopyrite veins are remarkably significant. These peculiar veins contain abundant tourmaline (of two markedly different generations), implying that they represent the early, barren stage of the hydrothermal system, yet they are of the open fracture-filling type, are surrounded by a halo of strong chloritic alteration, and contain cassiterite (features characteristic for the ore veins). This suggests that the main ore stage followed soon after the early barren stage, and that the formation of these veins overlapped the two stages. More importantly, these veins mark the onset of cassiterite and chlorite precipitation and record the major change in fluid chemistry, which accompanied mineralization (as evidenced by the strong increase in the iron content of tourmaline and the sharp change of its color). The fact that these changes were associated with a markedly different vein style, i.e., the first occurrence of open fracture-filling in the deposit paragenesis, implies that the onset of tin mineralization at San Rafael was brought

by a dramatic change in the plumbing of the hydrothermal system, i.e., a transition from a closed system (lithostatic conditions) to an open system (hydrostatic conditions). The hypothesis of a sudden "opening" of the hydrothermal system inevitably raises the issues of fluid boiling and of an influx of external fluids, both of which are very efficient mechanisms for triggering ore deposition. The lack of fluid inclusion assemblages recording boiling, as well as other fluid inclusion and stable isotope evidence suggest strongly the latter scenario, and point to fluid mixing (see Chapter V).

The transition from the pre-ore (tourmalinization) to the ore stage was probably abrupt, as can be deduced from the corrosion of early, Mg-rich tourmaline cores prior to the crystallization of schorl (Fig. 9a), and the sharp changes in composition of successive growth zones, dominated by strong iron enrichment (Fig. 10). The acicular habit of schorl precipitating with cassiterite, and the appearance of needle-tin (fine, acicular cassiterite), preceding the development of coarser crystals of cassiterite also indicate a fast rate of crystallization and, hence, strong gradients in physicochemical conditions (supersaturation). In this context, the strong trend of iron enrichment observed in the tourmaline, and evidenced by the appearance of Fe-chlorite and Fe-rich cassiterite likely reflects the progressive dilution of Fe-rich, magmatic brines by low-salinity fluids (e.g., meteoric waters). Thus, Kwak et al. (1986), have argued that the solubility of iron in hydrothermal brines depends primarily on fluid salinity, and to a lesser extent on temperature. The total iron solubility increases exponentially with the anion content of the fluid (namely, chlorinity) and, therefore, highly saline brines are typically undersaturated in iron. Their dilution by cooler, low-salinity fluids will, however, cause rapid iron saturation and the precipitation of Fe-rich minerals, such as silicates, oxides and sulfides (Fig. 11). Such late formation in the hydrothermal paragenesis of Fe-rich minerals (e.g., hematite, magnetite, pyrite or Fe-chlorite) has been described from some skarn, porphyry-copper and greisen-type deposits and cannot be produced by fluid boiling (Kwak et al., 1986).

The strong iron enrichment of tourmaline, which preceded cassiterite deposition at San Rafael, therefore, appears to be consistent with fluid mixing taking place in the hydrothermal system. We believe, that an episode of tectonic activity took place early in the evolution of the vein system, opening it to an influx of external fluids, which

FIGURE 11. Schematic representation of the inferred fluid evolution and associated paragenesis at San Rafael.
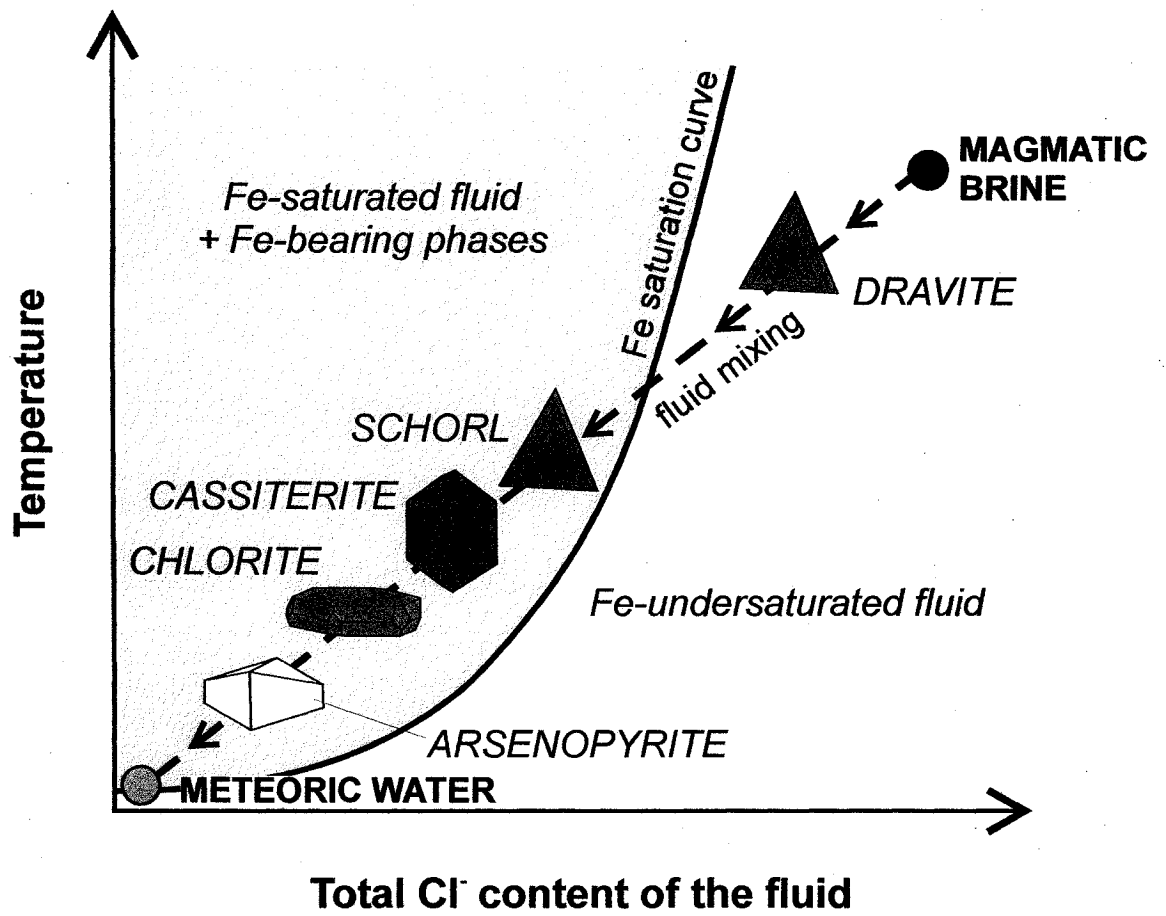
considering the shallow emplacement of the pluton were likely meteoric waters. The mixing of hot, tin and iron-rich magmatic brines with dilute, cooler, and possibly much more oxidizing meteoric waters would not only cause the saturation of Fe-rich gangue minerals, such as schorl and chlorite, but also provide an extremely efficient mechanism for the deposition of cassiterite (*cf.* Heinrich, 1990).

CONCLUSIONS

Tourmaline is the dominant mineral in the early (pre-ore) paragenesis of the San Rafael tin deposit and continued to crystallize until the onset of cassiterite precipitation. Although there are many varieties of tourmaline, there is a clearly recognizable, deposit-wide compositional trend, from early Mg-rich (mostly dravite) to late Fe-rich (schorl). This trend is reminiscent of the overprint by strongly Fe-rich minerals observed in some skarn, porphyry-copper and greisen-type hydrothermal systems, which is interpreted to form upon dilution of Fe-rich magmatic brines by cooler, low-salinity fluids of external origin. Based on structural evidence for an opening of the vein system immediately prior to mineralization, we conclude that the rich tin ores of San Rafael were the result of a sudden influx of dilute fluids (presumably meteoric waters) into the hydrothermal system and their mixing with tin- and iron-rich magmatic brines.

REFERENCES

Barth, W.H. (1988) Compositional variation of zoned tourmalines associated with Sn-W mineralisation. Geological Society of Australia, abstracts, 21, 439-440.

Burt, D.M. (1989) Vector representation of tourmaline compositions. American Mineralogist, 74, 826-839.

Broska, I., Uher, P., Lipka, J. (1998) Brown and blue schörl from the Spis-Gemer granite, Slovakia: composition and genetic relations. Journal of the Czech Geological Society, 43, 1/2, 9-16.

Chappell, B.W. and White, A.J.R. (1974) Two contrasting granite types. Pacific Geology, 8: 173-174.

Emond, D.S. (1985) Geology, mineralogy and petrogenesis of tin-bearing breccias, Oliver Creek, McQuesten River area, Yukon Territory. In: Granite-related mineral deposits; geology, petrogenesis and tectonic setting. Extended abstracts of papers presented at the CIM conference, Taylor, R.P. and Strong, D.F. (eds.), 116-119.

Eugster, H.P. and Wilson, G.A. (1985) Transport and deposition of ore-forming elements in hydrothermal systems associated with granites. In: Halls, C. (chairman) High heat production (HHP) granites, hydrothermal circulation and ore genesis. Institute of Mining and Metallurgy Conference, London, 87-98

Faye, G.H., Manning, P.G., Gosselin, J.R. and Tremblay, R.J. (1974) The optical absorption spectra of tourmaline: importance of charge-transfer processes. Canadian Mineralogist, 12, 370-380.

Farmer, C.B. and Halls, C. (1993) Paragenetic evolution of cassiterite-bearing lodes at South Crofty Mine, Cornwall, United Kingdom. In: Maurice, Y. (ed.) Proceedings of the 8th IAGOD Symposium, Ottawa 1990, E. Schweizerbart'sche Verlagsbuschhandlung, Stuttgart, 365-382.

Goldschmidt, V.M. (1958) Geochemistry. Oxford University Press, 730 p.

Griffin, W.L., Slack, J.F., Ramsden, A.R., Win, T.T. and Ryan, C.G. (1996) Trace elements in tourmalines from massive sulfide deposits and tourmalinites: geochemical controls and exploration applications. Economic Geology, 91, 657-675.

Halls, C. (1994) Energy and mechanism in the magmato-hydrothermal evolution of the Cornubian batholith: a review. In: Metallogeny of collisional orogens; Seltmann, R., Kämpf, H. and Möller, P. (eds.), Czech Geological Survey, Prague, 274-294.

Hawthorne, F.C. and Henry, D.J. (1999) Classification of the minerals of the tourmaline group. European Journal of Mineralogy, 11, 201-215.

Heinrich, C.A. (1990) The chemistry of hydrothermal tin (-tungsten) ore deposition. Economic Geology, 85, 457-481.

Henry, D.J. and Guidotti, C.V. (1985) Tourmaline as a petrogenetic indicator mineral: an example from the staurolite-grade metapelites of NW Maine. American Mineralogist, 70, 1-15.

Henry, D.J. and Dutrow, B.L. (1996) Metamorphic tourmaline and its petrologic applications. In: Grew, E.S., Anovitz, L.M. (eds.), Boron: mineralogy, petrology and geochemistry. Reviews in Mineralogy, 33, Mineralogical Society of America, 503-557.

Jiang, S.-Y., Palmer, M.R., Slack, J.F. and Shaw, D.R. (1998) Paragenesis and chemistry of multistage tourmaline formation in the Sullivan Pb-Zn-Ag deposit, British Columbia. Economic Geology, 93, 47-67.

Kwak, T.A.P., Brown, W.M., Abeysinghe, P.B., Tan, T.H. (1986) Fe solubilities in very saline hydrothermal fluids: Their relation to zoning in some ore deposits. Economic Geology, 81, 447-465.

LeBoutillier, N.G., Camm, G.S., Shail, R.K., Bromley, A.V., Jewson, C. and Hoppe, N. (2002) Tourmaline-quartz-cassiterite mineralization of the Land's End granite at Nanjizal, west Cornwall. Proceedings of the Ussher Society, 10, 3, 312-318.

Lehmann, B. (1990) Metallogeny of tin. Lecture Notes in Earth Sciences 32, Springer-Verlag, Berlin, 211 p.

London, D. and Manning, D.A.C. (1995) Chemical variation and significance of tourmaline from southwest England. Economic Geology, 90, 495-519.

Lynch, G. and Ortega, J. (1997) Hydrothermal alteration and tourmaline-albite equilibria at the Coxheath porphyry Cu-Mo-Au deposit, Nova Scotia. Canadian Mineralogist, 35, 79-94.

Manning, D.A.C. (1982) Chemical and morphological variation in tourmalines from the Hub Kapong batholith of peninsular Thailand. Mineralogical Magazine, 45, 139-147.

Manning, D.A.C. (1991) Chemical variation in tourmalines from south-west England. Proceedings of the Ussher Society, 7, 327-332.

Němec, D. (1973) Tin in tourmalines. Neues Jahrbuch für Mineralogie, Monatshefte, (2), 58-63.

Neiva, A.M.R. (1974) Geochemistry of tourmaline (schorlite) from granites, aplites and pegmatites from Northern Portugal. Geochimica et Cosmochimica Acta, 38, 1307-1317.

Novák, M. (1998) Blue dravite as an indicator of fluid composition during subsolidus replacement processes in Li-poor granitic pegmatites in the Moldanubicum, Czech Republic. Journal of the Czech Geological Society, 43, 1/2, 24-30.

Pabalan, R.T. (1986) Solubility of cassiterite (SnO_2) in NaCl solutions from 200°C - 350°C, with geologic applications. Unpublished Ph.D. thesis, Pennsylvania State University, U.S.A., 141 p.

Pichavant, M. (1981) An experimental study of the effect of boron on a water-saturated haplogranite at 1 Kbar vapour pressure. Contributions to Mineralogy and Petrology, 76, 430-439.

Pichavant, M. and Manning, D. (1984) Petrogenesis of tourmaline granites and topaz granites: the contribution of experimental data. Physics of the Earth and Planetary Interiors, 35, 31-50.

Pirajno, F. and Smithies, R.H. (1992) The FeO/(FeO+MgO) ratio of tourmaline: a useful indicator of spatial variations in granite-related hydrothermal mineral deposits. Journal of Geochemical Exploration, 42, 371-381.

Pollard, P.J., Pichavant, M. and Charoy, B. (1987) Contrasting evolution of fluorine- and boron-rich tin systems. Mineralium Deposita, 22, 315-321.

Power, G.M. (1968) Chemical variation in tourmalines from south-west England. Mineralogical Magazine, 36, 1078-1089.

Slack, J.F. (1996) Tourmaline associations with hydrothermal ore deposits. In: Grew, E.S., Anovitz, L.M. (eds.), Boron: mineralogy, petrology and geochemistry. Reviews in Mineralogy, 33, Mineralogical Society of America, 559-643.

Slack, J.F. and Coad, P.R. (1989) Multiple hydrothermal and metamorphic events in the Kidd Creek volcanogenic massive sulphide deposit, Timmins, Ontario: evidence from tourmalines and chlorites. Canadian Journal of Earth Sciences, 26, 694-715.

Slack, J.F., Ramsden, A.R., Griffin, W.L., Win, T.T., French, D.H. and Ryan, C.G. (1999) Trace elements in tourmaline from the Kidd Creek massive sulfide deposit and vicinity, Timmins, Ontario: a proton microprobe study. *In*: "The giant Kidd Creek

volcanogenic massive sulfide deposit, western Abitibi subprovince, Canada", Economic Geology Monograph 10, Hannington, M.D. and Barrie, C.T. (eds.), 415-430.

Sinclair, W.D. and Richardson, J.M. (1992) Quartz-tourmaline orbicules in the Seagull batholith, Yukon territory. Canadian Mineralogist, 30, 923-935.

Taylor, R.G. (1979) Geology of tin deposits. Elsevier, 543 p.

Taylor, B.E. and Slack, J.F. (1984) Tourmalines from Appalachian-Caledonian massive sulfide deposits: textural, chemical and isotopic relationships. Economic Geology, 79, 1703-1726.

von Goerne, G., Franz, G., and Heinrich, W. (2001) Synthesis of tourmaline solid solutions in the system $Na_2O-MgO-Al_2O_3-SiO_2-B_2O_3-H_2O-HCl$ and the distribution of Na between tourmaline and fluid at 300 to 700°C and 200MPa. Contributions to Mineralogy and Petrology, 141, 160-173.

Williamson, B.J., Spratt, J., Adams, J.T., Tindle, A.G., and Stanley, C.J. (2000) Geochemical constraints from zoned hydrothermal tourmalines on fluid evolution and tin mineralization: an example from fault breccias at Roche, SW England. Journal of Petrology, 41, 1439-1453.

Wood, S.A. and Samson, I. (1998) Ore minerals and metals in hydrothermal solutions. *In*: J.P. Richards and P.B. Larson (eds.) Techniques in hydrothermal ore deposits geology. SEG series – Reviews in Economic Geology 10, 256 p.

Yu, J.-M.and Jiang, S.-Y. (2003) Chemical composition of tourmaline from the Yunlong tin deposit, Yunnan, China: implications for ore genesis and mineral exploration. Mineralogy and Petrology, 77, 67-84.

INTRODUCTION TO CHAPTER V

In the previous chapters, I used the alteration geochemistry and the composition of the gangue minerals to estimate quantitatively the chemical changes associated with discrete hydrothermal episodes at the San Rafael deposit. A particularly important conclusion of these chapters is that the fluid-rock interaction did not favor tin deposition, as chloritic alteration of granitic rocks increases the fluid acidity, and this in turn increases Sn solubility. This explains why the bulk of cassiterite in the deposit is restricted to veins and breccias, as opposed to being disseminated in the chloritic alteration. In Chapter V I apply fluid inclusion and stable isotope data (S,O,H,C) to determining the origin of the ore fluids, their evolution, and the physico-chemical controls on mineralization. This, in turn, allows me to evaluate the possible mechanisms of ore deposition.

CHAPTER V

Stable isotope constraints on ore formation at the San Rafael cassiterite-sulfide deposit, SE Peru

M.S.J. Mlynarczyk, T. Wagner, and A.E. Williams-Jones

ABSTRACT

The San Rafael deposit in the Eastern Cordillera of the Peruvian Central Andes is the world's largest hydrothermal tin lode, with a total resource of ~1 million tonnes metal, at an average grade of 4.7 wt.% Sn. The mineralization is of the cassiterite-sulfide type and occurs in a vertically extensive vein-breccia system, centred on a shallow-level, Late Oligocene granitoid stock. The tin ores form cassiterite-quartz-chlorite-bearing veins and breccias, hosted by several large fault-jogs at depth in the lode. By contrast, copper ores, which contain disseminated acicular cassiterite, are localized in the upper part of the system. Both ore types are associated with a very distinctive strong chloritic alteration, which was preceded by intense sericitization, tourmalinization and tourmaline veining.

The $\delta^{34}S$ composition of San Rafael sulfides ranges between + 2 and + 6 ‰, and varies only very little with location in the deposit. This relatively narrow range of $\delta^{34}S$ values indicates that the hydrothermal system was large-scale, with a quite homogenous source of sulfur, likely of magmatic origin. This is confirmed by the stability relationships of ore minerals, consistent with an initially reducing character of the ore fluids.

Microthermometric studies of fluid inclusions in cassiterite, quartz, tourmaline and fluorite indicate that, whereas the fluids responsible for the early, barren stage were hot, hypersaline magmatic brines (>340-535°C, 34-62 wt.% NaCl eq.), the ore stage fluids had a moderate to low salinity (0-21 wt.% NaCl eq.), and a moderate temperature (>230-360°C), the latter confirmed sphalerite-stannite and chlorite geothermometry. In addition to the marked dilution of the ore fluids, they became progressively more oxidizing, as inferred by the local association of minor hematite with cassiterite, and the ubiquitous replacement of pyrrhotite by pyrite, marcasite and hematite. In parallel, the fluid $\delta^{18}O$ values decreased markedly, whereas the δD values increased slightly, as indicated by the the stable isotope composition of tourmaline, cassiterite, wolframite, quartz, chlorite, calcite, and siderite. This trend is consistent with mixing of the ore fluids with a cooler, isotopically lighter (O) fluid, and cannot be explained by boiling or simple cooling. In conjunction with structural evidence for an opening of the vein system and a transition from hydrostatic to lithostatic conditions at the onset of mineralization, we infer

that ore deposition was caused by an influx of heated meteoric waters and their mixing with tin-bearing, magmatic brines. The oxidation, dilution, cooling and acid neutralization of the ore fluids destabilized chloride complexes of tin and triggered the massive precipitation of cassiterite.

INTRODUCTION

Hydrothermal tin lodes represent a class of granite-related tin deposit characterized by a very high ore grade (~ 1-5 wt.% Sn) and a high tonnage, which makes them an ideal target in the exploration for economically viable primary tin deposits (Taylor, 1979; Hosking, 1988; Menzie et al., 1988). However, despite being mined since antiquity and being well described in the literature, there is still considerable uncertainty over key issues related to their genesis, such as the source of the tin, tungsten and base metals, the origin of the ore fluids and the mechanism of ore deposition. Although it is generally believed that the bulk of the metals is derived directly from an evolved granitic melt by being partitioned into a magmatic aqueous phase, the leaching of crystallized magmatic minerals by later fluids may be another significant metal source (Taylor, 1979; Lehmann, 1990). In addition, some metal could have been derived from the sequences of metasedimentary rocks, which host the granitic plutons (*cf.* Williamson et al., 2000; LeBoutillier et al., 2002). A variety of ore fluids have been invoked, including primary magmatic fluids, meteoric waters, basinal brines (formation waters), metamorphic fluids, and their mixtures. With regard to the meteoric fluids, the timing of their circulation and interaction with magmatic fluids may be relatively early or occur only in the waning stages of the hydrothermal system (for a review, see Alderton and Harmon, 1991; Collins, 1981; Farmer and Halls, 1993; Jackson et al., 2000; Primmer, 1985; Sheppard, 1994; Smith et al., 1996; Sun and Eadington, 1987; Walshe et al., 1996; Wilkinson et al., 1995). Finally, the following mechanisms have been proposed for the precipitation of cassiterite: cooling, pressure decrease, wallrock alteration, boiling, and fluid mixing (Eadington, 1985; Heinrich and Eadington, 1986; Heinrich, 1990; 1995). In particular, it has been suggested that mixing between magmatic and meteoric waters could produce unusually high ore grades (Heinrich, 1990). However, this suggestion remains to be properly tested

because the contribution of meteoric water to hydrothermal systems depositing lode tin mineralization has been poorly documented.

San Rafael, the world's richest primary Sn-Cu deposit, which is located in the high Andes of the Eastern Cordillera of SE Peru and currently exploited by MINSUR S.A., is an ideal natural laboratory, in which to investigate the various issues of lode tin genesis raised above. With a total resource of ~ 1 million metric tonnes Sn, and an average grade of 5 % Sn, the San Rafael lode, which has been exposed by mining activity over a vertical extent of > 1,300 m, allows an unprecedented opportunity to advance our understanding of the formation of this important deposit type. In addition, the deposit is very young (~ 25 Ma) and, therefore, was not affected by any later geological processes. Following a study of the deposit geology (Chapter II) and its alteration (Chapters III and IV), preliminary fluid inclusion microthermometry and a comprehensive investigation of the stable isotope (S,O,H,C) composition of the ore and gangue minerals were conducted, to evaluate the most likely mechanisms of ore deposition, such as fluid mixing, boiling, and cooling.

GEOLOGICAL SETTING

Regional Geology

The San Rafael deposit lies in the northwesternmost extension of the Central Andean Sn-W(-Ag) metallogenic province and crops out on the glaciated slopes of the Cordillera Carabaya, which forms a part of the Eastern Cordillera of Southern Peru (Fig. 1). The geology of this region is dominated by a thick sequence of Lower Paleozoic, marine clastic metasedimentary rocks, which experienced extensive crustal deformation and anatexis in the Cenozoic. The unexposed Precambrian gneissic basement is covered by a 10-15 km thick sequence of Ordovician to Siluro-Devonian metapelites and metapsammites (the San José, Sandía and Ananea Formations), followed by a 3-4 km sequence of late Paleozoic psammites and carbonates (Mississippian Ambo Group, Pennsylvanian Tarma Group, and Permian Copacabana Group) and 3 km of mid-Permian to Triassic red beds and intercalated volcanics (Mitu Group). These rocks are, in turn,

164

FIGURE 1. Geological map of the western part of the San Rafael district (modified after Arenas et al.,1980).
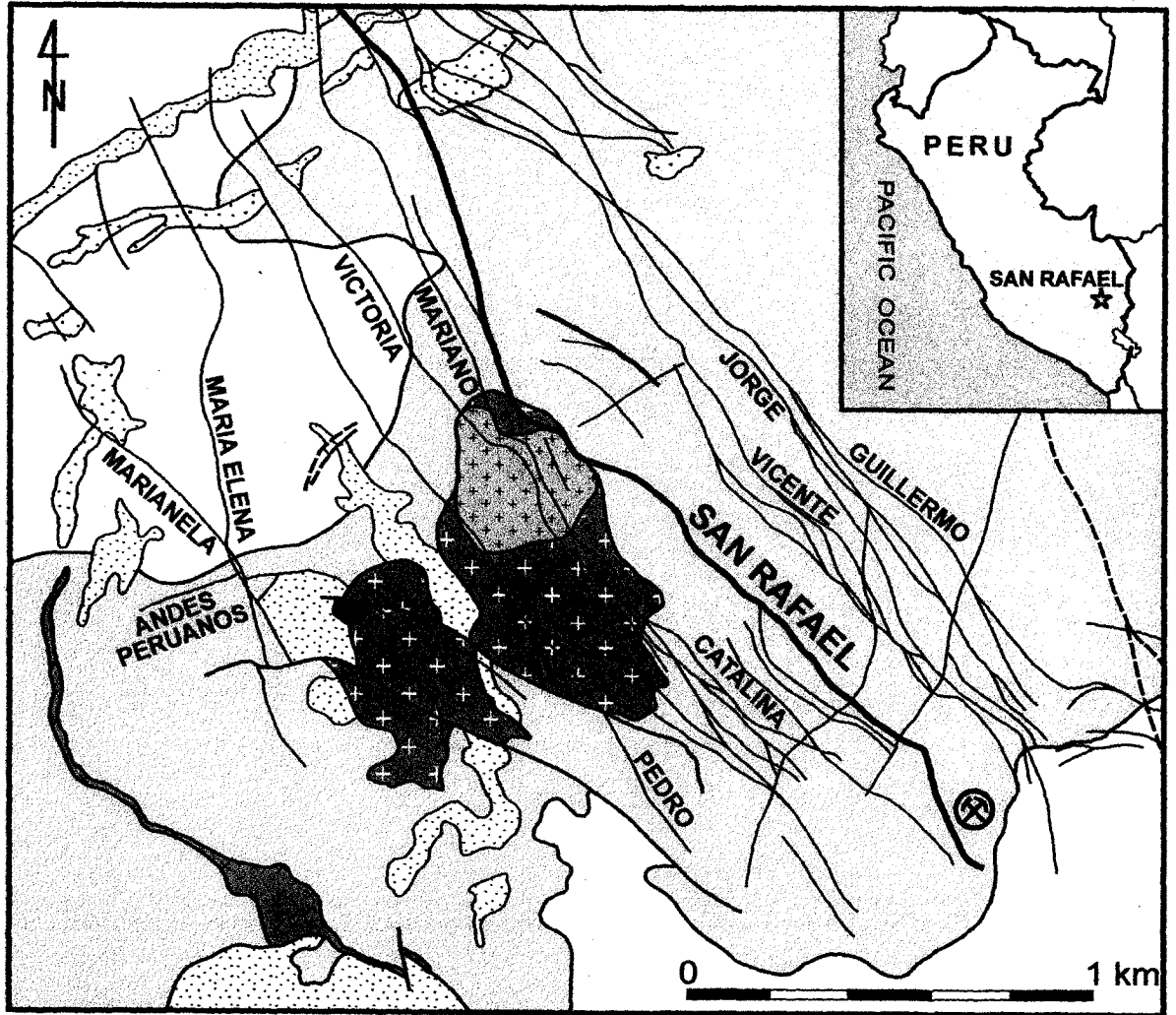
Phyllites (Sandía Fm.) Coarse-grained granitoids Tourmalinized granite

Quartzites (Sandía Fm.) Fine-grained granitoids Mineralized veins

Slates and hornfelses (Sandía Fm.) Dyke of granitoid porphyry Major faults

⊗ Access to the mine

overlain by ~1 km of Cretaceous psammites and carbonates (Cotacucho Group) and ~800 m of Miocene-Pliocene felsic ignimbrites and red beds (Crucero Supergroup). A detailed review of the geology of the area is provided by Laubacher (1978), Clark et al. (1990), and Sandeman et al. (1996). Granitic and granodioritic plutons (some of which host significant Sn-W-base metal mineralization) were emplaced between the Late Devonian and the late Tertiary. Examples of these are the large Permo-Triassic granitic batholiths, which host the Sarita polymetallic deposit, and the middle- to late-Tertiary granitic stocks, which host the San Rafael tin-copper and Palca XI tungsten deposits (Clark et al., 1983; Kontak and Clark, 1988; Kontak et al., 1990). In addition to granitoids, there are also subordinate peralkaline syenites and gabbro-diorites, however, most rocks of mafic composition are volcanic and form localized occurrences of shoshonite, minette, absarokite and high-K calc-alkaline basalt (Kontak et al., 1986; Sandeman et al., 1995).

Deposit Geology

The bulk of the tin in the San Rafael-Quenamari mining district is hosted by a single, large vein-breccia system, called the San Rafael lode. This lode is part of an array of a few dozen subparallel veins, which host minor Sn-(W)-Cu-Zn-Pb-Ag mineralization. Typically, the veins are planar, 500-3500 m long, have a northwestern strike and dip moderately-to-steeply to the north-east. They are centered on a small (< 15 km^2), high-level, late Oligocene granitoid pluton and straddle the contact with the surrounding Lower Paleozoic metasedimentary rocks, which consist dominantly of Ordovician phyllites and quartzites of the Sandía Formation (Fig. 1). The pluton is a polyphase intrusion composed of coarse- to medium-grained K-feldspar-megacrystic, cordierite-biotite-(±garnet-sillimanite) granites, leucogranites and granodiorites, with local minor enclaves of tonalites and quartz diorites. The magma was strongly peraluminous, S-type in character, and clearly formed due to the partial melting of metasediments. However, it was not geochemically evolved, and the different igneous phases do not represent a fractional crystallization series. The pluton is elongated to the northeast and corresponds to a prominent topographic high (Nevado Quenamari, 5300 m), but is only exposed locally,

although its horizontal extent is clearly evident from the distribution of the overlying contact metamorphic rocks (hornfelses and slates).

The San Rafael lode crops out on the eastern flanks of the glacier-capped Quenamari mountain, at an altitude between 4500 and 5100 m, and has a length of over 3 km. It has been exposed by mining over a vertical extent of ~1,300 m (from 5100 to 3800 m above sea level). The latter is presently restricted to the lower 500 m. The upper part of the lode is hosted by metasedimentary rocks, attains a width of up to 2 meters and contains appreciable chalcopyrite and subordinate needle-tin cassiterite. By contrast, the lower part of the lode is hosted by granitic rocks, opens into a series of subvertical shoots, up to 50 meters wide, and contains a large volume of high-grade cassiterite ore (Fig. 2). Quartz and chlorite are the principal gangue minerals, and are common in both the upper and lower parts of the deposit. The lode has an average strike of 330°, dips 40 to 75°NE, and is texturally quite complex, being characterized by multiple episodes of vein reopening and brecciation. Chapter II provides a detailed description of the deposit geology, and proposes that the large ore shoots at depth in the lode represent fault jogs formed during sinistral-normal strike-slip movement along the plane of the lode, which was synchronous with the circulation of the ore fluids.

ALTERATION AND VEIN PARAGENESIS

A detailed program of core-logging and underground mapping in the San Rafael lode outlined as many as 15 distinct vein types, which were arranged chronologically, based on crosscutting relationships (Chapter III). The mineralogy of these veins and the associated wallrock alteration are summarized below, within the framework of four principal paragenetic stages, adopted from a subdivision proposed by Palma (1981).

(I) Early, barren, tourmaline stage

The early, barren stage was initiated by pervasive sericitic alteration, followed by strong tourmalinization, which produced wide alteration halos around early tourmaline-quartz veins and tourmaline stringers. These early veins, which cut through large parts of the

FIGURE 2. Longitudinal section through the San Rafael lode, showing the location of hand samples collected during this study. The location of drill core samples (elevations below ~ 4300 m) is indicated in Tables 1-3.

SE

Nevado Quenamari

NW

5000 m

R165
R709
R708

R725
R726

R729

R428
R429

4500 m

R137
R65

R404
R573

R28 R27
R511
R55 R57

R113
R119
R123

R399

D3-27
D3-39
D3-69

A13

R17

Ore Shoot

Contact Orebody

Copper stopes

Tin orebodies

0

1000m

4000 m
a.s.l.
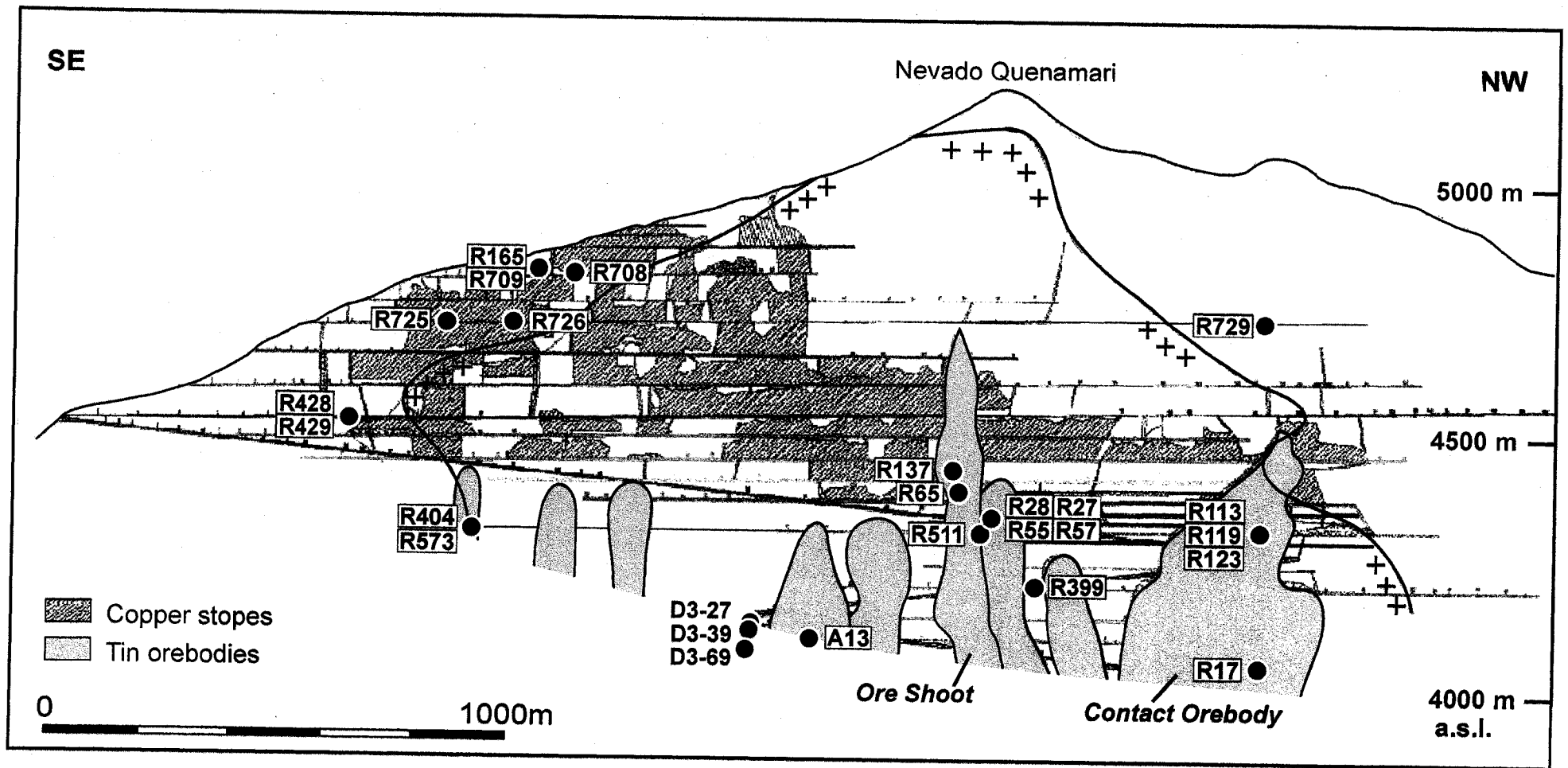
granitic pluton, are typically sealed and lack cassiterite. Locally, however, they host abundant arsenopyrite. The tourmaline is mainly dravite and Fe-rich dravite, but other varieties (foitite, Mg-foitite) were also observed. A detailed description of the mineralogy, chemistry, and temporal relationships of the different varieties of vein and alteration tourmaline can be found in Chapter IV.

In addition to the tourmaline-rich veins, laterally extensive (up to several meters wide) dykes of hydrothermal microbreccia are very common. These are composed of strongly tourmalinized rock flour and subordinate quartz, generally occur in series, and contain the bulk of the tourmaline in the deposit. Commonly, they are criss-crossed by a dense swarm of younger quartz veins, and are associated with subordinate silicification which, locally, could have been coeval with tourmaline precipitation. Both the tourmaline-rich veins and microbreccia dykes occur throughout the vertical extent of the lode, although they are more abundant in its central and upper parts. Petrographic observations indicate that reopening of the early tourmaline veins was quite common, and that there were many episodes of brecciation. It is also apparent that some of the major tourmaline-bearing veins and dykes, which clearly follow the lode along strike and were responsible for establishing its initial structural framework, subsequently reopened during the ore stage.

The principal chemical changes associated with the strong sericite-tourmaline alteration were a near complete removal of alkalis and alkali-earth elements (Na, K, Ca, Ba, Rb, Sr, Cs, Li, and Cl) from the wallrock, and a marked addition of B, Mg, and Fe, as well as possibly Sn, W, and In, though the latter could represent a late overprint.

(II) Main cassiterite stage

The initiation of the ore stage was related to a transition from a closed to an open vein system, as all subsequent vein types are characterized by evident open fracture-filling. The earliest phase of the ore stage is marked by a rare type of tourmaline-cassiterite-chlorite-arsenopyrite vein, in which an obvious but continous transition in mineral chemistry is observed. An early variety of orange dravite was progressively replaced by green schorl (a strongly Fe-rich tourmaline), and was accompanied by simultaneous

precipitation of cassiterite and chlorite, followed by massive arsenopyrite (see Chapter IV).

The majority of the veins and breccias of the main tin ore-stage, however, are characterized by a very simple mineralogy, which consists of cassiterite, chlorite and quartz (Fig. 3a,b). Cassiterite occurs principally as massive, dark-brown, locally botryoidal layers (up to 7 cm wide) or as the beige-colored, collomorph "wood tin". Chlorite is dark green and moderately to strongly Fe-rich, corresponding to ripidolite and daphnite. Locally, the cassiterite-chlorite-quartz veins also contain minor proportions of ferberite (Fe-rich wolframite) or arsenopyrite, which is the only sulfide associated with this stage. Some of the larger veins have quartz-rich centers with a high proportion of sulfides (e.g., chalopyrite, arsenopyrite, pyrite), but the later quartz and sulfides are interpreted to have precipitated mainly during the subsequent sulfide stage, as deduced from cross-cutting vein relationships. Finally, traces of hematite are associated with chlorite and cassiterite in the brecciated ores around elevation 4400 m. No tourmaline occurs in the cassiterite-chlorite-quartz veins, but hairline veinlets of a late, Fe-rich variety of dark-blue or dark-green tourmaline crosscut the early tourmaline veins and microbreccias of the barren stage.

The ubiquitous cassiterite-chlorite-quartz veins are surrounded by wide halos of strong chloritic alteration and display evidence of frequent reopening ("crack and seal" textures) and cockscomb textures, producing the characteristic recurrent alternance of cassiterite, chlorite and quartz layers. There is also ample evidence of multiple brecciation episodes, which led to a locally complex vein texture. The bulk of the tin ores is restricted to the lower, granite-hosted part of the San Rafael lode, especially the wide, subvertical fault-jogs, which form elongated sinuous zones up to 50-m-wide. The highest ore grades (up to 45 wt.% Sn) are associated with several-meter-wide breccia zones, which either contain fragments of cassiterite veins cemented by chlorite and quartz, or fragments of chloritized wallrock cemented by cassiterite and quartz. Cassiterite mineralization also has a very high tin grade in the major (1-2 m wide) footwall / hangingwall veins of the lode structure, as well as in locations where veins are deflected, branch, or intersect. It should be emphasized that the bulk of the tin is contained in the veins, veinlets and breccias, as opposed to being disseminated in the chloritized wallrock

FIGURE 3. Ores in hand samples. **a** – Complex, open-space filling; quartz-cassiterite-sulfide vein (the arrow indicates the direction of growth). Near the strongly chloritized margin of the vein there are alternating layers of cassiterite, chlorite and quartz. The center of the vein consists of large quartz crystals capped by arsenopyrite, with minor grains of sphalerite and chalcopyrite. (Sample SAR-R511, Ore Shoot, 4310 m level). **b** – An example of typical tin ore from a fault-jog in the lower part of the deposit. Layers of massive, dark-brown cassiterite overgrow fragments of early quartz-tourmaline breccia and chloritized wallrock (Sample SAR-R464, Contact Orebody, 4350 m level). **c** – Typical copper ore from the upper part of the deposit, composed mostly of chalcopyrite, with subordinate quartz and pyrite. (Sample SAR-R710, San Rafael lode, level 4820 m). **d** – Broken fragments of sphalerite and chalcopyrite, cemented by quartz, in the central part of a quartz-chalcopyrite vein. (Sample SAR-R722, San Rafael lode, 4730 m level).

a

cpy sph apy qtz

b

qtz

cas

5.5 cm

c

cpy

d

sph

qtz

3.5 cm
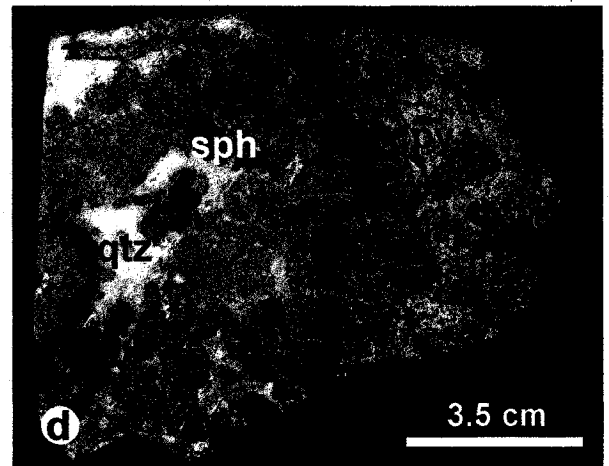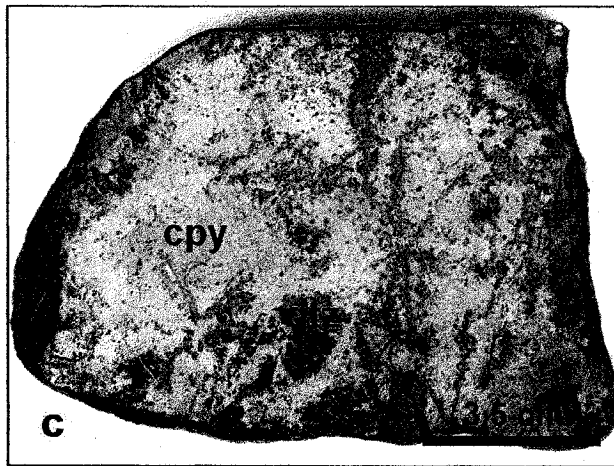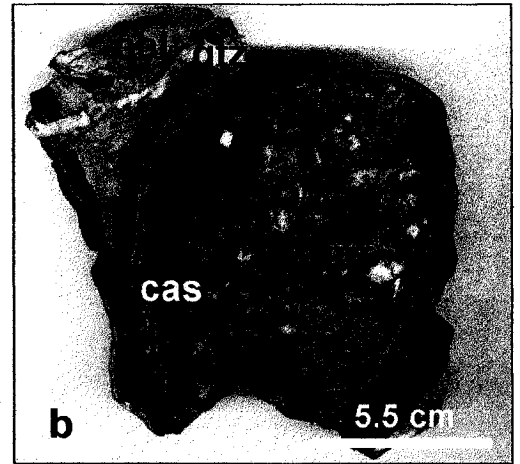
The entire structure of the San Rafael lode is enveloped by a wide zone of very strong, texturally destructive, chloritic alteration, which affected the host rocks during this and the following stage. Chloritization is the dominant type of alteration in the deposit, affecting its entire vertical extent and strongly overprinting all earlier alteration types. Locally, chloritization is associated with silicification, but the latter may have been developed late. Studies of the whole-rock chemistry indicate that chloritization leached the bulk of alkalis and alkali-earth elements from the granitic wallrocks (Na, K, Ca, Ba, Rb, Sr, Cs, and F, Cl, S) and introduced large amounts of Fe, H_2O, Mn, Sn, W, In and Mg.

(III) Sulfide stage

The bulk of the sulfide ores are restricted to the middle and upper parts of the San Rafael lode, and are especially well-developed where the lode straddles the intrusion-slate contact and in the slates. The sulfides postdate cassiterite deposition, and are characterized by a great mineralogical diversity. The dominant sulfide mineral is chalcopyrite (Fig. 3c), which is associated with subordinate amounts of needle-tin cassiterite and stannite, yielding a low grade (0.5-1%) tin ore. Other sulfides, which locally are very abundant, are pyrrhotite, arsenopyrite, pyrite, sphalerite and galena. In addition, hematite, marcasite, bismuthinite and native bismuth have also been observed. The main gangue minerals are quartz, chlorite, fluorite and carbonates (principally siderite and calcite).

The minerals formed during the sulfide stage occur either in distinct quartz-sulfide veins (commonly with a marked predominance of either quartz or sulfides) or as a late filling (or reopening) of stage II cassiterite-quartz-chlorite veins. The structural orientation of the veins formed during the sulfide stage is the same as that of Stage II veins, suggesting a common mechanism of formation. Moreover, they are associated with the same, pervasive chloritic alteration. In addition, the lode hosts breccias, which either contain sulfide fragments (Fig. 3d) or are cemented by sulfides, as well as large (10-30 cm) vugs filled by pyrite and marcasite. It is inferred that most of the pyrite, marcasite and siderite originated by hypogene replacement of pyrrhotite, as can be deduced, for

example, from cubes of pyrite (several cm long) grown inside large vugs in massive pyrrhotite ore, and siderite veinlets cutting across pyrrhotite.

Reflected light petrography suggests that the sulfide ores of San Rafael formed at high-temperature, as indicated by the widespread presence of well-developed sphalerite stars and common immiscibility features within chalcopyrite and sphalerite blebs enclosed in other sulfides. Examples of some of these ore textures are shown in Figure 4 and illustrate that, although specific paragenetic sequences can be determined for individual samples, these parageneses generally cannot be extended to the entire deposit, as most sulfides (aside from pyrite and marcasite) occur in multiple generations and are broadly coeval.

(IV) Late, barren quartz-carbonates stage

The last stage of veining is represented by numerous, barren quartz ± carbonate veins (they contain traces of chalcopyrite and sphalerite but no cassiterite), with narrow but strongly chloritized margins. These veins crosscut all other types of veins and breccias, locally producing dense stockworks, and are commonly quite thick (0.2-1 m), implying massive precipitation of quartz in the closing stages of the hydrothermal system. On this basis, the bulk of silicification observed in the deposit is tentatively assigned to this stage.

In addition to the four hypogene stages, a fifth, *supergene* stage is well developed in the uppermost, copper-rich part of the lode. This resulted in the alteration of the primary ores to Fe-oxides and hydroxides (limonite) and secondary Cu minerals, such as covellite and chalcocite. No secondary enrichment of tin minerals was observed.

FLUID INCLUSIONS

Petrography

A detailed study of fluid inclusions in the San Rafael ores is currently in progress and the preliminary results are summarized below. The minerals studied were quartz, cassiterite, tourmaline and fluorite, of which over two dozens fluid inclusion sections were made.

FIGURE 4. Reflected light microphotographs of ore samples. **a** – Alternating layers of chlorite, cassiterite and quartz, typical of the rich tin ores hosted by the fault-jogs in the deeper parts of the deposit. (Sample SAR-R119, vein selvage, Contact Orebody, 4310 m level). **b** – Aggregates of needle-tin cassiterite crystals (seen in cross-section), intergrown with chlorite, quartz and chalcopyrite in ore from the upper part of the deposit. (Sample SAR-R725, San Rafael lode, 4730 m level). **c** – Needle-tin cassiterite, rimmed and crosscut by stannite, associated with chlorite, chalcopyrite and pyrite, which contains inclusions of sphalerite and pyrrhotite. (Sample SAR-R119, center of the vein, Contact Orebody, 4310 m level). **d** – Euhedral arsenopyrite overgrown by chlorite, chalcopyrite and cassiterite. The host chalcopyrite contains abundant blebs of pyrrhotite (locally replaced by pyrite) and veinlets of sphalerite (Sample SAR-R55, Ore Shoot, 4330 m level). **e** – Arsenopyrite replaced by sphalerite and galena, and overgrown by chalcopyrite and pyrrhotite. Pyrrhotite is partly replaced by pyrite and marcasite (Sample SAR-A1-1, Orebody "150", level 4100 m). **f** – Sphalerite with abundant chalcopyrite inclusions, veined by chalcopyrite, quartz, and pyrite. The latter sulfides contain fine sphalerite inclusions (Sample SAR-R28, Ore Shoot, 4330 m level). **g** – Sphalerite rimmed by stannite, enclosed in quartz, and neighboring chalcopyrite and pyrite (Sample SAR-R119, center of the vein, Contact Orebody, 4310 m level). **h** – Euhedral crystals of late pyrite in small vugs hosted by chalcopyrite, and crosscut by late sphalerite veinlets. (Copper ore, characteristic of the upper levels of the deposit. Sample SAR-R710, San Rafael lode, level 4820 m).
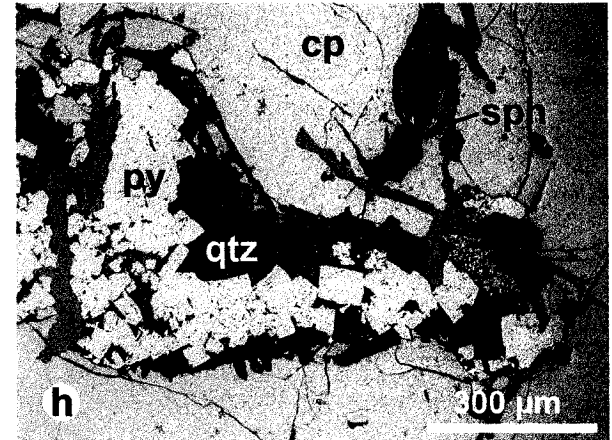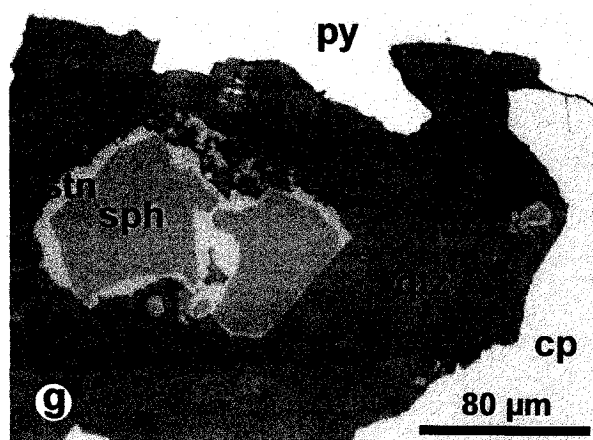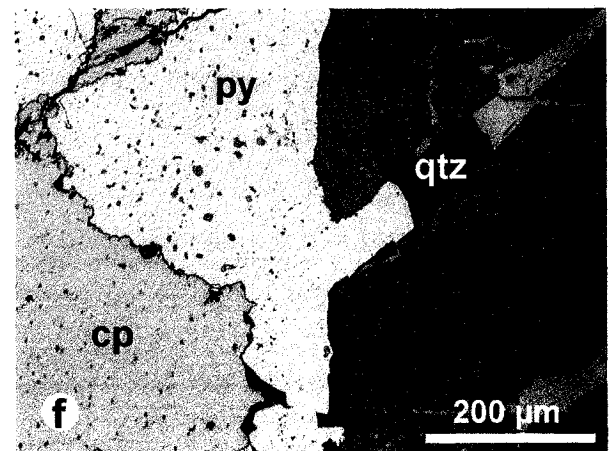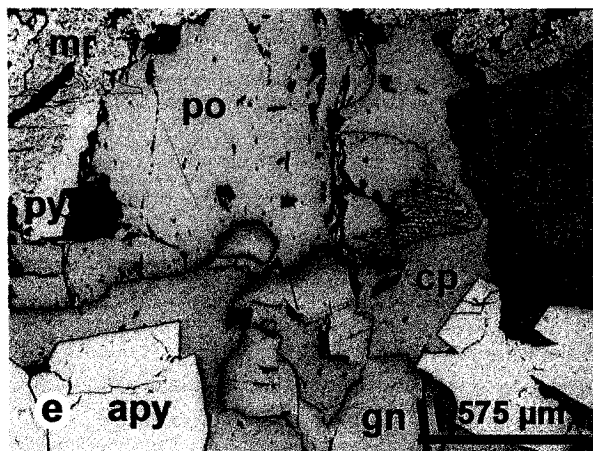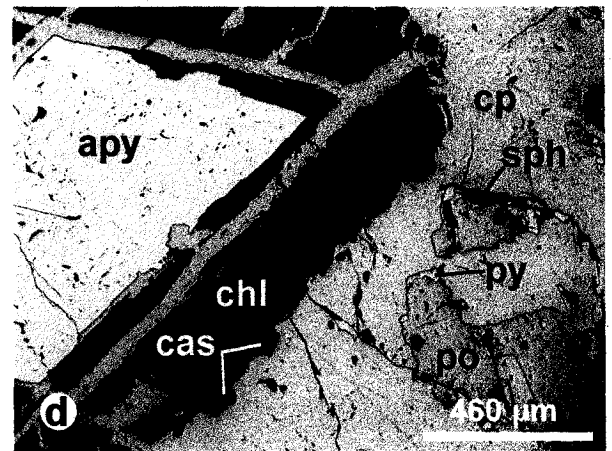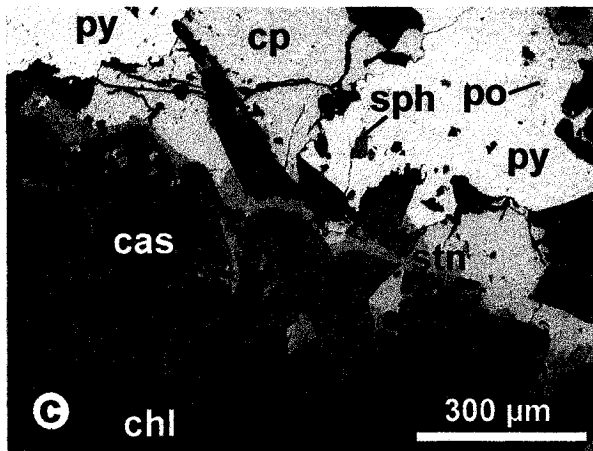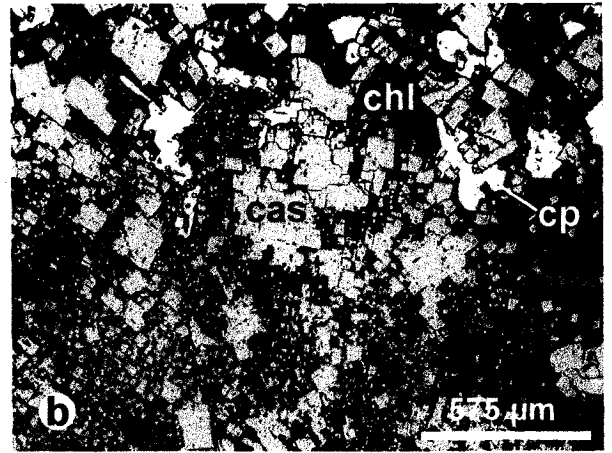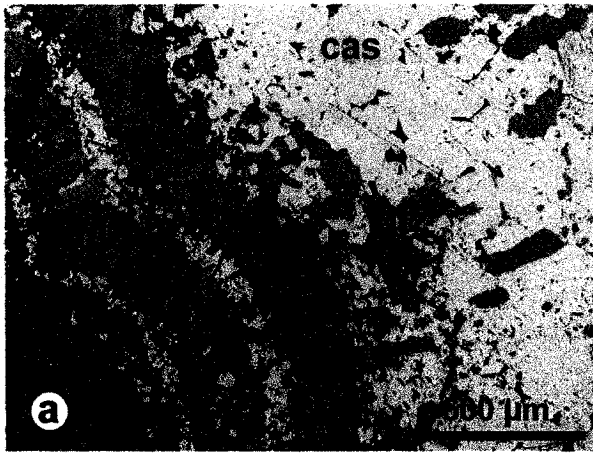
All of the doubly-polished sections contain an abundance of fluid inclusions, ranging in diameter between 2 and 200 μm, many of which clearly represent different generations of secondary inclusions. The majority of the inclusions are of the liquid-vapor type, with one or more solid phases commonly present. These comprise ubiquitous, highly birefringent, single fibre-like solids, which occasionally occur in bundles and could be hydrous phyllosilicates (chlorite or phengitic sericite-illite ?); sea urchin-like aggregates of radiating birefringent crystals (dawsonite ?); transparent, platy solids, some of which are birefringent (probable Fe-Al-Na-Ca-bearing chlorides and carbonates); single tiny specks of an equant opaque mineral (chalcopyrite ?); cubes of halite (in hypersaline inclusions); relatively uncommon, finely prismatic crystals of cassiterite (needle-tin variety); anhedral grains of cassiterite (occurring also as solid inclusions); and, finally, bladed crystals of calcite (in late quartz-calcite veins). With the exception of halite, most of these solids do not redissolve on heating. In addition to the solid-bearing inclusions (some of which are of the "multisolid" type), vapor-rich and vapor-only fluid inclusions are locally present, but evidence of boiling is restricted to the early (I) paragenetic stage. No aqueous-carbonic inclusions were observed in the minerals studied and preliminary gas chromatographic analyses of inclusion fluids indicate very low proportions of CO_2 and CH_4.

Two noteworthy problems were encountered during the study of fluid inclusions from San Rafael ores. The first concerns the unambigous identification of primary, pseudosecondary and secondary inclusions. It is related to the abundance of multiple generations of secondary inclusions, whose trails are locally very dense (implying a large chance that some of the primary inclusions were refilled). In addition, some of the secondary fractures in the host minerals (especially quartz) healed very well, producing scattered inclusions, which appear isolated but are in fact secondary. As a result, clusters of fluid inclusions displaying highly variable salinities, likely unrelated to primary entrapment are quite common. The second problem is related to post-entrapment phenomena, in particular necking down after a phase change (*cf.* Roedder, 1984; Goldstein and Reynolds, 1994), which was observed both in primary and secondary inclusions. This phenomenon produced highly variable phase proportions in the inclusions (e.g., the formation of liquid-only inclusions among high temperature

assemblages) and leads to a large scatter of T_h data. Both problems have been dealt with by an especially critical selection of primary and pseudosecondary inclusions, and by cross-checking several (distant) fluid inclusion assemblages, possibly in more than one host mineral, for every section studied.

Microthermometric studies

Microthermometric measurements were performed at McGill University on a Linkam THMSG-600 fluid inclusion stage, using synthetic fluid inclusions as temperature standards (calibration temperatures: -56.6, -21.2, -10.7, 0.0, and 374.1°C), freezing rates of 0.1°C and heating rates of 1°C, respectively. Several fluid inclusion assemblages (in the sense of Goldstein and Reynolds, 1994) were studied within each sample, using the cycling technique method of Tm_{ice} and T_h determination described by Haynes (1985).

The preliminary results of fluid inclusion microthermometry are presented on a homogenization temperature (T_h) - salinity diagram (Fig. 5). The total salinity of the inclusion fluids (wt.% NaCl eq.) was calculated using the equation of Bodnar (1993) - for low and moderate-salinity inclusions, and the equation of Sterner et al. (1988) - for hypersaline inclusions, i.e., those containing a crystal of halite. It should be noted that, although NaCl is the dominant solute, a high content of $CaCl_2$ and some subordinate KCl are present in the cassiterite-hosted primary and pseudosecondary inclusions. This was inferred from the microthermometric measurements (temperature of the eutectic between -50 to -60°C, temperature of hydrohalite dissolution close to -30°C) and, more directly, by electron microprobe analysis of fluid inclusion decrepitate mounds. Although the amount of iron detected in the analyzed decrepitate mounds was rather low, $FeCl_2$ also appears to have been an important solute, as indicated by the bright orange-red color, typically displayed by the products of fluid inclusion decrepitation upon rapid heating

Stage I quartz- and tourmaline-hosted inclusions have a salinity range of 34-62 wt.% NaCl eq. (with most data clustering between 41-56 wt.%) and homogenize by the disappearance of either halite or vapor in the range 240-535°C (mostly 340-475°C).

FIGURE 5. Homogenization temperature versus salinity of fluid inclusions from San Rafael ores. The host minerals investigated were quartz, fluorite, cassiterite and tourmaline. The abbreviations are: L - liquid, V - vapor, H - halite.
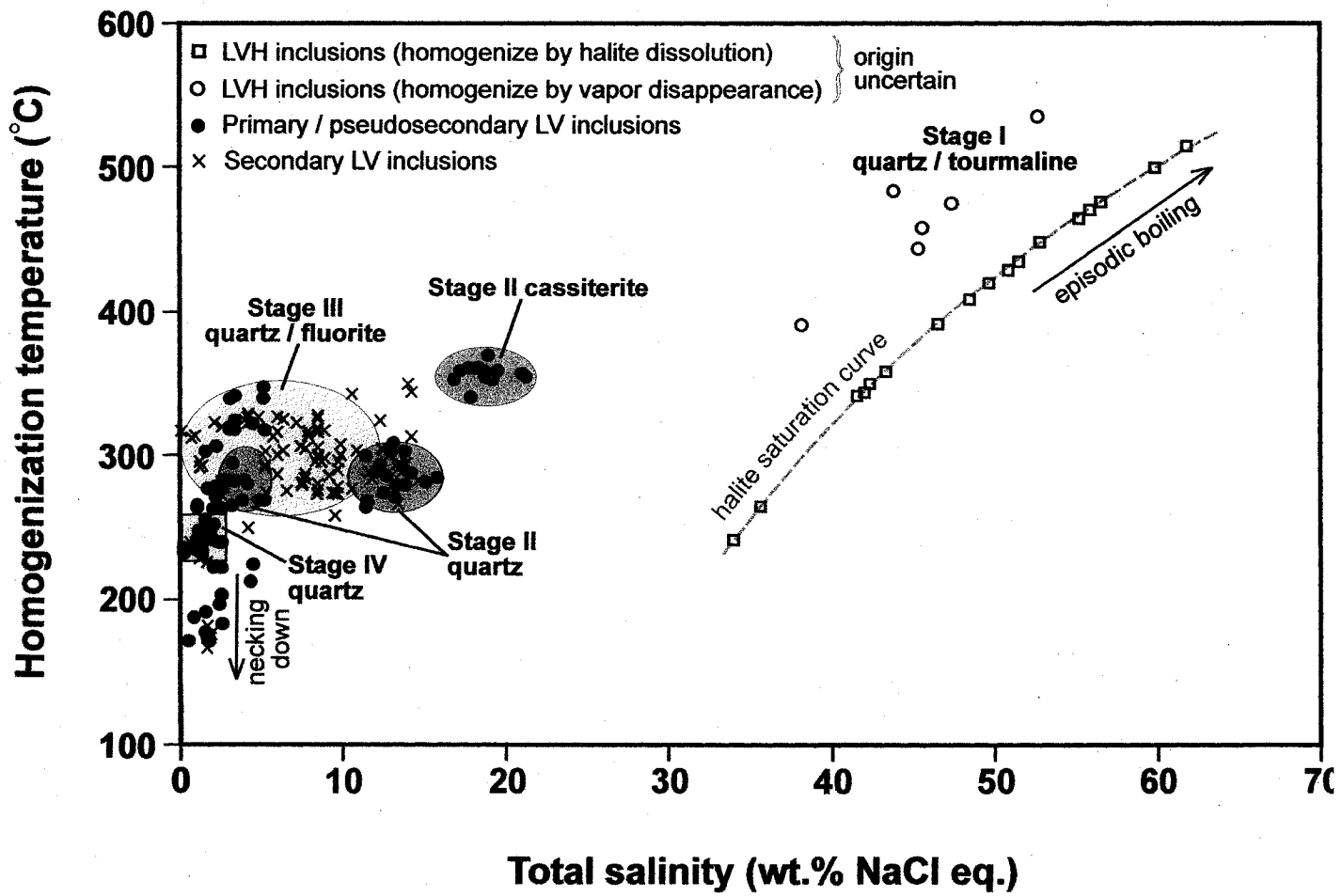
Based on petrographic evidence, it is inferred that the inclusions, which have a very high-salinity and homogenization temperature, formed due to local boiling of the early fluids, although necking down after a phase change could also explain the highly variable phase ratios observed within fluid inclusion assemblages. The data obtained are in broad agreement with the study of Kontak and Clark (2002) and show a similar salinity gap between 21-34 wt.% NaCl eq., which potentially has a very important ore-genetic significance (see below).

Stage II, cassiterite-hosted, primary and pseudosecondary fluid inclusions have a very narrow range of salinity (17-21 wt.% NaCl eq.) and T_h (354-361°C). On the other hand, quartz-hosted inclusions from the same stage exhibit a markedly lower temperature and salinity, which vary depending on the generation of the host quartz (11-16 wt.% NaCl eq. and 265-305°C or 2.5-5.5 wt.% NaCl eq. and 265-295°C). The salinity of the fluids, which precipitated Stage II quartz is likely to have spanned the entire range between 2.5 and 16 wt.% NaCl eq., as suggested by the fluids trapped in secondary inclusions, but what is most remarkable is the presence of fluids of a very low salinity (T_{mice} as high as -1.3°C), which are quite similar in composition and temperature to the fluids, which precipitated the barren quartz from Stage IV (Fig.5). In addition, the character of the ore veins, in which layers of cassiterite, chlorite and quartz repetitively alternate (*cf.* Fig.8), and the consistently lower homogenization temperature and salinity of fluid inclusions trapped in quartz layers (as opposed to those of cassiterite) indicate marked, periodic fluctuations in the physicochemistry of the fluids circulating in the vein system, an observation strongly indicative of repetitive fluid mixing.

Primary inclusions in Stage III quartz and fluorite are characterized by a salinity between 0.5-13 wt.% NaCl eq. (mostly 3-6 wt.%) and a T_h in the range 265-340°C. It should be noted here that pimary and pseudosecondary inclusions from phantom quartz associated with chalcopyrite from the upper zone of the deposit (sample R709, elevation 4820 m) have, on average, a T_h lower by ~ 40°C than inclusions hosted by a very similar phantom quartz, associated with the chalcopyrite-rich centers of deeper-seated Stage II/III veins (sample R119, elevation 4310 m). Another notable observation is an apparent lower

Th limit of ~ 265°C consistently displayed by all (primary/secondary) Stage II and Stage III inclusions.

Finally, inclusions hosted by Stage IV quartz exhibit the lowest salinity (0-2.5 wt.% NaCl eq.) and homogenization temperature (235-265°C). The presence of extremely dilute fluids is emphasized, as the the values for the final ice melting temperature (Tm_{ice}) are as high as -0.1°C, i.e., within the limits of the microthermometric stage precision from the value of zero. Last of all, when the results of fluid inclusion microthermometry for all four paragenetic stages are considered together (Fig. 5), it is quite significant that the sets of fluid temperature - salinity conditions recorded for the discrete stages form a broad linear trend, potentially suggestive of a mixing line.

OTHER GEOTHERMOMETERS

Chlorite geothermometry

In Chapter III, I have tested the empirical geothermometers of Cathelineau (1988) and Jowett (1991) on different samples of alteration and vein chlorite from Stage II of the paragenesis. The temperatures of tin ore formation obtained range between 335 and 415°C. The geothermometer of Jowett yields values 5-15°C higher than that of Cathelineau, and the values for alteration chlorite are, on average, ~50°C higher than those for vein chlorite. On the other hand, the theoretical geothermometer of Walshe (1986), yields temperatures in the range 295- 320°C for the alteration chlorite, which is considered an underestimation. Overall, the results suggest that the chlorite (and, by inference, the associated cassiterite) formed in the upper part of the temperature range 300-400°C, in good agreement with estimates from fluid inclusion microthermometry.

Sphalerite-stannite geothermometry

The Stage III sulfide ores commonly contain microscopic overgrowths of stannite on sphalerite (Fig. 4g), as well as less common intergrowths between these two minerals. Nekrasov et al. (1976, 1979), Shimizu and Shikazono (1985), and Bortnikov et al. (1990) have shown that the compositions of sphalerite and stannite, which are in equilibrium, can

be successfully used as a geothermometer. Carefully selected sphalerite-stannite intergrowths in about a dozen ore samples were analyzed by electron microprobe at McGill University, using an accelerating voltage of 20 kV, a beam current of 30 nA, and a spot size of ≤ 3 μm. Representative results and average data are given in Table 1. The equation of Nakamura and Shima (1982) was used to calculate the formation temperature of the intergrowths, which is interpreted to represent the lower temperature limit of Stage III ore formation. As can be seen in Table 1, this temperature is typically in the range 270-290°C, in very good agreement with the results of fluid inclusion studies.

STABLE ISOTOPE STUDIES

Analytical techniques

Separates of hydrothermal carbonate (siderite, calcite) and oxide/silicate minerals (quartz, cassiterite, wolframite, chlorite, tourmaline) were prepared by careful hand-picking under a binocular microscope, followed by cleaning in doubly-distilled water. Sulfide minerals (pyrite, pyrrhotite, arsenopyrite, chalcopyrite, sphalerite, galena) were analysed by *in situ* laser combustion from standard polished blocks. Whole-rock oxygen isotope compositions were analyzed from rock powders prepared by standard crushing and milling techniques. All mineral separates and whole-rock samples were dried at 80°C for at least 6 hours prior to isotopic analysis.

Sulfide minerals were combusted in an oxygen atmosphere using a SPECTRON LASERS 902Q CW Nd:YAG laser (1 W power); typical spot diameters in this study were 200-400 μm. Laser extraction was followed by cryogenic purification of the SO_2 gas and subsequent on-line mass-spectrometric analysis. Details of the laser extraction technique, calibration and correction procedures are provided by Kelley and Fallick (1990) and Kelley et al. (1992). Laser calibration data for arsenopyrite were taken from the study of Wagner et al. (2004). Reproducibility of the analytical results, and mass spectrometer calibration, was monitored through replicate measurements of international standards NBS-123 ($\delta^{34}S_{V-CDT}$: +17.1 ‰) and IAEA-S-3 ($\delta^{34}S_{V-CDT}$: −31.0 ‰), as well as the

180

TABLE 1. Composition of sphalerite-stannite intergrowths and equilibrium temperatures calculated using the geothermometer of Nakamura and Shima (1982).

Sample	R27		R119		R447	
Location	*Ore Shoot 4330 m*		*Contact Orebody 4310 m*		*Contact Orebody 4270 m*	
Mineral	Sphalerite	Stannite	Sphalerite	Stannite	Sphalerite	Stannite
S	33.19	30.13	33.45	30.02	33.05	29.62
Fe	11.14	14.94	11.79	15.24	11.465	14.4
Zn	54.55	2.11	53.69	1.80	52.8	1.43
Sn	0.04	25.56	0.00	24.99	0.0165	26.51
Cu	0.13	28.34	0.20	27.93	0.513	28.25
Total*	*99.50*	*101.59*	*99.65*	*100.76*	*98.3505*	*100.897*
(XFe/XZn)	0.204	7.081	0.220	8.467	0.217	10.070
Temp (Nakamura)		282		277		269

Sample	R404		A1-1		R65	
Location	*S Contact Orebody 4310 m*		*"150" Orebody 4100 m*		*Ore Shoot 4390 m*	
Mineral	Sphalerite	Stannite	Sphalerite	Stannite	Sphalerite	Stannite
S	34.20	30.41	33.91	29.52	33.605	30.1
Fe	12.70	13.75	13.69	14.23	11.32	13.95
Zn	52.83	2.59	50.60	1.69	53.55	1.42
Sn	0.01	26.85	0.00	25.40	0.068	26.32
Cu	0.10	28.53	0.82	28.27	0.4215	28.52
Total*	*100.35*	*102.90*	*99.36*	*99.70*	*99.266*	*101.209*
(XFe/XZn)	0.240	5.309	0.270	8.420	0.211	9.824
Temp (Nakamura)		305		288		269

* Only those elements that are of interest are listed in the table
The equilibrium temperature was calculated using the equation of Nakamura and Shima (1982) and is expressed in degrees Celsius.

internal lab standard CP-1 ($\delta^{34}S_{V-CDT}$: –4.6 ‰). The analytical precision (1σ) was around ± 0.2 ‰. All sulfur isotope compositions are reported in standard delta notation relative to V-CDT.

Oxygen was extracted from mineral separates and whole-rock powders by reacting 1-5 mg of sample with purified chlorine trifluoride in a laser fluorination system, based on techniques of Sharp (1990) and Mattey and Macpherson (1993). The oxygen was converted to CO_2 by reaction with a heated graphite rod; the isotopic composition of the cryogenically purified CO_2 gas was measured on-line with a VG PRISM III mass spectrometer. Analytical precision was controlled through replicate measurements of the internal laboratory standard SES-2 ($\delta^{18}O_{V-SMOW}$: +10.2 ‰) during the course of the study. The latter was calibrated against international standards IAEA-NBS-28 ($\delta^{18}O_{V-SMOW}$: +9.6 ‰) and IAEA-NBS-30 ($\delta^{18}O_{V-SMOW}$: +5.1 ‰). Precision (1σ) was found to be better than ± 0.2 ‰ for the whole dataset. Some additional tourmaline samples were analyzed by conventional techniques following the procedures of Clayton and Mayeda (1963). All O isotope data are reported relative to V-SMOW.

Hydrothermal carbonates were analysed for their C and O isotope composition using an Analytical Precision AP2003 continuous-flow mass spectrometer, equipped with an automated carbonate preparation system. About 1 mg of sample powder was placed in a 6 ml vacutainer, then sealed and loaded onto the autosampling unit. Each sample was flushed with helium, then a pre-determined amount of 93 % phosphoric acid was injected into each tube, essentially following the procedure of McCrea (1950). The acid reaction was conducted at a temperature of 70 ± 0.1 °C; reaction times were 24 hours for pure calcite samples and 120 hours for all other carbonates. After completion of the reaction, the samples were transferred to the processing system and analysed with the AP2003 mass spectrometer. Oxygen isotope data for siderite were corrected using a fractionation factor, $\alpha_{CO2-FeCO3}$, of 1.00971 calculated from Rosenbaum and Sheppard (1986). Reproducibility of the analytical results was monitored through replicate measurements of the internal Mab2b standard ($\delta^{13}C_{V-PDB}$: +2.48 ‰; $\delta^{18}O_{V-PDB}$: –2.40 ‰) before and after each batch of samples. Accuracy was controlled by replicate measurements of international standards IAEA-CO-1 ($\delta^{13}C_{V-PDB}$: +2.48 ‰; $\delta^{18}O_{V-PDB}$: –2.44) and IAEA-

NBS-19 ($\delta^{13}C_{V-PDB}$: +1.95 ‰; $\delta^{18}O_{V-PDB}$: –2.20 ‰). External precision (1σ) was found to be better than ± 0.2 ‰ for both carbon and oxygen isotope compositions. Carbon and oxygen isotope data are reported relative to V-PDB and V-SMOW, respectively.

Hydrogen isotope analyses of chlorite and tourmaline were carried in the laboratory of Dr. Kurt Kyser at Queens University (Ontario, Canada) by elemental analysis continuous flow-isotope ratio mass spectrometry (CF-IRMS), using a high-temperature reduction method (Sharp et al., 2001). This method involves passing the sample in a He stream through a carbon-packed furnace heated to 1450°C, and releasing the water, which is reduced to H_2. Hydrogen gas is purified by passing it through a 5A molecular sieve gas chromatographic column, after which it is admitted into the source of a Finnigan Mat Delta XL Plus mass spectrometer. The hydrogen isotope data are reported relative to the Vienna standard mean ocean water (VSMOW) standard.

Sulfur isotope data

A total of 64 *in-situ* laser sulfur isotope analyses were performed on polished blocks from 20 samples, spanning both the paragenesis and the vertical extent of the deposit. The majority of the samples are from Stage III (sulfide stage), characterized by the abundance of multiple sulfide species, in contrast to Stages I and II, where sulfides are scarce and represented only by arsenopyrite. The sulfides analyzed are arsenopyrite, chalcopyrite, pyrrhotite, pyrite, sphalerite and galena, and typically, several coexisting sulfides were analyzed in every sample (Fig. 6). The results of the analyses are listed in Table 2 and are summarized in the form of histograms in Figure 7. It is apparent that, overall, the sulfide ores have a relatively uniform $\delta^{34}S$ composition, ranging between + 2 and + 6 ‰. Although the range of $\delta^{34}S$ values is narrow, as could be expected from a deposit related to S-type granitoids (Ohmoto and Goldhaber, 1997), specific minerals within individual samples commonly display variable $\delta^{34}S$ values. For example, the $\delta^{34}S$ of arsenopyrite in sample D3-182b changes within the same growth zone from + 3.6 to + 6.2, whereas the $\delta^{34}S$ of galena in sample R428 varies from + 1.2 to + 5.1 within only a few mm (Fig.6, Table 2). There is, however, little variation in the $\delta^{34}S$ values of the sulfide minerals with respect to their location in the deposit. Thus, the range of $\delta^{34}S$ values only slightly

FIGURE 6. Location of selected in-situ laser S isotope analyses. The average diameter of the polished blocks is 2.5 cm. (apy - arsenopyrite, py - pyrite, cpy - chalcopyrite, po - pyrrhotite, sph - sphalerite, gn - galena, qtz - quartz, tur - tourmaline).

D3-27
- tur
- + 3.7 (apy)
- qtz
- tur
- + 3.6 (apy)
- apy
- + 5.4 (sph)

R 404
- qtz
- py
- (gn) + 5.3
- + 5.9 (sph)
- + 3.8 (py)
- + 4.2 (py)

R 119
- cpy
- + 5.0 (cpy)
- py
- + 5.1 (py)
- qtz
- + 5.5 (c

R 511a
- cpy
- + 3.9 (apy)
- apy
- qtz
- + 4.4 (apy)

J 410
- po
- py
- qtz
- + 4.8 (py)
- + 5.0 (po)
- + 3.7 (po)
- + 4.0 (po)

R 428
- gn
- + 5.1 (gn)
- + 1.2 (gn)
- + 2.4 (gn)
- + 6.3 (sph)
- qtz
- + 4.8 (sph)
- + 1.4 (gn)
- sph
- + 5.4 (sph)
- + 3.0 (cpy)
- cpy
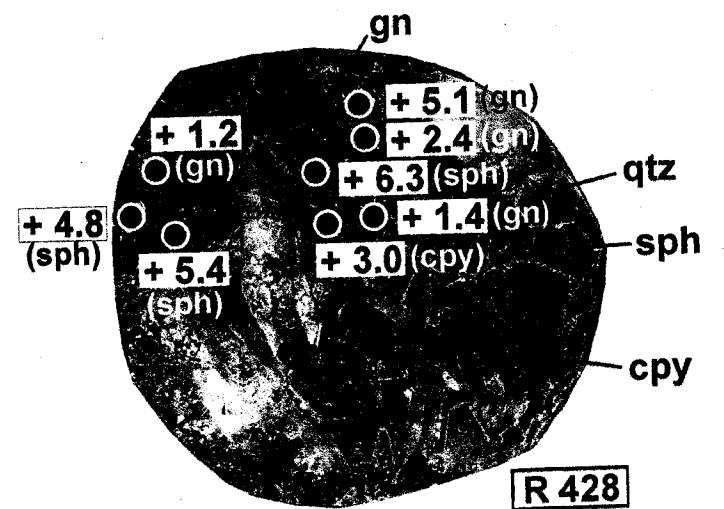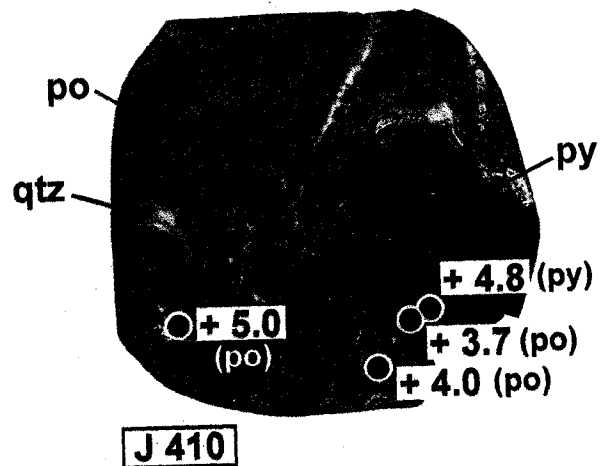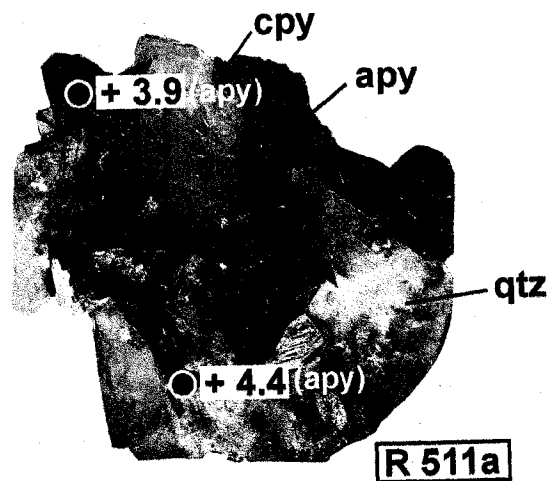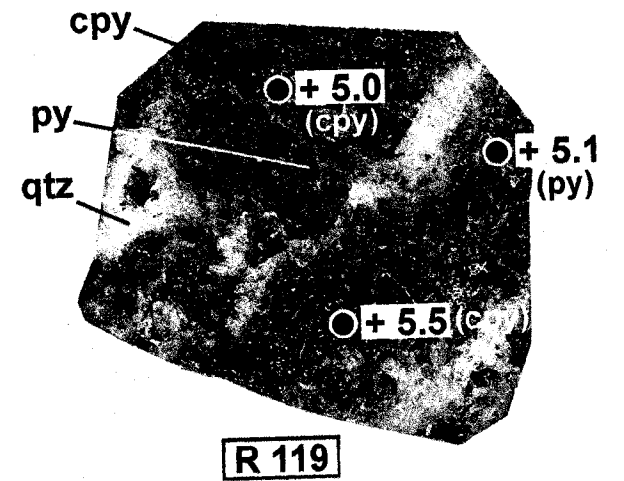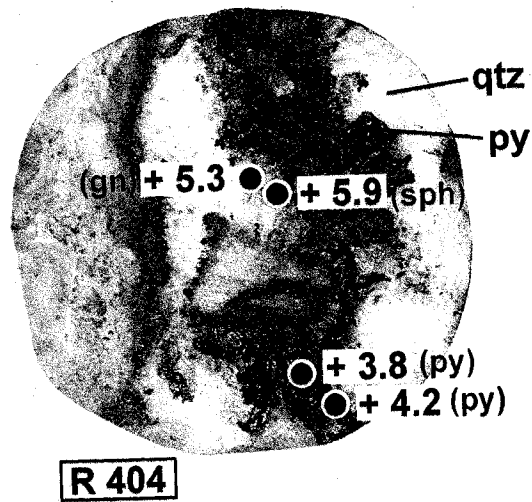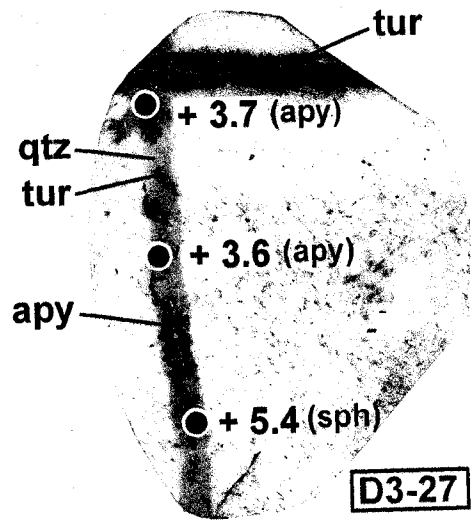
FIGURE 7. Sulfur isotope composition of San Rafael sulfides.

Frequency

(a) Arsenopyrite

(b) Chalcopyrite

(c) Pyrrhotite

(d) Pyrite

(e) Sphalerite

(f) Galena
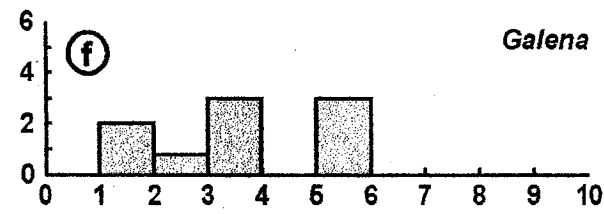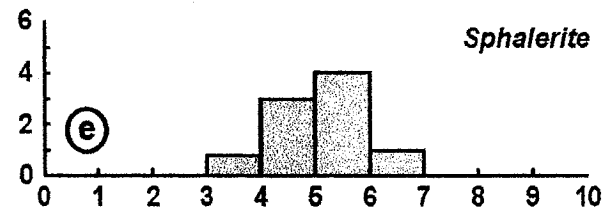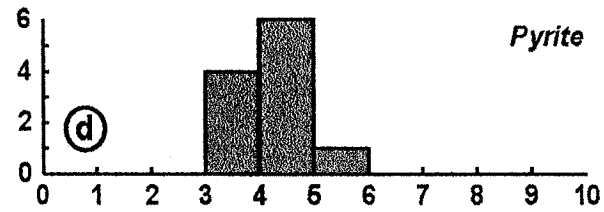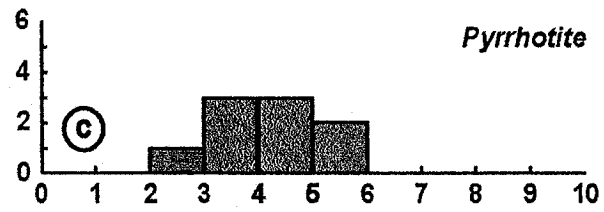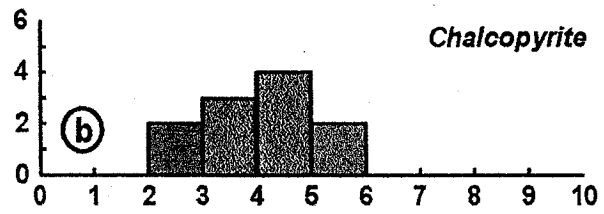
$\delta^{34}S_{\text{V-CDT}}$ (‰)

TABLE 2. Sulfur isotope data for the San Rafael Sn-Cu deposit (n = 64). All samples were analyzed *in situ* by a laser combustion system. Unless indicated otherwise, the samples are from the San Rafael vein and their location is shown in Figure 2.

Sample	Mineral	Textural relationships	$\delta^{34}S_{V\text{-CDT}}$ (‰)
Early, barren stage			
D3-39-1	Arsenopyrite	Subhedral, in early tourmaline-quartz vein (DDH # 3 to the Mariano vein, 39 m)	+ 2.02
D3-39-2	Arsenopyrite	Subhedral, in early tourmaline-quartz vein (DDH # 3 to the Mariano vein, 39 m)	+ 2.96
D3-27-1	Arsenopyrite	Subhedral, in very early quartz veinlet (DDH # 3 to the Mariano vein, 27 m)	+ 3.62
D3-27-2	Sphalerite	Anhedral, with arsenopyrite, in early quartz veinlet (DDH # 3 to the Mariano vein, 27 m)	+ 5.41
D3-27-3	Arsenopyrite	Subhedral, with tourmaline, in early quartz veinlet (DDH # 3 to the Mariano vein, 27 m)	+ 3.68
D8-50-1	Arsenopyrite	Early veinlets in slate, associated with tourmaline and quartz (DDH # 8, 50.5 m)	+ 3.82
D8-50-2	Arsenopyrite	Early veinlets in slate, associated with tourmaline and quartz (DDH # 8, 50.5 m)	+ 3.71
D3-182b-1	Arsenopyrite	Early zone, massive, in tourmaline-cassiterite vein (DDH # 3 to the Mariano vein, 182.5 m)	+ 2.35
D3-182b-2	Arsenopyrite	Late zone, massive, in tourmaline-cassiterite vein (DDH # 3 to the Mariano vein, 182.5 m)	+ 6.20
D3-182b-3	Arsenopyrite	Late zone, massive, in tourmaline-cassiterite vein (DDH # 3 to the Mariano vein, 182.5 m)	+ 3.64
Sulfide ore stage			
511b-1	Arsenopyrite	Large subhedral crystals, early zone, center of a quartz-chlorite-cassiterite-arsenopyrite vein	+ 3.91
511b-2	Sphalerite	Anhedral grain, with arsenopyrite, center of a quartz-chlorite-cassiterite-arsenopyrite vein	+ 4.24
511a-1	Arsenopyrite	Large subhedral crystals, latest zone, center of a quartz-chlorite-cassiterite-arsenopyrite vein	+ 3.91
511a-2	Arsenopyrite	Large subhedral crystals, late zone, center of a quartz-chlorite-cassiterite-arsenopyrite vein	+ 4.44
A13-1	Galena	Inclusions in massive pyrite ore	+ 5.44
A13-2	Pyrite	Coarse-grained massive ore	+ 4.03
R729-1	Pyrite	Narrow veinlet in chalcopyrite ore	+ 3.75
R729-2	Chalcopyrite	Coarse-grained, massive ore	+ 2.27
R17-1	Chalcopyrite	Vug fillings in quartz vein	+ 4.16
R17-2	Pyrite	Anhedral grains in quartz	+ 4.74
R573-1	Chalcopyrite	Rim around pyrrhotite	+ 3.67
R573-2	Pyrrhotite	Massive vein, with quartz	+ 2.99
R573-3	Pyrrhotite	Massive vein, with quartz	+ 3.08
R404-1	Pyrite	Fine-grained, replacing pyrrhotite, in a quartz vein	+ 3.77
R404-2	Pyrite	Euhedral, replacing fine pyrite in a quartz vein	+ 4.23
R404-3	Sphalerite	Subhedral, in a quartz vein	+ 5.92
R404-4	Galena	Subhedral, in a quartz vein	+ 5.28
R165-1	Chalcopyrite	Coarse-grained massive ore	+ 4.76
R165-2	Pyrite	Euhedral crystals in chalcopyrite ore	+ 4.86
R165-3	Chalcopyrite	Coarse-grained massive ore	+ 3.86
G4-1	Arsenopyrite	Euhedral crystals in massive chalcopyrite ore (San German vein, level 4650 m)	+ 3.85
G4-2	Pyrrhotite	Veinlets cross-cutting chalcopyrite (San German vein, level 4650 m)	+ 3.36
G4-3	Chalcopyrite	Coarse-grained massive ore (San German vein, level 4650 m)	+ 3.74
G4-4	Pyrrhotite	Veinlets cross-cutting chalcopyrite (San German vein, level 4650 m)	+ 4.01
R428-1	Galena	Subhedral inclusions in sphalerite, in a quartz-chalcopyrite-sphalerite vein	+ 1.44
R428-2	Chalcopyrite	Coarse-grained, overgrowing quartz, in a quartz-chalcopyrite-sphalerite vein	+ 2.95
R428-3	Sphalerite	Coarse-grained, overgrowing chalcopyrite, in a quartz-chalcopyrite-sphalerite vein	+ 6.30
R428-4	Galena	Subhedral inclusions in sphalerite, in a quartz-chalcopyrite-sphalerite vein	+ 5.08
R428-5	Sphalerite	Coarse-grained, overgrowing chalcopyrite, in a quartz-chalcopyrite-sphalerite vein	+ 5.44
R428-6	Sphalerite	Coarse-grained, overgrowing chalcopyrite, in a quartz-chalcopyrite-sphalerite vein	+ 4.79
R428-7	Galena	Subhedral inclusions in sphalerite, in a quartz-chalcopyrite-sphalerite vein	+ 1.22
R428-8	Galena	Subhedral inclusions in sphalerite, in a quartz-chalcopyrite-sphalerite vein	+ 2.41
R726-1	Galena	Anhedral inclusions in quartz, in a quartz-chalcopyrite vein	+ 3.08
R726-2	Sphalerite	Subhedral inclusions in quartz, in a quartz-chalcopyrite vein	+ 5.60
R726-3	Chalcopyrite	Massive, coarse-grained ore, with quartz	+ 5.10
R119-1	Pyrite	Veinlets cross-cutting chalcopyrite	+ 5.11
R119-2	Chalcopyrite	Massive, in the central part of a cassiterite-quartz-chlorite-chalcopyrite vein	+ 5.50
R119-3	Chalcopyrite	Massive, in the central part of a cassiterite-quartz-chlorite-chalcopyrite vein	+ 5.00
R65b-1	Pyrite	Massive, replacing pyrrhotite, in a chalcopyrite-arsenopyrite-pyrite vein	+ 3.35
R65b-2	Pyrite	Massive, replacing pyrrhotite, in a chalcopyrite-arsenopyrite-pyrite vein	+ 3.81
R65b-3	Pyrite	Fine-grained, replacing pyrrhotite, in a chalcopyrite-arsenopyrite-pyrite vein	+ 4.52
R55-1	Arsenopyrite	Euhedral crystal in chalcopyrite, in a quartz-chalcopyrite-pyrrhotite-arsenopyrite vein	+ 4.95
R55-2	Pyrrhotite	Anhedral inclusions in chalcopyrite, in a quartz-chalcopyrite-pyrrhotite-arsenopyrite vein	+ 5.84
R55-3	Chalcopyrite	Coarse-grained, massive ore, in a quartz-chalcopyrite-pyrrhotite-arsenopyrite vein	+ 4.93

R55-4	Pyrrhotite	Anhedral inclusions in chalcopyrite, in a quartz-chalcopyrite-pyrrhotite-arsenopyrite vein	+ 5.64
R55-5	Arsenopyrite	Euhedral crystal in chalcopyrite, in a quartz-chalcopyrite-pyrrhotite-arsenopyrite vein	+ 5.07
R28a-1	Galena	Anhedral crystals in a quartz-chalcopyrite-pyrite-sphalerite-galena vein	+ 3.30
R28a-2	Sphalerite	Anhedral crystals in a quartz-chalcopyrite-pyrite-sphalerite-galena vein	+ 3.86
R28a-3	Sphalerite	Anhedral crystals in a quartz-chalcopyrite-pyrite-sphalerite-galena vein	+ 4.49
R28a-4	Galena	Anhedral crystals in a quartz-chalcopyrite-pyrite-sphalerite-galena vein	+ 3.65
J410-1	Pyrrhotite	Inclusions in large pyrite crystal (Jorge vein, level 4000 m)	+ 3.67
J410-2	Pyrite	Large, blocky crystal replacing pyrrhotite (Jorge vein, level 4000 m)	+ 4.84
J410-3	Pyrrhotite	Coarse-grained, massive ore (Jorge vein, level 4000 m)	+ 4.03
J410-4	Pyrrhotite	Coarse-grained, massive ore (Jorge vein, level 4000 m)	+ 4.99

expands towards its lower end (i.e., from 3-6 ‰ to 1-6 ‰) both with increasing elevation and with decreasing distance from the surrounding metasedimentary rocks. On the other hand, arsenopyrite (the only sulfide to span all the paragenesis) displays a clear trend of increasing $\delta^{34}S$ values from Stage I (2.0-3.8 ‰) to Stage III (3.8-5.1 %).

The $\delta^{34}S$ compositions of sulfide pairs which, based on petrography, could potentially be in equilibrium were used to estimate the formation temperature of the assemblages, using the equilibrium fractionation factors listed by Ohmoto and Goldhaber (1997). In two samples located in the upper part of the deposit the pairs sphalerite-galena, chalcopyrite-galena, and pyrite-chalcopyrite yielded consistent values of 266 and 264°C (sample R726), and 280°C (sample R729), respectively. These values are in very good agreement with the results of fluid inclusion microthermometry, and with the observation from ore petrography that the sulfide stage had a comparatively high temperature of formation. Unfortunately, most other samples did not yield internally consistent values, suggesting either a lack of isotopic equilibrium or that the sulfides did not precipitate at the same time and from the same fluid, an inference supported by the common small-scale heterogeneity of $\delta^{34}S$ data.

Oxygen isotope data

Thirty-nine oxygen isotope analyses were performed on carefully handpicked mineral separates of oxides and silicates from 17 samples, including a complexely-layered, 50 cm-wide, quartz-chlorite-cassiterite-wolframite-chalcopyrite-pyrite vein, which was sampled in more detail (Fig. 8). In addition, 5 whole-rock samples of granitoids (ranging from fresh to strongly chloritized) and 12 vein carbonates (see section below) were also analyzed. The oxide/silicate minerals analysed were tourmaline, quartz, chlorite, cassiterite and wolframite, and the results are summarized in Figure 9 and listed in Table 3. The $\delta^{18}O$ values for the individual minerals are all positive and have relatively narrow ranges: 9.7-11.9 ‰ for tourmaline, 9.7-14.4 ‰ for quartz, 3.9-4.6 ‰ for chlorite, 1.8-3.4 ‰ for cassiterite, and 1.7-3.0 ‰ for wolframite. Among the tourmaline samples, the transition from the early, barren Stage I to the tin-rich Stage II is characterised by a marked decrease in $\delta^{18}O$ values. Thus, within the same vein, the $\delta^{18}O$ of early, orange-

FIGURE 8. Location of sample analyses for the oxygen isotope composition in a layered, cassiterite-quartz-chlorite-chalcopyrite vein (sample R 119, Contact Orebody, level 4310 m). The arrow indicates the direction of vein growth. The minerals analysed are: quartz (white background), cassiterite (yellow), chlorite (green) and wolframite (pink).

3 cm

+ 9.8 ● — qtz

py

cpy

+ 10.8 ●

○ + 2.7

+ 9.7 ○

○ + 10.1   ○ + 2.2

+ 4.6 ○   ○ + 3.0

○ + 3.3

○ + 3.3

cas

● + 10.6

qtz

○ + 2.9

chl

+ 10.6 ○

○ + 3.4

R 119
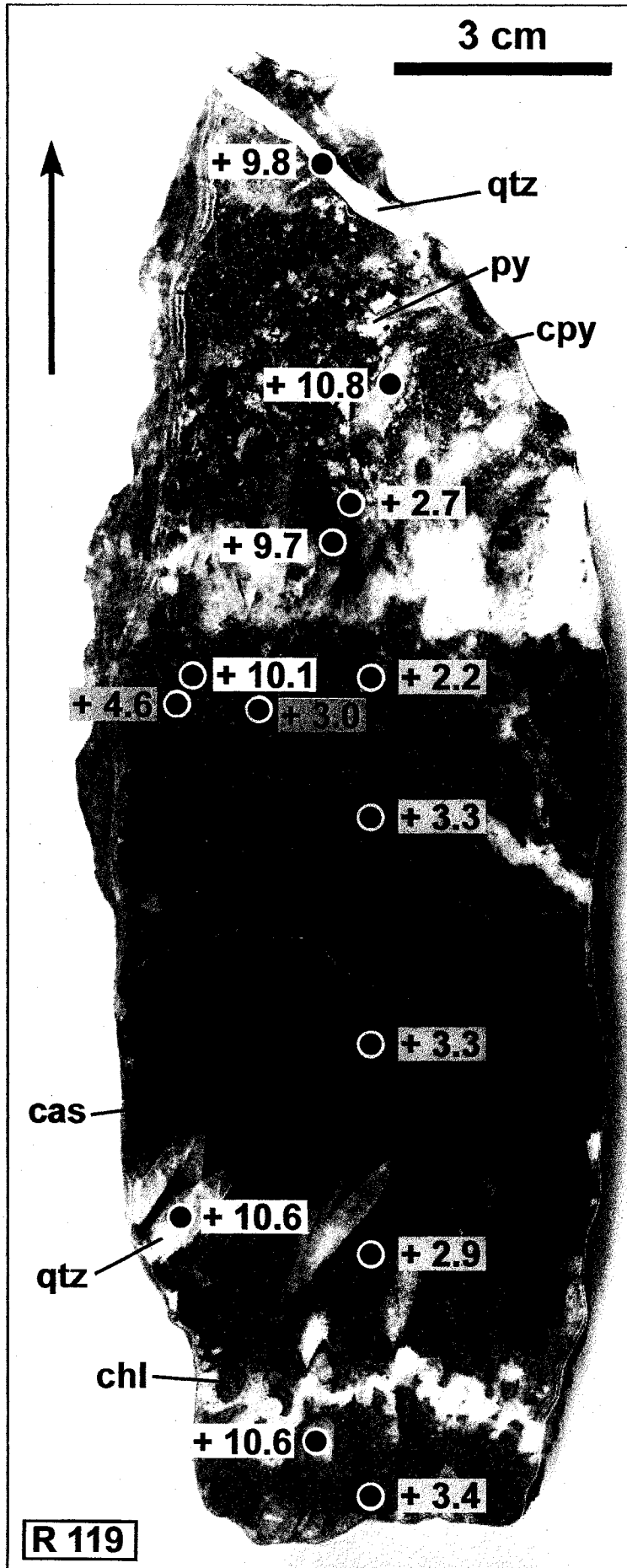
FIGURE 9. Oxygen isotope composition of San Rafael silicates and oxides.

Frequency

(a) Tourmaline

(b) Quartz

(c) Chlorite

(d) Cassiterite
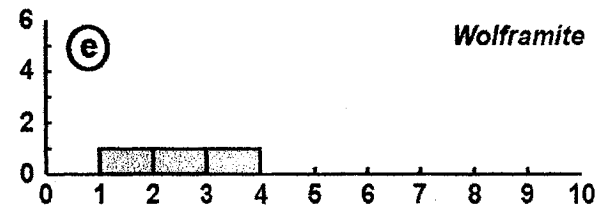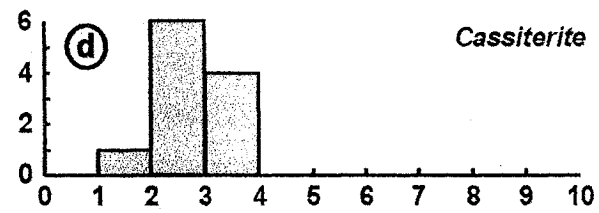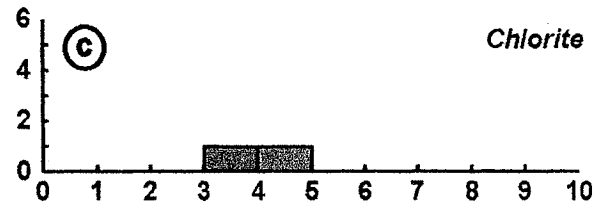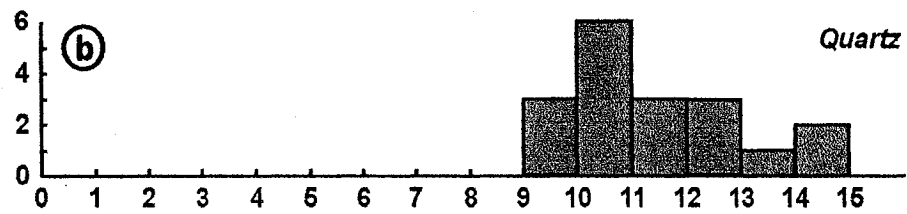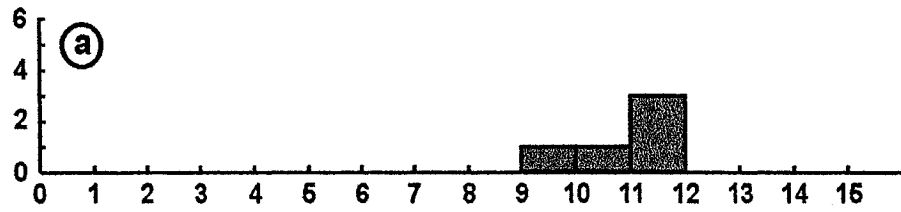
(e) Wolframite

$\delta^{18}O_{\text{V-SMOW}}$ (‰)

TABLE 3. Oxygen isotope data for quartz, cassiterite, wolframite, chlorite, tourmaline, and whole-rock samples from the San Rafael Sn-Cu deposit (n = 44). Unless indicated otherwise, the samples are from the San Rafael vein and their location is shown in Figure 2.

Sample	Mineral	Textural relationships	$\delta^{18}O_{V\text{-}SMOW}$ (‰)
Early, barren stage			
D5-70	Tourmaline	Tourmaline vein - euhedral, prismatic tourmaline (DDH # 5 to the San Rafael vein, 70 m)	+ 11.53
D5-94 tou	Tourmaline	Quartz-tourmaline vein (DDH # 5 to the San Rafael vein, 94 m)	+ 11.89
D5-94 qz	Quartz	Quartz-tourmaline vein (DDH # 5 to the San Rafael vein, 94 m)	+ 12.29
D1-280	Tourmaline	Tourmaline-quartz vein (DDH # 1 to the San Rafael vein, 280 m)	+ 10.82
D3-69	Quartz	Quartz-tourmaline veinlet: the quartz is very early and borders the tourmaline vein leader (DDH # 3 to the Mariano vein, 69 m)	+ 12.00
D3-182 a	Tourmaline	Tourmaline-cassiterite-chlorite-arsenopyrite vein (early, orange tourmaline) (DDH # 3 to the Mariano vein, 182.5 m)	+ 11.70
Main ore stage (tin and copper)			
D3-182 b	Tourmaline	Tourmaline-cassiterite-chlorite-arsenopyrite vein (late, green tourmaline, associated with cassiterite) - DDH # 3 to the Mariano vein, 182.5 m	+ 9.70
D3-182 b	Cassiterite	Tourmaline-cassiterite-chlorite-arsenopyrite vein (earliest cassiterite in the deposit) (DDH # 3 to the Mariano vein, 182.5 m)	+ 2.04
R119		*Complexly banded quartz-chlorite-cassiterite-wolframite-chalcopyrite-pyrite vein (Fig.4):*	
R119 qz1	Quartz	Euhedral quartz associated with chlorite, in between cassiterite bands (Qtz IB)	+ 10.58
R119 qz2	Quartz	Large, euhedral quartz crystals, preceding the deposition of massive cassiterite (Qtz IV)	+ 10.58
R119 qz3	Quartz	Small, euhedral quartz crystals, associated with chlorite and needle-tin cassiterite (Qtz VI)	+ 10.07
R119 qz4	Quartz	Large, euhedral quartz crystals, preceding needle-tin cassiterite deposition (Qtz VII)	+ 9.67
R119 qz5	Quartz	Large, subhedral quartz crystals, following needle-tin cassiterite deposition (Qtz VIII)	+ 10.78
R119 qz6	Quartz	Very late, barren, discordant quartz-chlorite veinlet (Qtz X)	+ 9.84
R119 cas1	Cassiterite	Earliest layer of massive, dark-brown cassiterite (Cas I)	+ 3.39
R119 cas2	Cassiterite	Bottom (earliest) zone of a 7-cm thick layer of dark-brown, massive cassiterite (Cas IIIA)	+ 2.94
R119 cas3	Cassiterite	Middle zone of a 7-cm thick layer of dark-brown, massive cassiterite (Cas IIIB)	+ 3.28
R119 cas4	Cassiterite	Upper (latest) zone of a 7-cm thick layer of dark-brown, massive cassiterite (Cas IIIC)	+ 3.25
R119 cas5	Cassiterite	Early needle-tin cassiterite (Cas IV)	+ 2.17
R119 cas6	Cassiterite	Late, needle-tin cassiterite, associated with chalcopyrite (Cas V)	+ 2.69
R119 chl	Chlorite	Chlorite, associated with quartz and needle-tin cassiterite	+ 4.59
R119 wol	Wolframite	Wolframite, associated with chlorite and quartz	+ 3.04
R113	Wolframite	Same occurrence as R119 wol	+ 2.07
R137		*Cassiterite, quartz and chlorite-cemented breccia of chloritized wallrock fragments:*	
R137 qz1	Quartz	Euhedral quartz preceding cassiterite deposition	+ 10.79
R137 cas	Cassiterite	Layer of massive, dark-brown cassiterite	+ 2.71
R137 qz2	Quartz	Euhedral quartz following cassiterite deposition	+ 11.21
D4 cas1	Cassiterite	Early layers of light-colored wood-tin cassiterite (San Rafael Lode, ~ elevation 4500 m)	+ 2.34
D4 cas2	Cassiterite	Late layers of dark wood-tin cassiterite (San Rafael Lode, ~ elevation 4500 m)	+ 3.35
R511 chl	Chlorite	Cassiterite-chlorite-quartz-arsenopyrite vein	+ 3.94
R511 qz	Quartz	Large, euhedral quartz crystals from a cassiterite-chlorite-quartz-arsenopyrite vein	+ 12.15
D1-219 wol	Wolframite	Quartz-chlorite-cassiterite-wolframite vein (DDH # 1 to the San Rafael vein, 219 m)	+ 1.67
D1-219 qz	Quartz	Quartz-chlorite-cassiterite-wolframite vein (DDH # 1 to the San Rafael vein, 219 m)	+ 10.12
R725	Cassiterite	Needle tin cassiterite-chalcopyrite-quartz vein (tin ore from the upper zone of the deposit)	+ 1.76
R429	Quartz	Anhedral quartz from a large quartz-sphalerite vein	+ 9.83
R708	Quartz	Subhedral quartz from a major quartz-chalcopyrite-fluorite-siderite vein	+ 11.06
Late, barren stage			
R399 qz1	Quartz	Late-stage, very large xl of euhedral vug quartz (core)	+ 14.04
R399 qz2	Quartz	Late-stage, very large xl of euhedral vug quartz (outer zone)	+ 13.14
R709	Quartz	Late-stage, barren, very large quartz vein	+ 14.42
D5M-155	Quartz	Quartz-calcite infill of a reopened tourmaline vein (DDH # 5 to the Mariano vein, 155 m)	+ 11.32
Whole-rock samples			
I 20	Whole rock	Fresh, alkali-feldspar megacrystic, cordierite-biotite leucogranite (Ramp, elevation 3930 m)	+ 10.93
D1M-61d	Whole rock	Fresh biotite-granodiorite (DDH # 1 to the Mariano vein, 61 m)	+ 9.64
D1M-61c	Whole rock	Mildly altered biotite-granodiorite (DDH # 1 to the Mariano vein, 61 m)	+ 9.56
D1M-61b	Whole rock	Strongly chloritized biotite-granodiorite (DDH # 1 to the Mariano vein, 61 m)	+ 8.01
D1M-61a	Whole rock	Chloritite adjacent to the center of a chloritic vein (DDH # 1 to the Mariano vein, 61 m)	+ 4.93

colored tourmaline is + 11.7 ‰, while the succeeding dark-green tourmaline, associated with abundant cassiterite and chlorite (the first to form in the paragenesis) has a $\delta^{18}O$ of + 9.7 ‰ (sample D3-182, Table 3). In the subsequent II and III Stages, the $\delta^{18}O$ values of cassiterite and quartz largely fluctuate, but nevertheless evidence an overall decrease with time, which for the ore vein investigated in detail corresponds to a change from + 3.4 to + 2.7 ‰ for cassiterite, and from + 10.6 to + 9.8 ‰ for quartz (sample R 119, Fig. 8, Table 3). The latest cassiterite in the paragenesis - Stage III needle-tin cassiterite, intergrown with chalcopyrite from the upper zone of the deposit, has an even lower $\delta^{18}O$ value of + 1.8 ‰ (sample R725, Table 3). On the other hand, paragenetically latest Stage IV quartz has markedly higher $\delta^{18}O$ values, in the range + 11.3-14.4 ‰, which are interpreted to relate to its lower temperature of formation.

Whole-rock $\delta^{18}O$ values of fresh granitic rocks range from + 9.6 (biotite-granodiorite) to + 10.9 ‰ (leucogranite). A sequence of four slabs of granodiorite with increasing chloritic alteration was investigated in detail and shows a systematic decrease of $\delta^{18}O$ with alteration, down to + 8.0 ‰ for the strongly chloritized granodiorite, and + 4.9 ‰ for the chloritite, which occupies the center of the vein (Table 3).

Although a lack of complete isotopic equilibrium between coexisting quartz and cassiterite was reported for some hydrothermal tin lodes (Alderton, 1989), several isotopic geothermometers were tested on the silicate-oxide assemblages from the thick ore vein, investigated in detail (sample R119, Fig. 8). A detailed list of fractionation equations tested is listed in the Appendix, but only those that were better constrained and yielded concordant results were used. Thus, the equation of Zheng (1991) yielded for early Stage II quartz and cassiterite an equilibrium temperature of 381°C, in excellent agreement with fluid inclusion microthermometry. For a much later mineral assemblage composed of cassiterite, quartz, wolframite and chlorite (Fig. 8), the temperature obtained was noticeably lower: 343°C for the pair quartz-cassiterite (Zheng, 1991), 300°C for the pair quartz-wolframite (Zheng, 1991), and 291-346°C for the pair quartz-chlorite, depending on whether chlorite composition was assumed to be chamosite or clinochlore (Zheng, 1993). Finally, a late assemblage quartz - needle-tin cassiterite from the same

vein yielded a temperature of 334°C (Zheng, 1991), confirming a gradual decrease of temperature with time in the vein system.

Hydrogen isotope data

Four samples of tourmaline and two of chlorite were analyzed for hydrogen isotope composition and the results are listed in Table 4. The δD values of tourmaline form a narrow range from -75.4 to -73.4 ‰, showing a slight increase for the latest generation of tourmaline, whereas the δD values of the two chlorite samples are -88.2 and -81.1, suggesting that the hydrogen isotope compositional variability of the chlorite is higher than that of the tourmaline.

Carbon and oxygen isotope data for hydrothermal carbonates

The oxygen and carbon isotope composition of late-stage vein carbonates (5 samples of calcite and 7 of siderite) is summarized in Figure 10 and detailed in Table 5. The composition of calcite samples ranges from + 8.6 to + 14.2 ‰ $\delta^{18}O$ and -3.2 to -8.5 ‰ $\delta^{13}C$, whereas that of siderite is more variable, in the range + 13.8 to + 23.1 ‰ $\delta^{18}O$ and - 6.5 to + 4.3 ‰ $\delta^{13}C$. In two samples, two successive generations of siderite were studied, but did not yield a consistent trend. Thus, while in sample R708 (from the upper part of the deposit), the later siderite has a higher $\delta^{18}O$ and a lower $\delta^{13}C$, in sample R27 (from the lower part of the deposit), the second siderite generation has a lower $\delta^{18}O$ and a similar $\delta^{13}C$ value to that of the first generation (Fig. 10). Lastly, an attempt was made to use quartz-calcite and quartz-siderite oxygen isotope geothermometry for those samples for which the $\delta^{18}O$ composition of quartz was available (references for all the fractionation equations used are listed in the Appendix). Depending on the equations used, the temperature calculated for the quartz-calcite pairs was either relatively low (171°C - Zheng, 1999; 203°C - Clayton and Kieffer, 1991) or too high (362°C - Sharp and Kirschner, 1994), whereas for the quartz-siderite pairs it was unrealistic. This is interpreted as evidence for a general lack of isotopic equilibrium between the late quartz and the carbonates.

TABLE 4. Hydrogen isotope data for tourmaline and chlorite from the San Rafael Sn-Cu deposit (n = 6). Unless indicated otherwise, the samples are from the San Rafael vein and their location is shown in Figure 2.

Sample	Mineral	Textural relationships	$\delta D_{\text{V-SMOW}}$ (‰)
Early, barren stage			
D5-70	Tourmaline	Tourmaline vein - euhedral, prismatic tourmaline (DDH # 5 to the San Rafael vein, 70 m)	-75.39
D1-280	Tourmaline	Tourmaline-quartz vein (DDH # 1 to the San Rafael vein, 280 m)	-74.94
D3-182 a	Tourmaline	Tourmaline-cassiterite-chlorite-arsenopyrite vein (early, orange tourmaline) (DDH # 3 to the Mariano vein, 182.5 m)	-73.88
Main ore stage			
D3-182 b	Tourmaline	Tourmaline-cassiterite-chlorite-arsenopyrite vein (late, green tourmaline, associated with cassiterite) - DDH # 3 to the Mariano vein, 182.5 m	-73.44
R119 chl	Chlorite	Associated with quartz and needle-tin cassiterite, from a complexly banded quartz-chlorite--cassiterite-wolframite-chalcopyrite-pyrite vein (Fig.4)	-88.25
R511 chl	Chlorite	Cassiterite-chlorite-quartz-arsenopyrite vein	-81.12

FIGURE 10. A plot of $\delta^{13}C$ versus $\delta^{18}O$ for carbonates from the San Rafael deposit. The arrows link successive generations of siderite from the same sample. The two data points in the lower right corner of the diagram correspond to samples collected in the uppermost part of the deposit (elevation 4820 m), the remaining samples were collected at or below an elevation of 4330 m.
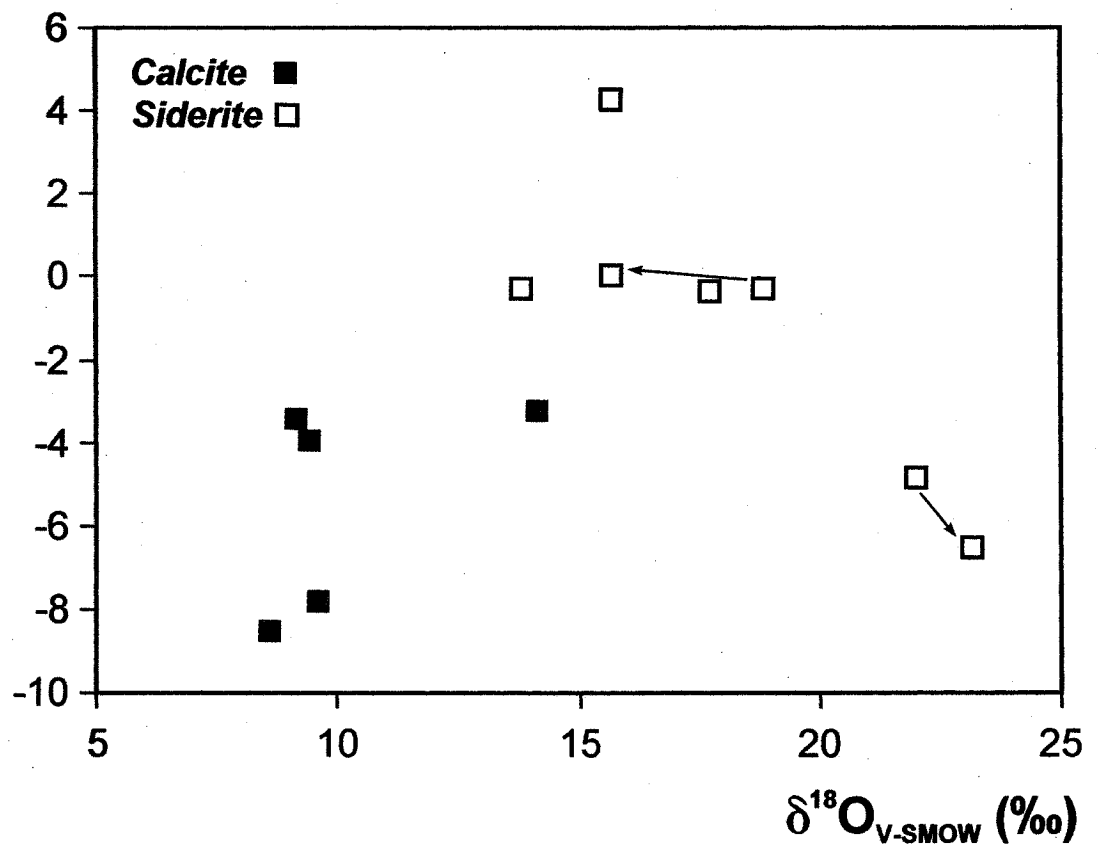
TABLE 5. Carbon and oxygen isotope data for vein carbonates from the San Rafael Sn-Cu deposit (n = 12). Unless indicated otherwise, the samples are from the San Rafael vein and their location is shown in Figure 2.

Sample	Mineral	Textural relationships	$\delta^{13}C_{V-PDB}$ (‰)	$\delta^{18}O_{V-SMOW}$ (‰)
Late, barren stage				
D1-118	Calcite	Quartz-calcite-sphalerite-chalcopyrite infill of a reopened tourmaline vein (DDH # 1 to the San Rafael vein, 118.5 m)	- 8.54	+ 8.59
D5-137	Calcite	Quartz-calcite infill of a reopened tourmaline vein (DDH # 5 to the San Rafael vein, 137.9 m)	- 3.96	+ 9.42
D5-165	Calcite	Quartz-calcite infill of a reopened tourmaline vein (DDH # 5 to the San Rafael vein, 165.8 m)	- 7.80	+ 9.60
D4-230	Calcite	Quartz-calcite-arsenopyrite infill of a reopened tourmaline vein (DDH # 4 to the San Rafael vein, 230.5 m)	- 3.23	+ 14.16
D5M-155	Calcite	Quartz-calcite infill of a reopened tourmaline vein (DDH # 5 to the Mariano vein, 155 m)	- 3.47	+ 9.14
R27 sid1	Siderite	Early, anhedral, reddish, opaque siderite from a quartz--sphalerite-pyrite-marcasite-chalcopyrite-galena-siderite vein	- 0.28	+ 18.84
R27 sid2	Siderite	Late, euhedral, greenish, translucent siderite from a quartz--sphalerite-pyrite-marcasite-chalcopyrite-galena-siderite vein	+ 0.01	+ 15.71
R28 sid	Siderite	Late, euhedral, greenish, translucent siderite from a quartz--sphalerite-pyrite-marcasite-chalcopyrite-galena-siderite vein	- 0.32	+ 13.78
R57 sid	Siderite	Late, orange, translucent siderite from a quartz-cassiterite--chlorite-siderite vein	- 0.34	+ 17.74
R123 sid	Siderite	Greenish, translucent siderite from a quartz-fluorite-pyrite--marcasite-siderite vein	+ 4.26	+ 15.69
R708 sid2	Siderite	Early, anhedral, reddish, opaque siderite from a quartz--chalcopyrite-fluorite-siderite vein	- 6.51	+ 23.15
R708 sid1	Siderite	Late, euhedral, greenish, translucent siderite from a quartz--chalcopyrite-siderite veinlet in chloritized wallrock	- 4.85	+ 21.99

DISCUSSION

Conditions of ore deposition

The history of the hydrothermal system at San Rafael consisted of two contrasting episodes. The first of these, Stage I, was characterized by the formation of numerous tourmaline-quartz (± arsenopyrite) veins, veinlets and stringers, with which sericitic and tourmaline alteration are associated. It is noteworthy that these structures are typically quite narrow, locally discontinuous, and invariably sealed, indicating pressures approaching lithostatic. Assuming this to be the case and stratigraphic reconstructions suggesting that ~2.5 km of rock has been eroded since the emplacement of the deposit at ~25 Ma, the pressure has been ~700 bars. Fluid inclusion microthermometric studies indicate that the fluids responsible for this early, barren stage were hot, hypersaline brines (>340-535°C, 34-62 wt.% NaCl eq.) and the alteration minerals, which formed, indicate that they were acidic (see Chapter III).

By contrast, the subsequent stages, i.e., tin-mineralized Stage II, copper-mineralized Stage III, and late, barren quartz Stage IV are all associated with a distinctive, strong chloritic alteration (and locally, silicification), and the veins have invariably an open fracture-filling character, with ubiquitous vugs, indicative of hydrostatic conditions. Evidence for multiple vein opening suggests that the pressure must have experienced large fluctuations (from > lithostatic to near hydrostatic during ore deposition, assuming a similar depth to that during Stage I). The fluids circulating in the system were cooler and had a moderate to low salinity (>230-360°C, 0-21 wt.% NaCl eq.).

The transition between early, barren Stage I and the subsequent tin and copper stages can be observed in rare tourmaline-cassiterite-chlorite-arsenopyrite veins, in which the early and main-stage mineral assemblages overlap, indicating that Stage II may have closely followed Stage I. It should be emphasized that these veins are of the open fracture-filling type and are surrounded by envelopes of strong chloritic alteration, identical to the ore-stage veins. This observation is very important, as it implies that the onset of ore deposition (Stage II) and its marked change in vein and alteration mineralogy

were directly related to a change in structural style, i.e., a transition from a closed vein system (lithostatic conditions) to an open vein system (hydrostatic conditions).

Although the tin stage (Stage II) and the copper stage (Stage III) were part of the same, protracted hydrothermal event, and were associated with the same chloritic alteration, the physico-chemical conditions of the ore fluid were markedly different, and thus resulted in the formation of contrasting mineral assemblages. In order to constrain the depositional conditions for each stage, we have modeled them in fO_2-pH and fO_2-$a\Sigma S$ space, using phase diagrams combining aqueous and mineral equilibria in the Cu-Fe-Sn-As-S-O-H system (Fig. 11). In addition, we modeled the speciation of tin in the system Sn-Na-Cl-O-H, to constrain the total solubility of Sn as a function of pH and the oxidation state of the hydrothermal fluid (Fig. 12). The details of the calculations are listed in Appendix I.

As indicated by fluid inclusion microthermometry, temperature during cassiterite precipitation (Stage II) was ~380°C, pressure ~300 bars, and fluid salinity ~20 wt.% NaCl eq. The equilibrium mineral assemblage was very simple and consisted of cassiterite, Fe-rich chlorite (daphnite) and quartz. Localized, subordinate arsenopyrite was the only sulfide present, and in one instance minor hematite was observed to grow coevally with cassiterite and chlorite. Based on these constraints, the activity diagrams in Fig. 11 (A,B), and tin solubility contours in Fig. 12, it is estimated that, during the precipitation of cassiterite fO_2 was $< 10^{-26}$, possibly between 10^{-26} and 10^{-28}, where, unlike arsenopyrite, the other iron sulfides were not stable. The pH was > 4, as required by the massive precipitation of cassiterite, and the predominant sulfur species in the fluid was H_2S, with $a\Sigma S \geq 0.002$.

During the sulfide stage (Stage III) the temperature was ~300°C, pressure ~300 bars, and fluid salinity ~5 wt.% NaCl eq. The mineral assemblage consisted mainly of chalcopyrite, pyrrhotite, Fe-rich chlorite (daphnite), quartz, and minor cassiterite, but locally other sulfides (e.g., arsenopyrite, sphalerite, galena, pyrite) were also present. Fig. 11 (C,D) shows the most relevant mineral stability relations, as well as the sulfur isotope isolines, calculated for chalcopyrite (see below). It can be inferred that, during much of

FIGURE 11. Log fO_2-pH and log fO_2-$a\Sigma S$ diagrams showing stability relationships in the system Fe-O-S, for Stage II (oxide - A,B) and Stage III (sulfide - C,D) of the paragenesis. The temperature and fluid salinity, for which the diagrams were drawn were constrained from fluid inclusion microthermometry, whereas pressure was estimated. Diagrams A and B show superimposed stability relationships for the As system (asp - arsenopyrite, as - native arsenic, loe - loellingite), whereas diagrams C and D show the stability field of chalcopyrite (cp; bn - bornite, py - pyrite) and of the principal alteration minerals (dap - daphnite, prl - pyrophyllite, ms - muscovite, kfs - K feldspar). The activities of alteration minerals were calculated from microprobe data (see Appendix-I for details), and the chemical reactions were balanced assuming conservation of Al and quartz saturation. Diagrams C and D (sulfide stage) show superimposed S isotope isolines, calculated for chalcopyrite, assuming $a\Sigma S$ = 0.01 and $\delta^{34}S_{total}$= +3.0 ‰, inferred from the S isotope composition of the sulfides from this stage (see text for explanation).
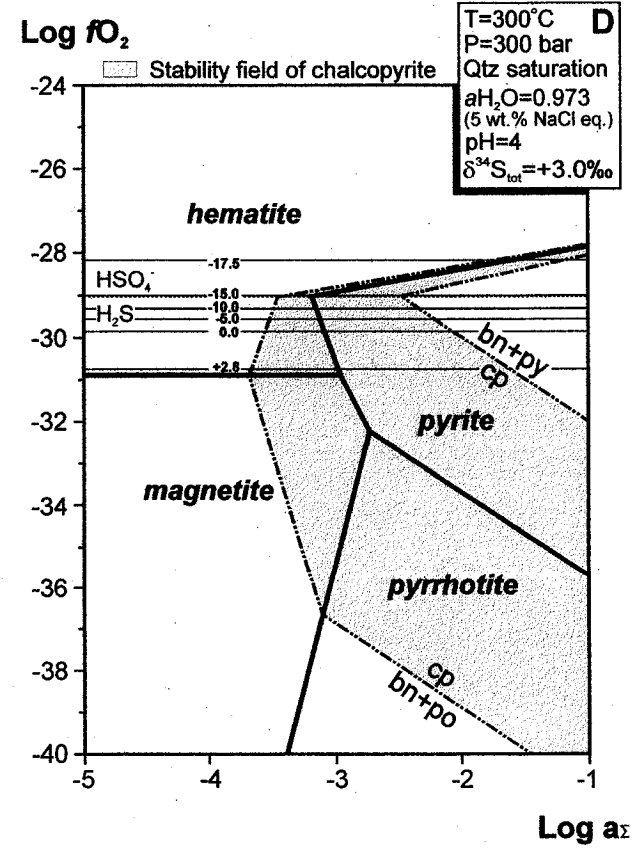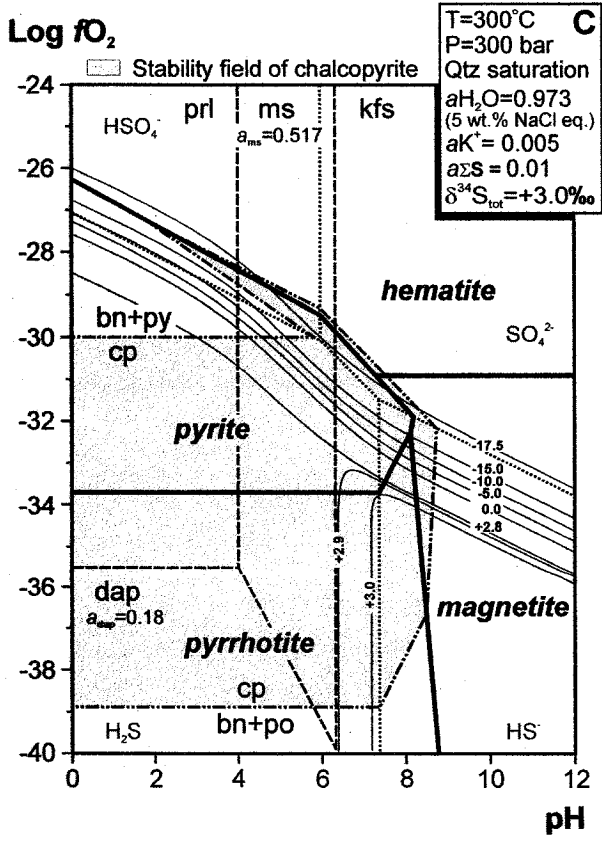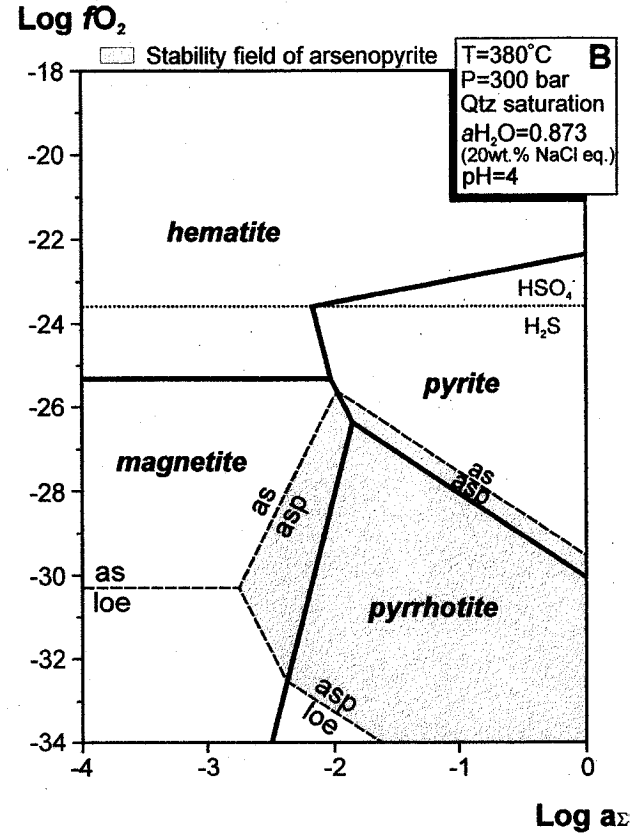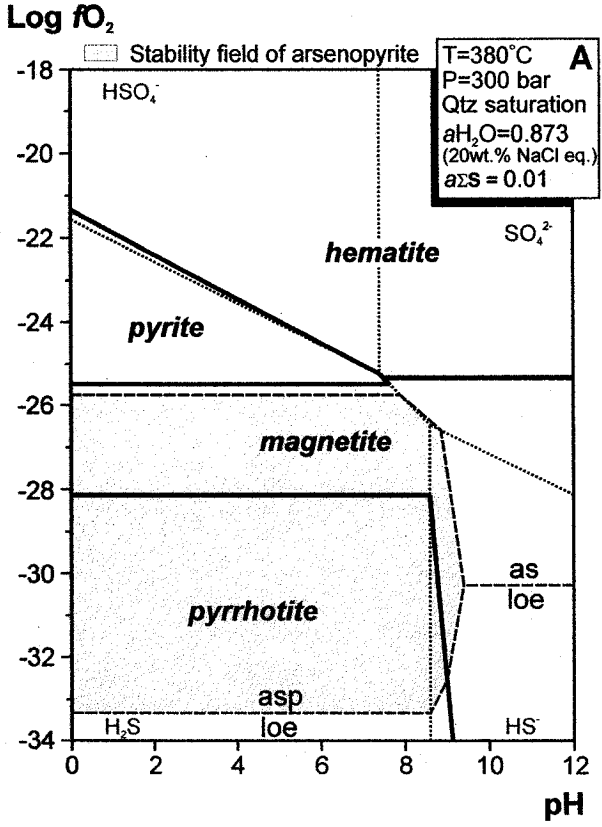
FIGURE 12. Total solubility of tin (mol/kg) in the system Sn-Na-Cl-O-H, as a function of pH and fO_2. For details of the calculations, see Appendix I.
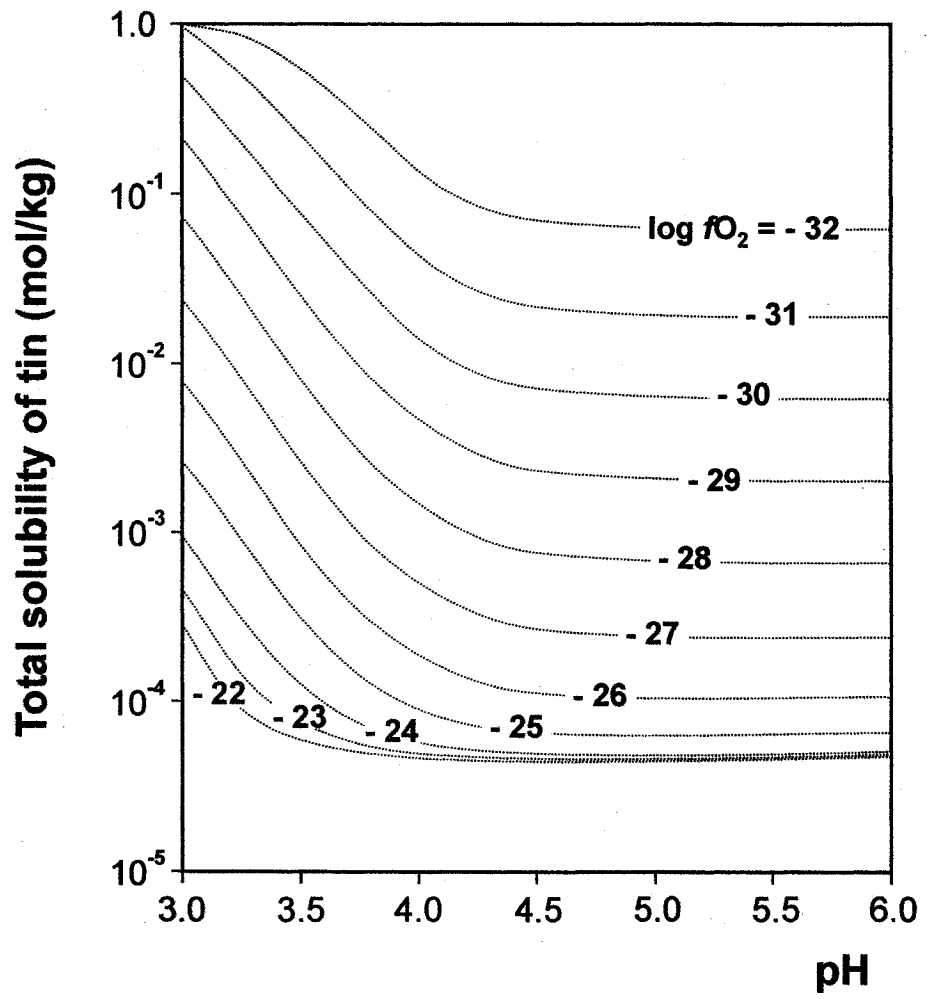
Stage III, fO_2 may have been significantly lower than during Stage II, i.e., $< 10^{-35}$, while pH was likely similar ($\sim$ 4). It should be noted, however, that in many locations in the deposit, pyrite is an abundant Stage III sulfide, and pyrrhotite displays an incipient or advanced replacement by pyrite, marcasite, or (subordinate) hematite. Although in some cases, this replacement of pyrrhotite is clearly late, the common presence of pyrite in Stage III ores indicates that large fluctuations in fO_2 must have taken place, and that the hydrothermal environment was becoming progressively more oxidizing with time.

Isotopic composition and source of the sulfur

The $\delta^{34}S$ composition of San Rafael sulfides ranges between + 2 and + 6 ‰, and displays only very little variation with respect to location in the deposit. These relatively uniform values point to a large-scale hydrothermal system with a very homogenous source of sulfur, likely of magmatic origin. As argued by Hattori and Keith (2001) for porphyry systems, the very narrow range of $\delta^{34}S$ values displayed by giant, granite-related deposits is best explained by a single, magmatic source of sulfur, rather than a variety of country rocks having diverse S isotope compositions. It should be noted, though, that San Rafael sulfides are slightly enriched in heavier sulfur, compared to some other tin deposits (cf. Kontak, 1990), implying an original enrichment of the source of the sulfur in ^{34}S. This is not surprising for S-type granitic magmas, which acquire most of their sulfur through assimilation of country rocks. Thus, for such plutons, the $\delta^{34}S_{ore\ sulfides} \approx \delta^{34}S_{local\ igneous\ rocks}$ $\approx \delta^{34}S_{local\ country\ rocks}$, and a precise discrimination between magmatic and sedimentary sulfur is not entirely possible (Ohmoto and Goldhaber, 1997).

Fig. 11 (C,D) shows sulfur isotope isolines calculated for chalcopyrite, the most common and economically relevant sulfide mineral of Stage III. The calculations assumed a value of $\delta^{34}S_{total}$ = + 3.0 ‰, i.e., slightly less than the value of H_2S in equilibrium with the sulfides having the lowest $\delta^{34}S$ at the temperature of this stage (300°C). The relatively narrow range in $\delta^{34}S$ values of San Rafael sulfides could indicate that H_2S was the dominant sulfur species, inhibiting a significant fractionation of S isotopes. This observation is in good agreement with the dominant mineral assemblage of this stage (chalcopyrite, pyrrhotite, daphnite), consistent with reducing conditions.

Nevertheless, the general lack of isotopic equilibrium between coexisting sulfides, implies periodic fluctuations in ore fluid physicochemistry, e.g., moderately oxidizing conditions.

Isotopic composition and source of the ore fluids

The oxygen and hydrogen isotope compositions of water in equilibrium with the principal ore and gangue minerals were calculated using the fractionation equations of Zheng, 1993a (O, tourmaline); Kotzer et al., 1993 (H, tourmaline); Zheng, 1993a (O, chlorite); Graham et al., 1987 (H, chlorite); Zheng, 1991 (O, cassiterite); Zheng, 1992 (O, wolframite); Zheng, 1993b (O, quartz); and Zheng, 1999 (O, calcite; O, siderite) and are shown in Figure 13. The formation temperature of the minerals was constrained from fluid inclusion microthermometry (see above) and a variety of geothermometers, including isotopic geothermometers.

The isotopic composition of the early fluids, which were in equilibrium with Stage I tourmaline is very close to the magmatic water values, which, considering the high temperature and salinity of these fluids, supports the idea that they were magmatic in origin. The composition of water in equilibrium with late, Fe-rich tourmaline, which formed at the onset of cassiterite precipitation (single analysis in the upper right corner of the magmatic water box, Figure 13) is, however, enriched in deuterium and has lighter oxygen. The trend of marked $\delta^{18}O$ decrease and slight δD increase of the ore fluid with time is further substantiated by the composition of water in equilibrium with ore-stage chlorite, which has a $\delta^{18}O$ lower by ~ 7 ‰ and a δD higher by ~ 10 ‰ than the fluid in equilibrium with early tourmaline. (It should be noted, however, that the δD composition of water in equilibrium with chlorite cannot be precisely constrained due to the lack of accurate fractionation factors; *cf.* Graham et al., 1987). The trend of decreasing fluid $\delta^{18}O$ with time is, nevertheless, clearly indicated by the oxygen isotope compositions of successive generations of quartz and cassiterite (see earlier section), and by minerals, which formed late in the paragenesis, such as calcite and siderite.

This decrease in ore fluid $\delta^{18}O$ with time is paralleled by a marked decrease in fluid salinity and temperature, as indicated by fluid inclusion studies (Fig. 5). These

FIGURE 13. Plot of $\delta^{18}O$ versus δD for tourmaline (open squares) and chlorite (open circles) from the San Rafael deposit and water in isotopic equilibrium with these minerals (black squares and circles). The trend of $\delta^{18}O$ for water in equilibrium with tourmaline to that in equilibrium with chlorite is interpreted. The lower diagram ($\delta^{18}O$ axis) shows the distribution of the calculated $\delta^{18}O$ values for water in equilibrium with the different ore and gangue minerals (cas - cassiterite, wol - wolframite, tur - tourmaline, chl - chlorite, qtz - quartz, cal - calcite, sd - siderite). The paragenetic sequence evolves broadly from right to left, and the latest quartz has the lowest $\delta^{18}O$ value. The equations used for the calculations are listed in Appendix II.
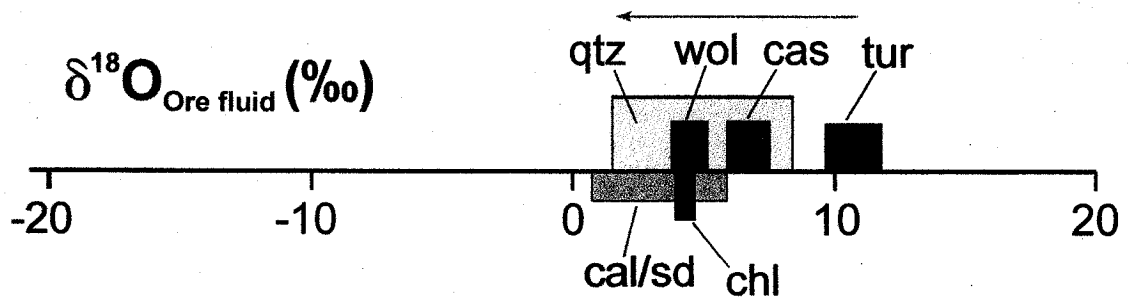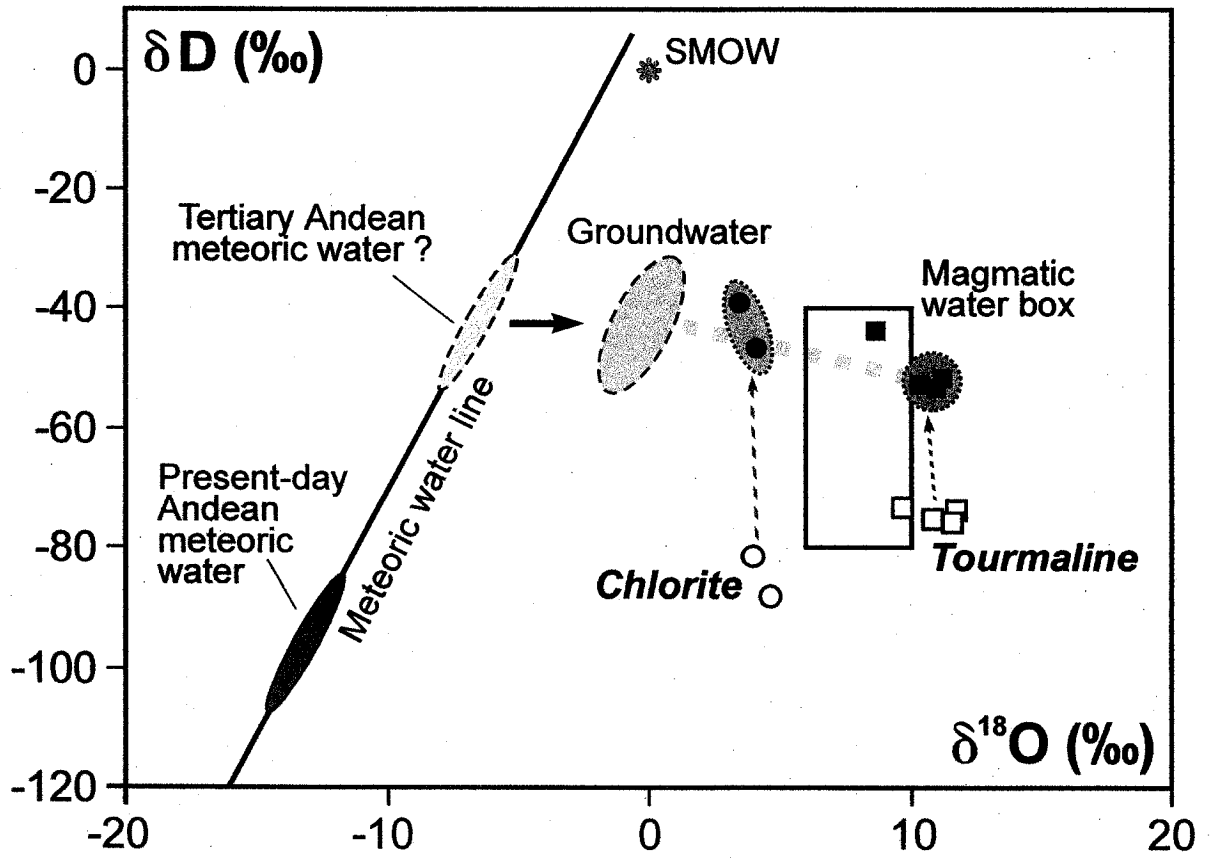
trends, which on the diagrams in Figures 5 and 13 appear broadly aligned, could represent mixing lines and are consistent with mixing of the early, hot, hypersaline (presumably magmatic) brine with a relatively warm fluid, enriched in isotopically lighter oxygen and deuterium. Considering the shallow level of emplacement of the San Rafael pluton and fluid inclusion evidence for the circulation in the system of fluids containing almost no salt (which could not be produced by simple boiling of a magmatic brine, *cf.* Kontak and Clark, 2002), a good candidate for this external fluid could be heated meteoric water, that had partly reequilibrated with the host rocks.

Unfortunately, it is presently not possible to constrain the composition of late Oligocene, Andean meteoric waters, coeval with the deposit formation, to further substantiate this hypothesis, because of the very large uncertainty over the rate of the uplift in this part of the Andes during the last 25 Ma. It is generally assumed that the elevation of the Central Andes in the late Oligocene was about a third of their current elevation (Gregory-Wodzicki, 2000; Anders et al., 2002), therefore ancient meteoric waters must have been considerably enriched in heavier O and D compared to their present counterparts, but their exact values can only be guessed (Fig. 13).

Depositional mechanism

The rich tin ores of San Rafael testify to an unusually effective mechanism of ore deposition, which caused massive supersaturation of tin and focused mineralization into several large fault-jogs, at depth in the lode. Experimental studies and chemical modeling have shown that in natural hydrothermal systems the solubility of tin is highest in hot, reduced, saline and acidic solutions (Fig. 12), and that the bulk of the tin is typically transported as stannous (Sn^{2+}) chloride complexes (Eugster and Wilson, 1985; Pabalan, 1986; Taylor and Wall, 1993; Müller and Seward, 2001). The precipitation of cassiterite (SnO_2), in which tin is in the tetravalent state, can, therefore, be induced by an increase in fO_2, as well as by decreases in temperature and ligand ion activity (chloride) and an increase in pH. Possible scenarios for tin deposition could involve the reaction of the ore fluids with the host rocks, cooling, boiling, redox-coupled precipitation, mixing of the ore fluids with fluids of a markedly different composition, or a combination of some of the

above (*cf.* Heinrich, 1990; 1995; Eadington, 1985), and each of these scenarios should be evaluated in terms of how it would affect the solubility of tin.

The fluid-rock interaction, which accompanied ore deposition at San Rafael produced a wide envelope of very strong chloritization, and is considered an unlikely mechanism, as mass-balance calculations show that chloritic alteration of granitoids increases the acidity of the fluid, leading to an increase in tin solubility (see Chapter III). The simplicity of the ore and alteration assemblages does not indicate either a significant role for redox-coupled precipitation (e.g., coupled precipitation of arsenopyrite and cassiterite), though it may have locally taken place. Similarly, although it can be inferred that the ore fluids in a hydrothermal system generally experienced progressive cooling, this mechanism alone appears insufficient by itself to have caused the voluminous deposition of high-grade cassiterite ore observed at San Rafael.

On the other hand, structural evidence for a transition from a closed to an open vein system, and a concomitant change from lithostatic to hydrostatic conditions, implies that boiling may have taken place. Boiling would oxidize the ore fluid, decrease its temperature and significantly increase its pH, due to the loss of acidic volatiles, thus it would promote the precipitation of cassiterite. However, the conspicuous fluid inclusions present in the ores and associated gangue minerals at San Rafael lack of vapor-rich inclusions (except where produced by necking-down). This indicates that if boiling occurred, it was relatively minor. By contrast, the coincidence of the ore stage with the opening of the vein system and the widespread appearance of cooler, much more dilute fluids (down to almost 0 wt.% NaCl eq.), as well as the ensuing periodic fluctuation of fluid salinity and temperature (>360°C and ~21 wt.% NaCl eq. during formation of massive layers of cassiterite, but <300°C and 2-16 wt.% NaCl eq. during formation of intervening quartz) is readily explained by an ingression of meteoric waters and their mixing with magmatic fluids. A model invoking the mixing of magmatic fluids with isotopically lighter waters could also explain the systematic decrease of cassiterite and quartz $\delta^{18}O$ values, which, considering that mineralization during Stages II and III took place at a quite high and relatively stable temperature, indicates a progressive decrease in the isotopic composition of the ore fluid. Assuming that the surface-derived, meteoric waters would not have had the time to significantly equilibrate with the host rocks, they

likely would be cooler and much more oxidizing than the magmatic fluids. Therefore, their mixing with tin-bearing magmatic fluids would oxidize the latter, increase their pH, and decrease their temperature and ligand activity, all of which would destabilize tin chloride complexes and trigger cassiterite precipitation.

A further evaluation of boiling and fluid mixing scenarios, and their relative importance is possible by considering the evolution of the O and H isotope composition of the ore fluid. Boiling increases the $\delta^{18}O$ and δD of the fluid, because of partitioning of the light isotopes into the vapor phase, and this is reflected in the paragenesis by a gradual increase in $\delta^{18}O$ with time. By contrast, mixing with meteoric waters generally supplies lighter isotopes to the ore fluid, and overall should have the opposite effect. It should be noted, however, that the temperature decrease associated with mixing will increase the isotopic fractionation between the ore fluid and the precipitating minerals, which in the case of O isotope composition of cassiterite and wolframite, and the H isotope composition of chlorite and tourmaline will counter the effect of addition of lighter isotopes (i.e., the minerals will get enriched in the heavier isotope). Because of such complexities, quantitative modeling of cooling, boiling, and fluid mixing scenarios is required to accurately discriminate among them.

Quantitative modeling of cooling and fluid mixing

To test the hypothesis of fluid mixing and compare it to one of a simple cooling of the ore fluid, the oxygen isotope composition of silicate and oxide minerals precipitating in each scenario was modeled quantitatively as a function of $\delta^{18}O$ versus temperature. Based on fluid inclusion microthermometry and the oxygen isotope composition of Stage I silicates, the parameters of the starting magmatic fluid were assumed to be 500°C, 45 wt.% NaCl eq., and $\delta^{18}O$ = + 11 ‰. One scenario considered that this fluid was cooling isochemically, down to a temperature of 200°C, whereas the other considered its mixing with a cooler, dilute fluid (230°C, 0 wt.% NaCl eq.) of three possible $\delta^{18}O$ compositions: + 2.0, 0.0, and − 2.0 ‰. A stepwise decrease of ore fluid temperature took place in each scenario and in the case of mixing was accompanied by a decrease in salinity and fluid $\delta^{18}O$, proportional to the aliquot of diluting fluid added. For simplicity, a linear

relationship between the temperature of the fluid mixture and the mole fractions and temperatures of the fluid end-members was assumed. The influence of fluid salinity on the concentration of oxygen was taken into account, but the mineral-water fractionation factors were assumed to be salinity-independent. They were determined for every temperature step (using the equations of Matsuhisa et al., 1979; Zhang et al., 1994; and Zheng, 1993b), enabling calculation of the $\delta^{18}O$ composition of quartz, cassiterite, chlorite and wolframite in equilibrium with the fluid. Selected results of the modeling are given in Table 6 and the predicted changes in the $\delta^{18}O$ composition of quartz and cassiterite with time are shown in Figure 14, together with the actual range of $\delta^{18}O$ values for ore-stage quartz and cassiterite from the deposit. From the calculations, it is evident that simple cooling and fluid mixing have a contrasting influence on the oxygen isotope composition of the precipitating minerals. Whereas mixing with an isotopically lighter fluid produces a systematic decrease in mineral $\delta^{18}O$ values (followed by a minor increase below 250°C), simple cooling strongly increases the $\delta^{18}O$ values of the oxides and silicates, a scenario clearly not supported by the paragenesis of San Rafael. In addition to the good agreement between the predicted and observed trend of decreasing mineral $\delta^{18}O$ values, the mixing model also reproduces closely the relatively narrow range of mineral $\delta^{18}O$ compositions observed in the deposit (Fig. 14). It is, however, noteworthy that this is only the case when the diluting fluid is assumed to be relatively hot (230°C), as mixing of the magmatic brine with cold (25-100°C), dilute water would drive the mineral $\delta^{18}O$ compositions towards very high values.

The effect that boiling of a hot, hypersaline brine would have on the isotopic composition of the precipitating minerals is much more difficult to model adequately in the case of San Rafael, because of the effect of salinity on the isotopic partitioning between liquid and vapor. Based on simple models, involving boiling of subcritical, low-salinity fluids, it can be predicted, however, that a boiling model would produce a substantial increase in mineral $\delta^{18}O$ values, similar to that of the cooling model. This would be expected to happen because boiling causes the lighter ^{16}O isotope to preferentially partition into the vapor phase, yielding an increasingly ^{18}O-rich brine, from which minerals progressively richer in $\delta^{18}O$ would precipitate. In addition, the

TABLE 6. Calculated oxygen isotope composition of quartz, cassiterite, chlorite and wolframite, in equilibrium with a magmatic brine (T = 500°C, $\delta^{18}O$ = +11.0 ‰), which is mixing with meteoric water (T = 230°C, $\delta^{18}O$ = +2.0 ‰) or undergoing simple cooling.

| | | | $\delta^{18}O_{\text{V-SMOW}}$ mineral | | | |

MIXING

F = mass fraction of brine	T mix (°C)	$\delta^{18}O$ fluid	quartz	cassiterite	chlorite	wolframite
1.00	500	11.0	13.3	6.7	10.0	7.8
0.95	487	10.4	13.0	6.2	9.5	7.3
0.90	473	9.9	12.6	5.7	9.0	6.8
0.85	460	9.4	12.3	5.2	8.4	6.3
0.80	446	8.9	12.0	4.7	8.0	5.8
0.75	433	8.3	11.8	4.3	7.5	5.4
0.70	419	7.9	11.6	3.9	7.0	5.0
0.65	406	7.4	11.4	3.5	6.6	4.6
0.60	392	6.9	11.2	3.1	6.2	4.2
0.55	379	6.4	11.0	2.8	5.8	3.8
0.50	365	6.0	10.9	2.6	5.4	3.5
0.45	352	5.6	10.8	2.3	5.1	3.2
0.40	338	5.1	10.8	2.1	4.8	2.9
0.35	325	4.7	10.8	2.0	4.5	2.6
0.30	311	4.3	10.8	1.9	4.3	2.4
0.25	298	3.9	10.9	1.9	4.1	2.1
0.20	284	3.5	11.0	1.9	4.0	1.9
0.15	271	3.1	11.2	2.0	3.9	1.8
0.10	257	2.7	11.4	2.1	3.8	1.6
0.05	244	2.4	11.6	2.4	3.9	1.5
0.00	230	2.0	12.0	2.7	4.0	1.5

COOLING

	T (°C)	$\delta^{18}O$ fluid	quartz	cassiterite	chlorite	wolframite
	500	11.0	13.3	6.7	10.0	7.8
	480	11.0	13.6	6.8	10.1	7.8
	460	11.0	13.9	6.8	10.1	7.9
	440	11.0	14.3	6.9	10.1	8.0
	420	11.0	14.7	7.0	10.2	8.1
	400	11.0	15.1	7.1	10.2	8.2
	380	11.0	15.6	7.3	10.3	8.4
	360	11.0	16.1	7.6	10.5	8.5
	340	11.0	16.7	7.9	10.7	8.7
	320	11.0	17.3	8.4	10.9	8.9
	300	11.0	18.0	8.9	11.2	9.2
	280	11.0	18.7	9.5	11.6	9.5
	260	11.0	19.6	10.3	12.0	9.8
	240	11.0	20.5	11.2	12.7	10.2
	230	11.0	21.0	11.7	13.0	10.5

FIGURE 14. Diagrams showing the effect of cooling and mixing of magmatic and meteoric fluids on the oxygen isotope composition of quartz (A) and cassiterite (B). The starting conditions for the magmatic brine were T = 500°C, salinity = 45 wt.% NaCl eq., and $\delta^{18}O$ = + 11‰. The equilibrium fractionation between water and quartz was calculated using the equation of Matsuhisa et al. (1979), and that between water and cassiterite using the equation of Zhang (1994). Mixing lines were calculated for a meteoric water at T = 230°C, salinity = 0 wt.% NaCl eq., and three different values of $\delta^{18}O$, that is +2.2 ‰, 0.0 ‰, and -2.0 ‰. The range of $\delta^{18}O$ values of ore-stage quartz and cassiterite from San Rafael and their inferred formation temperature (grey rectangles) are in very good agreement with a mixing model and do not support simple cooling or boiling as the principal depositional mechanism (see text for discussion).
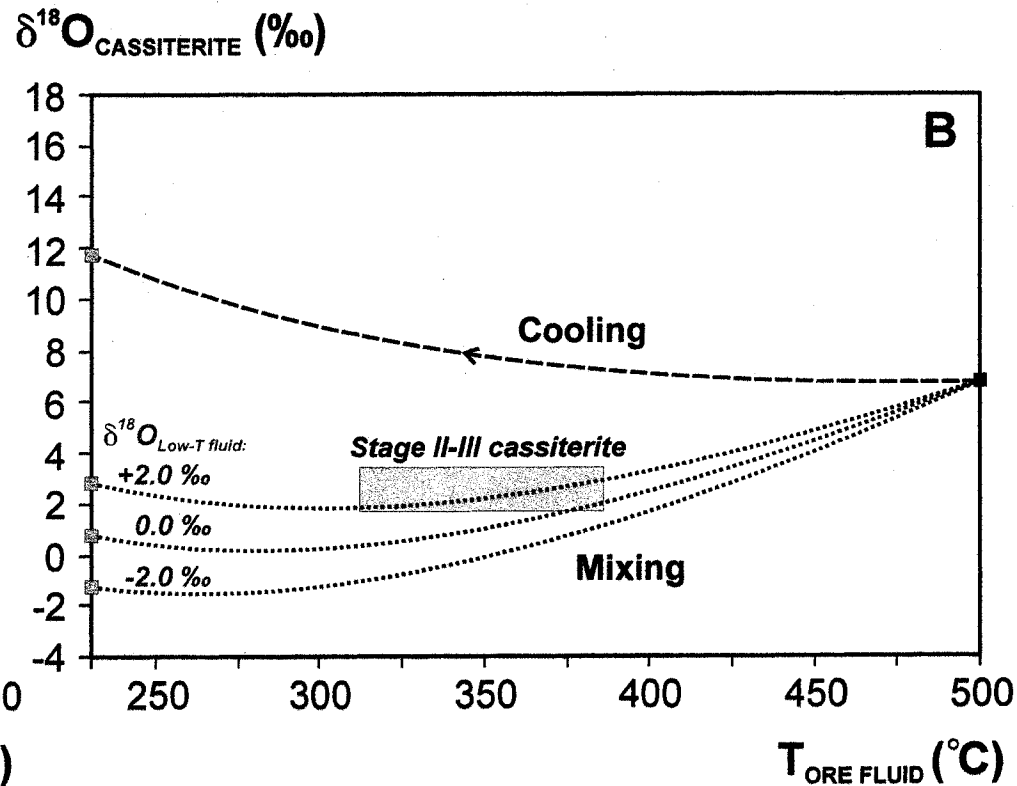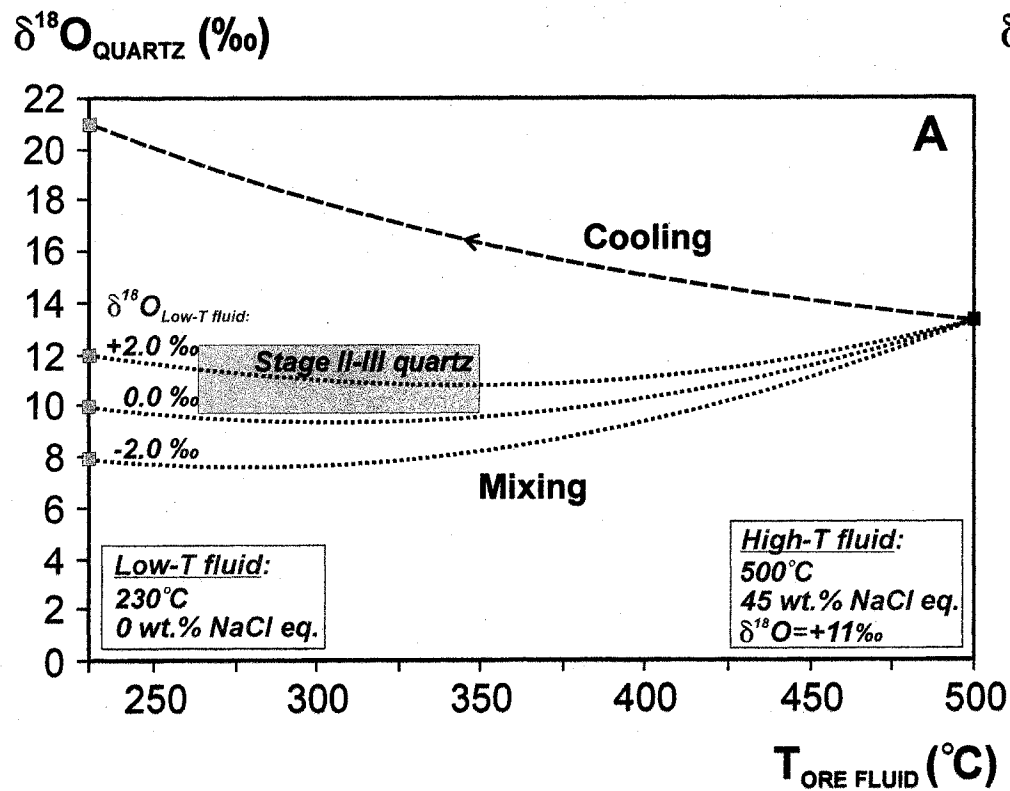
cooling associated with boiling would also drive mineral oxygen compositions towards very high values. The clear lack of a trend of increasing mineral $\delta^{18}O$ values at San Rafael (apart from that observed in the lower-temperature Stage IV, which is broadly consistent with the mixing model), therefore, precludes a significant role for simple cooling or boiling in cassiterite deposition. By contrast, the mixing of a magmatic brine with heated, dilute, isotopically light waters reproduces remarkably well the $\delta^{18}O$ composition of the ores.

CONCLUDING REMARKS

The hydrothermal history of the San Rafael vein system began with hot, acidic, saline and reducing fluids, which had an isotopic composition very close to that of typical magmatic fluids. These fluids likely exsolved from a late granitic melt, related to the San Rafael igneous center, and produced extensive sericitic and tourmaline alteration of the wall-rocks (Stage I). Although the modeling of tin solubility suggests that they could have transported high concentrations of tin, these fluids failed to deposit any cassiterite.

The onset of cassiterite deposition came with a major change in the plumbing of the hydrothermal system, inferred to correspond to a change from lithostatic to hydrostatic pressure conditions, upon a major reopening of the San Rafael lode. The change in structural style, indicated by the ubiquitous open fracture-filling character of Stage II-IV veins, was associated with a drop in temperature and major changes in fluid chemistry. This was evidenced by a distinctive strong chloritic alteration, and the massive deposition of cassiterite and, subsequently, sulfides. The ore fluids were considerably less saline and somewhat cooler than the early brines, as well as enriched in light oxygen and deuterium, and more oxidizing.

The precipitation of cassiterite, which formed the world-class ores was most likely caused by a marked increase in the fO_2 of the ore fluid (evidenced by rare, but nonetheless present, hematite), an increase in pH, and to a lesser extent, the decreases in temperature and chloride activity. The two depositional mechanisms that could explain the geological evidence are boiling of the magmatic brine or its mixing with cooler, oxidizing meteoric

waters. Quantitative modeling of mineral-water oxygen fractionation during fluid mixing predicts the observed decrease of fluid $\delta^{18}O$ values with time, whereas qualitative evaluation suggests that boiling will produce the opposite trend in $\delta^{18}O$ values. Also, the general evolution of the hydrothermal system towards domination by strongly dilute, cooler fluids is consistent with an incursion of heated meteoric waters. As the bulk of the tin ore at San Rafael is restricted to large fault-jogs at depth in the lode, we conclude that these jogs provided sites favorable for mixing between magmatic and meteoric fluids, which resulted in unusually efficient, structurally focused cassiterite deposition.

ACKNOWLEDGEMENTS

REFERENCES

Alderton DHM (1989) Oxygen isotope fractionation between cassiterite and water. Mineral Mag 53: 373-376.

Alderton DHM and Harmon RS (1991) Fluid inclusion and stable isotope evidence for the origin of mineralizing fluids in south-west England. Mineral Mag 55: 605-611.

Anders MH, Gregory-Wodzicki KM, and Spiegelman, M (2002) A critical evaluation of late Tertiary accelerated uplift rates for the Eastern Cordillera, Central Andes of Bolivia. J Geol 110: 89-100

Arenas MJ (1980) Mapa geologico superficial del Distrito Minero San Rafael, Puno. MINSUR Archives.

Barton PB (1969) Thermochemical study of the system Fe-As-S. Geochim Cosmochim Acta 33: 841-857

Becker RH and Clayton RN (1976) Oxygen isotope study of a Precambrian banded iron-formation, Hamersley Range, Western Australia. Geochim et Cosmochim Acta 40: 1153-1165.

Blamart D (1991) Les concentrations tungstifères et stannifères: caractérisation isotopique (H-O) des fluides minéralisateurs, sur l'exemple du gisement Sn-W de Walmes (Maroc central). Détermination de quelques fractionnements isotopiques (H-O) entre minéraux et eaux. Thèse de doctorat, Institut National Polytechnique de Lorraine.

Blamart D, Pichavant M, Sheppard SMF (1988) D/H isotopic fractionation between tourmaline and water: the experimental calibration of tourmaline-mineral geothermometers at 500 degrees to 700 degrees C. Chem Geol 70: 182 (abs).

Blamart D, Pichavant M, Sheppard SMF (1989) Determination experimentale du fractionnement isotopique D/H entre tourmaline et eau a 600, 500 C et 3 kbar. Comptes Rendus Acad Sci Paris t. 308, Serie II, 39-44

Bodnar RJ (1993) Revised equation and table for determining the freezing point depression of H_2O-NaCl solutions. Geochim et Cosmochim Acta 57: 683-684.

Bortnikov NS, Zaozerina ON, Genkin AD, Muravitskaya GN (1990) Stannite-sphalerite intergrowths - possible indicators of conditions of ore deposition. Int Geol Rev 32: 1132-1144.

Cathelineau M (1988) Cation site occupancy in chlorites and illites as a function of temperature. Clay Minerals 23: 471-485

Carothers WW, Adami LH, Rosenbauer RJ (1988) Experimental oxygen isotope fractionation between siderite-water and phosphoric acid liberated CO2-siderite. Geochim et Cosmochim Acta 52: 2445-2450.

Clark AH, Palma VV, Archibald DA, Farrar E, Arenas MJ, Robertson RCR (1983) Occurrence and age of tin mineralization in the Cordillera Oriental, Southern Peru. Econ Geol 78: 514-520

Clark AH, Farrar E, Kontak DJ, Langridge RJ, Arenas Figueroa MJ, France LJ, McBride SL, Woodman PL, Wasteneys HA, Sandeman HA, Archibald DA (1990) Geologic and geochronologic constraints on the metallogenic evolution of the Andes of southeastern Peru. Econ Geol 85: 1520-1583

Clayton RN and Mayeda TK (1963) The use of bromine pentafluoride in the extraction of oxygen from oxides and silicates for isotopic analysis. Geochim et Cosmochim Acta 27: 43-52

Clayton RN and Kieffer SW (1991) Oxygen isotopic thermometer calibrations. *In* Taylor, H.P., O'Neil, J.R. & Kaplan, I.R., eds., Stable Isotope Geochemistry, A tribute to Samuel Epstein, The Geochemical Society, Spec Publ 3: 3-10.

Clayton RN, O'Neil JR, Mayeda TK (1972) Oxygen isotope exchange between quartz and water. J Geophys Res 77: 3057-3067.

Cole DR, Ripley EM (1998) Oxygen isotope fractionation between chlorite and water from 170 to 350 °C: A preliminary assessment based on partial exchange and fluid/rock xperiments. Geochim et Cosmochim Acta 63: 449-457.

Collins PLF (1981) The geology and genesis of the Cleveland tin deposit, Western Tasmania: fluid inclusion and stable isotope studies. Econ Geol 76: 365-392.

Eadington PJ (1985) The solubility of cassiterite in hydrothermal solutions in relation to some lithological and mineral associations of tin ores. *In:* Recent Advances in the Geology of Granite-Related Mineral Deposits, Taylor RP and Strong DF (eds), Can Inst Mining and Metall, Spec Vol 39: 25-32

Eugster HP, Wilson GA (1985) Transport and deposition of ore-forming elements in hydrothermal systems associated with granites. In: Halls C (chairman) High heat production (HHP) granites, hydrothermal circulation and ore genesis. Inst Mining and Metall Conference, London, 87-98

Farmer CB and Halls C (1993) Paragenetic evolution of cassiterite-bearing lodes at South Crofty Mine, Cornwall, United Kingdom. In: Maurice, Y. (ed.) Proceedings of the 8th IAGOD Symposium, Ottawa 1990, E. Schweizerbart'sche Verlagsbuschhandlung, Stuttgart, 365-382.

Friedman I and O'Neil JR (1977) Compilation of stable isotope fractionation factors of geochemical interest. *In:* Fleischer M (ed.) Data of geochemistry. U.S. Geol.

Survey Professional Paper 440-KK, 12 pp.Goldstein RH and Reynolds TJ (1994) Systematics of fluid inclusions in diagenetic minerals. Society for Sedimentary Geology (SEPM) Short Course 31, 199 p

Golyshev SI, Padalko NL, Rechenkin SA (1981) Fractionation of stable oxygen and carbon isotopes in carbonate systems. Geochem Int 18: 85-99.

Graham CM, Atkinson J, Harmon RS (1984) Hydrogen isotope fractionation in the system chlorite-water, NERC 6th Progress Report of Research 1981-1984, NERC Publication Series D, No. 25., pp. 139

Graham CM, Viglino JA, Harmon RS (1987) Experimental study of hydrogen isotope exchange between aluminous chlorite and water and of hydrogen diffusion in chlorite. Am Mineral 72: 566-579.

Gregory-Wodzicki, KM (2000) Andean paleoelevation estimates: A review and critique, Geol Soc Am Bull 112: 1091-1105.

Grønvold F, Stølen S (1992) Thermodynamics of iron sulfides. II. Heat capacity and thermodynamic properties of FeS and of $Fe_{0.875}S$ at temperatures from 298.15 K to 1000 K, of $Fe_{0.98}S$ from 298.15 K to 800 K, and of $Fe_{0.89}S$ from 298.15 K to about 650 K. Thermodynamics of formation. J Chem.Thermodynam 24: 913-936

Guo J and Qian Y (1997) Hydrogen isotope fractionation and hydrogen diffusion in the tourmaline-water system. Geochim et Cosmochim Acta 61: 4679-4688.

Haynes, FM (1985) Determination of fluid inclusion compositions by sequential freezing. Econ Geol 80: 1436-1439.

Hattori KH and Keith JD (2001) Contribution of mafic melt to porphyry copper mineralization: evidence from Mount Pinatubo, Philippines, and Bingham Canyon, Utah, USA. Mineral Deposita 36: 799-806.

Heinrich CA (1990) The chemistry of hydrothermal tin (-tungsten) ore deposition. Econ Geol 85: 457-481

Heinrich CA (1995) Geochemical evolution and hydrothermal mineral deposition in Sn (-W-base metal) and other granite-related ore systems: some conclusions from Australian examples. *In:* Magmas, fluids and ore deposits, Thompson JFH (ed), MAC Short Course 23: 203-220

Heinrich CA and Eadington PJ (1986) Thermodynamic predictions of the hydrothermal chemistry of arsenic, and their significance for the paragenetic sequence of some cassiterite-arsenopyrite-base metal sulfide deposits. Econ Geol 81: 511-529

Holland TJB, Powell R (1998) An internally consistent thermodynamic data set for phases of petrological interest. J Metam Geol 16: 309-343

Hosking KFG (1988) The world's major types of tin deposit *In* Geology of tin deposits in Asia and the Pacific; mineral concentrations and hydrocarbon accumulations in the ESCAP region - selected papers from the International Symposium on the Geology of Tin Deposits, Nanning, China, October 1984, C.S. Hutchison (ed.), p. 3-49.

Jackson P, Changkakoti A, Krouse HR, and Gray J (2000) The origin of greisen fluids of the Foley's zone, Cleveland tin deposit, Tasmania, Australia. Econ Geol 95: 227-236.

Jiang S-Y (1998) Stable and radiogenic isotope studies of tourmaline: an overview. Journal of the Czech Geological Survey 43: 75-90.

Johnson JW, Oelkers EH, Helgeson HC (1992) SUPCRT92: A software package for calculating the standard molal thermodynamic properties of minerals, gases, aqueous species, and reactions from 1 to 5000 bar and 0 to 1000 °C. Comp Geosci 18: 899-947

Jowett EC (1991) Fitting iron and magnesium into the hydrothermal chlorite geothermometer. GAC-MAC-SEG Joint Meeting, Prog Abstr, A62

Kelley SP, Fallick AE (1990) High precision spatially resolved analysis of $\delta^{34}S$ in sulphides using as laser extraction technique. Geochim Cosmochim Acta 54: 883-888.

Kelley SP, Fallick AE, McConville P, Boyce AJ (1992) High precision, high spatial resolution analysis of sulfur isotopes by laser combustion of natural sulfide minerals. Scanning Microsc 6: 129-138.

Kim ST and O'Neil JR (1997) Equilibrium and nonequilibrium oxygen isotope effects in synthetic carbonates. Geochim et Cosmochim Acta 61: 3461-3475.

Kontak DJ (1990) A sulfur isotope study of main-stage tin and base metal mineralization at East Kemptville tin deposit, Yarmouth County, Nova Scotia, Canada: evidence for magmatic origin of metals and sulfur. Econ Geol 85: 399-407.

Kontak DJ, Clark AH, Farrar E, Pearce TH, Strong DF, and Baadsgaard H (1986) Petrogenesis of a Neogene shoshonite suite, Cerro Moromoroni, Puno, southeastern Peru. Can Mineral 24: 117-135.

Kontak DJ, Clark AH (1988) Exploration criteria for tin and tungsten mineralization in the Cordillera Oriental of southeastern Peru. In: Taylor RP, Strong DF (eds) Recent Advances in the Geology of Granite-Related Mineral Deposits. Proc CIM Conference on Granite-Related Mineral Deposits, Can Inst Mining and Metall, Spec Vol 39: 157-169

Kontak DJ, Clark AH (2002) Genesis of the giant, bonanza San Rafael lode tin deposit, Peru: origin and significance of pervasive alteration. Econ Geol 97: 1741-1777

Kontak DJ, Cumming GL, Krstic D, Clark AH, and Farrar E (1990) Isotopic composition of lead in ore deposits of the Cordillera Oriental, southeastern Peru. Econ Geol 85: 1584-1603.

Kotzer TG, Kyser TK, King RW, Kerrich R (1993) An empirical oxygen- and hydrogen-isotope geothermometer for quartz-tourmaline and tourmaline-water. Geochim et Cosmochim Acta 57: 3421-3426.

Landis GP and Rye RO (1974) Geologic, fluid inclusion and stable isotope studies of the Pasto Bueno tungsten-base metal ore deposit, northern Peru. Econ Geol 69: 1025-1059.

Laubacher G (1978) Estudio geologico de la region norte del Lago Titicaca. Inst Geol Mineria (Peru) 5, 120 pp

LeBoutillier NG, Camm GS, Shail RK, Bromley AV, Jewson C, and Hoppe N (2002) Tourmaline-quartz-cassiterite mineralization of the Land's End granite at Nanjizal, west Cornwall. Proceedings of the Ussher Society, 10, 3, 312-318.

Lehmann B (1990) Metallogeny of tin. Lecture Notes in Earth Sciences 32, Springer-Verlag, Berlin, 211 p

Matsuhisa Y, Goldsmith JR, Clayton RN (1979) Oxygen isotopic fractionation in the system quartz-albite-anorthite-water. Geochim et Cosmochim Acta 43: 1131-1140.

Mattey DP and Macpherson CG (1993) High-precision oxygen isotope microanalysis of ferromagnesian minerals by laser fluorination. Chem Geol 105: 305-318.

Matthews A and Beckinsale RD (1979) Oxygen isotope equilibration systematics between quartz and water. Am Mineral 64: 232-240.

McCrea JM (1950) On the isotopic chemistry of carbonates and a palaeotemperature scale. J Chem Phys 18: 849-857.

Menzie WD, Reed BL, and Singer DA (1988) Models of grades and tonnages of some lode tin deposits *In* Geology of tin deposits in Asia and the Pacific; mineral concentrations and hydrocarbon accumulations in the ESCAP region - selected papers from the International Symposium on the Geology of Tin Deposits, Nanning, China, October 1984, C.S. Hutchison (ed.), p. 73-88.

Migdisov AA, Williams-Jones AE, Lakshtanov LZ, Alekhin YV (2002) Estimates of the second dissociation constant of H_2S from the surface sulfidation of crystalline sulfur. Geochim Cosmochim Acta 66: 1713-1725

Müller B, Seward TM (2001) Spectrophotometric determination of the stability of tin (II) chloride complexes in aqueous solution up to 300°C. Geochim et Cosmochim Acta, 65, 4187-4199 Nekrasov IY, Sorokin VI, Osadchiy EG (1976) Partition of iron and zinc between sphalerite and stannite at T=300 to 500°C and P=1kb. Trans Rus Acad Sci (Doklady) v. 226, n. 1-6, 136-138.

Nekrasov IJ, Sorokin VI, Osadchiy EG (1979) Fe and Zn partitioning between stannite and sphalerite and its application in geothermometry. Phys Chem Earth 11: 739-742.

Nakamura Y and Shima H (1982) Fe and Zn partitioning between sphalerite and stannite. Joint Meeting Soc. Mining Geol. Japan, Assoc. Miner. Petr. Econ. Geol., Miner. Soc. Japan, A8 (in Japanese).

Oelkers EH, Helgeson HC (1990) Triple-ion anions and polynuclear compexing in supercritical electrolyte solutions. Geochim et Cosmochim Acta 54: 727-738

Ohmoto H (1972) Systematics of sulfur and carbon isotopes in hydrothermal ore deposits.

Econ Geol 67: 551-578

Ohmoto H and Goldhaber MB (1997) Sulfur and carbon isotopes. *In*: Barnes HL (ed.) Geochemistry of hydrothermal ore deposits. 3rd ed., Wiley, New York, pp. 517-611.

Pabalan RT (1986) Solubility of cassiterite (SnO_2) in NaCl solutions from 200°C - 350°C, with geologic applications. Unpub PhD thesis, Pennsylvania State University, U.S.A., 141 pp

Palma VV (1981) The San Rafael tin-copper deposit, Puno, SE Peru. Unpub MSc thesis, Queen's University, Kingston, Ontario, Canada, 235 pp

Pashkinin AC, Muratova VA, Moiseyev NV, Bazhenov JV (1991) Heat capacity and thermodynamic functions of iron diarsenide in the T range 5 K to 300 K. J Chem Thermodynam 23: 827-830

Primmer TJ (1985) Discussion on the possible contribution of metamorphic water to the mineralising fluid of south-west England: preliminary stable isotope evidence. Proc Ussher Soc 6: 224-228.

Robie RA, Seal RR II, Hemingway BS (1994) Heat capacity and entropy of bornite (Cu_5FeS_4) between 6 and 760 K and the thermodynamic properties of phases in the system Cu-Fe-S. Can Mineral 32: 945-956

Robie RA, Hemingway BS (1995) Thermodynamic properties of minerals and related substances at 298.15 K and 1 Bar (105 Pascals) pressure and at higher temperatures. US Geol Surv Bull 2131, 461 p

Roedder E (1984) Fluid inclusions. Mineralogical Society of America series: Reviews in mineralogy, 12, 646 p.

Rosenbaum J and Sheppard SMF (1986) An isotopic study of siderites, dolomites and ankerites at high temperatures. Geochim et Cosmochim Acta 50: 1147-1150.

Ryzhenko BN, Shvarov YV, Kovalenko NI (1997) The Sn-Cl-F-C-S-H-O-Na system: Thermodynamic properties of components within the conditions of the Earth's crust. Geochem Int 35: 1016-1020

Sandeman HA, Clark AH, Farrar E (1995) An integrated tectono-magmatic model for the evolution of the Southern Peruvian Andes (13-20°S) since 55 Ma. Int Geol Rev 37: 1039-1073

Sandeman HA, Clark AH, Farrar E, Arroyo-Pauca G (1996) A critical appraisal of the Cayconi Formation, Crucero Basin, southeastern Peru. J South Amer Earth Sci 9: 381-392

Savin SM and Lee M (1988) Isotopic studies of phyllosilicates. *In*: Bailey SW (ed.) Hydrous phyllosilicates. Rev. Mineral., 19, pp. 189-223.

Sharp ZD (1990) A laser-based microanalytical method for the in situ determination of oxygen isotope ratios of silicates and oxides. Geochim et Cosmochim Acta 54: 1353-1357.

Sharp ZD and Kirschner DL (1994) Quartz-calcite oxygen isotope thermometry: a calibration based on natural isotopic variations. Geochim et Cosmochim Acta 58: 4491-4501.

Sharp ZD, Atudorei V, and Durakiewicz T (2001) A rapid method for determination of hydrogen and oxygen isotope ratios from water and hydrous minerals. Chem Geol 178: 197-210.

Sheppard SMF (1994) Stable isotope and fluid inclusion evidence for the origin and evolution of hercynian mineralizing fluids. *In:* Metallogeny of collisional orogens; Seltmann R, Kämpf H, and Möller P (eds.), Czech Geological Survey, Prague, p. 49-60.

Shimizu M and Shikazono N (1985) Iron and zinc partitioning between coexisting stannite and sphalerite: a possible indicator of temperature and sulfur fugacity. Mineral Deposita 20: 314-320.

Shock EL, Oelkers EH, Johnson JW, Sverjensky DA, Helgeson HC (1992) Calculation of the thermodynamic properties of aqueous species at high pressures and temperatures. J Chem Soc Faraday Transact 88: 803-826

Shock EL, Sassani DC, Willis M, Sverjensky DA (1997) Inorganic species in geological fluids: Correlations among standard molal thermodynamic properties of aqueous ions and hydroxide complexes. Geochim et Cosmochim Acta 61: 907-950

Shvarov YV (1978) Minimization of the thermodynamic potential of an open chemical system. Geochem Int 15: 200-203

Shvarov YV (1981) A general equilibrium criterion for an isobaric-isothermal model of a chemical system. Geochem Int 18: 38-45

Shvarov YV, Bastrakov, E (1999) HCh: A software package for geochemical equilibrium modeling. User's guide. Australian Geological Survey Organisation, Department of Industry, Science and Resources, 61 p

Smith M, Banks DA, Yardley BWD, and Boyce A (1996) Fluid inclusion and stable isotope constraints on the genesis of the Cligga Head Sn-W deposit, S.W. England. Eur J Mineral 8: 961-974.

Sterner SM, Hall DL, Bodnar RJ (1988) Synthetic fluid inclusions. V. Solubility relations in the system $NaCl-KCl-H_2O$ under vapor-saturated conditions. Geochim et Cosmochim Acta 52: 989-1005.

Sun S and Eadington PJ (1987) Oxygen isotope evidence for the mixing of magmatic and meteoric waters during tin mineralization in the Mole granite, New South Wales, Australia. Econ Geol 82: 43-52.

Sverjensky DA, Shock EL, Helgeson HC (1997) Prediction of the thermodynamic properties of aqueous metal complexes to 1000 °C and 5 kb. Geochim et Cosmochim Acta 61: 1359-1412

Taylor HP (1974) The application of oxygen and hydrogen isotope studies to problems of hydrothermal alteration and ore deposition. Econ Geol 69: 843-883.

Taylor JR, Wall VJ (1993) Cassiterite solubility, tin speciation and transport in a magmatic aqueous phase. Econ Geol 88: 437-460

Taylor RG (1979) Geology of tin deposits. Dev Econ Geol 11, Elsevier, 543 pp

Wagner T, Boyce AJ, Jonsson E, Fallick AE (2004) Laser microprobe sulphur isotope analysis of arsenopyrite: experimental calibration and application to the Boliden Au-Cu-As massive sulphide deposit. Ore Geol Rev 25: 311-325.

Walshe JL (1986) A six-component chlorite solid-solution model and the conditions of chlorite formation in hydrothermal and geothermal systems. Econ Geol 81: 681-703

Walshe JL, Halley SW, Anderson JA, and Harrold BP (1996) The interplay of groundwater and magmatic fluids in the formation of the cassiterite-sulfide deposits of western Tasmania: Ore Geol Rev, v. 10, p. 367-387.

Wenner DB and Taylor HP (1971) Temperatures of serpentinization of ultramafic rocks based on 18O/16O fractionation between coexisting serpentine and magnetite. Contrib Mineral Petrol 32: 165-185.

Williamson BJ, Spratt J, Adams JT, Tindle AG, and Stanley CJ (2000) Geochemical constraints from zoned hydrothermal tourmalines on fluid evolution and tin mineralization: an example from fault breccias at Roche, SW England. J Petrol, 41, 1439-1453.

Wilkinson JJ, Jenkin GRT, Fallick AE, and Foster RP (1995) Oxygen and hydrogen isotopic evolution of Variscan crustal fluids, south Cornwall, U.K. Chem Geol 123: 239-254.

Zhang X and Spry PG (1994) FO2PH: a quickBASIC program to calculate mineral stabilities and sulphur isotope contours in log fO_2-pH space. Mineral Petrol 50: 287-291

Zhang L, Liu J, Zhou H, Chen Z (1989) Oxygen isotope fractionation in the quartz-water-salt system. Econ Geol 84: 1643-1650.

Zhang L, Liu J, Chen Z, Zhou H (1994) Experimental investigations of oxygen isotope fractionation in cassiterite and wolframite. Econ Geol 89: 150-157.

Zhang CL, Horita J, Cole DR, Zhou J, Lovley DR, Phelps TJ (2001) Temperature-dependent oxygen and carbon isotope fractionations of biogenic siderite. Geochim et Cosmochim Acta 65: 2257-2271.

Zheng Y-F (1991) Calculation of oxygen isotope fractionation in metal oxides. Geochim et Cosmochim Acta 55: 2299-2307.

Zheng Y-F (1992) Oxygen isotope fractionation in wolframite. Eur J Mineral 4: 1331-1335.

Zheng Y-F (1993a), Calculation of oxygen isotope fractionation in hydroxyl-bearing silicates. Earth & Planet Sci Let, 120: 247-263.

Zheng Y-F (1993b) Calculation of oxygen isotope fractionation in anhydrous silicate minerals. Geochim et Cosmochim Acta 57: 1079-1091.

Zheng Y-F (1999) Oxygen isotope fractionation in carbonate and sulfate minerals. Geochem J 33:109-126

APPENDIX - I

Details of the thermodynamic calculations

We have modeled the depositional conditions prevalent during (1) the main cassiterite stage and (2) the late sulfide stage at San Rafael. This involved calculations of phase diagrams combining aqueous and mineral equilibria in the Cu-Fe-Sn-As-S-O-H system with those for isolines of sulfur isotope fractionation. In addition, we have carried out a series of speciation calculations in the simple model system Sn-Na-Cl-O-H in order to obtain the total solubility of Sn as a function of pH and the oxidation state of the hydrothermal fluid.

All the calculations were carried out with the HCh software package (Shvarov and Bastrakov, 1999), which models heterogeneous equilibria and reaction progress by minimization of the Gibbs free energy of the total system (Shvarov, 1978, 1981). Thermodynamic data for most aqueous species were taken from the SUPCRT92 database and subsequent updates (Johnson et al., 1991; Shock et al., 1997; Sverjensky et al., 1997). Data for a number of aqueous Sn species came from Ryzhenko et al. (1997). Thermodynamic data for rock-forming silicate and oxide minerals were taken from the internally consistent dataset of Holland and Powell (1998).

The data for cassiterite, pyrite, chalcopyrite, bornite, and pyrrhotite (not contained in this dataset) were compiled from Robie and Hemingway (1995). As heat capacity functions for pyrrhotite and bornite are not given in Robie and Hemingway (1995), the experimentally determined heat capacity data from the original sources (pyrrhotite: Grønvold and Stølen, 1992; bornite: Robie et al., 1994) were fitted with a four-term polynominal of the form used by Holland and Powell (1998). It should be noted that the entropy values for bornite and pyrrhotite given in Robie and Hemingway (1995) originate also from Grønvold and Stølen (1992) and Robie et al. (1994), thereby ensuring internal consistency of these datasets. Data for the calculation of the stability fields of arsenic phases (arsenopyrite, loellingite, native arsenic) were compiled from Robie and Hemingway (1995) and Barton (1969). The heat capacity function for loellingite was

fitted to the original data given in Pashkinin et al. (1991), which were the source of the entropy data tabulated in Robie and Hemingway (1995). All calculations of individual activity coefficients of aqueous species applied an expanded Debye-Hückel model using the b-gamma equation for NaCl as the background electrolyte (Oelkers and Helgeson, 1990; Shock et al., 1992). The set of equations of Zhang and Spry (1994) and the most recent set of isotopic fractionation factors given in Ohmoto and Goldhaber (1997) were used to calculate the sulfur isotope isolines. The model of Zhang and Spry (1994), which excludes the aqueous S^{2-} species, is preferred over the original formalism of Ohmoto (1972), because the second dissociation constant of H_2S is too small for S^{2-} to be a significant species at geologically realistic values of pH (*cf.* Migdisov et al., 2002).

APPENDIX II

Compilation of references for the O and H isotope fractionation equations tested in this study

• Oxygen isotopes

quartz-calcite	Clayton and Kieffer (1991), Sharp and Kirschner (1994), Zheng (1999)
quartz-cassiterite	Zhang et al. (1994), Zheng (1991)
quartz-chlorite	Zheng (1993a)
quartz-siderite	Zheng (1999)
quartz-tourmaline	Blamart (1991), Kotzer et al. (1993), Jiang (1998), Zheng (1993a)
quartz-wolframite	Zhang et al. (1994), Zheng (1991)
calcite-water	Clayton (1989), Friedman and O'Neil (1977), Golyshev et al. (1981), Kieffer & Clayton (1989), Kim & O'Neil (1997), Zheng (1999)
cassiterite-water	Zhang et al. (1994), Zheng (1991)
chlorite-water	Cole and Ripley (1998), Savin and Lee (1988), Wenner and Taylor (1971), Zheng (1993)
quartz-water	Clayton et al. (1972), Kieffer and Clayton (1989), Matthews (1979), Matsuhisa et al. (1979), Zhang et al. (1989), Zheng (1993b)
siderite-water	Becker and Clayton (1976), Carothers et al. (1988), Zhang et al. (2001), Zheng (1999)
tourmaline-water	Blamart (1991), Kotzer et al. (1993), Zheng (1993a)
wolframite-water	Landis and Rye (1974), Zhang et al. (1994), Zheng (1992)

• Hydrogen isotopes

chlorite-water	Graham et al. (1987)
tourmaline-water	Blamart (1988), Guo et al. (1997), Jiang (1998), Kotzer et al. (1993)

INTRODUCTION TO CHAPTER VI

Chapter VI is designed to provide a general metallogenic framework for mineralization at San Rafael. The deposit is located in the Inner Arc of the Central Andes, which hosts a large concentration of world-class, Tertiary and Triassic Sn-W-Ag-base metal deposits. I integrate the latest advances in understanding of the tectonics, geophysics, petrology, geochemistry and economic geology of this region, to show how the specific location and genesis of this metallogenic province were controlled directly by regional-scale processes, associated with mountain-building. In what is a novel hypothesis, I propose that recurrent "collisions" between the Farallon/Nazca oceanic plate and the South American continent periodically generated voluminous, peraluminous magmas in the back arc of the orogen. These magmas evolved by fractional crystallization and exsolved the fluids responsible for the rich Sn-W(-Ag) mineralization.

CHAPTER VI

The role of collisional tectonics in the metallogeny of the Central Andean tin belt

M.S.J. Mlynarczyk and A.E. Williams-Jones

ABSTRACT

The Inner Arc of the Central Andes, broadly corresponding to the Eastern Cordillera, is the location of a well-known Tertiary and Triassic Sn-W-(Ag-base metal) metallogenic province, commonly referred to as the Bolivian tin belt. We propose that the Tertiary metallogeny, which generated most of the tin, was a direct consequence of discrete "collisions" between the South American plate and the Nazca slab and sub-slab mantle, during the ongoing Andean orogeny. Evidence supporting this proposal include: (1) the coincidence of the tin province and the Inner Arc in a marked "hump" in the Andean orogen, which may represent tectonic indentation; (2) the symmetry of the tin province with respect to the Bolivian orocline, the axis of which corresponds to the direction of highest compression; (3) the relative symmetry of the magmatism and tin metallogeny with respect to this axis; (4) the concurrent timing of mineralization and compressional pulses; (5) the similar host rock geochemistry and ore lead isotope data, testifying to a common crustal reservoir; and (6) the striking similarity of the igneous suites, associated with the ore deposits to those from "typical" collisional orogens. A number of studies have called upon a persistent tin anomaly to explain the metallogeny of the region. We propose, instead, that the latter is better explained by periodic compressional interaction between the Farallon/Nazca oceanic plate and the South American continent. This led to the generation of peraluminous magmas, which during fractional crystallization exsolved the fluids responsible for the voluminous Sn-W mineralization.

INTRODUCTION

The Central Andean tin belt is an elongated metallogenic province, confined to the Eastern Cordillera of the Andean orogen and extending for more than 1,000 km from southeastern Peru, through Bolivia, up to northern Argentina (Fig.1). Hundreds of Sn-W-(Ag) deposits, many of which are world-class (e.g., Llallagua, Cerro Rico de Potosi, Oruro, San Rafael), define the province, and have been mined since the 16th century, providing the foundation for the economy of colonial Spain and, subsequently, Bolivia.

FIGURE 1. Principal geological features of the Central Andes. A. Topography (modified from the 1:31 000 000 map of the World by RV Reise- und Verkehrsverlag, Berlin, 1995). B. Physiographic subdivisions (modified from Jaillard et al., 2000; and Sillitoe, 1976). The Western and Eastern Cordilleras are sensu lato. C. Metallogenic provinces (after Sillitoe, 1976, and Lehmann, 1979). D. Plate tectonics, volcanism and lithospheric thickness (modified from Oyarzún, 2000, Ramos and Aleman, 2000, and Jaillard et al., 2000). The abbreviations NVZ, CVZ, and SVZ, refer to the Northern, Central and Southern volcanic zones, respectively. These zones are separated by zones of flat subduction, which lack volcanism. Arrows indicate the direction of the plate motions. The shaded area represents thickened continental crust.

A

Guayaquil
Lima
Arica
PACIFIC OCEAN
Santiago
0 500 km

10°
20°
30°

B

Coastal areas
Western Cordillera
Altiplano / Puna
Eastern Cordillera
Subandean ranges
Pampean ranges

Eastern lowlands

C

Metallogenic belts:
Fe
Porphyry Cu-(Mo-Au)
Cu-Pb-Zn-Ag
Sn-(W-Ag-Sb-Bi)

D

NVZ
South American Plate
flat subduction
-100
-200
-300
CVZ
Nazca Plate
Arica bend
Peru-Chile trench
flat subduction
SVZ
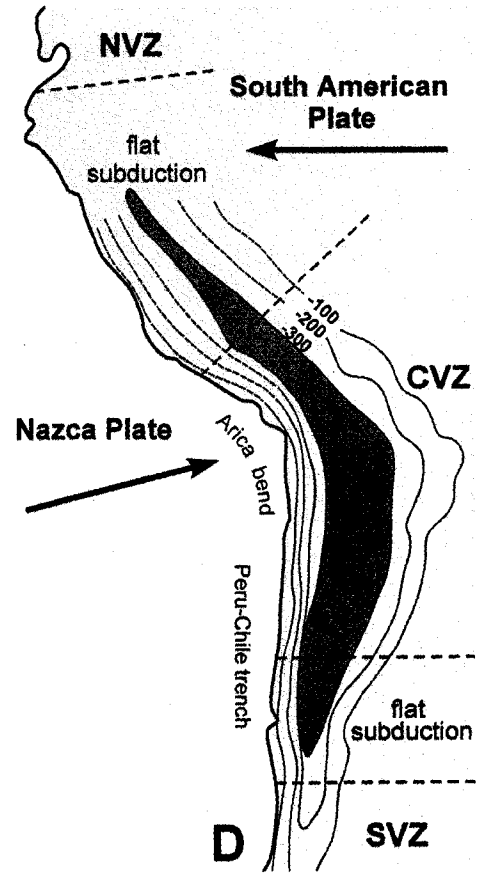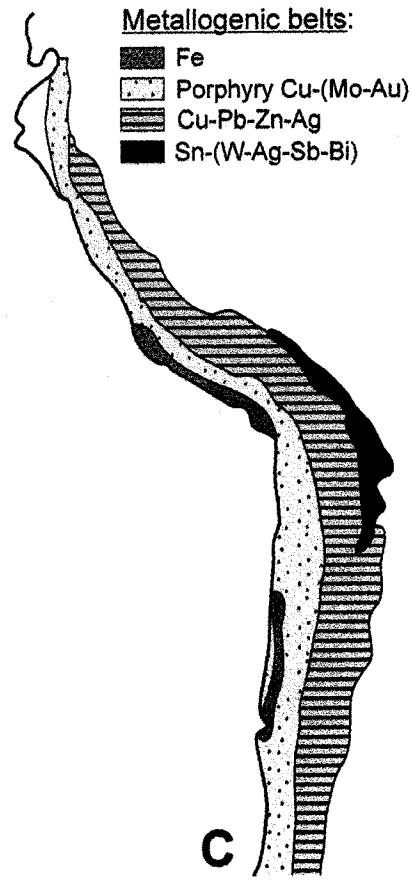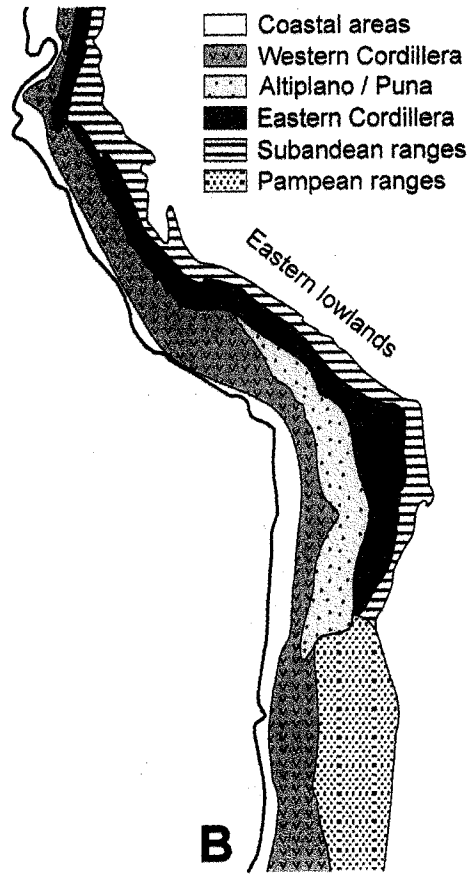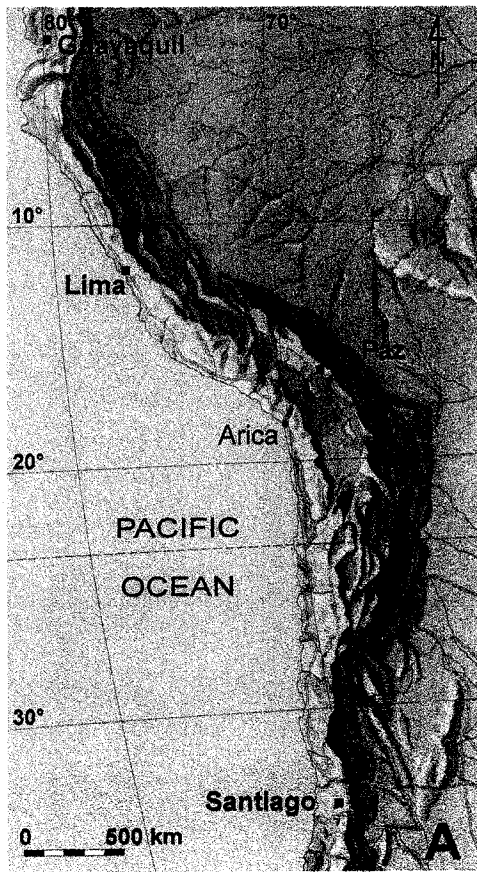
These deposits formed mainly in two metallogenic episodes: a Late Triassic-Early Jurassic episode (restricted mostly to northwestern Bolivia) and a much more significant, Late Oligocene to Miocene episode, which encompassed the entire length of the province. The deposits are associated with felsic to intermediate, plutonic and subvolcanic rocks, and are of the hydrothermal vein type, commonly exhibiting a diversified sulfide and sulfosalt mineralogy and a distinct metal zonation (for a review, see Ahlfeld and Schneider-Scherbina, 1964; Kelly and Turneaure, 1970; Turneaure, 1971; Rivas, 1979; Urquidi-Barrau, 1989). In addition, southern Bolivia hosts a suite of giant, low-grade deposits referred to as "porphyry tin" deposits (so named after their similarity to porphyry copper deposits; see Sillitoe et al., 1975; Grant et al., 1980), in which the ores occur as disseminations, stockworks and breccia fillings.

An early hypothesis for the origin of the Central Andean tin belt was based on the idea of "geochemical heritage", i.e., it was proposed that the location of the metallogenic province was controlled by a persistent tin anomaly, associated with either the country rocks, the underlying Precambrian basement or the upper mantle, which was tapped periodically (Schuiling, 1967; Ahlfeld, 1967; Clark et al., 1976). This hypothesis was eliminated, however, when it was established that the metasedimentary rocks of the region do not contain anomalous levels of tin, and the tin content of the granitic rocks can be related directly to the degree of fractionation of the corresponding magmas (Lehmann, 1982; 1987; Lehmann et al., 1988). Furthermore, the isotopic composition of lead in ores of the successive metallogenic episodes differs markedly (Kontak et al., 1990). Subsequent hypotheses focused on the fact that the Andean Cordillera hosts a succession of parallel, north-south trending, metallogenic belts (Fig. 1c), which comprise from west to east: the iron deposits of the Coastal Belt; the porphyry-type Cu-Mo-Au deposits of the Western Cordillera; the polymetallic vein- and replacement-type Cu-Pb-Zn-Ag deposits and sedimentary Cu deposits of the Altiplano; and finally the vein and porphyry-style Sn-W-(Ag) deposits of the Eastern Cordillera (Stoll, 1965; Ahlfeld, 1967; Sillitoe, 1976; Grant et al., 1980). Sillitoe (1972; 1976) explained this distribution of deposit types as resulting from a sequential incorporation of different metal suites in magmas generated at progressively greater depths above a shallow-dipping subduction zone below the Andean orogen. However, Clark et al. (1976; 1984) argued that the formation of the Central

Andean tin province (located farthest from the trench) can be "only tenuously" related to the process of subduction. Finally, Lehmann (1982) and Lehmann et al. (1990) proposed that the west-east metal zonation in the Andes reflects the contrasting character of the source regions in the different zones, together with an eastward decrease in the role of subduction-related igneous processes in the metallogeny. Thus, magmatism of the Western Cordillera and Altiplano, which involved a major mantle input and mostly igneous protoliths, produced large volumes of I-type, magnetite-series, felsic melts, whereas in the Eastern Cordillera magmatism was largely the result of extensive melting of the 10-15 km-thick succession of carbon- and boron-rich, pelitic rocks. The latter generated melts of a distinctly peraluminous and reduced character (S-type, ilmenite-series granitoids), and their extensive fractional crystallization led to Sn and W enrichment (Ishihara, 1981; Lehmann et al., 1990; 2000).

Although this last model explains the relative location of the metallogenic belts, it does not explain why the (porphyry-style) Cu-Mo-Au province and the polymetallic province extend along most of the Andean chain, whereas the tin province is restricted to the central section (Fig.1c). It appears, therefore, that the ultimate control on tin metallogeny in the Andes has to be sought in regional-scale processes, which were specific to the central part of the chain, and a comprehensive genetic model requires integration of the most recent structural, geophysical and petrogenetic studies of this region. A useful starting point is to examine spatial relationships among the different features that characterize this tin province.

SPATIAL RELATIONSHIPS

The most obvious geographic feature of the Central Andean tin belt is its location precisely in the central segment of an arcuate mountain range, which represents a marked landward broadening of the Andean orogen (Fig.1). This region, referred to as the *Inner Arc* (Clark et al., 1984; 1990) is restricted to the Eastern Cordillera of the centermost Andes, and lies to the east of the zone of high intra-andean plateaus (Altiplano-Puna, Fig.1b), which marks an interface between the oceanward *Main Arc* (Western Cordillera) and the South American craton. The region is characterized by very high mountains, an

229

unusually thick crust and lithosphere (Fig.1d), and a very high heat flow (James and Sacks, 1999). At present, there is only limited volcanic activity in the Inner Arc, in contrast to the Main Arc, which hosts most of the volcanoes of the Central Volcanic Zone (Thorpe et al., 1982). The Inner Arc, which is largely composed of early Paleozoic, marine clastic sedimentary rocks, experienced extensive Cenozoic crustal deformation and anatexis, and it is these processes that ultimately must have led to the accumulation of large amounts of metals in the upper crust.

It is noteworthy that both the Inner Arc and the tin province, which it hosts, straddle the axis of the Bolivian orocline, a marked bend in the continental margin near longitude 18°S, which resulted largely from wholesale opposed rotations (anticlockwise north of the bend and clockwise south of it; Kley, 1999) of the two limbs of the orocline, and which Isacks (1988), Russo and Silver (1996), Kley and Monaldi (1998) and Kley (1999) showed to have been the locus of maximum crustal shortening in the last 25-30 Ma (Fig. 2). The tin belt is, therefore, located in the segment of the Andean orogen which experienced the greatest compression, and resulting horizontal shortening and vertical thickening. This is particularly interesting in light of the numerous similarities that have been recently shown between the Central Andes (an orogen formed at a convergent, non-collisional margin) and collisional mountain belts, such as the Himalayas (Russo and Silver, 1996; Kley and Eisbacher, 1999). For example, the Central Andes and the Himalayas-Tibet both have an extremely mountainous topography, high plateaus underlain by thickened (≥ 70 km) continental crustal roots, and are undergoing large-scale crustal underthrusting (Kley and Eisbacher, 1999). By contrast, although the western Pacific is rimmed by convergent margins, it lacks Andean-style chains, which led Russo and Silver (1996) to conclude that convergence alone could not have produced the prominent Andean orogen. They proposed instead that the Andes formed by a *"collision"* between the trenchward-moving South American plate and the Nazca slab and sub-slab mantle, in a manner analogous to a classic Wilson Cycle continental collision (Silver and Russo, 1995; Russo and Silver, 1996). Their conclusion is substantiated by the fact that the orocline occurs at the mid-width of the subducting Nazca plate, and the Inner Arc forms a distinct "hump", clearly superimposed on the continent-wide linear trend of the Andean orogen (Fig.1a). This unusual convexity in the trend of the Cordillera is restricted

FIGURE 2. Schematic location of the Central Andean tin belt (in black, outline after Lehmann, 1979) with respect to the axis of highest tectonic compression and oroclinal bending, which has been taking place since ~25 Ma before present. The outline of the forearc position prior to shortening is from Isacks (1988), the arrows showing the rotation of the orocline limbs are from Kley (1999) and the direction of maximum shortening is from Kennan (2000).

N

Andean
orogen

Forearc
position
prior to
shortening

15-20°

Bolivian orocline

Highest compression

Maximum shortening
> 300 km

15-20°
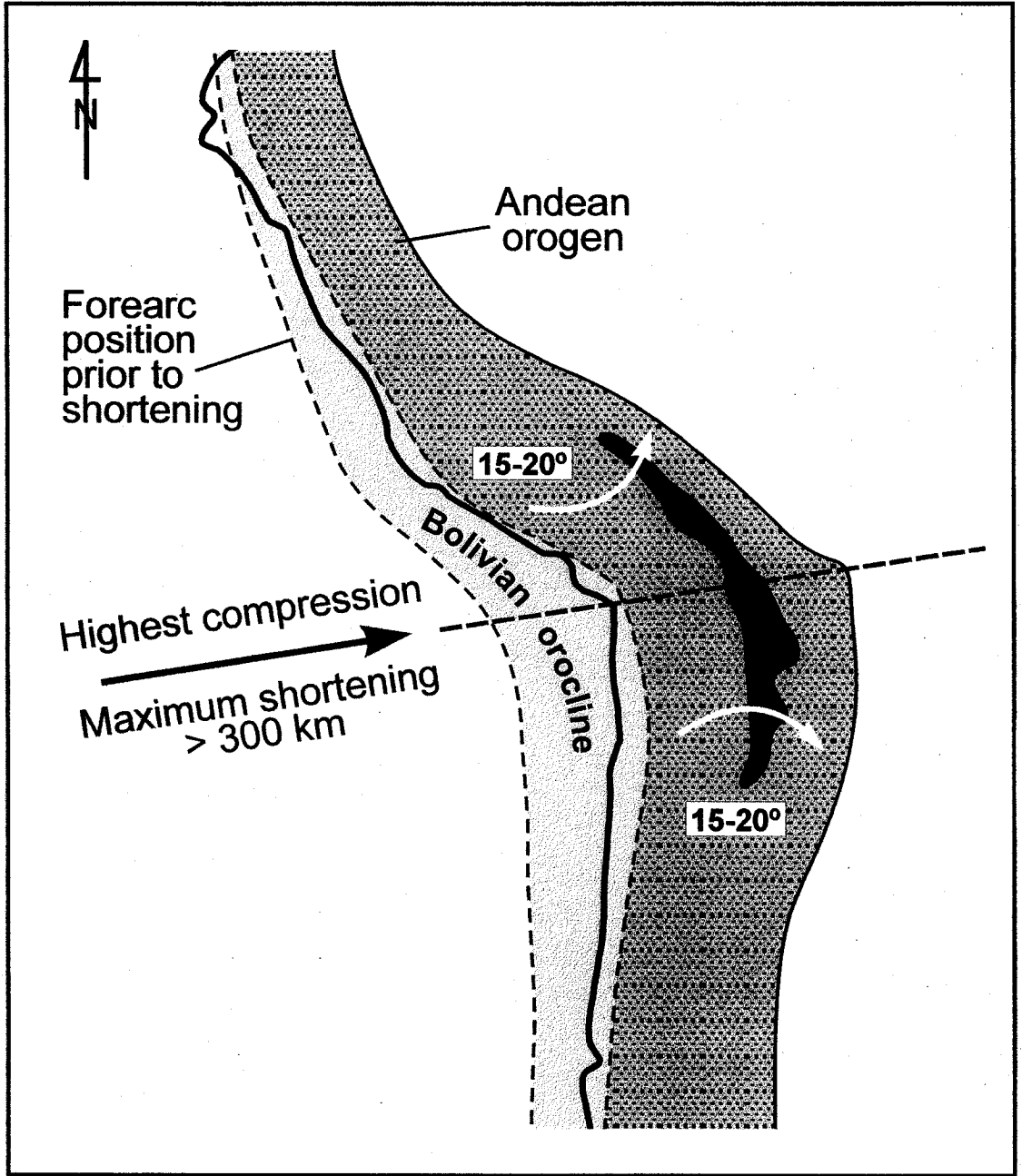
to the vicinity of the orocline and points strongly to "tectonic indentation" and resulting crustal shortening and thickening. Given the marked resemblance in the morphology and tectonics of the Central Andes to those of collisional mountain belts, it is reasonable to speculate that granitic magmatism and metallogeny in the Central Andes may have been driven by processes similar to those operating in collisional orogens.

TEMPORAL RELATIONSHIPS

Having made the case that the distinctive location of the Central Andean tin province was controlled by large-scale Tertiary tectonics, it is now appropriate to consider the temporal relationships between the orogeny and ore-related magmatism. According to Pardo-Casas and Molnar (1987) and Sempere et al. (1990), the progressive breakup of the Farallon plate into the Nazca and Cocos plates, which took place in the late Oligocene (at 27-25 Ma), produced rapid, nearly orthogonal plate convergence and a major tectonic and magmatic crisis in southeastern Peru and Bolivia. The increase in the trenchward velocity of the overriding South American plate triggered an enormous, horizontal, compressive stress, which resulted in large scale failure and underthrusting of the Brazilian shield beneath the Andes. Consequences of this were the development of the sub-Andean external foreland basin and the Altiplano intermontane basin, which were separated by a zone of thrusting and crustal anatexis in the region of the present Inner Arc (Sempere et al., 1990; Russo and Silver, 1996). Most of the oroclinal bending of the Andean margin is also believed to have taken place at this time, in the interval 25-10 Ma (James and Sacks, 1999).

The dramatic onset of the orogeny coincided broadly with a major resumption of magmatism throughout the Central Andean region. There is, however, considerable debate over the exact timing of the first igneous event (*cf.*, Clark et al., 1990; Soler and Bonhomme, 1990; Sebrier and Soler, 1991; Sandeman et al., 1995a; James and Sacks, 1999). The chronology given below follows the reconstruction of Sandeman et al. (1995a) for southeastern Peru, which is the most recent and detailed. According to these authors, rejuvenation of the narrow, volcano-plutonic Main Arc (Western Cordillera) could have occurred as early as 31 Ma, with the eruption of the Tacaza Group volcanics. They also

established that between 30 and 29 Ma there was magmatism along the Main Arc front, and that at 28.5 ± 1 Ma the latter experienced a sudden eastward broadening to a width of ~235 km, encompassing the entire Western Cordillera and Altiplano. By 25 Ma, the magmatic belt had attained a total width of ~360 km, and extended into the Inner Arc (Eastern Cordillera), where upper-mantle sourced, high-K to shoshonitic basalt-andesite melts caused localized, intense crustal melting and produced peraluminous, felsic suites (Kontak et al., 1986; Clark et al., 1984; 1990; Sandeman et al., 1995a; 1995c).

A remarkable feature of the above magmatism is that it occurred in many places along the Inner Arc, and was associated with a major Sn-W metallogenic event (Fig.3a). Thus, in southeastern Peru (at latitude 14°13'S), the San Rafael (Quenamari) granitic porphyry was shallowly emplaced at ~25 Ma (Fig. 3b), and some 1-2 Ma later became host to the world's richest lode tin deposit (Fig. 3a), presumably as a result of a subsequent magmatic pulse (Clark et al., 1983; Kontak et al., 1987; Mlynarczyk et al., 2003). Coeval mineralization centres in this region of SE Peru include: Santo Domingo (Zn-Pb-Cu-Sn-Ba), Rosario (Mo-W-Sn-Cu) and Condoriquiña (Cu-Zn-Pb-Sn), as well as the high-grade Palca 11 tungsten(-polymetallic) deposit, located ~100 km southeastward (Clark et al., 1990; Farrar et al., 1990). In northwestern Bolivia, the Quimsa Cruz granodioritic batholith was shallowly emplaced at ~26 Ma, and was the site of a second pulse of porphyritic granite intrusion at ~24 Ma (McBride et al., 1983), with which the Viloco and Caracoles tin deposits are associated. A similar age is inferred for the Chicote and Kami tungsten deposits (Thorn, 1988). Further south, in the Morococala area, the San Pablo stock, with which vein-type tin mineralization is associated, has an age of ~23.3 Ma, while the eruptive complexes of Lllallagua and Colquechaca (~100 km SE), which host rich tin-silver veins, have been dated at ~21 Ma and ~22.6 Ma, respectively (Grant, 1979; Lehmann et al., 1979). Finally, as far south as latitude 19°50'S, in the Los Frailes-Potosi area, the Kari-Kari batholith and the Kumurana pluton were emplaced between 23 and 21 Ma, and initiated a major Sn-W metallogenic episode (Lehmann, 1979; Clark et al., 1990). Overall, it can be seen that coeval formation of major Sn-W deposits, the first to occur in the Central Andes after the Early Jurassic, took place along the Inner Arc very shortly after (i.e., within a few Ma) the initiation of compression and deformation, which

FIGURE 3. A. Migration of metallogeny with time in the Central Andean tin belt (grey field). The white arrows, indicating the direction of compression in the Late Oligocene, are from Sandeman et al. (1996). The ages of the ore deposits were taken from Lehmann (1979), Grant et al. (1979), Grant et al. (1980), Kontak and Clark (1985), Thorn (1988), Kontak et al. (1990), and Petersen (1999). B. Permo-Triassic, Early Jurassic and Tertiary plutons and volcanics in the Central Andean tin belt (modified after Botello et al., 1973; Grant et al., 1979; and Clark et al., 1990).

234

a

72°   69°   66°

14°

Age of the onset of mineralization:

△ Mid-Miocene
▲ Early Miocene
▲ Late Oligocene
+ Late Triassic - Early Jurassic

Santo Domingo   San Rafael
Quenamari
Sarita
Rosario
Condoriquiña
Palca XI

Sn or **W**

?

Initial compression (Late Oligocene)

Fabulosa
Milluni
Chacaltaya
Chojlla
Bolsa Negra
Viloco
Caracoles
Chicote
Kami
Oruro - San José
Japo
Santa Fe - Morococala
Huanuni
Llallagua - Catavi
Colquechaca

Sn or **W**

Sn

18°

migration of metallogeny in time

Sn-Ag

Cerro Rico de Potosi

Tasna
Chorolque
Tatasi
Iscaisca
Chocaya

22°

PACIFIC OCEAN

Pirquitas

N

0   200 km

b

72°   69°   66°

Macusani volcanics

Cordillera Carabaya granites

Coasa
Aricoma
Limbani

14°

▦ Zone devoid of Oligocene-Miocene intrusions/volcanics
⌵ Miocene-Pliocene volcanics
⬗ Oligocene-Miocene intrusions
⬗ Permo-Triassic and Early Jurassic intrusions

San Rafael-Quenamari granite
Crucero volcanics
Picotani volcanics

Choquene stock

Sorata
Zongo
Taquesi

Cordillera Real granites

Illimani pluton
Quimsa Cruz batholith
Santa Vera Cruz pluton

18°

San Pablo stock
Morococala ignimbrite

Los Frailes ignimbrite

Kari-Kari batholith

Kumurana stock

22°

PACIFIC OCEAN

N

0   200 km

must have been the trigger for granitic magmatism and, therefore, the associated metallogeny.

A striking feature of the Tertiary tin metallogeny in the Central Andes is the temporal coincidence between successive compressional pulses and the magmatic-metallogenic episodes, (Figure 4; *cf.* Soler and Bonhomme, 1990; Cheilletz et al., 1992). Five short-lived, compressional events of regional extent have been described and dated at approximately: 26, 17, 10, 7 and 2 Ma (Sébrier and Soler, 1991). The late Oligocene (*Aymara, F2*) event at ~26 Ma initiated the ongoing Andean deformation, and produced the major metallogenic event, described above, which lasted until early Miocene (from approximately 25 to 19 Ma). After an apparent hiatus of 2 Ma (Grant et al., 1980), the early Miocene (*Quechua 1, F3*) compressional event at 17 Ma coincided with the resumption of magmatism and major Sn-Ag mineralization in central and southern Bolivia (from 17 to 12 Ma; Grant et al., 1980), as well as with volcanism and minor mineralization in southeastern Peru (e.g., the ~17 Ma-old Jésica Sn-Zn showing at Cerro Lintere, Clark et al. 1990; and the 16.9-16.6 Ma Huacchane and 16.4-16.2 Quebrada Escalera silicic tuff formations, Sandeman et al., 1995b). Finally, the mid-Miocene (*Quechua 2, F4*) event at 10 Ma and the late-Miocene (*Quechua 3, F5*) event at 7 Ma coincided closely with the emplacement of extensive ignimbrite sheets in southeastern Peru and southern Bolivia, after which, magmatic activity (in the Pliocene) retreated westward (Clark et al., 1990; Cheilletz et al., 1992; Poupeau et al., 1992; Koeppen et al., 1987; Pichavant et al., 1988a; 1988b; Morgan et al., 1998). Although mid- and late-Miocene volcanics are only associated with uranium veins, they share the same petrological chararacteristics and unusual lithophile element enrichment as the granitic rocks, which host earlier tin mineralization (see below).

It is worth noting that the late Miocene ignimbrite fields, i.e., the Macusani volcanic field in southeastern Peru (~1200 km^2), and the Morococala (~1500 km^2) and Los Frailes (~8500 km^2) volcanic fields in southern Bolivia, are located at the opposite ends of the tin province (Fig.3b). Assuming that the axis of tectonic indentation experienced a minor clockwise rotation in time and, initially, was located NW of the Cordillera Real of Bolivia (*cf.* Sandeman et al., 1995a), the locations of these volcanic fields and that of the Late Oligocene Sn-W deposits display a remarkable symmetry with

FIGURE 4. Generalized chronology of compressional tectonics, magmatism and mineralization in the Central Andes of Peru and Bolivia (modified after Clark et al., 1990; McBride et al., 1983, Sandeman et al., 1995a; Sebrier and Soler, 1991; Soler and Bonhomme, 1990). The abbreviation BM refers to base metals (Cu-Zn-Pb).
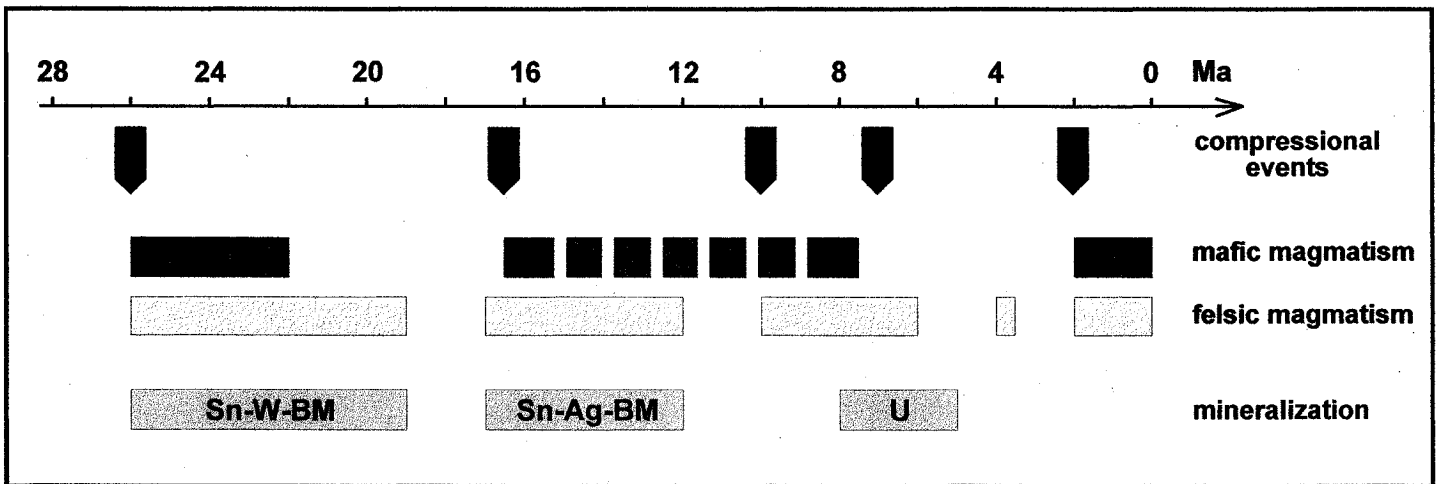
regard to this axis of compression (Fig.3a,b). This suggests that the Tertiary magmatism in the Inner Arc was driven directly by the compressional interaction between the Nazca and the South American plates.

PETROLOGY OF THE IGNEOUS SUITES

The Central Andean igneous suites associated with Tertiary Sn-W metallogeny are preserved either as plutonic or subvolcanic rocks, depending on the local level of erosion. In southeastern Peru, as well as in central and southern Bolivia, they form shallow-level intrusions and volcanics, whereas in northwestern Bolivia (inferred to have undergone a more significant uplift), they are represented by epizonal plutons. In general, the intrusions are of small size, have a granitic to granodioritic composition, are markedly peraluminous (as evidenced by the common occurence of cordierite, biotite ± muscovite, and in some cases sillimanite, andalusite or garnet), strongly reduced ("S-type" and "ilmenite-series"), and commonly enriched in lithophile trace elements, such as Rb, Li, Cs, B and Sn (McBride et al., 1983; Kontak and Clark, 1988; Clark et al., 1990; Avila-Salinas, 1990; Lehmann et al., 1990; 2000). The volcanics, which are far more voluminous (Fig. 3b), are compositionally similar, and consist of moderately- to highly-fractionated, two-mica peraluminous rhyolites, which are also reduced and unusually enriched in B, Li, Be, Rb, Cs, Nb, Ta, Sn, W, As, Sb, Zn, and U (e.g., the Macusani and Morococala ignimbrite fields; Noble et al., 1984; Pichavant et al., 1988b; Sandeman et al., 1993; 1995a; Morgan et al., 1998). Although the southern Bolivian porphyry tin deposits are hosted by quartz-latites and dacites, recent melt inclusion studies by Dietrich et al. (2000) suggest that the metals were introduced by highly fractionated rhyolitic melts, which are not exposed on the surface. The bulk of the Tertiary rocks of the tin province have a strongly peraluminous, felsic character, making this one of the largest provinces of peraluminous rocks in the world.

Based on their mode of emplacement, mineral assemblage, as well as petrographic, chemical and isotopic characteristics, the granitic rocks of the tin province correspond closely to two of the six types of granitoids classified by Barbarin (1996, 1999), namely the biotite-rich, cordierite-bearing peraluminous granitoids (CPG's) and

237

the muscovite-bearing peraluminous granitoids (MPG's). Thus, the Quenamari pluton (SE Peru), which hosts the world-class San Rafael tin deposit, is an excellent example of a CPG, whereas the northern part of the Quimsa-Cruz batholith (NW Bolivia), which hosts the Viloco tin deposit, is a MPG. Both of these granitoid types are produced by the partial melting of crustal rocks and, significantly, are associated with zones of continental collision and associated crustal thickening. According to Barbarin (1996), the CPG's form when hot, mantle-derived magmas are injected into or underplate deep crustal rocks, yielding conditions of "dry" anatexis. The latter generates peraluminous, tonalitic to monzogranitic melts, from which water-poor to water-free aluminosilicates such as cordierite can crystallize. By contrast, the MPG's are generated when major crustal shear zones and thrusts provide water to the thickened crust, resulting in "wet" anatexis and the formation of two-mica granites. Thus, both types of granitic suites can be produced during the same geodynamic event and from the same source (Barbarin, 1996).

The protoliths of the felsic magmas emplaced in the Central Andean tin belt consisted mostly of crustal, aluminous rocks, rich in graphite, which is indicated by their peraluminous, S-type chemistry (including the presence of early ilmenite), their trace element compositions, elevated $\delta^{18}O$ values, ϵ_{Nd} values between -5 and -10, high initial Sr isotope ratios (0.706-0.718), as well as the nature of restitic enclaves (Kontak et al., 1983; 1990; MacFarlane et al., 1990; Lehmann et al., 1990; 2000; Morgan et al., 1998; Faure, 2001). Moreover, ore lead isotope data for Tertiary mineralization centres in SE Peru and NW Bolivia are very similar, suggesting that the ore metals (Sn, W) were derived from a common, laterally extensive, crustal source region (Kontak et al., 1990), most likely a thick pile of Lower Paleozoic metapelites of marine origin and the underlying Precambrian gneissic basement.

In addition to the dominant peraluminous felsic rocks, the tin province also hosts minor, but noteworthy, occurrences of coeval basic rocks. These form local mafic igneous centers containing absarokites, shoshonites and high-K calc-alkaline basalts, as well as rocks of intermediate composition (e.g., dacites), inferred to be the result of mixing of rhyolitic and basaltic magmas. Rare mafic enclaves occur locally in the felsic rocks and have Pb and Sr isotopic compositions with a mantle signature, indicating that the asthenospheric mantle wedge contributed mafic melts to the crustal reservoir (Pichavant

et. al., 1988b; Kontak et al., 1986; 1990; Sandeman and Clark, 1993; Sandeman et al., 1995a; Dietrich et al., 2000).

DISCUSSION

Towards a model for the Central Andean tin province

A comprehensive model for the Tertiary tin metallogeny of the Central Andes needs to consider three fundamental issues: (1) a source for the ore-bearing magmas (there is little doubt about the igneous origin of the metals); (2) a mechanism for concentrating and depositing the metals; and (3) a large-scale geodynamic process capable of driving the magmatism. The first two issues are relatively well understood. The 10-15 km-thick pile of carbon- and boron-rich, Lower Paleozoic marine metasediments and the Precambrian gneissic basement, which underlie the Eastern Cordillera, are very favourable protoliths for the generation of felsic magmas, which subsequently could become enriched in tin. This is because peraluminous, S-type granitic magmas, which equilibrate with a graphite-rich, metapelitic source have a very low oxidation state and consequently are able to dissolve high concentrations of tin (Taylor and Wall, 1992). Moreover, the minerals, which could be the most significant hosts for tin (i.e., pyroxene, amphibole, titanite and magnetite) are absent, causing tin to behave as an incompatible element with respect to the crystallizing phases (Ishihara, 1981; Taylor and Wall, 1992). As a result, unusually strong tin enrichment in the melt is possible with protracted fractional crystallization. Since the magma is relatively acidic (peraluminous versus metaluminous or peralkaline) and exsolution of an aqueous fluid is late (relatively dry anatexis), the latter is acidic and chlorine-rich, which make it ideal for the transport and concentration of tin (Wilson and Eugster, 1990; Taylor and Wall, 1993).

It is more difficult to constrain the exact nature of the geodynamic trigger for the magmatism and metallogeny. As can be inferred from the relative scarcity, short duration (compared to the geological time scale), and timing of such metallogenic events, they require a very special set of geotectonic conditions, which are also shared by coeval, large-scale orogeny. A key feature which needs to be addressed here, is the sudden flaring and eastward migration of magmatism and crustal deformation that preceded tin

mineralization, and the late withdrawal of magmatic activity to the west (Main Arc), where it was restricted in the Holocene. As discussed in the earlier sections, there is a strong association with compressional tectonics, which evokes scenarios of tectonic indentation. In this light, the hypothesis advanced by Sébrier and Soler (1991) is of particular interest. These authors proposed that, normally, most of the westward movement of the South American plate is accommodated by the retreat of the Nazca slab (i.e., the trench is moving westwards) and the subduction process takes place relatively smoothly. During these periods, the shortening is only minor and an extensional tectonic regime prevails in most of the Andean Cordillera. However, when the retreat of the Nazca slab is slow or even blocked, short-lived compressional events take place, as most of the westward drift of the South American plate is accommodated by tectonic shortening in the back arc of the Cordillera (Fig.5). The restriction of the most intense deformation to the Eastern Altiplano and Eastern Cordillera can, in turn, be explained by them being underlain by a relatively weak lithosphere and, therefore, serving as "buffer zone" between the strong cratonic root of the Western Central Andes (the Arequipa-Antofalla massif, accreted to the continental margin in the Late Paleozoic) and the large Brazilian craton to the east (Clark et al., 1990; James and Sacks, 1999).

In addition to focusing crustal deformation in the zone of the Inner Arc and thereby triggering intense anatexis, sporadic "collision" between the South American plate and the Nazca slab must also have markedly shallowed the angle of subduction (*cf.* Carlowicz, 1995; Scholz and Campos, 1995). This would have forced the asthenospheric wedge to retreat to the east, and would have caused a corresponding shift of magmatism in the overriding plate, an inference which agrees well with the observed petrogenetic history of the region. In a more radical, alternative scenario, a slab blocked during a major compressional event could even break up and, as pointed by Sébrier and Soler (1991), the vicinity of the orocline, where the continental margin has a strong concavity is a favorable place for this to occur. In this scenario, the "slab window" so created would permit a sudden upwelling of asthenospheric mantle, and the associated high heat flow would generate a front of intense magmatism migrating eastward, in the trail of the sinking broken slab. This model satisfactorily explains the dramatic arc broadening observed at ~28.5 ± 1 Ma in the Central Andes (Clark et al., 1990; Sandeman et al.,

FIGURE 5. Schematic cross-section of the Andean continental margin, in the vicinity of the orocline, showing the relationships between the rate of convergence, the corresponding retreat of the subducted slab, the angle of subduction, and the width of the magmatic arc.

a
"Normal" subduction and
a narrow magmatic arc, above
the section of the slab, which
undergoes dehydration and
triggers lower crustal melting

b
A "collisional" episode between
the continental and oceanic plates
leads to shallower subduction, crustal
shortening and magmatic arc broadening
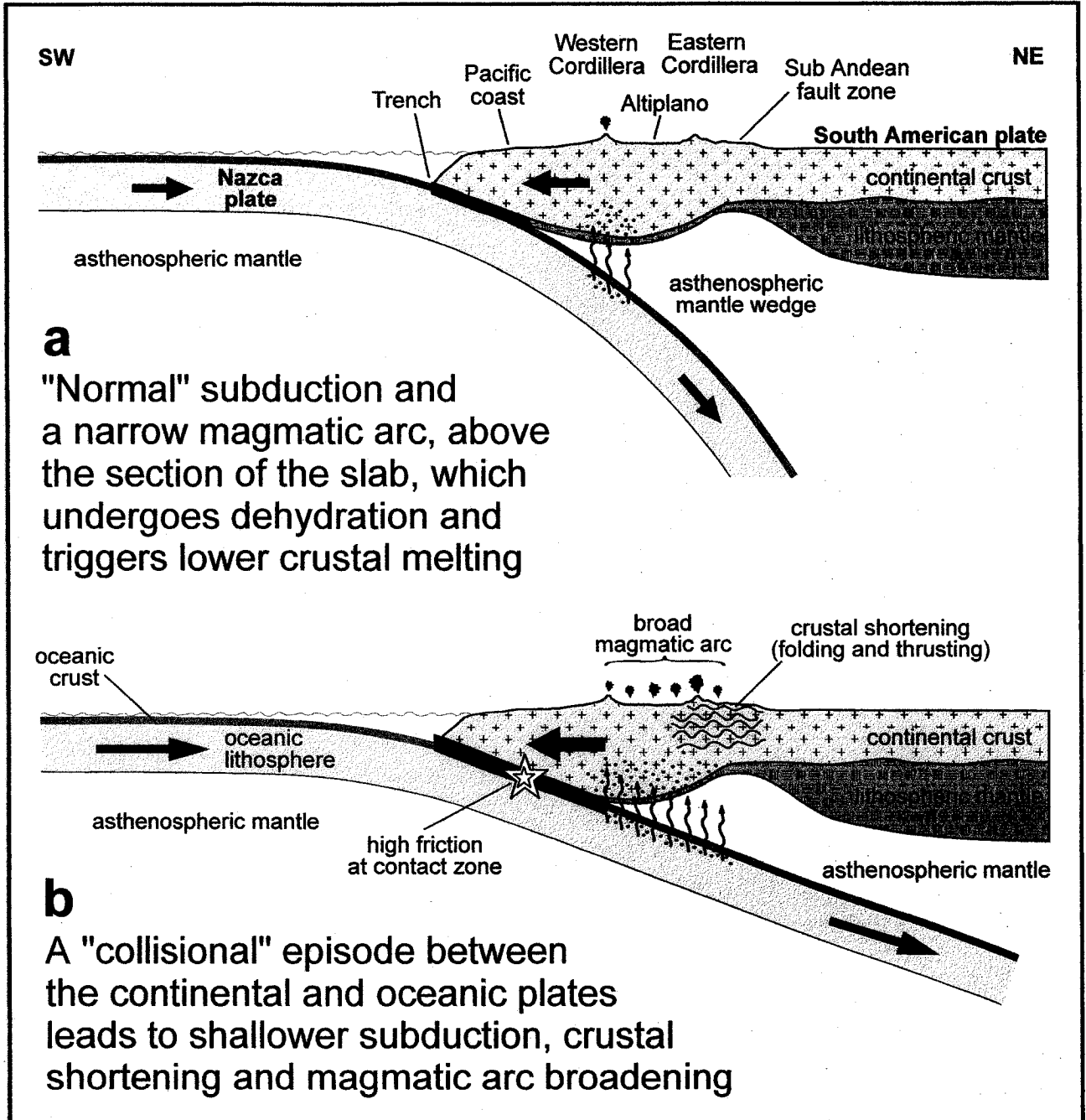
1995a). However, it does not explain the observed succession of short-lived magmatic episodes, matching periods of compression, or the westward retraction of magmatism in the Pliocene, which are readily accounted for by a return to steeper subduction. On the other hand, if the eastward migration of magmatism in the Oligocene was controlled by a shallowing angle of subduction, this would imply a broadening of the magmatic arc (since a wider section of the subducted slab would occur at the depth where dehydration takes place; Figure 5) and a concurrent decrease in igneous activity in the Western Andes, facts which are well supported by the observations of other researchers (*cf.* Figs. 1-6 in Petersen, 1999; Fig. 17 in Clark et al., 1990). The trigger for the initial "collisional" event, which set up the chain of events leading to orogenesis, magmatism and tin metallogeny, was likely a major plate tectonic reorganization in the Pacific region and the breakup of the Farallon plate into the Nazca and Cocos plates, which were initiated at ~27 Ma and caused a significant increase in the convergence rate (from ~5 to ~10 cm/yr; Soler and Bonhomme, 1990). The ensuing tectonic indentation of the central segment of the Andean margin, located approximately at the midpoint of the eastern boundary of the newly formed Nazca plate, resulted in an unprecedented shortening of the thermally weakened continental crust and the formation of an increasingly thick crustal root. The depression of the lower crust to mantle depths, radiogenic heat produced by the substantial thickening of the continental crust, shear heating along the deep crustal thrusts, and underplating by hot, voluminous mafic melts, ascending from a shallowing slab, then caused extensive crustal anatexis. This, in turn, increased the ductility of the crust and favored further deformation (*cf.* James and Sacks, 1999). Naturally, the contribution of heat from the aforementioned sources was uneven and evolved in time, with mantle magmatism being initially dominant, and radiogenic heating gaining importance once orogeny progressed and the crustal root grew. The outcome in all cases, however, was a high heat flow in the zone of strongest compression and the creation of extensive pools of magma, particularly underneath the Inner Arc, both of which are observed to this day (*cf.* Figs. 4 and 6 in James and Sacks, 1999; Yuan et al., 2000).

As was implied earlier, the difference in the nature of the protoliths in adjacent parts of the Central Volcanic Zone satisfactorily explains the persistently different character of the corresponding felsic magmas, namely I-type granitoids in the Western

Cordillera and Altiplano region, and S-type granitoids in the Eastern Cordillera (Ishihara, 1981; Cobbing, 1990). In addition, the presence of a thick crustal root and ponding of the melts in deep reservoirs likely protracted the processes of assimilation and fractional crystallization, yielding increasingly evolved, "fertile tin granites". The ascent of these melts probably took place along systems of deep crustal thrusts, such as the Eastern Cordillera fault system, as there is growing evidence throughout the Andes, that major lineaments periodically controlled the location of magmatism and mineralization (Hanuš et al., 2000). Finally, when the loci of Tertiary magmatic activity in the Central Andean tin province are examined in detail (Fig. 3b), it is striking that the ca. 250-km long stretch of the Eastern Cordillera in NW Bolivia, which directly faces the inferred vector of tectonic indentation, conspicuously lacks magmatism (Sandeman et al., 1995). This is precisely what would be expected in the zone of maximum compression where the absence of structural pathways would prevent the rise of magma, and further supports our contention that collisional tectonics is a primary cause of tin metallogeny.

The Triassic-Jurassic Sn-W metallogenic episode

An earlier and potentially significant event in the Central Andes, that has not been discussed so far, is the mid-Triassic - early Jurassic emplacement of large granitic batholiths in the Cordillera Real of NW Bolivia, with which several notable tin deposits are associated (Figs. 3a, b). This region experienced subsequent erosion, which removed all but the deeper epizonal plutons and, unfortunately, has been much less studied than the much richer and wider Tertiary metallogenic province. The numerous, vein-type hydrothermal tin-tungsten deposits in the Cordillera Real are structurally and mineralogically very similar to those deposits of the Tertiary episode, which were deeper-seated, but they are of smaller size and richer in tungsten (Turneaure, 1971; Rivas, 1979; Urquidi-Barrau, 1989). They are associated with a chain of large plutons of granitic-granodioritic composition, which are mostly peraluminous, S-type, reduced and have high tin contents. These granitoids are believed to have formed during a period of "Andino-type" compressional tectonism, namely the Kolla orogenic phase (McBride et al., 1983; Pitcher, 1979; Avila-Salinas, 1990). Considering that these intrusions share a similar

243

petrology with the Tertiary granitoids and also face the Bolivian orocline, a large component of which is currently believed to have predated Tertiary tectonics (Isacks, 1988; MacFadden et al., 1995), it is quite likely that they, too, are closely related to it. The mid-Triassic - early Jurassic Sn-W metallogeny of the Central Andes was then, apparently, also associated with an orogenic event and may have formed by a geodynamic process similar to the one, which produced its richer Tertiary counterpart.

We, therefore, conclude that it is not necessary to invoke a "persistent tin anomaly" in the Inner Arc region to explain the formation of the Central Andean tin belt (Ahlfeld, 1967; Schuiling, 1967). Instead, we propose that the metallogeny of the region is satisfactorily explained by a recurrent tectono-magmatic mechanism based on compressional interaction between the Farallon/Nazca oceanic plate and the South American continent. This periodically generated large volumes of peraluminous melts, which evolved by fractional crystallization and exsolved aqueous fluids that enriched the region in tin and tungsten.

Comparison to typical collisional orogens

Detailed comparisons with other magmatic arcs and tin provinces are beyond the scope of this paper, but it has to be emphasized that there are striking similarities between the Tertiary magmatism and tin metallogeny of the Central Andes and analogous episodes in more "typical" collisional orogenic belts, such as the Carboniferous Variscan fold belt of NW Europe, the Permo-Triassic Main Range of Peninsular Malaysia (extending into Thailand), the Cretaceous Sikhote Alin fold belt (Russian Far East), and even, to some extent the late Cenozoic Himalayas-Tibet. With the exception of the Himalayas, where relatively few tin deposits are known (probably because there has been insufficient erosion to expose them), all these belts host major resources of tin, and together with the Central Andes account for the bulk of the world's non-alluvial reserve of this commodity. They also share similar geodynamic histories, involving extensive partial melting of the middle crust and the generation of large volumes of S-type (and mixed S-I type) granites, as well as a localized, but probably symptomatic presence of K-rich mafic rocks, signalling a deep heat source (Seltmann and Faragher, 1994).

CONCLUSIONS

Tertiary magmatism in the Inner Arc of the Central Andes and the associated world-class tin mineralization are directly related to discrete episodes of "collisional" interaction between the Nazca slab and the South American plate. During these geodynamic events, the asthenospheric mantle wedge undergoing intense melting, was shifted eastward by a shallowing of subduction and caused the underplating of thick continental crust by hot mafic melts. This, together with shear heating generated by crustal thrusting, radiogenic heat from crustal thickening, and the depression of the lower crust into the mantle caused an extensive anatexis of the thick sequences of metasedimentary rocks and the gneissic basement, which underlie the Inner Arc. Voluminous, tin-rich magmas of peraluminous composition were produced and upon emplacement gave rise to large masses of high grade tin mineralization. We infer that this process has taken place repeatedly since the onset of the Andean orogeny and, therefore, conclude that it may also be responsible for the earlier episodes of tin mineralization in the Central Andes.

REFERENCES

Ahlfeld, F., and Schneider-Scherbina, A., 1964, Los yacimientos minerales y de hidrocarburos de Bolivia: Boletin Especial del Departamento Nacional de Geologia (Bolivia), v. 5, 388 p.

Ahlfeld, F., 1967, Metallogenetic epochs and provinces of Bolivia: Mineralium Deposita, v. 2, p. 291-311.

Avila-Salinas, W.A., 1990, Tin-bearing granites from the Cordillera Real, Bolivia; a petrological and geochemical review: *In* Kay, S.M., and Rapela, C.W., (eds.), "Plutonism from Antarctica to Alaska", Geological Society of America Special Paper, v. 241, p. 145-159.

Barbarin, B., 1996, Genesis of the two main types of peraluminous granitoids: Geology, v. 24, p. 295-298.

Barbarin, B., 1999, A review of the relationships between granitoid types, their origins and their geodynamic environments, Lithos, v.46, p. 605-626.

Botello, R., Subieta, T., Martinez, C., and Tomasi, P., 1973, Carte tectonique de Bolivie. Geological Survey of Bolivia / O.R.S.T.O.M.

Carlowicz, M., 1995, Anchor-like force proposed for subduction zones: EOS, Transactions, American Geophysical Union, v.76, no.49, p.497-498.

Cheilletz, A., Clark, A.H., Farrar, E., Arroyo Pauca, G., Pichavant, M., and Sandeman, H.A., 1992, Volcano-stratigraphy and $^{40}Ar/^{39}Ar$ geochronology of the Macusani ignimbrite field: monitor of the Miocene geodynamic evolution of the Andes of southeast Peru: Tectonophysics, v. 205, p. 307-327.

Clark, A.H., Farrar, E., Caelles, J.C., Haynes, S.J., Lortie, R.B., McBride, S.L., Quirt, G.S., Robertson, R.C.R., and Zentilli, M., 1976, Longitudinal variations in the metallogenetic evolution of the central Andes: a progress report: Geological Association of Canada Special Paper, v. 14, p. 23-58.

Clark, A.H., Palma, V.V., Archibald, D.A., Farrar, E., Arenas, M.J., and Robertson, R.C.R., 1983, Occurrence and age of tin mineralization in the Cordillera Oriental, Southern Peru: Economic Geology, v. 78, p. 514-520.

Clark, A.H., Kontak, D.J., and Farrar, E., 1984, A comparative study of the metallogenetic and geochronological relationships in the northern part of Central Andean tin belt, SE Peru and NW Bolivia: Proceedings of the Sixth Quadrennial IAGOD Symposium, Stuttgart, Germany, p. 269-279.

Clark, A.H., Farrar, E., Kontak, D.J., Langridge, R.J., Arenas, F. M.J., France, L.J., McBride, S.L., Woodman, P.L., Wasteneys, H.A., Sandeman, H.A., and Archibald, D.A., 1990, Geologic and geochronologic constraints on the metallogenic evolution of the Andes of southeastern Peru: Economic Geology, v. 85, p. 1520-1583.

Cobbing, E.J., 1990, A comparison of granites and their tectonic settings from the South American Andes and the Southeast Asian tin belt: *in* Plutonism from Antarctica to Alaska: Geological Society of America Special Paper, v. 241, Kay, S.M. and Rapela, C.W., (eds.), p. 193-204.

Dietrich, A., Lehmann, B., and Wallianos, A., 2000, Bulk rock and melt inclusion geochemistry of Bolivian tin porphyry systems: Economic Geology, v. 95, p. 313-326.

Faure, G., 2001, Origin of igneous rocks: the isotopic evidence. Springer Verlag Berlin, 496 p.

Farrar, E., Yamamura, B.K., Clark, A.H., and Taipe A., J., 1990, $^{40}Ar/^{39}Ar$ ages of magmatism and tungsten-polymetallic mineralization, Palca 11, Choquene district, southeastern Peru: Economic Geology, v. 85, p. 1669-1676.

Grant, J.N., Halls, C., Avila Salinas, W., and Snelling, N.J., 1979, K-Ar ages of igneous rocks and mineralization in part of the Bolivian tin belt. Economic Geology, v. 74, p. 838-851.

Grant, J.N., Halls, C., Sheppard, S.M.F., and Avila, W., 1980, Evolution of the porphyry tin deposits of Bolivia: Mining Geology, Special Issue, no. 8, p. 151-173.

Hanuš, V., Vaněk, J., Špičák, A., 2000, Seismically active fracture zones and distribution of large accumulations of metals in the central part of Andean South America: Mineralium Deposita, v. 35, p. 2-20.

Isacks, B.L., 1988, Uplift of the Central Andean plateau and bending of the Bolivian orocline. Journal of Geophysical Research, v. 93, p. 3211-3231.

Ishihara, S., 1981, The granitoid series and mineralization. Economic Geology, 75th anniversary volume, p. 458-484.

James, D.E., and Sacks, I.S., 1999, Cenozoic formation of the Central Andes: a geophysical perspective: *in* Geology and ore deposits of the Central Andes, Society of Economic Geologists, Special Publication no. 7, B.J. Skinner (ed.), p. 1-25.

Jaillard, E., Hérail, G., Monfret, T., Diaz Martinez, E., Baby, P., Lavenu, A., and Dumont, J.F., 2000, Tectonic evolution of the Andes of Equador, Peru, Bolivia and northernmost Chile. *In:* Tectonic evolution of South America, 31st International Geological Congress in Rio de Janeiro, Cordani, U.G., Milani, E.J., Thomaz Filho, A., and Campos, D.A. (eds.), p. 481-559.

Kelly, W.C., and Turneaure, F.S., 1970, Mineralogy, paragenesis and geothermometry of the tin and tungsten deposits of the Eastern Andes, Bolivia: Economic Geology, v. 65 , p. 609-680.

Kennan, L., 2000, Large-scale geomorphology of the Andes: interrelationships of tectonics, magmatism and climate. *In:* Geomorphology and global tectonics, Summerfield, M.A. (ed.), Wiley, p. 167-199.

Kley, J., 1999, Geologic and geometric constraints on a kinematic model of the Bolivian orocline: Journal of South American Earth Sciences, v. 12, p. 221-235.

Kley, J., and Monaldi, C.R., 1998, Tectonic shortening and crustal thickness in the Central Andes: how good is the correlation ? Geology, v. 26, p. 723-726.

Kley, J., and Eisbacher, G.H., 1999, How Alpine or Himalayan are the Central Andes ? International Journal of Earth Sciences, v. 88, p. 175-189.

Koeppen, R.P., Smith, R.L., Kunk, M.J., Flores, M., Luedke, R.G., and Sutter, J.F., 1987, The Morococala volcanics: highly peraluminous rhyolite ash flow magmatism in the Cordillera Oriental, Bolivia: Abstracts with Programs, Geological Society of America, v. 19, n. 1, p. 731.

Kontak, D.J., Clark, A.H., Farrar, E., Pearce, T.H., Strong, D.F., and Baadsgaard, H., 1986, Petrogenesis of a Neogene shoshonite suite, Cerro Moromoroni, Puno, southeastern Peru: Canadian Mineralogist, v. 24, p. 117-135.

Kontak, D.J., Clark, A.H., Farrar, E., Archibald, D.A., and Baadsgaard, H., 1987, Geochronological data for Tertiary granites of the southeast Peru segment of the Central Andean Tin Belt: Economic Geology, v. 82, p. 1611-1618.

Kontak, D.J., and Clark, A.H., 1988, Exploration criteria for tin and tungsten mineralisation in the Cordillera Oriental of southeastern Peru: Recent Advances in the Geology of Granite-Related Mineral Deposits - Proceedings of the CIM Conference on Granite-Related Mineral Deposits, September 1985. The Canadian Institute of Mining and Metallurgy, Special Volume 39, Taylor, R.P., and Strong, D.F., (eds.), p. 157-169.

Kontak, D.J., Cumming, G.L., Krstic, D., Clark, A.H., and Farrar, E., 1990, Isotopic composition of lead in ore deposits of the Cordillera Oriental, southeastern Peru: Economic Geology, v. 85, p. 1584-1603.

Lehmann, B., 1979, Schichtgebundene Sn-Lagerstätten in der Cordillera Real, Bolivien. Berliner Geowissenschaftliche Arbeiten, A(14), 135 p.

Lehmann, B., 1982, Metallogeny of tin: magmatic differentiation versus geochemical heritage: Economic Geology, v. 77, p. 50-59.

Lehmann, B., 1987, Tin granites, geochemical heritage, magmatic differentiation. Geologische Rundschau, v. 76, p.177-185.

Lehmann, B., Petersen, U., Santivañez, R., and Winkelmann, L., 1988, Distribución geoquímica de estaño y boro en la secuencia Paleozoica de la Cordillera Real de Bolivia. Boletin de la Sociedad Geologica del Peru, v. 77, p. 19-27.

Lehmann, B., Ishihara, S., Michel, H., Miller, J., Rapela, C., Sanchez, A., Tistl, M., and Winkelmann, L., 1990, The Bolivian tin province and regional tin distribution in the Central Andes: a reassessment: Economic Geology, v. 85, p. 1044-1058.

Lehmann, B., Dietrich, A., Heinhorst, J., Metrich, N., Mosbah, M., Palacios, C., Schneider, H.-J., Wallianos, A., Webster, J., and Winkelmann, L., 2000, Boron in the Bolivian tin belt: Mineralium Deposita, v. 35, p. 223-232.

MacFadden, B.J., Anaya, F., Swisher III, C.C., 1995, Neogene paleomagnetism and oroclinal bending of the central Andes of Bolivia: Journal of Geophysical Research, v. 100, p. 8153-8167.

MacFarlane, A.W., Marcet, P., LeHuray, A.P., and Petersen, U., 1990, Lead isotope provinces of the Central Andes inferred from ores and crustal rocks: Economic Geology, v. 85, p. 1857-1880.

McBride, S.L., Robertson, R.C.R., Clark, A.H., and Farrar, E., 1983, Magmatic and metallogenetic episodes in the Northern Tin Belt, Cordillera Real, Bolivia: Geologische Rundschau, v. 72, p. 685-713.

Mlynarczyk, M.S.J., Sherlock, R.L. and Williams-Jones, A.E. (2003) San Rafael, Peru: geology and structure of the worlds richest tin lode. Mineralium Deposita, 38, 555-567.

Morgan, G.B.VI, London, D., and Luedke, R.G., 1998, Petrochemistry of late Miocene peraluminous, silicic volcanic rocks from the Morococala field, Bolivia: Journal of Petrology, v. 39, p. 601-632.

Noble, D.C., Vogel, T.A., Peterson, P.S., Landis, G.P., Grant, N.K., Jezek, P.A., and McKee, E.H., 1984, Rare-element-enriched, S-type ash-flow tuffs containing phenocrysts of muscovite, andalusite and sillimanite, southeastern Peru: Geology, v. 12, p. 35-39.

Oyarzún, J., 2000, Andean metallogenesis – a synoptical review and interpretation. *In:* Tectonic evolution of South America, 31st International Geological Congress in Rio de Janeiro, Cordani, U.G., Milani, E.J., Thomaz Filho, A., and Campos, D.A. (eds.), p. 725-753.

Pardo-Casas, F., and Molnar, P., 1987, Relative motion of the Nazca (Farallon) and South American plates since Late Cretaceous time: Tectonics, v. 6, p. 233-248.

Petersen, U., 1999, Magmatic and metallogenic evolution of the Central Andes. *In:* Geology and ore deposits of the Central Andes, Society of Economic Geologists Special Publication 7, Skinner, B.J., (ed.), p. 109-153.

Pichavant, M., Kontak, D.J., Valencia Herrera, J., and Clark, A.H., 1988a, The Miocene-Pliocene Macusani volcanics, SE Peru: I. Mineralogy and magmatic evolution of a two-mica aluminosilicate-bearing ignimbrite suite: Contributions to Mineralogy and Petrology, v. 100, p. 300-324.

Pichavant, M., Kontak, D.J., Briqueu, L., Valencia Herrera, J., and Clark, A.H., 1988b, The Miocene-Pliocene Macusani volcanics, SE Peru: II. Geochemistry and origin of a felsic peraluminous magma: Contributions to Mineralogy and Petrology, v. 100, p. 325-338.

Pitcher, W.S., 1979, Comments on the geological environment of granites, *in*: Atherton, M.P., Tarney, J., (eds.), Origin of granite batholiths: geochemical evidence; Cheshire, U.K., Shiva Publications, p. 1-8.

Poupeau, G., Sabil, N., Villa, I.M., Bigazzi, G., Vatin-Perignon, N., Flores, P., Pereyra, P., Salas, G., and Arroyo, G., 1992, Fission-track and K-Ar ages of "macusanite" obsidian glasses, (SE Peru): geodynamic implications: Tectonophysics, v. 205, p. 295-305.

Ramos, V.A., and Aleman, A., 2000, Tectonic evolution of the Andes. *In:* Tectonic evolution of South America, 31st International Geological Congress in Rio de

Janeiro, Cordani, U.G., Milani, E.J., Thomaz Filho, A., and Campos, D.A. (eds.), p. 635-685.

Rivas, S., 1979, Geology of the principal tin deposits of Bolivia: Geological Society of Malaysia Bulletin, v. 11, p. 161-180.

Russo, R.M., and Silver, P.G, 1996, Cordillera formation, mantle dynamics, and the Wilson cycle: Geology, v. 24, p. 511-514.

Sandeman, H.A., and Clark, A.H., 1993, Mingling and mixing of minette and "S-type", anatectic, rhyodacitic magmas, Crucero Supergroup, Puno, SE Peru: Geological Association of Canada / Mineralogical Association of Canada, Joint Annual Meeting, May 17-19, 1993, Edmonton, Program with abstracts, p. 92.

Sandeman, H.A., Clark, A.H., Farrar, E., and Arroyo, G., 1993, The Crucero Supergroup, Puno, SE Peru: Oligocene-Miocene "collisional" magmatism in a non-collisional arc setting: Geological Association of Canada / Mineralogical Association of Canada, Joint Annual Meeting, May 17-19, 1993, Edmonton, Program with abstracts, p. 92.

Sandeman, H.A., Clark, A.H., and Farrar, E., 1995a, An integrated tectono-magmatic model for the evolution of the Southern Peruvian Andes (13-20°S) since 55 Ma: International Geology Review, v. 37, p. 1039-1073.

Sandeman, H.A., Clark, A.H., and Farrar, E., 1995b, An integrated tectonomagmatic model for the evolution of the central Andes in the vicinity of the Bolivian orocline from 22 Ma-to-the present day: Geological Society of America, Abstracts with Programs, v. 27, p. 409.

Sandeman, H.A., Clark, A.H., Farrar, E., Wasteneys, H.A., and Satterly, J., 1995c, An integrated tectonomagmatic model for the evolution of the central Andes in southern Peru from 55 to 20 Ma: implications for the generation of orogenic potassic-to-ultrapotassic magmas: Geological Association of Canada / Mineralogical Association of Canada, Joint Annual Meeting, May 17-19, 1995, Victoria, Program with abstracts,v. 20, p. 93.

Schuiling, R.D., 1967, Tin belts on the continents around the Atlantic Ocean: Economic Geology, v. 62, p. 540-550.

Sébrier, M., and Soler, P., 1991, Tectonics and magmatism in the Peruvian Andes from late Oligocene time to the Present: *in* Andean magmatism and its tectonic setting, Geological Society of America Special Paper 265, Harmon, R.S., and Rapela, C.W., (eds.), p. 259-278.

Seltmann, R., and Faragher, A.E., 1994, Collisional orogens and their related metallogeny – a preface: *in* Metallogeny of collisional orogens; Seltmann R., Kämpf H., and Möller P. (eds.), Czech Geological Survey, Prague, p. 7-19.

Sempere, T., Herail, G., Oller, J., and Bonhomme, M.G., 1990, Late Oligocene-early Miocene major tectonic crisis and related basins in Bolivia: Geology, v. 18, p. 946-949.

Scholz, C.H., and Campos, J., 1995, On the mechanism of seismic decoupling and back arc spreading at subduction zones: Journal of Geophysical Research, v. 100, p. 22,103-22,115.

Sillitoe, R.H., 1972, Relation of metal provinces in western America to subduction of oceanic lithosphere: Geological Society of America Bulletin, v. 83, p. 813-818.

Sillitoe, R.H., Halls, C., and Grant, J.N., 1975, Porphyry tin deposits in Bolivia, Economic Geology, v. 70, p. 913-927.

Sillitoe, R.H., 1976, Andean mineralization: a model for the metallogeny of convergent plate margins: Geological Association of Canada Special Paper, v. 14, p. 59-100.

Silver, P.G., and Russo, R.M., 1995, Cordillera formation, the Wilson cycle, and mantle flow: Abstracts with Programs, Geological Society of America, v. 27, n. 6, p. 337.

Soler, P., and Bonhomme, M.G., 1990, Relation of magmatic activity to plate dynamics in central Peru from Late Cretaceous to present: *in* Plutonism from Antarctica to Alaska: Geological Society of America Special Paper 241, Kay, S.M. and Rapela, C.W., (eds.), p. 173-192.

Stoll, W.C., 1965, Metallogenic provinces of South America. Mining Magazine, v. 112, p. 22-33 and 90-99.

Taylor, J.R., and Wall, V.J., 1992, The behavior of tin in granitoid magmas: Economic Geology, v. 87, p. 403-420.

Taylor, J.R., and Wall, V.J., 1993, Cassiterite solubility, tin speciation and transport in a magmatic aqueous phase: Economic Geology, v. 88, p. 437-460.

Thorn, P.G., 1988, Fluid inclusion and stable isotope studies at the Chicote tungsten deposit, Bolivia. Economic Geology, v. 83, p. 62-68.

Thorpe, R.S., Francis, P.W., Hammill, M., and Baker, M.C.W., 1982, The Andes. *In:* Andesites – orogenic andesites and related rocks, Thorpe, R.S. (ed.), Wiley, p. 188-205.

Turneaure, F.S., 1971, The Bolivian tin-silver province: Economic Geology, v. 66, p. 215-225.

Urquidi-Barrau, F., 1989, Tin and tungsten deposits of the Bolivian tin belt: Geology of the Andes and its relation to hydrocarbon and mineral resources: Houston, Texas, Circum-Pacific Council for Energy and Mineral Resources Earth Science Series; Ericksen, G.E., Cañas Pinochet, M.T., and Reinemund, J.A., (eds.), v. 11, p. 313-323.

Wilson, G.A. and Eugster, H.P., 1990, Cassiterite solubility and tin speciation in supercritical chloride solutions. *In:* Spencer RJ, Chou-I-Ming (eds) Fluid-mineral interactions; a tribute to H.P. Eugster. The Geochemical Society, Special Publication no. 2, p. 179-195.

Yuan, X., Sobolev, S.V., Kind, R., Oncken, O., Bock, G., Asch, G. , Schurr, B., Graeber, F., Rudloff, A., Hanka, W., Wylegalla, K., Tibi, R., Haberland, Ch., Rietbrock, A., Giese, P., Wigger, P., Röwer, P., Zandt, G., Beck, S., Wallace, T., Pardo, M., Comte, D., 2000, Subduction and collision processes in the Central Andes constrained by converted seismic phases: Nature, v. 408, p. 958-961.

CHAPTER VII

Conclusions

CONCLUSIONS

The San Rafael tin-copper deposit formed in the Late Oligocene, marking the onset of the most important metallogenic episode in the Inner Arc of the Central Andes, a region known for rich Sn-W-Ag-base metal mineralization, and commonly referred to as the "Bolivian tin belt". The mineral wealth of this area, which is adjacent to a major active continental margin, is related to periodic compressional interactions between the Nazca oceanic slab and sub-slab mantle and the South American continent. Recurrent "collisions" between these two tectonic plates focus strong compressional forces on the central segment of the continental margin, resulting in a marked crustal shortening and vertical thickening. In addition, during these continent-scale geodynamic events the angle of subduction shallows, shifting the asthenospheric mantle wedge eastward and causing the underplating of thickened continental crust by hot mafic melts. The heat advected by basaltic melts, together with the shear heating generated by crustal thrusting, radiogenic heat from crustal thickening, and the depression of the lower crust into the mantle all contribute to extensive anatexis of the thick sequences of metasedimentary rocks, which underlie the Inner Arc. A consequence of this is the generation of voluminous magmas of peraluminous composition, which subsequently evolve by fractional crystallization and exsolve fluids that deposit rich tin-(tungsten-silver) mineralization, notably the San Rafael deposit.

The mineralization at San Rafael is hosted by a single, vertically extensive, and structurally complex hydrothermal lode, which is part of a wider vein-breccia system, centered on a shallow-level polyphase granitoid stock. The early hydrothermal fluids, exsolved from a batch of highly fractionated granitic melt, and were hot, hypersaline, acidic brines (400-530°C and 34-62 wt.% NaCl eq.). They produced intense sericitization and tourmalinization of the host-rocks, and enriched them in B, Mg and Fe, at the expense of alkalis and alkali-earth elements, which are strongly depleted. This resulted in a total mass gain of $\leq$ 6 % and a volume increase of $\geq$ 6 % in the alteration envelopes. Swarms of barren, narrow tourmaline-quartz veins formed contemporaneously with alteration, all of which are sealed, suggesting near lithostatic pressure conditions. It is inferred that these early fluids, were reducing, iron-rich, and that they transported large amounts of tin,

255

mostly in the form of stannous (Sn^{2+}) chloride complexes, but they failed to deposit cassiterite.

A subsequent, large-scale tectonic reopening of the vein system produced a dramatic change in its plumbing and in the physico-chemical conditions of the fluids. Sinistral-normal strike-slip along the San Rafael fault created several large fault-jogs, at depth, which focused dilute, heated, oxidizing meteoric waters. These waters mixed thoroughly with the magmatic brines and produced fluids of intermediate temperature (~380°C), salinity (~20 wt.% NaCl eq.), and redox state. The marked dilution of the early brines caused supersaturation of dissolved iron and triggered strong, distinctive chloritization, which overprinted all earlier alteration (apart from tourmalinization), as well as the precipitation of Fe-rich chlorite and subordinate Fe-rich tourmaline (schorl). The chloritizing fluids introduced large amounts of Fe, Mn, Sn, W and In, and largely removed alkalis and alkali-earth elements from the rocks, producing a mass increase of ~ 4 % and a volume decrease of 3-4 % in the alteration envelopes. Moreover, the mixing of tin-bearing magmatic fluids with meteoric waters caused their oxidation, dilution, cooling and acid neutralization, which destabilized the chloride complexes of tin and triggered massive deposition of cassiterite. Thus, high-grade tin ores were preferentially deposited in the sites of fluid mixing, i.e., the fault-jogs. It is estimated that the deposition of cassiterite took place at an fO_2 between 10^{-35} and 10^{-30} and an ($a Fe^{2+}/a^2 H^+$) ratio between $10^{3.8}$ and $10^{4.6}$, from fluids which became progressively cooler and more oxidizing, as indicated by the localized presence of hematite, associated with cassiterite and chlorite. Fluid-rock interaction was not a control on tin deposition, as chloritic alteration of granitic rocks increases the fluid acidity, and this in turn increases tin solubility. The bulk of the tin resource was deposited during this first stage of mineralization, in the form of numerous cassiterite-quartz-chlorite-bearing veins and breccias, which are restricted to the lower part of the lode. These veins are all of the open fracture-filling type, with ubiquitous vugs, and provide evidence of a shift from lithostatic towards near-hydrostatic pressure conditions.

The formation of cassiterite ores was followed by a volumetrically smaller episode of sulfide deposition. Chalcopyrite-dominated ores, with disseminated acicular cassiterite were deposited in the upper part of the system and in the centers of some of

large, preexisting cassiterite-quartz-chlorite veins. The comparatively narrow range of $\delta^{34}S$ values of the San Rafael sulfides (between +2 and +6 ‰), indicates that the hydrothermal system was large-scale, and had a relatively homogenous source of the sulfur, presumably of magmatic origin. The alteration associated with this stage was also chloritic, but the temperature and salinity of the ore fluids were lower (>230-360°C, 0-21 wt.% NaCl eq.). In addition to the marked dilution of the ore fluids, they were also more oxidizing, as inferred by the ubiquitous replacement of pyrrhotite by pyrite, marcasite and hematite. The $\delta^{18}O$ of the ore fluids decreased markedly, consistent with the mixing of the ore fluids with cooler, isotopically lighter fluids of meteoric origin. The hydrothermal system closed with extensive precipitation of quartz, which formed numerous, barren veins, superimposed over the earlier vein types.

CONTRIBUTIONS TO KNOWLEDGE

The following are the most significant contributions to knowledge from this thesis:

1. This study represents the most comprehensive investigation of the structural geology, fluid evolution, wall-rock alteration, and ore mineralogy of a lode tin deposit from the Central Andean tin belt (a major metallogenic province). In addition it is the first to quantitatively evaluate the physico-chemical controls of ore deposition.

2. The study established that the ore-shoots of the world's largest hydrothermal tin lode represent wide fault-jogs, which formed by sinistral-normal, strike-slip movement. These jogs host unusually rich cassiterite mineralization because they provided sites for the effective mixing of meteoric fluids with tin-bearing magmatic brines, and thereby focused ore deposition.

3. The study is only the second to quantitatively investigate mass-transfer associated with host-rock alteration in a lode-type tin deposit. Two discrete hydrothermal episodes (early sericitization + tourmalinization, versus ore-stage chloritization) were identified and the associated fluids characterized from the corresponding alteration assemblages. The study

also established that chloritic alteration was not favorable for cassiterite deposition, as it increased the fluid acidity and, therefore, increased tin solubility.

4. This study is one of only a small number to have documented in detail the stable isotope (S,O,H,C) composition of ore and gangue minerals in a single hydrothermal tin lode. In addition, the sulfur isotope composition of ore minerals was determined by *in situ* laser sulfur analysis, a state of the art technique, which provides a unique opportunity to analyse small amounts of sulfide minerals directly in the polished samples.

5. A new hypothesis was developed to explain tin metallogeny in the Central Andes. This hypothesis proposes that Tertiary tin mineralization in this province (and possibly also the earlier metallogenic episodes) was produced by recurrent compressional interactions between the Farallon/Nazca oceanic plate and the South American continent. These periodic "collisions" generated voluminous, peraluminous magmas in the back arc of the orogen, which evolved by fractional crystallization, and exsolved the fluids responsible for the rich Sn-W(-Ag) mineralization.

TOPIC AREAS CONSIDERED FOR FUTURE WORK

This thesis is part of an ongoing program of research on the genesis of hydrothermal tin lodes (and, specifically, on the San Rafael deposit) by the author and presents only those results, which were complete enough to form publishable manuscripts. Several other lines of investigation are being pursued and others are being considered, which will form the basis of post-doctoral research. These include:

1. A full, microchemical characterization of fluid evolution at the San Rafael deposit, by laser ablation ICP-MS analysis of individual fluid inclusions, supplemented by Raman spectroscopy, gas chromatography, and electron microprobe analyses of inclusion solids.

2. A detailed petrological investigation of the host granitic rocks, focusing on the most evolved members of the suite, and including studies of melt inclusions.

3. The thermodynamic modelling of alteration and ore deposition, using software for reaction path calculations (e.g., HcH, Chiller), to quantitatively reproduce the pattern of alteration and mineral zoning observed in the deposit and relate them to those observed in other tin veins/lodes.